Toward LISA-Accurate Binary-Black-Hole Waveforms: Waveform Hybridization and Strong-Field Matching

Thesis by
Dongze Sun

In Partial Fulfillment of the Requirements for the
Degree of
Doctor of Philosophy

CALIFORNIA INSTITUTE OF TECHNOLOGY
Pasadena, California

2026
Defended May 26, 2026

Dongze Sun
ORCID: 0000-0003-0167-4392

ACKNOWLEDGEMENTS

I would first like to thank my thesis advisor, Saul Teukolsky, and my co-advisor, Mark Scheel. They have supported me with extraordinary generosity throughout my Ph.D., in project discussions, paper writing, code debugging, job applications, and many moments when I needed guidance. I have learned a great deal from both of them, not only about physics, but also about what it means to do science carefully and honestly.

One example I learned from Saul is the importance of scientific rigor. An idea that appears to work is not necessarily an idea that is correct. It is not enough to follow a method because it seems successful, or because it has become the common way of doing things. One must understand why it works, what assumptions it rests on, and where those assumptions may fail. The correct way is often more difficult than the common way, but "This is the way". I am deeply grateful to Saul and Mark for teaching me this standard of work, and for showing me, by example, how patience, precision, and integrity shape good science.

I would also like to thank Leo Stein. Much of the work in this thesis was done in collaboration with Leo, and he has been like an additional advisor to me. I have benefited enormously from his insight, generosity, and guidance. Many of the ideas in this thesis became clearer through our discussions, and I am grateful for the care and depth he brought to our collaborations.

I am grateful to my main collaborators, Nils Vu, Béatrice Bonga, Michael Boyle, Keefe Mitman, and Vijay Varma. I especially thank Nils and Béatrice for their generous support during my postdoctoral applications. I also thank Mike and Keefe for developing much of the infrastructure for asymptotic frame transformations that played an important role in my work.

I would also like to thank all the contributors to the SpEC and SpECTRE codes. Most of my research has been built on these two numerical-relativity codes. I am grateful to the SXS Collaboration for providing an extraordinary scientific environment, as well as the resources, collaborations, and support that made this work possible. This thesis stands on a large foundation of shared effort, and I am fortunate to have worked within a community that has built so much with such care.

I thank my parents, who raised me with unconditional love, patience, and trust. They gave me the freedom to follow my own path, respected my choices even when those choices took me far from home, and supported me through every uncertainty along the way. Their love has been the quiet ground beneath everything I have done, giving me strength in difficult times and joy in good ones. Whatever I have accomplished in these years carries their love within it.

I also thank my partner, Qing Dai, who has been beside me through the long and often difficult years of graduate school. Qing has shared with me not only the burdens of uncertainty and work, but also the warmth, tenderness, and closeness that made these years deeply human. Her love and companionship have given me comfort, courage, and happiness, and I am deeply grateful to have walked this part of life with her.

Finally, I would like to thank my friends: Guido Da Re, Himanshu Chaudhary, Kyle Nelli, Linhao Ma, Yoonsoo Kim, Sarah Habib, Isabella Pretto, Iago Mendes, Yaozhong Shi, Sihe Chen, and many others. I have learned so much from our countless discussions, and I am grateful for the many wonderful moments we have shared together: from the bottom of the Grand Canyon to the summit of Mount Whitney, from the shadow of a total solar eclipse to the glow of the northern lights. These years were shaped not only by equations, simulations, and papers, but also by friendship, laughter, and the landscapes we crossed together. I am very lucky to have you in my life.

ABSTRACT

The next generation of gravitational-wave detectors will require waveform models that are both substantially longer and substantially more accurate than those used for current ground-based observations. This requirement is especially important for massive binary black holes observed by the Laser Interferometer Space Antenna (LISA), for which signals can remain in band for hundreds to thousands of orbits and can accumulate signal-to-noise ratios large enough that small modeling errors become measurable. At this accuracy, waveform modeling is not only a problem of improving individual approximation schemes. It is also a problem of constructing controlled interfaces between the different descriptions used to model a binary black hole.

This dissertation develops a framework for constructing LISA-accurate binary-black-hole waveforms by connecting post-Newtonian theory, numerical relativity, and black-hole perturbation theory in a consistent way. The first part of the dissertation formulates the LISA-driven accuracy requirements and develops a post-Newtonian–numerical-relativity hybridization framework for producing long waveforms. In this framework, the waveforms are compared at future null infinity after fixing the Bondi–Metzner–Sachs frame, and the intrinsic post-Newtonian parameters are determined as part of the matching procedure rather than assumed to be identical to the quasi-local parameters used to label the numerical-relativity simulation. This construction makes waveform hybridization not only a method for extending waveform duration, but also a diagnostic of asymptotic-frame errors, numerical errors, post-Newtonian truncation errors, and parameter-definition errors.

The second part of the dissertation addresses the parameter-definition problem directly. The masses and spins used in post-Newtonian theory, numerical relativity, and black-hole perturbation theory are physically meaningful within their own constructions, but they are not automatically identical at finite binary separation. To relate these quantities from first principles, this dissertation develops a strong-field matching framework in which black-hole perturbation theory provides the local inner-zone description near each black hole. By constructing gauge-preserving coordinate transformations between local comoving coordinates and the global coordinates used by post-Newtonian theory or numerical relativity, the framework relates point-particle parameters, local black-hole parameters, and quasi-local horizon quantities through the spacetime geometry itself. This provides a route toward parameter

maps that can be used in waveform hybridization, numerical-relativity catalogs, and gravitational-wave inference.

The final part of the dissertation develops analytical and numerical infrastructure needed for this program. On the analytical side, the dissertation studies the convergence and regime of validity of high-order post-Newtonian information by comparing successive post-Newtonian truncation orders with a long, high-accuracy numerical-relativity simulation after BMS-frame fixing and parameter fitting. This comparison identifies the velocity range in which higher post-Newtonian orders improve agreement with numerical relativity and the region near merger where the expansion loses quantitative reliability. On the numerical side, the dissertation develops gauge boundary conditions in the Spectral Einstein Code that suppress long-timescale coordinate drift in binary-black-hole simulations, improving the quality of the numerical data needed for precision hybridization and strong-field matching.

Together, these results show that LISA-accurate waveform modeling requires simultaneous control of waveform length, asymptotic frame, intrinsic parameter definitions, post-Newtonian truncation error, and numerical gauge effects. The dissertation therefore provides a framework in which hybridization, strong-field parameter matching, and gauge-controlled numerical relativity become complementary parts of a single program for precision binary-black-hole waveform modeling.

PUBLISHED CONTENT AND CONTRIBUTIONS

[1] Dongze Sun et al. "Hybridization-guided numerical-relativity requirements for LISA massive-black-hole binaries". to be submitted soon.
D.S. did all the calculations, developed the relevent code module, analyzed the data, and wrote the manuscript.

[2] Dongze Sun et al. "Strong-Field Matching for PN–BHPT–NR Parameter Maps in Binary Black Holes". to be submitted soon.
D.S. conceived the framework, did all the calculations, developed the relevent code module, performed simulations, analyzed the data, and wrote the manuscript.

[3] Dongze Sun et al. "Convergence of post-Newtonian for quasi-circular non-precessing comparable mass ratios BBHs". In: (May 2026). arXiv: 2605.20562 [gr-qc].
D.S. did all the calculations, developed the relevent code module, analyzed the data, and wrote most of the manuscript.

[4] Dongze Sun et al. "Gauge Boundary conditions to mitigate center-of-mass drift in BBH simulations". In: *Physical Review D* 113 (2026), p. 044016. DOI: 10.1103/b1cd-qysb. arXiv: 2510.25465 [gr-qc].
D.S. conceived the framework, did all the calculations, developed the relevent code module, performed simulations, analyzed the data, and wrote the manuscript.

[5] Guido Da Re et al. "Modeling the BMS transformation induced by a binary black hole merger". In: *Physical Review D* 111 (2025), p. 124019. DOI: 10.1103/PhysRevD.111.124019. arXiv: 2503.09569 [gr-qc].
D.S. participated in the discussions, wrote and debugged some of the code.

[6] Mark A. Scheel et al. "The SXS Collaboration's third catalog of binary black hole simulations". In: *Classical and Quantum Gravity* 42 (2025), p. 195017. DOI: 10.1088/1361-6382/adfd34. arXiv: 2505.13378 [gr-qc].
D.S. performed part of the simulations.

[7] Dongze Sun and Leo C. Stein. "Parameter matching between horizon quasi-local and point-particle definitions at 1PN for quasi-circular and non spinning BBH systems in harmonic gauge". In: (2025). arXiv: 2510.25618 [gr-qc].
D.S. conceived the framework, did all the calculations, and wrote the manuscript.

[8] Dongze Sun et al. "Optimizing post-Newtonian parameters and fixing the BMS frame for numerical-relativity waveform hybridizations". In: *Physical Review D* 110 (2024), p. 104076. DOI: 10.1103/PhysRevD.110.104076. arXiv: 2403.10278 [gr-qc].

D.S. developed the code package, did the calculations, analyzed the data, and wrote the manuscript.

[9] Guobin Mou et al. "Asymmetric eROSITA bubbles as the evidence of a circumgalactic medium wind". In: *Nature Communications* 14 (2023), p. 781. DOI: 10.1038/s41467-023-36478-0. arXiv: 2212.02270 [astro-ph.GA].
D.S. performed simulations and analyzed the data.

[10] Dongze Sun. *NRPNHybridization*. https://github.com/dongzesun/NRPNHybridization.
D.S. developed the code package.

[11] *The Spectral Einstein Code*. http://www.black-holes.org/SpEC.html.
D.S. is one of the contributors to the package.

TABLE OF CONTENTS

Acknowledgements . . . iii
Abstract . . . v
Published Content and Contributions . . . vii
Table of Contents . . . viii
List of Illustrations . . . xii
List of Tables . . . xxiv
Chapter I: Introduction . . . 1
1.1 Accuracy requirements for LISA . . . 3
1.2 Waveform hybridization as a response to the LISA requirement . . . 4
1.3 The parameter-definition problem . . . 6
1.4 Strong-field matching as the central framework . . . 9
1.5 Analytical and numerical waveform infrastructure . . . 12
1.6 Future directions . . . 14
1.7 Dissertation outline . . . 16

Part I Waveform Accuracy and Hybridization **23**

Chapter II: Hybridization-guided numerical-relativity requirements for LISA massive-black-hole binaries . . . 24
2.1 Introduction . . . 25
2.2 Waveform-Error Target . . . 27
2.3 Hybridization Requirements . . . 28
2.4 Hybridization Frequency . . . 29
2.5 NR Accuracy Requirement . . . 30
2.6 Intrinsic-Parameter and Frame Tolerances . . . 31
2.7 Summary of Requirements . . . 32
2.8 SXS Catalog Audit . . . 34
2.9 Conclusion . . . 35
Chapter III: Optimizing post-Newtonian parameters and fixing the BMS frame for numerical-relativity waveform hybridizations . . . 40
3.1 Introduction . . . 41
3.2 Waveforms . . . 44
3.3 Matching PN and NR parameters . . . 48
3.4 Hybridization procedure . . . 55
3.5 Results . . . 59
3.6 Sources of error . . . 66
3.7 Choice of matching window . . . 72
3.8 Conclusions . . . 82

Part II Strong-Field Matching 93
Chapter IV: Parameter matching between horizon quasi-local and point-particle definitions at 1PN for quasi-circular and non-spinning BBH systems in harmonic gauge . . . 94
4.1 Introduction . . . 95
4.2 Mass Definitions in PN and NR . . . 99
4.3 Constructing global metric . . . 101
4.4 Slicing condition . . . 109
4.5 AH quasi-local mass . . . 110
4.6 Conclusions . . . 113
Chapter V: Strong-Field Matching for PN–BHPT–NR Parameter Maps in Binary Black Holes . . . 117
5.1 Introduction . . . 117
5.2 PN–NR matching and BHPT as a strong-field bridge . . . 120
5.3 Coordinate transformations and conventions . . . 122
5.4 Elliptic equation for the residual map . . . 123
5.5 Horizon-regular inner boundary condition . . . 125
5.6 Outer boundary surface and angular relabeling . . . 126
5.7 Mass update from monopolar residuals . . . 129
5.8 Iterative matching procedure . . . 130
5.9 Numerical setup and results . . . 131
5.10 Conclusions . . . 137

Part III Applications, Infrastructure, and Outlook 143
Chapter VI: Convergence of Post-Newtonian Theory for Quasi-Circular Non-Precessing Comparable-Mass-Ratio Binary Black Holes . . . 144
6.1 Introduction . . . 144
6.2 Method . . . 147
6.3 Results . . . 151
6.4 Discussion and conclusions . . . 154
Chapter VII: Gauge Boundary Conditions To Mitigate Center-of-Mass Drift In BBH Simulations . . . 163
7.1 Introduction . . . 163
7.2 CoM drift as a gauge effect . . . 168
7.3 Sommerfeld boundary condition . . . 169
7.4 CoM dynamics . . . 173
7.5 Modified boundary conditions . . . 176
7.6 The effect on waveforms . . . 188
7.7 Alternative Boundary Conditions . . . 189
7.8 Conclusions . . . 192
Chapter VIII: Future Directions . . . 198
8.1 Closing the PN–BHPT–NR parameter map at high accuracy . . . 198
8.2 Strong-field matching for generic binary configurations . . . 198
8.3 Parameter- and gauge-consistent waveform hybridization . . . 199

8.4 Strong-field QNM extraction 200
8.5 Spatial hybrids for EMRI modeling 201
8.6 Toward a unified interface between theory, simulation, and observation 201

LIST OF ILLUSTRATIONS

Number *Page*

1.1 Schematic domains of applicability of PN theory, NR, and BHPT for BBHs with comparable mass. b is the binary seperation, and r is the distance between the field point to the BH's central singularity. The grey regions show the overlap buffer zone between different descriptions. 2

1.2 Schematic of the near zone, inner zone, and buffer region used in strong-field matching. The PN metric $g_{ab}^{\rm PN}$ describes the binary for $r \gg m$, while the inner-zone metric $\bar{g}_{\bar{a}\bar{b}}^{\rm IZ}$ describes a tidally perturbed black hole in comoving coordinates for $r \ll b$. The two descriptions overlap in the buffer region $m \ll r \ll b$. The NR metric $g_{ab}^{\rm NR}$ is valid in the whole domain. The barred indices refer to tensor components in the comoving coordinates, while unbarred indices refer to components in the inertial coordinates. 10

2.1 Distribution of $\mathcal{M}_{\rm NR}[f_{\rm hyb}^{\nu=0.25}, f_{\rm merger}]$ for the public SXS waveform catalog, evaluated for $M = 10^6 M_\odot$ and $\rho = 10^3$. The mismatches are computed for the highest two resolutions avaliable, after aligning their time and phase at merger. Each histogram bin is split into simulations that satisfy the length requirement ($M\omega_{22}^{\rm clean} \leq M\omega_{22}^{{\rm hyb},\nu=0.25}$; lower portion) and those that fail it (upper portion). The vertical dashed line marks the required loud-case phase-accuracy threshold. Simulations to the left of the line and in the lower stack satisfy both the phase-accuracy and length requirements. We have dropped the deprecated simulations. 34

3.1 NR and PN parameter spaces are distinct because of the different gauges and different definitions of parameters used in PN and NR models. The maps into infinite-dimensional waveform space differ at each NR resolution and PN order. We optimize PN parameters and adjust the BMS frame to minimize the "vertical" difference transverse to the images of NR and PN parameter spaces. 43

3.2 The parameter space of the NR simulations that we use. The color shows the length of the waveform in terms of orbits. 47

3.3 The profile of the cost function $\mathcal{E}$ with respect to parameters for system SXS:BBH:2617. The matching window is 20 orbits long, and ends 8000 M before merger. In each plot, the 10 other parameters are fixed to their best-fit values. The slanting long and narrow valleys show the degeneracy between these parameters, which can drastically slow down the optimization. 51

3.4 The profile of the cost function $\mathcal{E}$ with respect to the new parameters for system SXS:BBH:2617. The matching window is 20 orbits long, and ends at 8000 M before merger. In each plot, the 10 parameters that are not varied are fixed at the best-fit values. These new parameters are no longer degenerate. If the cost function has a narrow diagonal valley, as in Fig. 3.3, the optimizer tends to zigzag within the valley, leading to a significant slowdown in the optimization process. However, if the valley aligns with an axis, the optimizer can easily re-scale the axis, leading to more efficient optimization. 52

3.5 Strain and residual of two PN waveforms, for a test in which we match the two waveforms by varying the parameters of one of them. The target PN waveform has parameters $q = 1.5$, $M = 1.0$, $\chi_1 = (0.5, 0.2, 0.3)$, $\chi_2 = (0.1, 0.3, 0.4)$, and is rotated away by $\mathbf{R} = \exp(0.05, 0.02, 0.03)$ from the original frame in which the PN waveform is generated. The initial guess is $q = 1.65$, $M = 1.05$, $\chi_1 = (0.42, 0.24, 0.47)$, $\chi_2 = (0.01, 0.20, 0.41)$. The parameters obtained by the optimization are $q = 1.500004$, $M = 1.000005$, $\chi_1 = (0.10001, 0.200002, 0.30003)$, $\chi_2 = (0.399994, 0.09998, 0.20006)$. The matching window is the region between two vertical dotted lines, which is 5000 M long. 54

3.6 The convergence of different parametrization methods for a PN-PN matching test, in which we match the two waveforms by varying the parameters of one of them. The target PN waveform has parameters $q = 1.5$, $M = 1.0$, $\chi_1 = (0.5, 0.2, 0.3)$, $\chi_2 = (0.1, 0.3, 0.4)$, and is rotated away by $\mathbf{R} = \exp(0.0, 0.0, 0.05)$ from the original frame in which the PN waveform is generated. The initial guess is $q = 1.65$, $M = 1.05$, $\chi_1 = (0.42, 0.24, 0.47)$, $\chi_2 = (0.01, 0.20, 0.41)$. The matching window is $5000\,M$ long. The result using the new parametrization in Eqs. (3.6) and (3.7) is shown as the red curve, which converges much faster and better than the original PN parametrization, which is shown as the blue dashed curve. The green dotted curve also uses the original PN parametrization but incorporates the $\frac{x_0}{2}\mathbf{\Omega}_{\rm tot}$ term in the frame rotor $\mathbf{R}$ defined in Eq. (3.7). In other words, it uses (x_0, q, M, χ_1 and χ_2) and (x_9 through x_{11}) as parameters. The green dotted curve shows better convergence than the blue dashed curve. 55
3.7 The convergence of the 12-D nonlinear least-squares optimization for system SXS:BBH:2617 in the second iteration of step 6 of the procedure in Sec. 3.4, using the parameters from the first iteration as the initial guess. The horizontal axis is the iteration number for the 12-D optimization. The end of the matching window is $5000\,M$ before merger, and is 20 orbits long. The blue curve shows the value of the cost function, and the green solid and red dotted curves show the reduction of the function value and the norm of change in parameters after each iteration. The norm of the gradient of the cost function is shown in dashed purple. 56

3.8 The convergence of iterations of step 6 of the procedure in Sec. 3.4 for system SXS:BBH:1414. The 0th iteration is step 3 of the procedure in Sec. 3.4, for which the NR waveform is mapped into the superrest frame, and for this iteration the error does not include the $m = 0$ modes since the value of the strain in these modes in the superrest frame does not agree with PN. For the other iterations, the NR waveform is mapped to the PN BMS frame, and the errors include the $\ell \leq 8$ modes. The blue curve uses a 10-orbit long matching window that ends 8000 M before merger, and the green curve uses a 5-orbit long matching window that ends 2000 M before merger. Both curves converge within 4 iterations. The cost function for the shorter matching window is smaller and converges less rapidly than the case with a longer matching window, likely because the short waveforms are being overfit. This overfitting is explored in Sec. 3.7. 57

3.9 Strain and residual of the hybridized spin-aligned system SXS:BBH:1412. The matching window is the region between the two vertical dotted lines, which is 20 orbits long and ends at $-6000\,M$. The blue, green and red curves in the upper panel are the strain modes of the NR, PN and hybrid waveforms. The blue curves in the lower panel are the residuals between the NR and PN strain modes. 60

3.10 Strain and residual of the hybridized precessing system SXS:BBH:2619. The matching window is the region between the two vertical dotted lines, which is 20 orbits long and ends at $-6000\,M$. The blue, green and red curves in the upper panel are the strain modes of the NR, PN and hybrid waveforms. The blue curves in the lower panel are the residuals between the NR and PN strain modes. 61

3.11 Hybridization errors in the matching window, Eq. (3.5), for different waveforms and for different methods of choosing PN parameters and matching the BMS frame. See text for details. All the errors are measured after adjusting the 3-D rotation and time shift. The BMS frame for extrapolated waveforms cannot be modified using the method described in this paper because those waveforms do not have an accurate value of Ψ_2 to calculate the Moreschi supermomentum. We only adjust the BMS frame for CCE waveforms. Systems on the left of the vertical dotted line are spin-aligned systems; systems on the right are precessing systems, and systems are ordered left to right by χ_p. The mass ratios for SXS:BBH:2617–2635 systems are $1 < q < 10$ and for SXS:BBH:2636–2640 systems are $q \approx 8$. The matching window is 10 orbits. For systems other than the SXS:BBH:2636–2640 systems, the matching window ends 8000 M before merger. For the SXS:BBH:2636–2640 systems the matching window ends 5000 M before merger because these systems are not long enough. The brown markers use the full hybridization procedure described in Sec. 3.4. e is the eccentricity measured from the trajectory at the NR reference time, and $\Delta\phi$ is the dephasing between the two highest resolution NR runs of the last 20 orbits before merger. It is important to recognize that this dephasing does not directly reflect the inaccuracy of the NR waveforms, as the NR parameters within the matching window for different Levs can deviate by 10^{-2}, given their evolution over nearly a hundred orbits prior to the matching window. 63
3.12 The differences in parameters between NR and PN for selected waveforms hybridized using the procedure of Sec. 3.4. Plotted ΔX is $|X_{\rm NR} - X_{\rm PN}|$ for selected parameters X. Systems on the left of the vertical dotted line are spin-aligned systems; systems on the right are precessing systems, and systems are ordered left to right by χ_p. The mass ratio for SXS:BBH:2617–2635 systems are $1 < q < 10$, for SXS:BBH:2636–2640 systems are $q \approx 8$. The error bars show the uncertainties of the optimization, and the markers show the best-fit value of the parameters. 64

3.13 The differences in parameters between NR and PN with respect to $\mathcal{E}$ in a 10-orbit long matching window. Each color represents a different system. The points with the same color represent the same system with different matching windows. All the systems in this figure are precessing systems. 65
3.14 Hybridization error for different locations of the matching window for system SXS:BBH:1412. 67
3.15 The L^2 normalized error $\mathcal{E}$ versus eccentricity e for 10 different systems: SXS:BBH:1412–1416, SXS:BBH:1153, 1164, 1165, 1168; and the additional system 3618. We include SXS:BBH:3618 for reference as a higher-eccentricity point ($e = 0.0496$). It is spin-aligned with $\chi_1 = \chi_2 = 0.6$ and $q = 1.0$, and will be added to the public SXS catalog soon. The end time of the matching window is $-5000\,M$, and the length of the matching window is 10 orbits. The green dotted curve is a quadratic fit to the plotted points. 68
3.16 Measurement of eccentricity e from both strain and news (the time derivative of strain), and in different BMS frames, for system SXS:BBH:1412. When transforming to a superrest frame, the frame is determined from the middle of the inspiral. 69
3.17 Hybridization error, Eq. (3.5), inside the matching window for precessing systems SXS:BBH:2617–2635. The horizontal axis is the spin-precession parameter χ_p for the upper panel, and $S_\perp/M^2$ for the lower panel. Here $\boldsymbol{S}_i = \chi_i m_i^2$ is the spin angular momentum, and $S_\perp$ is the magnitude of the projection in the orbital plane. Results are shown for two different choices of the resolution parameter "Lev" used to compute the NR simulation. Lev4 uses a finer tolerance for the adaptive-mesh-refinement algorithm than Lev3, so Lev4 has smaller numerical errors. The additional purple markers use only the leading order spin-spin and spin-orbit terms in both strain and Ψ_M for Lev4, whereas the other markers use all PN terms listed in Sec. 3.2, which have higher order terms in the strain, but the same terms in Ψ_M. The matching window is 10 orbits long, and the end time is 8000 M before merger. 71

3.18 Test window error for 10 long waveforms from Fig. 3.11. The center of the test window is 30 orbits earlier than the center of the matching window. The matching window is the same with Fig. 3.11. For most systems, the optimization over PN parameters can result in smaller error in both the matching window and the test window. 72
3.19 The hybridization error for different lengths of matching window for spin-aligned system SXS:BBH:1412. We fix the end time of the matching window to be 5000 M before merger. The test window is 10 orbits long, and the center of the test window (in number of orbits) is 30 orbits earlier than the center of the matching window. "Lev" labels the resolution of the NR simulations, as in Fig. 3.17. 75
3.20 The residual of spin-aligned system SXS:BBH:1412 corresponding to the rightmost points for Lev3 in Fig. 3.19. The matching window is 50 orbits long and ends at 5000 M before merger, and the test window is 10 orbits long and immediately before the matching window. The error increases rapidly outside the matching window, so that the error in the test window is much larger than the error in the matching window. The error increases outside the matching window because of slight differences between the PN and NR waveforms. In this spin-aligned case, we use non-eccentric PN to hybridize with a slightly eccentric NR waveform. While we can minimize the error within the matching window, the inherent differences between the models prevent us from reducing the error outside. 76
3.21 The L^2 normalized error $\mathcal{E}$ in the matching window as a function of orbital angular velocity for system SXS:BBH:2621. The matching window is 10 orbits long, but the end time of the matching window is varied, and the orbital angular velocity is the mean value over the matching window. The test window is 10 orbits long, and the center of the test window (in number of orbits) is 30 orbits earlier than the center of the matching window. 78
3.22 The predicted L^2 normalized error $\mathcal{E}$ for a 10-orbit matching window based on Eq. (3.15). The horizontal axis is the approximate center of the matching window, where $\nu = m_1 m_2/(m_1 + m_2)^2$, and u is the retarded time. The vertical axis is the maximum of the in-plane component of the two dimensionless spin momenta. 79

3.23 The L^2 normalized error $\mathcal{E}$ for different lengths of the matching window for system SXS:BBH:2617. The test window is between 30 and 40 orbits before $-8000\,M$. We fix the start time of the matching window to be $8000\,M$ before merger. The upper and lower panel show $\mathcal{E}$ in the matching window and the test window, respectively. The dotted curves use extrapolated NR waveforms, while the solid curves use CCE NR waveforms. All the curves are obtained after adjusting the 3-D rotation and time shift, and all the curves using CCE waveforms are obtained after mapping to the PN BMS frame. In addition to the 3-D rotation and time shift, the green curves optimize all 12 parameters, which is the full hybridization procedure described in Sec. 3.4. 81
3.24 The L^2 normalized error $\mathcal{E}$ for different lengths of the matching window for system SXS:BBH:2617. The test window is between 30 and 40 orbits before $-8000\,M$. We fix the start time of the matching window to be $8000\,M$ before merger. The crosses use extrapolated NR waveforms, while the dots use CCE NR waveforms. All the data are obtained after adjusting the 3-D rotation and time shift, and all the dots using CCE waveforms are obtained after mapping to the PN BMS frame. The blue and the green data points are the same data as the blue and green curves in Fig. 3.23. The extrapolated waveforms all have the same error in the matching window, because for those waveforms the matching window error is dominated by incorrect gravitational-wave memory. 82
4.1 A schematic diagram showing the domain setup and symbols. 102
5.1 Schematic matching regions for a binary black-hole spacetime. PN theory describes the weak-field near zone and supplies long inspiral information; NR describes the nonlinear binary spacetime, including the strong-field neighborhoods of the horizons; BHPT describes the local inner zone of each black hole as a perturbed KS background. The present construction solves the NR–BHPT strong-field matching problem in one inner zone, providing the NR-side component of the PN–BHPT–NR parameter map. 121
5.2 Constant-Kretschmann outer matching surface for the $b = 80M$ equal-mass, nonspinning SpECTRE test, shown in NR inertial coordinates. 132

5.3 Time derivative of the NR gauge source on the $x^0 = 500M$ slice, evaluated in the corotating frame. Together with the computed ξ^0, this diagnostic shows that the neglected term $\xi^0 \partial_0 H^a_{\mathrm{comov}}$ is of order 10^{-6} in the matching domain. 133

5.4 Convergence of the local matching iteration on the line $y = z = 0$. The left column shows the pulled-back metric components g_{00}, g_{xx}, and the Kretschmann scalar K, compared with the Schwarzschild Kerr–Schild target. The right column shows the corresponding residuals. The excised region lies between the two inner vertical lines, and the outer matching radius is $R_{\mathrm{out}} = 3M$. The mass is held fixed at $m = 0.5M$ through iteration 012. Beginning with iteration 013, the mass inferred from the $\ell = 0$ residual of g_{00} is fed back into the Kerr–Schild target, the elliptic operator, and the boundary conditions. The post-update curves show that the monopole mass calibration removes the dominant scalar offset while leaving the expected nonmonopolar finite-separation residuals. 134

5.5 Spherical-harmonic amplitudes of the transformed-metric residuals on coordinate spheres in the local KS frame. The panels show the modes of Δg_{00}, Δg_{rr}, and $\Delta K/K_{\mathrm{KS}}$, where K is the Kretschmann scalar. Up to Iteration 012 the KS mass is held fixed at $m = 0.5M$. The monopole mass update is enabled starting at Iteration 013, and the Iteration 024 residuals show the result after the mass calibration has converged. 135

5.6 Mass correction δm_{00} fitted from the sphere-averaged residual of g_{00}. The KS mass is held fixed through iteration 12, so the early plateau measures the monopole mismatch of the fixed-mass solve. After the mass update is activated at iteration 13, the correction decreases to the 10^{-6} level. 135

5.7 KS mass m used in the coordinate operator, boundary conditions, and target metric. The mass is fixed to $0.5M$ through iteration 12. Once the monopole update is activated, the mass converges to $m_{\mathrm{KS}} \simeq 0.50049M$, corresponding to a fractional offset $\simeq 1.8 \times 10^{-4}$. 136

5.8 Final fractional mass offset $|\Delta m|/m$ obtained from the monopole part of Δg_{00} as a function of binary separation b/M. The offset decreases at larger separation, as expected for a finite-separation correction to the identification between the nominal NR mass and the local KS/BHPT mass parameter. 136

6.1 Solid colored curves: differences in energy flux $\Delta\dot{E}$ between NR and different PN order. Dotted black: the NR $\dot{E}$ from the highest resolution. Solid black: $\Delta\dot{E}$ between two highest NR resolutions after they are mapped to the same BMS frame, which measures the NR truncation error. Dotted brown line: the extrapolated 6PN $\dot{E}$, fitted in the region $0.32 \leq v \leq 0.4$. The slope k (rounded to the nearest integer in the legend) for the solid colored lines are fitted in the region $0.22 \leq v \leq 0.3$, which is the region between the two vertical dotted lines. The PN systems are frame-fixed in a 5-orbit matching window starting $v = 0.21$, or around 60 orbits before merger (shortly after the junk radiation left the system).

* The 6PN energy fluxes are not complete and we have only included the known results in the EMR limit. 152

6.2 The energy flux residual $\Delta\dot{E}$ between different PN orders and NR at some v values, with respect to the PN truncation orders. These are vertical slices of Fig. 6.1 at different v. The cross markers appearing at 6PN are the extrapolated data from the dotted brown line of Fig. 6.1. 153

7.1 The CoM displacement from the origin for different outer boundary radii. The system is equal mass and non-spinning. 166

7.2 The upper panel shows the evolution of CoM coordinates and the lower panel shows their corresponding CoM charge. The outer boundary radius is set as $100\,M$. 167

7.3 Reflection coefficient $|\rho^{\ell}_{\ell' m'}|$ for different ℓ. Given $m' = 0, \ell' = \ell, k = 1, t = 0, \theta = \phi = 0$. 172

7.4 Reflection coefficient $|\rho|$ for a spherical wave whose source is localized at $\mathbf{r_s}/R = 0.15$, with $k = 1, t = 0, \theta = \phi = 0$. 173

7.5 A schematic diagram showing the domain setup and symbols. 174

7.6 The green and blue lines are the results for $R = 100\,M, \lambda = 5$ and $R = 200\,M, \lambda = 80$, respectively, under gauge boundary condition Eq. (7.32). The wider gray lines are there fits. The system is equal-mass and non-spinning. The initial separation is $19\,M$ and the merger time is around $11000\,M$. 178

7.7 Different results with similar $(\lambda - 1)/R^2$ ratio under gauge boundary condition Eq. (7.32). The system is equal-mass and non-spinning. The initial separation is $19\,M$ and the merger time is around $11000\,M$. 181

7.8 CoM drift and velocity under the gauge boundary condition Eq. (7.34) with $\lambda = 1 + (R/100)^2$. The upper panel shows the CoM drift and the lower panel shows the CoM velocities. The black curves are the results obtained using the original Sommerfeld boundary condition, and the other curves are results with the new boundary condition for $R = 100M, 200M$ and $400M$. The system is equal-mass and non-spinning. The initial separation is $19\,M$ and the merger time is around $11000\,M$. 182

7.9 CoM drift and velocity under gauge boundary condition Eq. (7.32) with $\mathbf{r_0}$ specified by Eq. (7.38), where $\lambda = 1 + (R/100)^2$. The upper panel shows the CoM drift and the lower panel shows the CoM velocities. The black curves are the results obtained using the original Sommerfeld boundary condition, and other curves are results under the new boundary condition for $R = 200M, 400M$ and $800M$. The system is equal-mass and non-spinning. The initial separation is $29\,M$ and the merger time is around $50000\,M$. 183

7.10 CoM drift and velocity under gauge boundary condition Eq. (7.39) with $\mathbf{r_0} = \mathbf{r}_s + \eta R \dot{\mathbf{r}}_s$, where $\eta = R/4$. The upper panel shows the CoM drift and the lower panel shows the CoM velocities. The black curves are the results obtained using the original Sommerfeld boundary condition, and the other curves are results under the new boundary condition for $R = 200M, 400M$ and $800M$. The system is equal-mass and non-spinning. The initial separation is $29\,M$ and the merger time is around $50000\,M$. 184

7.11 CoM trajectory under gauge boundary condition Eq. (7.32) with $\mathbf{r_0}$ specified by Eq. (7.38), where $\lambda = 1 + (R/100)^2$, with a zoom-in near the origin in the upper smaller panel. The black curve is obtained using the original Sommerfeld boundary condition, and the blue curve is obtained using the new boundary condition. The system has $q = 1$, $\chi_1 = (0.1, 0.2, 0.3)$, $\chi_2 = (0.2, 0.4, 0.1)$, and $R = 200\,M$. The initial separation is $29\,M$ and the merger time is around $65000\,M$. The vectorial displacement of the CoM under the new BC is shown in Fig. 7.12, and the overall CoM drifting is shown in Fig. 7.13. 185

7.12 The x and y coordinates of CoM under the new boundary condition with the same configuration with Fig. 7.11. 186

7.13 CoM drift and velocity under gauge boundary condition Eq. (7.32) with $\mathbf{r_0}$ specified by Eq. (7.38), where $\lambda = 1 + (R/100)^2$. The upper panel shows the CoM drift and the lower panel shows the CoM velocities. The black curves are the results obtained using the original Sommerfeld boundary condition, and the other curves are results under new boundary condition for $R = 200M, 400M$ and $800M$. The system has $q = 1$, $\chi_1 = (0.1, 0.2, 0.3)$, and $\chi_2 = (0.2, 0.4, 0.1)$. The initial separation is $29\,M$ and the merger time is around $65000\,M$. The black curves end earlier because the CoM displacement gets so large that the simulation crashes. 187

7.14 Waveform differences under modified and original gauge boundary conditions for two systems. 188

7.15 CoM drift and velocity for an equal-mass and non-spinning system with an initial separation of $29\,M$, outer boundary radius $R = 200\,M$, and the merger time is around $50000\,M$. The upper panel shows the CoM drift and the lower panel showx the CoM velocities. The black curves are the results obtained using the original Sommerfeld boundary condition Eq. (7.13). The blue curves are results under gauge boundary condition Eq. (7.32), with $\mathbf{r_0}$ specified by Eq. (7.38), where $\lambda = 1 + (R/100)^2$. The green curves are results under the gauge constraint damping boundary condition Eq. (7.47). The green curves end earlier because the CoM displacement gets so large that the simulation crashes. 192

LIST OF TABLES

Number *Page*

2.1 Representative hybridization, NR-accuracy, intrinsic-parameter, and boost requirements. All masses are detector-frame masses. We take $q = 1$, $\nu = 1/4$, $f_{\rm low} = 10^{-4}$ Hz, and $\mathcal{M}_{\rm target} = 1/(2\rho^2)$. The typical noise value $S_n^{\rm typ} \equiv S_n(f_{\rm typ})$, with $f_{\rm typ} = \sqrt{f_{\rm low} f_{\rm merger}}$, is evaluated using the effective LISA sensitivity curve of Ref. [32]. The residual 4.5PN phase coefficient is using $\beta_9 = (\pi M)^{4/3}$. Dashes indicate that the analytic-truncation condition gives $f_{\rm hyb} > f_{\rm merger}$, so the analytic model itself is accurate enough to describe the inspiral for detection, and NR is only needed for the merger and ringdown part. For the very loud case, the $f_{\rm hyb}$ lies below $f_{\rm low}$, so a LISA-accurate hybrid would therefore require either a more accurate analytic inspiral or NR coverage over the full observing band from $f_{\rm low}$ to $f_{\rm merger}$. 33

6.1 The intrinsic parameters for the NR and PN systems. 150

Chapter 1

INTRODUCTION

The direct observation of gravitational waves (GWs) from compact binary coalescences has made it possible to study these systems with increasing precision [1, 2]. GW signals probe the strong-field, nonlinear dynamics of gravity, reveal the properties of compact objects, and constrain the astrophysical processes that govern binary formation and evolution [3, 2, 4]. As detector sensitivity improves, waveform models play an increasingly important role in the interpretation of GW data [5, 6, 7]. Waveform models are no longer used only for signal detection or approximate source characterization, but also play a central role in determining the accuracy of parameter estimation, the robustness of tests of general relativity (GR), and the extent to which genuine physical effects can be separated from modeling limitations [7, 5, 3, 8].

A waveform model suitable for precision inference must remain accurate over long phases of inspiral, remain reliable in the nonlinear strong-field regime, and assign source parameters in a way that remains physically consistent throughout the construction [5, 6, 9, 10]. In this setting, waveform accuracy depends not only on the quality of the description in each regime, but also on the consistency with which different regimes are connected to one another [11, 12, 13, 14].

This challenge is particularly significant for binary black holes (BBHs), because no single theoretical framework can describe the full signal with both sufficient accuracy and sufficient efficiency, as shown in Fig. 1.1 [15, 16, 17]. Post-Newtonian (PN) theory provides an efficient description of the weak-field inspiral, with corrections that can be incorporated systematically order by order in the expansion, but the expansion breaks down as the binary approaches merger [15, 18]. Numerical relativity (NR) provides the most accurate description of the late inspiral, merger, and ringdown, but remains too computationally expensive to cover the full signal duration and parameter space relevant for future detectors; in addition, numerical errors accumulate over very long simulations [19, 16, 9, 20]. Black-hole perturbation theory (BHPT) naturally describes the strong-field geometry near each black hole, but is only directly applicable when the black holes (BHs) are well separated or when the mass ratio is large [21, 17]. It can also be used to describe the ringdown phase, when the merged black hole settles down to equilibrium [22]. Long and accurate

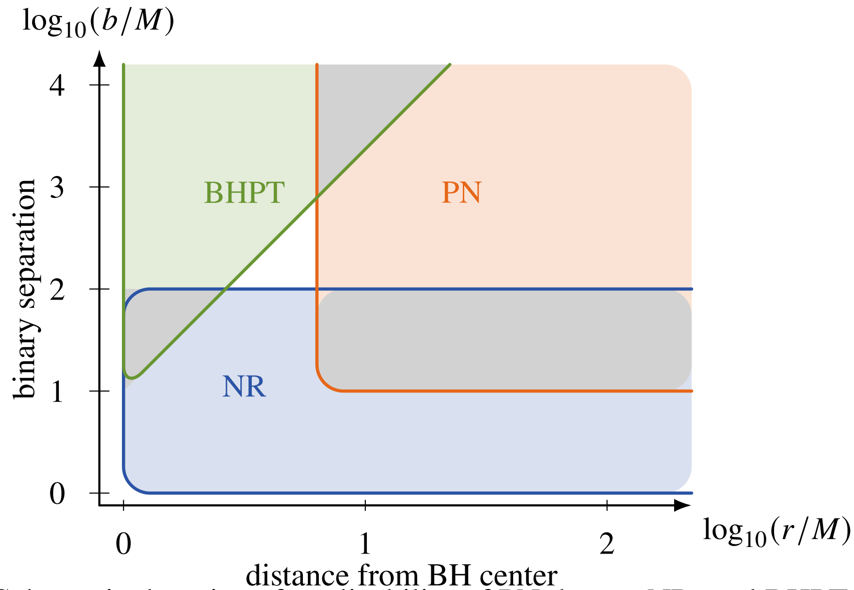

Figure 1.1: Schematic domains of applicability of PN theory, NR, and BHPT for BBHs with comparable mass. b is the binary seperation, and r is the distance between the field point to the BH's central singularity. The grey regions show the overlap buffer zone between different descriptions.

waveforms therefore cannot be obtained from any single framework alone, but must be built by matching together descriptions that are valid in different regimes [11, 12, 23].

This dissertation develops a framework for constructing BBH waveforms at the accuracy and signal durations required by next-generation detectors such as the Laser Interferometer Space Antenna (LISA), by connecting the different descriptions used in BBH modeling in a consistent way. More broadly, the goal is to build a bridge between PN, NR, BHPT, and ultimately GW observations [23, 24].

The remainder of this introductory chapter reviews the waveform-accuracy requirements motivated by next-generation detectors, particularly LISA, and explains how waveform hybridization enters the corresponding error budget. It then summarizes the main theoretical descriptions used in BBH modeling, namely PN theory, NR, and BHPT, with emphasis on their respective regimes of validity and on the limitations that prevent any one of them from describing the full signal alone. The chapter also discusses two issues that arise in connecting these descriptions: the choice of asymptotic frame at future null infinity $\mathscr{I}^+$ and the consistent identification of intrinsic parameters such as masses and spins across different theoretical descriptions [25, 26, 27, 28, 23, 24]. It concludes with a detailed outline of the remaining chapters of the dissertation.

1.1 Accuracy requirements for LISA

The Laser Interferometer Space Antenna (LISA) provides the main observational motivation for the waveform-modeling project developed in this dissertation. LISA will observe GWs in the millihertz band, where massive black-hole binaries can remain visible for long durations and can accumulate very large signal-to-noise ratios (SNRs) [29, 30, 31, 32, 33]. These properties make LISA qualitatively different from current ground-based observations of stellar-mass binary black holes. The relevant signals are not only loud; they also contain long inspirals before merger. As a result, small phase errors, imperfect mode content, inconsistent frame choices, or small errors in the physical parameters of the source can accumulate over the observed signal and become measurable [7, 5, 6, 31].

A useful way to estimate the required waveform accuracy is to compare the waveform error with the statistical uncertainty set by detector noise [7, 5, 6]. Let $h_{\rm exact}$ denote the exact waveform and $h_{\rm model}$ a model waveform. The modeling error is

$$\delta h = h_{\rm model} - h_{\rm exact}. \tag{1.1}$$

The standard noise-weighted inner product is

$$\langle a|b\rangle = 4\,\mathrm{Re}\int_0^\infty \frac{\tilde{a}(f)\tilde{b}^*(f)}{S_n(f)}\,df, \tag{1.2}$$

where $S_n(f)$ is the detector noise power spectral density [34, 35, 36]. The SNR of the signal is

$$\rho^2 = \langle h|h\rangle. \tag{1.3}$$

For parameter estimation, a common accuracy criterion is that the modeling error should be small compared with the statistical error scale, so that waveform systematics do not dominate the inference [5, 6, 7]. In terms of the mismatch,

$$\mathcal{M}(h_1, h_2) = 1 - \max_{\Delta t, \Delta\phi} \frac{\langle h_1|h_2\rangle}{\sqrt{\langle h_1|h_1\rangle\langle h_2|h_2\rangle}}, \tag{1.4}$$

here the maximization over time and phase alignment will be discussed further in Sec. 3.3 of Chapter. 3. This requirement gives a characteristic target

$$\mathcal{M}_{\rm target} \sim \frac{1}{\rho^2}, \tag{1.5}$$

up to factors that depend on the precise accuracy criterion and on which waveform parameters are optimized over [35, 5, 6]. For a LISA massive black-hole binary with $\rho \sim 10^3$, this estimate gives $\mathcal{M}_{\rm target} \sim 10^{-6}$ [7, 33, 31]. This number should not be interpreted as a universal threshold for every source or every analysis. It is instead a useful scale: LISA can make the acceptable waveform error orders of magnitude smaller than what is required for current ground-based detectors.

The long duration of LISA signals makes this requirement especially restrictive. A waveform with a small instantaneous error can still fail the accuracy requirement if the error accumulates coherently over many cycles. For massive black-hole binaries, the relevant signal may include hundreds to thousands of orbits in band, depending on the total mass, mass ratio, redshift, and the low-frequency cutoff of the analysis [29, 32, 31]. The accuracy requirement therefore applies to the full observable waveform, not only to the last few orbits before merger. In particular, the inspiral phasing, the transition to merger, the ringdown, and the physical interpretation of the source parameters must all be controlled at a level compatible with the same error budget.

For the binary black-hole systems studied in this dissertation, the LISA requirement can be summarized as follows. A useful waveform model must be long enough to cover the signal in band of LISA, accurate enough to keep the mismatch at or below the scale set by ρ^{-2}, and physically consistent enough that the parameters inferred from the model correspond to the same binary system throughout the calculation. The last condition is essential because LISA accuracy is not limited only by truncation errors in a single approximation scheme. At the level of $\mathcal{M} \sim 10^{-6}$, errors in frame choices, time and phase alignment, intrinsic parameter (mass and spin) definitions, and finite-separation parameter identification can become part of the measurable waveform error.

These considerations set the scale for the rest of the dissertation. Chapter 2 develops the LISA-oriented waveform-accuracy requirements in more detail, with particular emphasis on signal duration, target mismatch, numerical-relativity accuracy, and the additional constraints introduced by waveform hybridization for massive black-hole binaries. The remaining chapters then address the theoretical and numerical ingredients needed to construct waveforms that can approach this accuracy scale [23, 24].

1.2 Waveform hybridization as a response to the LISA requirement

The LISA accuracy requirement cannot be met by relying on a single description of binary-black-hole dynamics. PN theory can describe the early inspiral efficiently, but its expansion in powers of the orbital velocity loses accuracy as the binary approaches merger [15]. NR provides the most accurate description of the late inspiral, merger, and ringdown, but simulations long enough to cover the full LISA signal are computationally expensive, and numerical errors accumulate over long evolutions [16, 9, 20]. BHPT gives a controlled description of perturbations of a black-hole spacetime, and is directly applicable to EMRIs, where the smaller object is treated as a perturbation of the larger black-hole background [21, 17]. For comparable-mass binaries, BHPT can describe the metric only in the local strong-field region near one black hole when the two black holes are sufficiently far apart [37, 38]. A long and accurate waveform must therefore combine information from different descriptions, as shown in Fig. 1.1.

Waveform hybridization provides a direct way to construct long BBH waveforms by combining the regimes in which PN theory and NR are most reliable [11, 12, 39, 40]. The basic idea is to use a PN inspiral waveform at early times and an NR waveform at late times, and to join the two in a window where both descriptions are expected to be accurate. If h_{PN} denotes the PN waveform and h_{NR} denotes the NR waveform, a schematic hybrid waveform can be written as

$$h_{\mathrm{hyb}}(t) = \left[1 - \tau(t)\right] h_{\mathrm{PN}}(t) + \tau(t) h_{\mathrm{NR}}(t), \tag{1.6}$$

where $\tau(t)$ is a smooth transition function that changes from 0 to 1 across the matching window. This expression is only schematic, because the two waveforms must first be placed in a common frame, assigned consistent intrinsic parameters, and aligned in time and phase [27, 28, 23]. At LISA accuracy, these operations become crucial components of the waveform construction.

The hybridization window introduces a direct tradeoff between analytic and numerical errors. If the matching is performed too late, the analytic inspiral waveform may already have accumulated a significant truncation error. If the matching is performed too early, the NR waveform must cover more orbits, increasing both computational cost and accumulated numerical error. The matching window must therefore be chosen so that the total error,

$$\delta h_{\mathrm{total}} = \delta h_{\mathrm{PN}} + \delta h_{\mathrm{NR}} + \delta h_{\mathrm{hyb}}, \tag{1.7}$$

remains below the accuracy scale required by the detector [5, 6]. Here δh_{PN} represents the PN truncation error, δh_{NR} represents the NR error, and δh_{hyb} represents the additional error introduced by the hybridization procedure itself. The last term includes errors from the time and phase alignment, asymptotic frame fixing, and the identification of masses and spins between the two descriptions [27, 28, 23, 24].

Hybridization provides the central link between the LISA accuracy requirement and the technical chapters that follow. In Chapter 2, the target mismatch sets the accuracy that the final waveform must achieve, while hybridization specifies how the early inspiral description and the late-time NR description are joined into a single model. For this construction to be meaningful at LISA accuracy, the two waveforms must represent the same binary in the same asymptotic frame and with compatible intrinsic parameters. Chapter 3 develops this framework for PN–NR hybridization by placing the NR waveform in a PN-consistent Bondi–Metzner–Sachs (BMS) frame and by determining the PN masses and spins as part of the matching procedure, rather than assuming that they are identical to the quasi-local masses and spins used to label the NR simulation. This construction identifies several ingredients that must be controlled in high-accuracy waveform models, including PN truncation error, NR numerical error, asymptotic-frame alignment, and intrinsic-parameter identification [23]. These ingredients motivate the later chapters: Chapters 4 and 5 study how masses and spins should be related across PN, BHPT, and NR [24], Chapter 6 uses the PN–NR comparison framework to study PN convergence [41], and Chapter 7 addresses gauge effects in long NR simulations [42]. Together, these chapters develop the ingredients needed to connect PN, BHPT, NR, and observations in a consistent waveform-modeling framework.

1.3 The parameter-definition problem

Waveform hybridization requires the PN and NR waveforms to represent the same physical binary. This requirement is nontrivial because the intrinsic parameters used to label a binary are not necessarily defined in the same way in PN theory, NR, and BHPT. Gauge-invariant notions of mass and angular momentum are naturally defined as global charges only when suitable asymptotic or exact symmetries are available [43, 25, 26, 44, 45]. For an interacting binary at finite separation, the individual mass of each black hole, the binding energy of the binary, and the energy carried by radiation cannot be separated in a completely gauge-independent way. The masses and spins used in PN, NR, and BHPT are nevertheless physically meaningful within their respective constructions, and they should agree in the limit of infinite separation, where each black hole becomes isolated. At finite separation, however, these quantities are tied to different choices of gauge, slicing, and local geometric definition, so the relation between the corresponding parameter definitions must be established rather than assumed.

Parameters in PN

In PN theory, each compact object is represented by an effective point-particle source [15, 46]. The intrinsic parameters are the masses and spins attached to these sources,

$$\lambda_{\rm PN} = \left\{m_1^{\rm PN}, m_2^{\rm PN}, \mathbf{S}_1^{\rm PN}, \mathbf{S}_2^{\rm PN}\right\}. \tag{1.8}$$

These quantities enter the equations of motion, source multipole moments, and waveform modes. At leading order, for example, the masses appear in the Newtonian potential

$$U(\mathbf{x}, t) = \sum_{A=1}^{2} \frac{m_A^{\rm PN}}{|\mathbf{x} - \mathbf{z}_A(t)|}, \tag{1.9}$$

where $\mathbf{z}_A(t)$ is the coordinate position of body A.

More generally, the PN metric is organized as an expansion in the small orbital velocity,

$$g_{\mu\nu}^{\rm PN} = \eta_{\mu\nu} + h_{\mu\nu}^{(2)} + h_{\mu\nu}^{(3)} + h_{\mu\nu}^{(4)} + \cdots, \tag{1.10}$$

where the terms at each order are functions of $\lambda_{\rm PN}$, the orbital variables, and the chosen PN gauge [15, 46].

Horizon absorption introduces an additional subtlety in the interpretation of PN masses. For black holes, part of the gravitational radiation is absorbed by the horizons rather than radiated to future null infinity [47, 48, 49]. This absorbed flux can be described schematically by

$$\frac{dm_A}{dt} = \mathcal{F}_{H,A}, \qquad \frac{dS_A}{dt} = \mathcal{G}_{H,A}, \tag{1.11}$$

where $\mathcal{F}_{H,A}$ and $\mathcal{G}_{H,A}$ are the energy and angular-momentum fluxes through the horizon of black hole A. In PN waveform and flux calculations, however, these effects are usually incorporated as explicit horizon-absorption terms in the fluxes, phasing, and waveform modes, written as functions of the orbital frequency or of the PN expansion parameter v. The frequency evolution associated with absorption is carried by the horizon-flux terms themselves, not by replacing the PN masses with instantaneous finite-separation masses. The masses appearing in the coefficients of these expressions are therefore the constant PN mass parameters assigned to the point-particle sources, rather than the instantaneous masses at finite separation. In this sense, $m_A^{\rm PN}$ is the reference mass parameter associated with the isolated-body limit, corresponding to the mass definition obtained at infinite separation.

Parameters in NR

In NR, the individual black holes are identified geometrically on spatial slices of the numerical spacetime [50, 51]. The masses and spins used to label an NR simulation are usually computed quasi-locally from these apparent horizons. On a given spatial slice, an apparent horizon is a closed two-surface $\mathcal{H}_A$ for which the expansion of the outgoing null congruence vanishes,

$$\Theta_{(\ell)} = g^{(2)\mu\nu}\nabla_\mu \ell_\nu = 0, \tag{1.12}$$

where ℓ^μ is the outgoing null normal to the surface and $g^{(2)}_{\mu\nu}$ is the induced metric on $\mathcal{H}_A$. If $\mathcal{H}_A$ has area A_A, the irreducible mass defined as

$$m_{\mathrm{irr},A} = \sqrt{\frac{A_A}{16\pi}}. \tag{1.13}$$

The spin is computed from a surface integral over the horizon. A standard form is [52, 44, 51]

$$S_A = \frac{1}{8\pi}\oint_{\mathcal{H}_A}\left(K_{ij} - K g^{(3)}_{ij}\right)\phi^i s^j \, dA, \tag{1.14}$$

where $g^{(3)}_{ij}$ is the spatial metric, K_{ij} is the extrinsic curvature, $K = g^{(3)ij}K_{ij}$, s^i is the outward-pointing unit normal to the horizon within the spatial slice, and ϕ^i is an approximate rotational vector field on the horizon. The corresponding Christodoulou mass is

$$m^{\mathrm{NR}}_A = \sqrt{m^2_{\mathrm{irr},A} + \frac{S^2_A}{4m^2_{\mathrm{irr},A}}}. \tag{1.15}$$

The NR intrinsic parameters are therefore

$$\lambda_{\mathrm{NR}} = \left\{m^{\mathrm{NR}}_1, m^{\mathrm{NR}}_2, \mathbf{S}^{\mathrm{NR}}_1, \mathbf{S}^{\mathrm{NR}}_2\right\}. \tag{1.16}$$

These quantities are geometrically useful and are the natural way to characterize the black holes in a simulation, since they only depend on local quantities on a slice. However, because apparent horizons are slice-dependent and the surface integrals are evaluated in the simulation gauge, λ_{NR} is not automatically identical to λ_{PN}.

Parameters in BHPT

BHPT introduces a third closely related set of parameters. In a perturbative description near one black hole (inner zone), the metric is written as a background black-hole spacetime plus a perturbation [53, 54, 55, 21, 17],

$$g^{\mathrm{IZ}}_{\mu\nu} = g^{\mathrm{BH}}_{\mu\nu}\left(M^{\mathrm{BHPT}}_A, \mathbf{S}^{\mathrm{BHPT}}_A\right) + h^{\mathrm{tidal}}_{\mu\nu} + \cdots, \tag{1.17}$$

where $g_{\mu\nu}^{\mathrm{BH}}$ is the background black-hole metric and $h_{\mu\nu}^{\mathrm{tidal}}$ contains the perturbation produced by the companion and the binary environment. The parameters

$$\lambda_{\mathrm{BHPT}} = \left\{M_A^{\mathrm{BHPT}}, \mathbf{S}_A^{\mathrm{BHPT}}\right\} \tag{1.18}$$

therefore characterize the local background black hole. This is different from both the PN point-particle definition and the NR apparent-horizon definition, although all three definitions should agree in the isolated-black-hole limit.

Parameter ambiguity in waveform modeling

The parameter-definition problem is the question of how $\lambda_{\mathrm{PN}}, \lambda_{\mathrm{NR}}, \lambda_{\mathrm{BHPT}}$ are related for a binary at finite separation. At infinite separation, the two black holes become isolated and one expects the different notions of mass and spin to agree. At finite separation, however, the distinction between individual masses, spins, tidal perturbations, and gauge effects becomes subtle. A small difference between these definitions can become important when the waveform must satisfy a LISA-level accuracy requirement [7, 31].

This issue appears directly in PN–NR waveform hybridization. The PN parameters that best match an NR waveform can differ systematically from the quasi-local horizon parameters used to label the NR simulation, with representative shifts of order 10^{-3} in mass and 10^{-2} in spin for aligned-spin systems [23]. Although these shifts are numerically small, they can be important at the accuracy level required for LISA. The LISA-motivated error budget indicates that fractional mass errors at the 10^{-3} level can already be relevant for high-SNR sources. Parameter identification is therefore part of the waveform-accuracy problem, not merely a convention for labeling simulations.

1.4 Strong-field matching as the central framework

The conceptual center of this dissertation is the idea that parameter mapping between PN, BHPT, and NR should be derived from the spacetime geometry based on explicit gauge conditions as the first principle, rather than inferred only from waveform optimization at $\mathscr{I}^+$ [24]. Hybridization can reveal that different parameter definitions lead to measurable differences in the waveform, but such differences are inferred indirectly through an optimization procedure and can be affected by degeneracies or overfitting [23]. A first-principles relation between parameter definitions should instead be obtained by comparing the spacetime descriptions in the strong-field region, where the black holes and their quasi-local properties are defined.

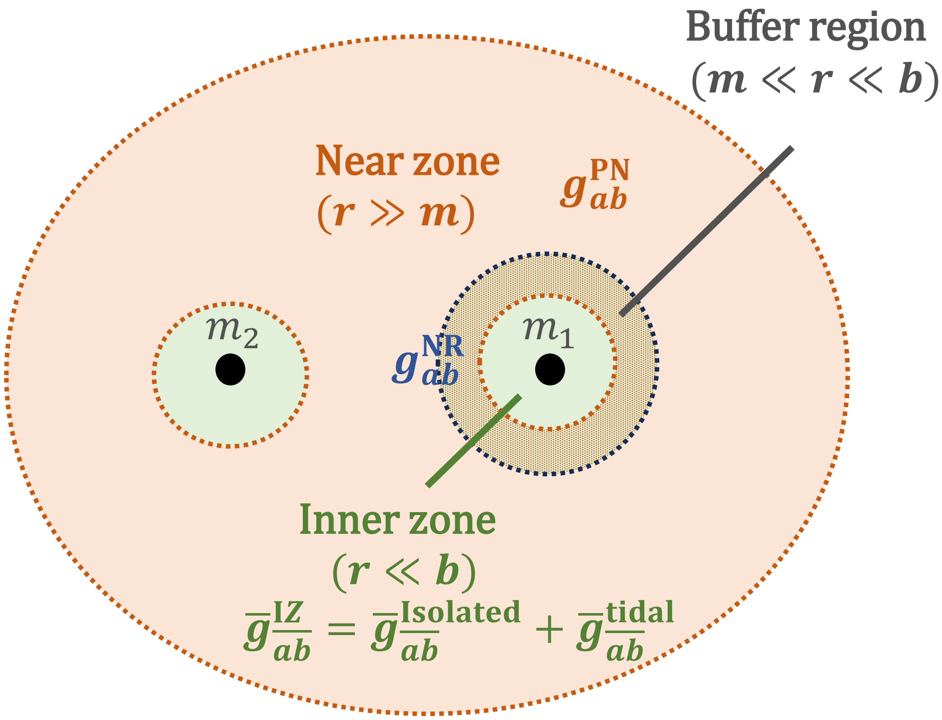

Figure 1.2: Schematic of the near zone, inner zone, and buffer region used in strong-field matching. The PN metric $g_{ab}^{\rm PN}$ describes the binary for $r \gg m$, while the inner-zone metric $\bar{g}_{\bar{a}\bar{b}}^{\rm IZ}$ describes a tidally perturbed black hole in comoving coordinates for $r \ll b$. The two descriptions overlap in the buffer region $m \ll r \ll b$. The NR metric $g_{ab}^{\rm NR}$ is valid in the whole domain. The barred indices refer to tensor components in the comoving coordinates, while unbarred indices refer to components in the inertial coordinates.

Figure 1.2 illustrates the different spacetime descriptions that are connected in the strong-field matching. The NR metric $g_{ab}^{\rm NR}$ is obtained by solving the Einstein equations numerically and is valid throughout the numerical domain, including the near-zone region and the strong-field neighborhood of each black hole (inner-zone), up to numerical and boundary errors [19, 16]. This makes NR the most complete description available. The PN metric $g_{ab}^{\rm PN}$, by contrast, describes the binary in the near zone, where the distance from each black hole is large compared with its mass, $r_A \gg m_A$ [15]. The PN description efficiently captures the orbital dynamics and the radiation source, but the black holes are represented by point-particle degrees of freedom, so the horizon geometry in the inner-zone is not resolved. BHPT provides the bridge between these descriptions through the inner-zone metric near black hole A, which gives the corresponding local strong-field description in the frame that is comoving with the BH [37, 38, 21]. This metric is written as a tidally perturbed black-hole metric,

$$\bar{g}^{\rm IZ}_{\bar{a}\bar{b}} = \bar{g}^{\rm isolated}_{\bar{a}\bar{b}} + \bar{g}^{\rm tidal}_{\bar{a}\bar{b}}, \tag{1.19}$$

where $\bar{g}^{\rm isolated}_{\bar{a}\bar{b}}$ is the metric of an isolated black hole with parameters $\lambda_{\rm BHPT}$, and $\bar{g}^{\rm tidal}_{\bar{a}\bar{b}}$ describes the perturbation produced by the companion. Here barred indices refer to tensor components in the comoving coordinates, while unbarred indices refer to components in the inertial PN or NR coordinates. This inner-zone description is valid near the horizon when the local radius is small compared with the binary separation, $r_A \ll b$. The PN and inner-zone descriptions overlap in the buffer region

$$m_A \ll r_A \ll b, \tag{1.20}$$

where both expansions are valid. Matching in this region relates the PN parameters $\lambda_{\rm PN}$ to the local black-hole parameters $\lambda_{\rm BHPT}$. Similarly, matching the inner-zone metric to the NR metric in the strong-field neighborhood of the horizon relates $\lambda_{\rm BHPT}$ to the quasi-local parameters measured in the NR spacetime. In this way, the figure shows the role of the BHPT inner-zone description as the bridge that connects the near-zone PN expansion, the full NR solution, and their parameter definitions:

$$\lambda_{\rm PN} \longleftrightarrow \lambda_{\rm BHPT} \longleftrightarrow \lambda_{\rm NR}. \tag{1.21}$$

To construct the matching, let $x^{\bar{a}}$ denote the comoving inner-zone coordinates near black hole A, and let x^a denote the global inertial coordinates used by either the PN or NR description. The coordinate transformation from the comoving frame to the global frame is written as

$$x^a = x^a(x^{\bar{a}}). \tag{1.22}$$

To compare the inner-zone metric with a near-zone metric g_{ab}, it is convenient to transform the near-zone metric to the comoving frame:

$$\bar{g}^{\rm NZ}_{\bar{a}\bar{b}} = \frac{\partial x^a}{\partial x^{\bar{a}}}\frac{\partial x^b}{\partial x^{\bar{b}}} g^{\rm NZ}_{ab}\big(x^a(x^{\bar{a}})\big), \tag{1.23}$$

where $g^{\rm NZ}_{ab}$ is either $g^{\rm PN}_{ab}$ or $g^{\rm NR}_{ab}$. The transformation $x^a(x^{\bar{a}})$ is fixed by two coupled requirements. First, in the buffer region, the transformed near-zone metric must agree with the inner-zone metric to the desired order or accuracy in the expansion. This matching condition supplies the asymptotic or boundary data that identify the near-zone PN or NR description with the local BHPT description. Second, in the whole domain, in particular the strong-field neighborhood of the horizon, the transformation must preserve the target gauge used by the global description. Thus the coordinate map is not merely an alignment chosen in the buffer region; it is determined by a gauge equation whose solution extends the matching into the strong field.

In the generalized-harmonic formulation, the gauge condition can be written as

$$\Box x^a \equiv \bar{g}^{\bar{a}\bar{b}}\bar{\nabla}_{\bar{a}}\bar{\nabla}_{\bar{b}}x^a = H^a, \tag{1.24}$$

where the coordinate functions $x^a(x^{\bar{a}})$ are treated as scalar fields on the inner-zone coordinates, $\bar{\nabla}_{\bar{a}}$ is the covariant derivative with respect to the inner-zone comoving metric $\bar{g}_{\bar{a}\bar{b}}$, and H^a specifies the target global gauge [19, 56].

Chapter 4 carries out the PN–BHPT matching at leading order in harmonic gauge ($H^a = 0$). A key result is that, on a horizon-penetrating harmonic slicing, the apparent-horizon mass agrees with the PN point-particle mass at 1PN order. For more general harmonic slicings that differ from the horizon-penetrating slicing at 1PN order, the apparent-horizon mass acquires a corresponding 1PN slicing-dependent correction. Thus, even within harmonic gauge, finite-separation differences between point-particle and horizon-based quasi-local masses can arise from the slicing used to define the horizon quantities [24].

Chapter 5 extends this framework to NR–BHPT matching, using production NR gauges, in particular the damped harmonic gauge [57]. This construction produces a practical map between $\lambda_{\rm NR}$ and $\lambda_{\rm BHPT}$, and ultimately between $\lambda_{\rm NR}$ and $\lambda_{\rm PN}$.

1.5 Analytical and numerical waveform infrastructure

The waveform-modeling framework developed in this dissertation relies on two complementary ingredients: an analytic inspiral description whose accuracy can be quantified, and NR simulations whose numerical and gauge errors remain controlled over long evolutions.

On the analytic side, PN theory is an approximation to GR in the weak-field, slow-motion limit, with the orbital velocity v as the expansion parameter [15, 46]. This expansion should not be interpreted as a convergent sequence whose infinite-order limit necessarily gives the exact binary dynamics at nonzero v. Rather, PN theory is an asymptotic expansion about the limit $v = 0$ [58, 59]. Let $f(v)$ denote the exact solution of a physical quantity, such as the energy flux or a waveform mode, and let $s_N(v)$ denote its PN approximation truncated at order N. The statement that PN is asymptotic as $v \to 0$ means that, for each fixed N, the truncation error

$$\epsilon_N(v) \equiv f(v) - s_N(v) \tag{1.25}$$

is of higher order than the terms retained in $s_N(v)$ as $v \to 0$,

$$\epsilon_N(v) \ll \mathcal{O}(v^N), \qquad v \to 0. \tag{1.26}$$

This is a statement about the small-v behavior of each finite truncation. It does not imply that the sequence $s_N(v)$ converges to $f(v)$ when $N \to \infty$ at fixed nonzero v. At finite orbital velocity, the PN sequence may instead behave as a divergent asymptotic series. As N is increased, the error may initially decrease, reach a minimum at a velocity-dependent optimal truncation order,

$$N_{\text{opt}}(v) = \arg\min_N |\epsilon_N(v)|, \tag{1.27}$$

and then increase when still higher-order terms are included. The useful PN approximation at finite v is therefore the best finite truncation, not the formal infinite series.

In practice, the exact quantity $f(v)$ is not known for comparable-mass BBHs, so Chapter 6 uses a long, high-accuracy NR simulation as the reference solution [41]. The comparison is made using the energy flux at $\mathscr{I}^+$, which provides a direct diagnostic of the inspiral dynamics once the PN and NR systems have been placed in the same BMS frame and the PN intrinsic parameters have been fitted to the NR waveform [25, 26, 28, 23]. For a PN truncation order N, the flux residual is defined schematically by

$$\Delta_N(v) = \left| \dot{E}^{(N)}_{\infty,\text{PN}}(v) - \dot{E}_{\infty,\text{NR}}(v) \right|. \tag{1.28}$$

Because the leading energy flux scales as v^{10}, the truncation error at PN order N is expected to follow the corresponding asymptotic power-law scaling [15]. Chapter 6 therefore examines both the size of $\Delta_N(v)$ and its scaling with v. This comparison shows that, for $v \lesssim 0.45$, higher PN orders continue to reduce the PN–NR flux difference, with the incomplete 6PN flux giving the best agreement among the orders considered [41]. As v approaches 0.5, near the innermost circular orbit, the PN residuals from different truncation orders cluster together and higher-order terms no longer improve the agreement, indicating the loss of convergence. The same analysis also shows that, at around 5 orbits before merger for non-spinning BBH, the 6PN truncation error can fall below the NR error, so further tests of high-order PN information would require substantially more accurate NR simulations. More importantly, this suggests that when constructing PN–NR hybrids for accurate waveform modeling, the NR portion of the waveform need not extend as far into the inspiral.

On the numerical side, long NR simulations must remain sufficiently clean that gauge artifacts and boundary effects do not contaminate the waveform or the spacetime data used for hybridization and strong-field matching [57, 20]. Chapter 7 addresses this numerical requirement by developing a gauge boundary condition that suppresses long-timescale coordinate drift in SpEC simulations [60, 42].

Together, these chapters provide the analytical and numerical infrastructure needed for high-accuracy waveform construction.

1.6 Future directions

The strong-field matching presented in this dissertation is a step toward a broader goal for connecting analytical models, numerical simulations, and GW observations through explicit gauge and parameter control. The main future directions are to extend the strong-field matching framework to more general binary configurations, use the resulting parameter maps in waveform hybridization and apply the strong-field matching framework to ringdown analysis and EMRI modeling.

Strong-field matching for generic binary configurations

Chapter 5 develops the extension of strong-field matching toward the gauges used in production NR simulations. A natural next step is to generalize this framework beyond the simplest configurations considered in this thesis. In particular, I would like to construct the matching for spinning, eccentric, and eventually precessing binary black holes.

Parameter-consistent waveform hybridization

The parameter maps developed from the strong-field matching would also improve waveform hybridization. The hybridization framework developed in this thesis currently treats intrinsic PN parameters as free variables determined by waveform matching at $\mathscr{I}^+$ [23]. A strong-field parameter map would instead fix these parameters from the spacetime geometry, leaving the waveform matching to control only the remaining BMS-frame and time-phase alignment freedoms. This would reduce the overfitting risk and would make the long-term phasing of the resulting hybrid waveforms more reliable.

A common parameter language

The strong-field parameter map would provide a common language for PN models, BHPT calculations, NR catalogs, and observations. Currently, each framework uses its own native parameters, even different NR catalogs can have systematic parameter shifts because of differences in gauge choices, initial data, horizon diagnostics, and conventions [15, 51, 21, 9].

The parameter map would translate these native labels into a common PN parameter set,

$$\lambda_{\text{native}} \longrightarrow \lambda_{\text{PN}}. \tag{1.29}$$

The PN parameters are the natural reference because they correspond to the infinite-separation limit, where the black holes become isolated and ambiguities from binding energy, tidal fields, and slicing effects disappear. Reporting systems in terms of λ_{PN} would therefore make PN, BHPT, different NR catalogs, and GW observations directly comparable.

Ringdown and EMRI applications

The strong-field matching can also be used beyond inspiral-merger hybridization. For merger-ringdown studies, it provides local comoving frames in which NR volume data can be projected onto BHPT quasinormal-mode bases, giving a bulk diagnostic of QNM excitation, nonlinear mode coupling, and the validity of simple Kerr-spectroscopy models [22, 61, 62]. It would also complement current QNM analyses performed primarily at $\mathscr{I}^+$, where the reliability of the extracted mode content depends on the fitting algorithm, the choice of fitting window, the removal of numerical and gauge-related noise from the waveform [63, 64], and possible overfitting.

For extreme-mass-ratio inspirals, the strong-field matching suggests a spatial-hybrid strategy in which the small body and its local neighborhood are described analytically by BHPT, while the outer region is supplied by an NR solution and the two descriptions are matched through the gauge-preserving transformation. This could potentially allow efficient and accurate EMRI modeling.

Toward controlled interfaces in waveform modeling

Together, these directions extend the central theme of the dissertation: waveform accuracy in the next-generation detector era requires not only improving individual models, but also controlling the interfaces between the different descriptions used to construct a waveform. Strong-field parameter maps, BMS-consistent waveform comparisons, NR simulations with required efficiency and accuracy, and validated analytic expansions are complementary parts of a single framework for precision gravitational-wave modeling.

1.7 Dissertation outline

The dissertation is organized into three parts. Part I develops the waveform-accuracy requirements and hybridization framework. Chapter 2 derives the LISA-oriented accuracy requirements for massive black-hole binary waveforms, including the signal durations, target mismatches, NR accuracy levels, and hybridization constraints relevant for next-generation space-based observations. Chapter 3 develops the PN–NR hybridization framework used throughout the thesis. In this construction, the NR waveform is placed in a PN-consistent BMS frame at $\mathscr{I}^+$, and the PN intrinsic parameters are determined through waveform matching rather than assumed to be identical to the quasi-local NR parameters.

Part II develops the strong-field matching framework. Chapter 4 studies PN–BHPT matching in harmonic gauge and derives a first-principles relation between PN point-particle masses and horizon-based quasi-local masses. Chapter 5 extends the same geometric idea to NR–BHPT matching in production NR gauges, with the goal of relating the local BHPT parameters to the quasi-local masses and spins measured in NR simulations.

Part III presents applications, supporting infrastructure, and future extensions of the framework. Chapter 6 uses the hybridization framework to study PN convergence by comparing successive PN truncation orders with NR after BMS-frame fixing and parameter fitting. Chapter 7 develops gauge boundary conditions in SpEC that suppress long-timescale coordinate drift in binary-black-hole simulations, improving the numerical data needed for precision hybridization and strong-field matching. Chapter 8 summarizes future directions. These include extending strong-field matching to spinning, eccentric, and precessing binaries; using parameter maps in waveform hybridization; establishing a common PN-compatible parameter language for PN, BHPT, NR catalogs, and observations; and applying the same strong-field coordinate framework to ringdown and EMRI modeling.

References

[1] B. P. Abbott et al. "Observation of Gravitational Waves from a Binary Black Hole Merger". In: *Physical Review Letters* 116.6 (2016), p. 061102. DOI: 10.1103/PhysRevLett.116.061102. arXiv: 1602.03837 [gr-qc].

[2] B. P. Abbott et al. "Properties of the Binary Black Hole Merger GW150914". In: *Physical Review Letters* 116.24 (2016), p. 241102. DOI: 10.1103/PhysRevLett.116.241102. arXiv: 1602.03840 [gr-qc].

[3] B. P. Abbott et al. "Tests of General Relativity with GW150914". In: *Physical Review Letters* 116.22 (2016), p. 221101. DOI: 10.1103/PhysRevLett.116.221101. arXiv: 1602.03841 [gr-qc].

[4] B. P. Abbott et al. "Astrophysical Implications of the Binary Black-Hole Merger GW150914". In: *The Astrophysical Journal Letters* 818.2 (2016), p. L22. DOI: 10.3847/2041-8205/818/2/L22. arXiv: 1602.03846 [astro-ph.HE].

[5] Lee Lindblom, Benjamin J. Owen, and Duncan A. Brown. "Model waveform accuracy standards for gravitational-wave data analysis". In: *Physical Review D* 78 (2008), p. 124020. DOI: 10.1103/PhysRevD.78.124020.

[6] Lee Lindblom, John G. Baker, and Benjamin J. Owen. "Improved time-domain accuracy standards for model gravitational waveforms". In: *Physical Review D* 82 (2010), p. 084020. DOI: 10.1103/PhysRevD.82.084020.

[7] Curt Cutler and Michele Vallisneri. "LISA detections of massive black hole inspirals: Parameter extraction errors due to inaccurate template waveforms". In: *Physical Review D* 76.10 (2007), p. 104018. DOI: 10.1103/PhysRevD.76.104018. arXiv: 0707.2982 [gr-qc].

[8] Nicolás Yunes and Frans Pretorius. "Fundamental theoretical bias in gravitational wave astrophysics and the parametrized post-Einsteinian framework". In: *Physical Review D* 80.12 (2009), p. 122003. DOI: 10.1103/PhysRevD.80.122003. arXiv: 0909.3328 [gr-qc].

[9] Abdul H. Mroue et al. "Catalog of 174 Binary Black Hole Simulations for Gravitational Wave Astronomy". In: *Physical Review Letters* 111.24 (2013), p. 241104. DOI: 10.1103/PhysRevLett.111.241104. arXiv: 1304.6077 [gr-qc].

[10] Tony Chu et al. "On the accuracy and precision of numerical waveforms: Effect of waveform extraction methodology". In: *Classical and Quantum Gravity* 33.16 (2016), p. 165001. DOI: 10.1088/0264-9381/33/16/165001. arXiv: 1512.06800 [gr-qc].

[11] P. Ajith et al. "Phenomenological template family for black-hole coalescence waveforms". In: *Classical and Quantum Gravity* 24.19 (2007), S689–S700. DOI: 10.1088/0264-9381/24/19/S31. arXiv: 0704.3764 [gr-qc].

[12] Ilana MacDonald et al. "Suitability of post-Newtonian/numerical-relativity hybrid waveforms for gravitational wave detectors". In: *Classical and Quantum Gravity* 28.13 (2011), p. 134002. DOI: 10.1088/0264-9381/28/13/134002. arXiv: 1102.5128 [gr-qc].

[13] Michael Boyle. "Transformations of asymptotic gravitational-wave data". In: *Physical Review D* 99.8 (2019), p. 084059. DOI: 10.1103/PhysRevD.99.084059. arXiv: 1810.00018 [gr-qc].

[14] Keefe Mitman et al. "Computation of displacement and spin gravitational memory in numerical relativity". In: *Physical Review D* 102.10 (2020), p. 104007. DOI: 10.1103/PhysRevD.102.104007. arXiv: 2007.11562 [gr-qc].

[15] Luc Blanchet. "Gravitational Radiation from Post-Newtonian Sources and Inspiralling Compact Binaries". In: *Living Reviews in Relativity* 17 (2014), p. 2. DOI: 10.12942/lrr-2014-2. arXiv: 1310.1528 [gr-qc].

[16] Joan Centrella et al. "Black-hole binaries, gravitational waves, and numerical relativity". In: *Reviews of Modern Physics* 82 (2010), pp. 3069–3119. DOI: 10.1103/RevModPhys.82.3069. arXiv: 1010.5260 [gr-qc].

[17] Leor Barack and Adam Pound. "Self-force and radiation reaction in general relativity". In: *Reports on Progress in Physics* 82.1 (2019), p. 016904. DOI: 10.1088/1361-6633/aae552. arXiv: 1805.10385 [gr-qc].

[18] Alessandra Buonanno and Thibault Damour. "Effective one-body approach to general relativistic two-body dynamics". In: *Physical Review D* 59.8 (1999), p. 084006. DOI: 10.1103/PhysRevD.59.084006. arXiv: gr-qc/9811091.

[19] Frans Pretorius. "Evolution of Binary Black-Hole Spacetimes". In: *Physical Review Letters* 95.12 (2005), p. 121101. DOI: 10.1103/PhysRevLett.95.121101. arXiv: gr-qc/0507014.

[20] Béla Szilágyi et al. "Approaching the Post-Newtonian Regime with Numerical Relativity: A Compact-Object Binary Simulation Spanning 350 Gravitational-Wave Cycles". In: *Physical Review Letters* 115.3 (2015), p. 031102. DOI: 10.1103/PhysRevLett.115.031102. arXiv: 1502.04953 [gr-qc].

[21] Eric Poisson, Adam Pound, and Ian Vega. "The Motion of Point Particles in Curved Spacetime". In: *Living Reviews in Relativity* 14 (2011), p. 7. DOI: 10.12942/lrr-2011-7. arXiv: 1102.0529 [gr-qc].

[22] Emanuele Berti, Vitor Cardoso, and Andrei O. Starinets. "Quasinormal modes of black holes and black branes". In: *Classical and Quantum Gravity* 26.16 (2009), p. 163001. DOI: 10.1088/0264-9381/26/16/163001. arXiv: 0905.2975 [gr-qc].

[23] Dongze Sun et al. "Optimizing post-Newtonian parameters and fixing the BMS frame for numerical-relativity waveform hybridizations". In: *Physical Review D* 110 (2024), p. 104076. DOI: 10.1103/PhysRevD.110.104076. arXiv: 2403.10278 [gr-qc].

[24] Dongze Sun and Leo C. Stein. "Parameter matching between horizon quasi-local and point-particle definitions at 1PN for quasi-circular and non spinning BBH systems in harmonic gauge". In: (2025). arXiv: 2510.25618 [gr-qc].

[25] H. Bondi, M. G. J. van der Burg, and A. W. K. Metzner. "Gravitational waves in general relativity. VII. Waves from axi-symmetric isolated systems". In: *Proceedings of the Royal Society of London. Series A* 269.1336 (1962), pp. 21–52. DOI: 10.1098/rspa.1962.0161.

[26] R. K. Sachs. "Gravitational waves in general relativity. VIII. Waves in asymptotically flat space-time". In: *Proceedings of the Royal Society of London. Series A* 270.1340 (1962), pp. 103–126. DOI: 10.1098/rspa.1962.0206.

[27] Michael Boyle. "Transformations of asymptotic gravitational-wave data". In: *Physical Review D* 99.8 (2019), p. 084059. DOI: 10.1103/PhysRevD.99.084059. arXiv: 1810.00018 [gr-qc].

[28] Keefe Mitman et al. "Fixing the BMS frame of numerical relativity waveforms with BMS charges". In: *Physical Review D* 106.8 (2022), p. 084029. DOI: 10.1103/PhysRevD.106.084029. arXiv: 2208.04356 [gr-qc].

[29] Pau Amaro-Seoane et al. "Laser Interferometer Space Antenna". In: (2017). LISA mission proposal. DOI: 10.48550/arXiv.1702.00786. arXiv: 1702.00786 [astro-ph.IM].

[30] Travis Robson, Neil J. Cornish, and Chang Liu. "The construction and use of LISA sensitivity curves". In: *Classical and Quantum Gravity* 36.10 (2019), p. 105011. DOI: 10.1088/1361-6382/ab1101. arXiv: 1803.01944 [astro-ph.HE].

[31] Niayesh Afshordi et al. "Waveform modelling for the Laser Interferometer Space Antenna". In: *Living Reviews in Relativity* 28.1 (2025), p. 9. DOI: 10.1007/s41114-025-00056-1. arXiv: 2311.01300 [gr-qc].

[32] Monica Colpi et al. "LISA Definition Study Report". In: (2024). arXiv: 2402.07571 [astro-ph.CO].

[33] Alexandre Toubiana et al. "Measuring source properties and quasinormal mode frequencies of heavy massive black-hole binaries with LISA". In: *Physical Review D* 109.10 (2024), p. 104019. DOI: 10.1103/PhysRevD.109.104019. arXiv: 2307.15086 [gr-qc].

[34] Curt Cutler and Éanna E. Flanagan. "Gravitational waves from merging compact binaries: How accurately can one extract the binary's parameters from the inspiral waveform?" In: *Physical Review D* 49.6 (1994), pp. 2658–2697. DOI: 10.1103/PhysRevD.49.2658. arXiv: gr-qc/9402014.

[35] Benjamin J. Owen. "Search templates for gravitational waves from inspiraling binaries: Choice of template spacing". In: *Physical Review D* 53.12 (1996), pp. 6749–6761. DOI: 10.1103/PhysRevD.53.6749. arXiv: gr-qc/9511032.

[36] Michele Maggiore. *Gravitational Waves. Volume 1: Theory and Experiments*. Oxford University Press, 2008. DOI: 10.1093/acprof:oso/9780198570745.001.0001.

[37] Kashif Alvi. “Approximate binary-black-hole metric”. In: *Physical Review D* 61.12 (2000), p. 124013. DOI: 10.1103/PhysRevD.61.124013. arXiv: gr-qc/9912113.

[38] Nicolás Yunes et al. “Binary black hole initial data from matched asymptotic expansions”. In: *Physical Review D* 74.10 (2006), p. 104011. DOI: 10.1103/PhysRevD.74.104011. arXiv: gr-qc/0503011.

[39] Frank Ohme. “Analytical meets numerical relativity: status of complete gravitational waveform models for binary black holes”. In: *Classical and Quantum Gravity* 29.12 (2012), p. 124002. DOI: 10.1088/0264-9381/29/12/124002. arXiv: 1111.3737 [gr-qc].

[40] Dongze Sun et al. “Optimizing post-Newtonian parameters and fixing the BMS frame for numerical-relativity waveform hybridizations”. In: *Physical Review D* 110.10 (Nov. 2024). ISSN: 2470-0029. DOI: 10.1103/physrevd.110.104076. URL: http://dx.doi.org/10.1103/PhysRevD.110.104076.

[41] Dongze Sun et al. “To be updated”. In: (2026).

[42] Dongze Sun et al. “Gauge Boundary conditions to mitigate center-of-mass drift in BBH simulations”. In: *Physical Review D* 113 (2026), p. 044016. DOI: 10.1103/b1cd-qysb. arXiv: 2510.25465 [gr-qc].

[43] Richard Arnowitt, Stanley Deser, and Charles W. Misner. “The dynamics of general relativity”. In: *General Relativity and Gravitation* 40 (2008). Originally published in Gravitation: An Introduction to Current Research, Wiley, 1962, pp. 1997–2027. DOI: 10.1007/s10714-008-0661-1.

[44] Abhay Ashtekar and Badri Krishnan. “Isolated and dynamical horizons and their applications”. In: *Living Reviews in Relativity* 7 (2004), p. 10. DOI: 10.12942/lrr-2004-10. arXiv: gr-qc/0407042.

[45] László B. Szabados. “Quasi-local energy-momentum and angular momentum in general relativity”. In: *Living Reviews in Relativity* 12 (2009), p. 4. DOI: 10.12942/lrr-2009-4.

[46] Eric Poisson and Clifford M. Will. *Gravity: Newtonian, Post-Newtonian, Relativistic*. Cambridge University Press, 2014. DOI: 10.1017/CBO9781139507486.

[47] Eric Poisson and Misao Sasaki. “Gravitational radiation from a particle in circular orbit around a black hole. V. Black-hole absorption and tail corrections”. In: *Physical Review D* 51.10 (1995), pp. 5753–5767. DOI: 10.1103/PhysRevD.51.5753. arXiv: gr-qc/9412027.

[48] Kashif Alvi. “Energy and angular momentum flow into a black hole in a binary”. In: *Physical Review D* 64.10 (2001), p. 104020. DOI: 10.1103/PhysRevD.64.104020. arXiv: gr-qc/0107080.

[49] Katerina Chatziioannou, Eric Poisson, and Nicolás Yunes. "Improved next-to-leading order tidal heating and torquing of a Kerr black hole". In: *Physical Review D* 87.4 (2013), p. 044022. DOI: 10.1103/PhysRevD.87.044022. arXiv: 1211.1686 [gr-qc].

[50] Jonathan Thornburg. "Event and apparent horizon finders for 3+1 numerical relativity". In: *Living Reviews in Relativity* 10 (2007), p. 3. DOI: 10.12942/lrr-2007-3. arXiv: gr-qc/0512169.

[51] Gregory B. Cook and Bernard F. Whiting. "Approximate Killing vectors on S^2". In: *Physical Review D* 76.4 (2007), p. 041501. DOI: 10.1103/PhysRevD.76.041501. arXiv: 0706.0199 [gr-qc].

[52] J. David Brown and James W. York. "Quasilocal energy and conserved charges derived from the gravitational action". In: *Physical Review D* 47.4 (1993), pp. 1407–1419. DOI: 10.1103/PhysRevD.47.1407.

[53] Tullio Regge and John A. Wheeler. "Stability of a Schwarzschild Singularity". In: *Physical Review* 108.4 (1957), pp. 1063–1069. DOI: 10.1103/PhysRev.108.1063.

[54] Frank J. Zerilli. "Effective potential for even-parity Regge-Wheeler gravitational perturbation equations". In: *Physical Review Letters* 24.13 (1970), pp. 737–738. DOI: 10.1103/PhysRevLett.24.737.

[55] Saul A. Teukolsky. "Perturbations of a Rotating Black Hole. I. Fundamental Equations for Gravitational, Electromagnetic, and Neutrino-Field Perturbations". In: *The Astrophysical Journal* 185 (1973), pp. 635–648. DOI: 10.1086/152444.

[56] Lee Lindblom et al. "A new generalized harmonic evolution system". In: *Classical and Quantum Gravity* 23.16 (2006), S447–S462. DOI: 10.1088/0264-9381/23/16/S09. arXiv: gr-qc/0512093.

[57] Bela Szilagyi, Lee Lindblom, and Mark A. Scheel. "Simulations of binary black hole mergers using spectral methods". In: *Physical Review D* 80.12 (2009), p. 124010. DOI: 10.1103/PhysRevD.80.124010. arXiv: 0909.3557 [gr-qc].

[58] Carl M. Bender and Steven A. Orszag. *Advanced Mathematical Methods for Scientists and Engineers I: Asymptotic Methods and Perturbation Theory*. Springer, 1999. DOI: 10.1007/978-1-4757-3069-2.

[59] R. B. Dingle. *Asymptotic Expansions: Their Derivation and Interpretation*. Academic Press, 1973.

[60] *The Spectral Einstein Code*. http://www.black-holes.org/SpEC.html.

[61] Emanuele Berti, Kent Yagi, and Nicolás Yunes. "Extreme Gravity Tests with Gravitational Waves from Compact Binary Coalescences: I. Inspiral-Merger". In: *General Relativity and Gravitation* 50.4 (2018), p. 46. DOI: 10.1007/s10714-018-2362-8. arXiv: 1801.03208 [gr-qc].

[62] Mark Ho-Yeuk Cheung et al. "Extracting linear and nonlinear quasinormal modes from black hole merger simulations". In: *Physical Review D* 109.4 (2024), p. 044069. DOI: 10.1103/PhysRevD.109.044069. arXiv: 2310.04489 [gr-qc].

[63] Matthew Giesler et al. "Black Hole Ringdown: The Importance of Overtones". In: *Physical Review X* 9.4 (2019), p. 041060. DOI: 10.1103/PhysRevX.9.041060. arXiv: 1903.08284 [gr-qc].

[64] Matthew Giesler et al. "Overtones and Nonlinearities in Binary Black Hole Ringdowns". In: *Physical Review D* 111.8 (2025), p. 084041. DOI: 10.1103/PhysRevD.111.084041. arXiv: 2411.11269 [gr-qc].

Part I

Waveform Accuracy and Hybridization

Chapter 2

HYBRIDIZATION-GUIDED NUMERICAL-RELATIVITY REQUIREMENTS FOR LISA MASSIVE-BLACK-HOLE BINARIES

To be submitted as: Dongze Sun et al. "Hybridization-guided numerical-relativity requirements for LISA massive-black-hole binaries". to be submitted soon.

Abstract

LISA observations of massive-black-hole binaries will require waveform systematics far below the level relevant for most current ground-based analyses. For comparable-mass and moderately unequal-mass systems, fully numerical waveforms over the entire LISA band are impractical. Numerical relativity (NR) must instead supply the late-inspiral, merger, and ringdown signal to be joined to an analytic early-inspiral model. We derive a source-dependent accuracy budget for this construction by comparing the LISA-weighted waveform error with the indistinguishability scale $\mathcal{M}_{\text{target}} \sim 1/(2\rho^2)$. The resulting criterion fixes three coupled requirements: the analytic model must remain accurate up to the matching region, the NR waveform must be accurate from that region through merger, and the PN–NR parameter map must be controlled tightly enough that residual offsets do not accumulate observable phase error. Using leading PN scalings, we obtain analytic estimates for the required matching frequency, the required NR accuracy from matching to merger, and the allowed uncertainties in total mass, symmetric mass ratio, and spin projections. These estimates define a practical readiness test for existing and future NR simulations: for each candidate LISA source, one can determine whether a simulation starts early enough, is accurate enough, and admits sufficiently controlled parameter and frame alignment to support a LISA-accurate hybrid waveform. We applied this test to the SXS waveform catalog, and we show that LISA-ready hybrids require further improvements in NR accuracy, in addition to intrinsic parameter matching between analytic waveform models and NR.

2.1 Introduction

The Laser Interferometer Space Antenna (LISA) will observe massive-black-hole binaries (MBHBs) with signal-to-noise ratios (SNRs) large enough that waveform modeling errors can produce systematic biases comparable to, or larger than, the statistical errors from detector noise [2, 3]. Forecasts for cosmological MBHBs commonly find high-SNR events with $\rho \sim 10^2$–10^3, with the loudest systems reaching the regime in which waveform mismatches below 10^{-6} become relevant [2, 4, 5]. We therefore keep the requirements source dependent. For a waveform h with SNR $\rho \equiv \sqrt{(h|h)}$, a small residual waveform error δh after the chosen alignment produces a mismatch

$$\mathcal{M} = 1 - \frac{(h|h+\delta h)}{\|h\| \cdot \|h+\delta h\|} \simeq \frac{1}{2\rho^2}(\delta h_\perp|\delta h_\perp), \tag{2.1}$$

where $\|a\| \equiv \sqrt{(a|a)}$, $(\cdot|\cdot)$ denotes the LISA noise-weighted inner product, which in the single-effective-channel approximation is

$$(a|b) = 4\,\mathrm{Re}\int_0^\infty \frac{a^*(f)b(f)}{S_n(f)}\,df \tag{2.2}$$

with $S_n(f)$ the effective one-sided LISA noise spectrum, and $\delta h_\perp$ denotes the part of the waveform error that remains after projecting out the directions over which the overlap is optimized, such as an overall time and phase shift. The usual indistinguishability requirement $(\delta h_\perp|\delta h_\perp) \lesssim 1$ therefore corresponds to the fiducial target

$$\mathcal{M}_{\text{target}} \simeq \frac{1}{2\rho^2}, \tag{2.3}$$

up to order-unity factors set by the chosen parameter-estimation criterion, confidence threshold, and safety margin [6]. Thus $\rho = 10^3$ gives $\mathcal{M}_{\text{target}} \simeq 5 \times 10^{-7}$, while an exceptionally loud $\rho = 10^4$ event would require $\mathcal{M}_{\text{target}} \simeq 5 \times 10^{-9}$, before this budget is allocated among analytic-inspiral truncation, NR truncation, waveform extraction, hybridization, intrinsic-parameter mapping, and asymptotic-frame alignment.

For the comparable-mass and moderately unequal-mass MBHBs considered here, NR provides the only first-principles description of the nonlinear late inspiral, merger, and ringdown, but evolving the same system numerically over the full LISA band is not practical [7, 8, 3]. A LISA-length waveform that uses NR information must therefore combine the numerical late-time signal with an analytic or semi-analytic description of the earlier inspiral. Depending on the region of parameter space, this inspiral description may be based on PN theory, an effective-one-body (EOB) model, or black-hole perturbation theory (BHPT)/self-force (SF) [9, 10, 11, 3]. In this Letter, we focus on the accuracy of this hybridization interface: the matching frequency must be low enough that the analytic inspiral is still accurate, the NR waveform must be accurate from that frequency through merger, and the intrinsic parameters and asymptotic frames of the two descriptions must be aligned within the LISA error budget [12, 13, 14].

The key subtlety is that hybridization uses waveform descriptions whose parameters and frames are defined in different ways. NR masses and spins are typically quasi-local horizon quantities [7], whereas the analytic inspiral model carries its own intrinsic parameters. For example, PN masses and spins are parameters assigned to point particles, with spin definitions depending on gauges such as the spin supplementary condition [9, 15, 16]. In BHPT and SF descriptions, the intrinsic parameters are those of a perturbative expansion about a background black hole with background mass and spin, together with the smaller body's mass, spin, and orbital degrees of freedom [17, 18, 11]. The waveform also has a frame ambiguity at future null infinity $\mathcal{I}^+$: a Bondi-Metzner-Sachs (BMS) transformation changes the constant-retarded-time slices of $\mathcal{I}^+$ on which the radiation is represented, so boosts, translations, and supertranslations can change the time series entering a PN–NR comparison [19, 20, 21, 22]. The residual parameter and frame errors therefore enter the waveform error as the usual truncation errors.

To obtain closed-form requirements, we model the analytic-inspiral error by a parametric PN phase residual and evaluate it with Eq. (2.1). The frequency at which this residual reaches $\mathcal{M}_{\rm target}$ sets the hybridization frequency. Applying the mismatch budget Eq. (2.3) to the NR part from the hybridization frequency to merger yields the required NR accuracy. Applying the same mismatch budget to the waveform perturbations induced by residual offsets in the intrinsic parameters then gives tolerances on M, ν, and the spin projections. With leading order frequency-domain PN amplitude and phase, these conditions become analytic functions of the source parameters and detector noise.

These estimates define a practical diagnostic for NR waveform catalogs. For each candidate LISA source, one can identify whether the limiting requirement is the starting frequency of the simulation, the post-hybridization NR truncation error, or the accuracy of the BMS-frame and parameter alignment. We apply this framework to the SXS catalog [7, 23], complementing previous studies of NR accuracy requirements for future detectors and of the impact of existing NR errors on high-precision analyses [8, 24, 14].

We focus on vacuum BBH systems whose merger and ringdown require NR. The extensions to Extreme-mass-ratio inspirals (EMRIs), where the long inspiral is modeled with BHPT and SF methods, and to environmental effects [11, 3] are left for future work.

We work in units $G = c = 1$ throughout the letter.

2.2 Waveform-Error Target

For the closed-form estimates below, we use a simplified frequency-domain inspiral waveform. The detector strain is

$$h(f) = F^{+}(f)h_{+}(f) + F^{\times}(f)h_{\times}(f), \tag{2.4}$$

with

$$\begin{aligned} h_{+}(f) &= A(f)\frac{1+\cos^2\iota}{2}e^{\mathrm{i}\Psi(f)}, \\ h_{\times}(f) &= \mathrm{i}A(f)\cos\iota\, e^{\mathrm{i}\Psi(f)}. \end{aligned} \tag{2.5}$$

For the analytic estimates we replace the inclination and detector-response factor by a constant effective value $Q^2 = 4/5$, so that $|h(f)|^2 \simeq Q^2 A(f)^2$.

We use detector-frame masses for the waveform mode, with $m_i = (1+z)m_{i,\mathrm{src}}$ and $M = m_1 + m_2$. The symmetric mass ratio $\nu = m_1 m_2/M^2$ and dimensionless spins $\chi_i = \boldsymbol{S}_i/m_i^2$ are invariant under the common redshift rescaling. At leading order in the restricted stationary-phase approximation, the observed frequency-domain amplitude is [25, 26, 9]

$$A(f) = \sqrt{\frac{5}{24}}\,\frac{M^{5/6}\nu^{1/2}f^{-7/6}}{\pi^{2/3}D_L}, \tag{2.6}$$

For the parameter-tolerance estimates, we keep the nonspinning phase through 1PN order and include the leading spin-orbit contribution [27, 28, 29],

$$\begin{aligned} \Psi(f) =& 2\pi f t_c - \phi_c - \frac{\pi}{4} + \frac{3}{128\nu}(\pi M f)^{-5/3}\Bigg[1 + \left(\frac{3715}{756} + \frac{55}{9}\nu\right)(\pi M f)^{2/3} \\ &+ \left(-16\pi + \frac{1}{3}\sum_{i=1,2}\left(113\frac{m_i^2}{M^2} + 75\nu\right)\chi_{iL}\right)(\pi M f)\Bigg], \end{aligned} \tag{2.7}$$

When the LISA noise varies slowly over the relevant frequency interval, the waveform model gives the SNR scaling

$$\rho^2 \equiv (h|h) \simeq \frac{M^{5/3}\nu}{2\pi^{4/3}D_L^2 S_n}\left(f_{\mathrm{low}}^{-4/3} - f_{\mathrm{merger}}^{-4/3}\right), \tag{2.8}$$

where f_{low} denotes the lower cutoff of the frequency interval being integrated. For rough full-band LISA estimates one commonly takes $f_{\text{low}} = 10^{-4}$ Hz, the lower edge of the nominal LISA band [30]. For estimates we take the merger frequency to be

$$f_{\text{merger}} = \frac{1}{\pi M}\Big(2.9740 \times 10^{-1}\nu^2 \\ +4.4810 \times 10^{-2}\nu + 9.5560 \times 10^{-2}\Big), \tag{2.9}$$

following the phenomenological inspiral-merger-ringdown fit of Ref. [28]. Combining Eq. (2.8) with Eq. (2.3) gives

$$\mathcal{M}_{\text{target}} \simeq \frac{\pi^{4/3} D_L^2 S_n(f_{\text{low}})}{M^{5/3}\nu\left(f_{\text{low}}^{-4/3} - f_{\text{merger}}^{-4/3}\right)}. \tag{2.10}$$

2.3 Hybridization Requirements

Let f_{hyb} be the frequency at which the analytic inspiral is joined to the NR waveform. A hybrid waveform may be written schematically as

$$h_{\text{hyb}}(f) = W(f; f_{\text{hyb}})\, h_{\text{NR}}(f; \lambda_{\text{NR}}, \mathcal{B}) \\ + \left[1 - W(f; f_{\text{hyb}})\right] h_{\text{analytic}}(f; \lambda_{\text{analytic}}), \tag{2.11}$$

where W is a smooth transition function, λ denotes intrinsic parameters, and $\mathcal{B}$ denotes the asymptotic frame.

We evaluate each residual with the mismatch measure of Eq. (2.1), restricted to the frequency interval on which that residual is present. For any error contribution δh_X, define

$$\mathcal{M}_X[f_1, f_2] \equiv \frac{1}{2\rho^2}(\delta h_{X,\perp}|\delta h_{X,\perp})_{[f_1,f_2]}, \tag{2.12}$$

where $\rho^2 = (h|h)$ is the SNR of the full signal and $(\cdot|\cdot)_{[f_1,f_2]}$ is the same noise-weighted inner product restricted to that frequency band.

The analytic-inspiral error sets the hybridization frequency:

$$\mathcal{M}_{\text{analytic}}[f_{\text{low}}, f_{\text{hyb}}] = \mathcal{M}_{\text{target}}. \tag{2.13}$$

Hybridizing at a higher frequency would make the accumulated analytic-inspiral residual exceed the target. Once f_{hyb} is fixed, the NR waveform must satisfy

$$\mathcal{M}_{\text{NR}}[f_{\text{hyb}}, f_{\text{merger}}] = \frac{1}{2\rho^2}(\delta h_{\text{NR},\perp}|\delta h_{\text{NR},\perp})_{[f_{\text{hyb}},f_{\text{merger}}]} \\ \leq \mathcal{M}_{\text{target}}, \tag{2.14}$$

with $\delta h_{\rm NR}$ including numerical truncation and waveform-extraction error.

Residual errors in the analytic–NR parameter map are treated as waveform perturbations. For parameters Λ^α, including M, ν, spin projections, and frame degrees of freedom,

$$\delta h_{\rm hyb} = \partial_\alpha h_{\rm analytic}\, \delta\Lambda^\alpha. \tag{2.15}$$

We treat the analytic intrinsic parameters and frame choice as the reference, as they incorporate information from past infinity. The corresponding tolerance for the error accumulated in the NR part is then

$$\begin{aligned} \mathcal{M}_{\rm hyb}[f_{\rm hyb}, f_{\rm merger}] =& \frac{1}{2\rho^2}(\delta h_{{\rm hyb},\perp}|\delta h_{{\rm hyb},\perp})_{[f_{\rm hyb}, f_{\rm merger}]} \\ &\leq \mathcal{M}_{\rm target}, \end{aligned} \tag{2.16}$$

where repeated indices are summed over the residual intrinsic-parameter and frame offsets included in Λ^α. For a one-parameter estimate this gives

$$|\delta\Lambda^\alpha| \lesssim \left(\partial_\alpha h_{\rm analytic}\middle|\partial_\alpha h_{\rm analytic}\right)^{-1/2}_{\perp,[f_{\rm hyb}, f_{\rm merger}]}, \tag{2.17}$$

with no sum over α.

2.4 Hybridization Frequency

Equation (2.13) determines how early the NR waveform must begin. For a small residual in the analytic inspiral, we write

$$\delta h \simeq \left(\frac{\delta A}{A} + \mathrm{i}\delta\Psi\right) h. \tag{2.18}$$

For the long inspirals considered here, the phase residual usually dominates, so the pre-hybridization mismatch is approximated by

$$\mathcal{M}_{\rm analytic}[f_{\rm low}, f_{\rm hyb}] \simeq \frac{1}{2\rho^2}\left(\delta\Psi\, h_{\rm analytic}\middle|\delta\Psi\, h_{\rm analytic}\right)_{[f_{\rm low}, f_{\rm hyb}]}. \tag{2.19}$$

We parameterize the leading omitted phase contribution by the first unknown frequency-domain PN phase coefficient beyond 4PN,

$$\delta\Psi(f) = \beta_9 f^{4/3}. \tag{2.20}$$

Here the subscript 9 denotes the v^9 term in the relative PN phase expansion, with $v = (\pi M f)^{1/3}$, and β_9 is the residual coefficient not included in the analytic inspiral model.

Using the leading amplitude in Eq. (2.6), the flat-noise approximation, and $f_{\rm hyb} \gg f_{\rm low}$, Eq. (2.19) gives

$$\mathcal{M}_{\rm analytic} \simeq \frac{\beta_9^2 M^{5/3}\nu}{4\rho^2\pi^{4/3}D_L^2 S_n} f_{\rm hyb}^{4/3}. \tag{2.21}$$

Using the fiducial target $\mathcal{M}_{\rm target}$, Eq. (2.13) yields

$$f_{\rm hyb} \simeq \left[\frac{2\pi^{4/3}D_L^2 S_n}{\beta_9^2 M^{5/3}\nu}\right]^{3/4}. \tag{2.22}$$

The number of remaining orbits illustrates the cost sensitivity. At Newtonian order, the number of orbital cycles from $f_{\rm hyb}$ to merger is

$$N_{\rm orb}(f_{\rm hyb}) \simeq \frac{1}{64\pi^{8/3}\mathcal{M}_c^{5/3}}\left(f_{\rm hyb}^{-5/3} - f_{\rm merger}^{-5/3}\right), \tag{2.23}$$

where $\mathcal{M}_c = M\nu^{3/5}$ is the detector-frame chirp mass. The steep dependence on $f_{\rm hyb}$ is why the analytic truncation model and the NR starting frequency must be considered together.

2.5 NR Accuracy Requirement

Equation (2.14) gives the waveform accuracy required of the NR part of the hybrid. The SNR contribution from the NR part is given by

$$\begin{aligned} \rho_{\rm NR}^2 &= (h_{\rm NR}|h_{\rm NR})_{[f_{\rm hyb}, f_{\rm merger}]} \\ &\simeq \frac{M^{5/3}\nu}{2\pi^{4/3}D_L^2 S_n}\left(f_{\rm hyb}^{-4/3} - f_{\rm merger}^{-4/3}\right). \end{aligned} \tag{2.24}$$

Thus, Eqs. (2.14) and (2.18) implies that the required relative amplitude accuracy and accumulated phase to satisfy

$$\left|\frac{\delta A_{\rm NR}}{A}\right| \lesssim \rho_{\rm NR}^{-1}, \qquad |\delta\Psi_{\rm NR}| \lesssim \rho_{\rm NR}^{-1}. \tag{2.25}$$

It is useful to express the phase requirement as a tolerance per orbit or per unit simulation time. If a coherent NR phase bias accumulates approximately linearly over the remaining orbital cycles, then

$$|\delta\Psi_{\rm NR}|_{\rm per\,orbit} \lesssim \frac{\rho_{\rm NR}^{-1}}{N_{\rm orb}(f_{\rm hyb})}, \tag{2.26}$$

with $N_{\rm orb}$ given by Eq. (2.23). Equivalently, if the bias accumulates approximately linearly over the NR simulation time duration $\Delta t_{\rm NR}$, then

$$M|\delta\dot{\Psi}_{\rm NR}| \lesssim \frac{\rho_{\rm NR}^{-1}}{\Delta t_{\rm NR}/M}, \tag{2.27}$$

where, at leading order,

$$\Delta t_{\rm NR} \simeq \frac{5}{256\pi^{8/3}\mathcal{M}_c^{5/3}}\left(f_{\rm hyb}^{-8/3} - f_{\rm merger}^{-8/3}\right). \tag{2.28}$$

Equations (2.25)–(2.28) translate the global LISA mismatch budget into local NR accuracy targets for the waveform amplitude and phase.

2.6 Intrinsic-Parameter and Frame Tolerances

We now evaluate Eq. (2.17) for the intrinsic parameters that enter Eq. (2.7). In the phase-dominated approximation,

$$\partial_\alpha h_{\rm analytic} \simeq \mathrm{i} h_{\rm analytic}\, \partial_\alpha \Psi. \tag{2.29}$$

For single-parameter estimates at fixed values of the other parameters, define

$$\Delta_{14} \equiv f_{\rm hyb}^{-14/3} - f_{\rm merger}^{-14/3}, \qquad \Delta_8 \equiv f_{\rm hyb}^{-8/3} - f_{\rm merger}^{-8/3}. \tag{2.30}$$

Keeping the leading Newtonian phase dependence for M and ν, and using Eqs. (2.6) and (2.7), Eq. (2.17) gives

$$\begin{aligned} |\delta M| &\lesssim \frac{128\sqrt{7}}{5}\pi^{7/3}M^{11/6}\nu^{1/2}\frac{D_L\sqrt{S_n}}{\sqrt{\Delta_{14}}}, \\ |\delta \nu| &\lesssim \frac{128\sqrt{7}}{3}\pi^{7/3}M^{5/6}\nu^{3/2}\frac{D_L\sqrt{S_n}}{\sqrt{\Delta_{14}}}. \end{aligned} \tag{2.31}$$

For the spin projections $\chi_{iL} \equiv \boldsymbol{\chi}_i \cdot \hat{\boldsymbol{L}}_N$, the leading spin-orbit phase term gives

$$|\delta\chi_{iL}| \lesssim \frac{256}{|C_i|}\pi^{4/3}M^{-1/6}\nu^{1/2}\frac{D_L\sqrt{S_n}}{\sqrt{\Delta_8}}, \tag{2.32}$$

where

$$C_i \equiv 113\frac{m_i^2}{M^2} + 75\nu. \tag{2.33}$$

Frame errors enter through the transformation of the strain under changes of asymptotic frame. Following Ref. [31], a BMS-frame transformation consists of a Lorentz transformation, including rotations and boosts, together with time and spatial translations and supertranslation. Following Ref. [31], a transformation of asymptotic frame acts on the retarded time u on $\mathcal{I}^+$ as

$$u' = K(\hat{\boldsymbol{n}})\,[u - \gamma(\hat{\boldsymbol{n}})], \tag{2.34}$$

with K the Lorentz conformal factor and γ the time and space translation and supertranslation. Rotations change the sky direction and mix the angular modes, while spatial translations and proper supertranslations shift u by an angle-dependent but time-independent amount. These transformations can mix modes and change the waveform used in a comparison, but they do not rescale the frequency, therefore they don't introduce a phase error that accumulates with time. The boost is different: it shifts the retarded time, and hence the frequency. For a small residual boost, define the fractional frequency error

$$\delta\kappa \equiv \delta \ln f \simeq \hat{\boldsymbol{n}} \cdot \delta\boldsymbol{v}, \tag{2.35}$$

up to the sign convention for the boost direction. The leading phase perturbation is then

$$\delta\Psi_{\text{boost}} = \frac{\partial\Psi}{\partial \ln f}\,\delta\kappa \simeq -\frac{5}{128\nu}(\pi M f)^{-5/3}\delta\kappa. \tag{2.36}$$

Applying Eq. (2.17) gives the boost tolerance

$$|\delta\kappa| \lesssim \frac{128\sqrt{7}}{5}\,\pi^{7/3}M^{5/6}\nu^{1/2}\frac{D_L\sqrt{S_n}}{\sqrt{\Delta_{14}}}. \tag{2.37}$$

Equivalently, Eq. (2.37) bounds the line-of-sight component of the residual boost, $|\hat{\boldsymbol{n}} \cdot \delta\boldsymbol{v}|$, in the simplified single-direction estimate.

2.7 Summary of Requirements

To illustrate the scale of the requirements, Table 2.1 evaluates the preceding formulas for three representative equal-mass MBHBs. The cases vary both total SNR and detector-frame mass, spanning a weak source, a loud source, and an exceptionally loud source. For the constant-noise estimate used in the table, we take the LISA noise at a typical value,

$$S_n^{\text{typ}} \equiv S_n(f_{\text{typ}}), \qquad f_{\text{typ}} \equiv \sqrt{f_{\text{low}} f_{\text{merger}}}, \tag{2.38}$$

evaluated with the sky-averaged effective LISA sensitivity curve of Ref. [32], including the Galactic foreground. The luminosity distance in each column is fixed by the stated SNR through Eq. (2.8).

Quantity	Weak	Loud	Very loud
	Input source and waveform parameters		
SNR ρ	10^2	10^3	10^4
M [$M_\odot$]	10^5	10^6	10^7
ν	0.25	0.25	0.25
D_L [Gpc]	2.16×10^2	7.96	6.48×10^{-1}
$f_{\rm low}$ [Hz]	10^{-4}	10^{-4}	10^{-4}
$f_{\rm typ}$ [Hz]	2.85×10^{-3}	9.00×10^{-4}	2.85×10^{-4}
$S_n^{\rm typ}$ [Hz^{-1}]	3.65×10^{-40}	1.24×10^{-37}	8.17×10^{-36}
$f_{\rm merger}$ [Hz]	8.10×10^{-2}	8.10×10^{-3}	8.10×10^{-4}
	Hybridization and NR-accuracy requirements		
$f_{\rm hyb}$ [Hz]	4.18 ($> f_{\rm merger}$)	1.32×10^{-3}	$< f_{\rm low}$
$\rho_{\rm NR}$	–	1.71×10^2	1.00×10^4
$\mathcal{M}_{\rm NR}[f_{\rm hyb}, f_{\rm merger}]$	–	5.0×10^{-7}	5.0×10^{-9}
$\lvert\delta A_{\rm NR}\rvert/A$	–	5.84×10^{-3}	1.00×10^{-4}
$\lvert\delta\Psi_{\rm NR}\rvert_{\rm total}$	–	5.84×10^{-3}	1.00×10^{-4}
$N_{\rm orb}(f_{\rm hyb})$	–	12.4	20.1
$\Delta t_{\rm NR}/M$	–	2.50×10^3	5.23×10^3
$\lvert\delta\Psi_{\rm NR}\rvert_{\rm per\,orbit}$	–	4.69×10^{-4}	4.98×10^{-6}
$M\lvert\delta\dot{\Psi}_{\rm NR}\rvert$	–	2.34×10^{-6}	1.91×10^{-8}
	Intrinsic-parameter and boost tolerances		
$\lvert\delta M\rvert/M$	–	1.02×10^{-4}	1.11×10^{-6}
$\lvert\delta\nu\rvert$	–	4.23×10^{-5}	4.64×10^{-7}
$\lvert\delta\chi_{iL}\rvert$	–	4.02×10^{-4}	5.80×10^{-6}
$\lvert\delta\kappa\rvert$	–	1.02×10^{-4}	1.11×10^{-6}

Table 2.1: Representative hybridization, NR-accuracy, intrinsic-parameter, and boost requirements. All masses are detector-frame masses. We take $q = 1$, $\nu = 1/4$, $f_{\rm low} = 10^{-4}$ Hz, and $\mathcal{M}_{\rm target} = 1/(2\rho^2)$. The typical noise value $S_n^{\rm typ} \equiv S_n(f_{\rm typ})$, with $f_{\rm typ} = \sqrt{f_{\rm low} f_{\rm merger}}$, is evaluated using the effective LISA sensitivity curve of Ref. [32]. The residual 4.5PN phase coefficient is using $\beta_9 = (\pi M)^{4/3}$. Dashes indicate that the analytic-truncation condition gives $f_{\rm hyb} > f_{\rm merger}$, so the analytic model itself is accurate enough to describe the inspiral for detection, and NR is only needed for the merger and ringdown part. For the very loud case, the $f_{\rm hyb}$ lies below $f_{\rm low}$, so a LISA-accurate hybrid would therefore require either a more accurate analytic inspiral or NR coverage over the full observing band from $f_{\rm low}$ to $f_{\rm merger}$.

The weak-signal case in Table 2.1 has $f_{\rm hyb} > f_{\rm merger}$, so the analytic truncation model is accurate enough to describe the inspiral for the detection, and NR is only needed for the merger and ringdown part. On the other hand, the exceptionally loud case has $f_{\rm hyb} < f_{\rm merger}$, so a LISA-accurate hybrid would therefore require either a more accurate analytic inspiral or NR coverage over the full observing band. For the loud case, the tolerances $|\delta M|/M$, $|\delta\nu|$, and $|\delta\chi_{iL}|$ are much smaller than the parameter discrepancies that can arise between analytic-inspiral parameters and NR quasi-local horizon quantities, or from hybridization without a proper asymptotic-frame fix [12, 33, 13, 14]. This makes an accurate analytic–NR parameter map essential for loud LISA MBHB detections [34].

2.8 SXS Catalog Audit

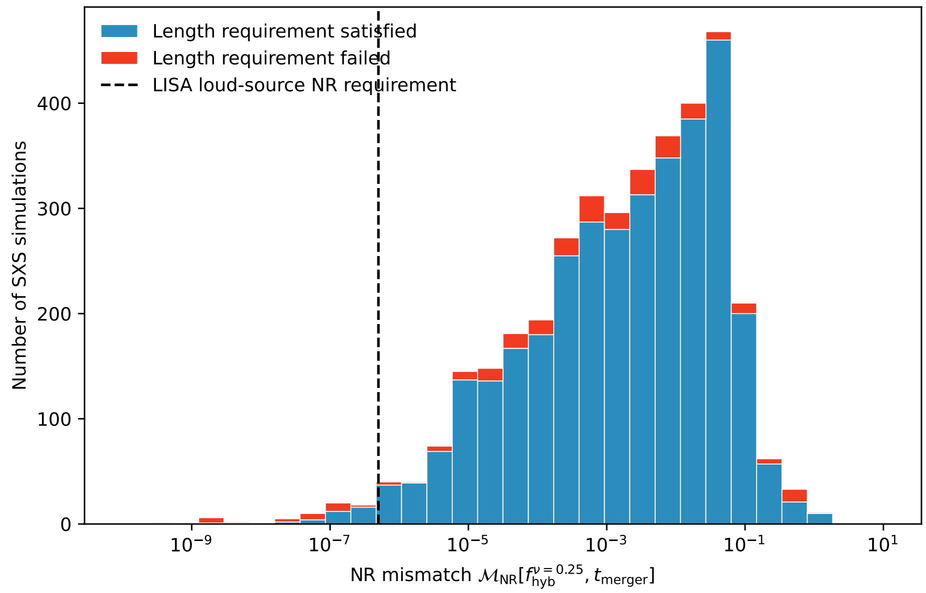

Figure 2.1: Distribution of $\mathcal{M}_{\rm NR}[f_{\rm hyb}^{\nu=0.25}, f_{\rm merger}]$ for the public SXS waveform catalog, evaluated for $M = 10^6 M_\odot$ and $\rho = 10^3$. The mismatches are computed for the highest two resolutions avaliable, after aligning their time and phase at merger. Each histogram bin is split into simulations that satisfy the length requirement ($M\omega_{22}^{\rm clean} \leq M\omega_{22}^{{\rm hyb},\nu=0.25}$; lower portion) and those that fail it (upper portion). The vertical dashed line marks the required loud-case phase-accuracy threshold. Simulations to the left of the line and in the lower stack satisfy both the phase-accuracy and length requirements. We have dropped the deprecated simulations.

The SXS catalog is the natural first target for this readiness test because it contains high-accuracy, multi-resolution binary-black-hole simulations with waveform metadata and broad coverage of the parameter space relevant to current ground-based observations [33, 23]. For each waveform we propose the following audit. Given a candidate LISA source, compute the source-specific requirements $f_{\rm hyb}$ and $\mathcal{M}_{\rm NR}[f_{\rm hyb}, f_{\rm merger}]$, then check whether the clean post-junk portion of the NR waveform starts early enough and is accurate enough over the post-hybridization interval. This test should be applied case by case, since the requirements depend on the source mass, SNR, mass ratio, spins, detector weighting, and analytic-inspiral error model.

Here we give only a demonstration, using the loud row of Table 2.1. For that representative source, $M = 10^6 M_\odot$ and $\rho = 10^3$, Eq. (2.22) gives the earliest required hybridization point for the equal-mass case, $\nu = 0.25$: $f_{\rm hyb}^{\nu=0.25} = 1.32 \times 10^{-3}$ Hz. We therefore use the equal-mass values as conservative requirements for this demonstration. Any simulation that satisfies these bounds also satisfies the corresponding length and NR-error requirements evaluated at its own mass ratio, for the same M and ρ.

The corresponding dimensionless NR angular frequency is

$$M\omega_{22}^{\rm hyb,\nu=0.25} = 2\pi M f_{\rm hyb}^{\nu=0.25} \simeq 4.1 \times 10^{-2}. \tag{2.39}$$

Thus a waveform passes the length requirement for this source only if its clean starting frequency satisfies

$$\omega_{22}^{\rm post-junk} \leq \omega_{22}^{\rm hyb,\nu=0.25}. \tag{2.40}$$

The same loud-source row gives the post-hybridization NR requirements

$$\mathcal{M}_{\rm NR}[f_{\rm hyb}^{\nu=0.25}, f_{\rm merger}] \lesssim 5.0 \times 10^{-7}. \tag{2.41}$$

Fig. 2.1 shows the distribution of $\mathcal{M}_{\rm NR}[f_{\rm hyb}^{\nu=0.25}, f_{\rm merger}]$ for the public SXS waveform catalog, evaluated for $M = 10^6 M_\odot$ and $\rho = 10^3$. The mismatches are computed for the highest two resolutions avaliable, after aligning their time and phase at merger. Each bin is split into waveforms that do and do not satisfy the length requirement. The vertical dashed line marks the required loud-case phase-accuracy threshold. Simulations to the left of the line and in the lower stack satisfy both the phase-accuracy and length requirements. Although most public SXS simulations in this demonstration satisfy the length requirement, only 39 out of 3669 simulations pass both the length requirement and the mismatch requirement for $M = 10^6 M_\odot$ and $\rho = 10^3$. This indicates that improving NR accuracy is necessary for LISA-ready hybrids in the loud-source regime.

2.9 Conclusion

We have derived source-dependent accuracy requirements for analytic–NR hybrid waveforms for LISA massive-black-hole binaries. For a specified source, the LISA mismatch target fixes the required hybridization frequency, the allowed post-hybridization NR mismatch, and the tolerances on analytic–NR parameter and frame alignment.

We demonstrated the resulting audit on the public SXS catalog for a loud representative source with $M = 10^6 M_\odot$ and $\rho = 10^3$. Although most simulations satisfy the length requirement, only 39 out of 3669 simulations pass both the length requirement and the NR-mismatch bound. This shows that LISA-ready hybrids require improvements in NR accuracy, in addition to intrinsic parameter matching between analytic waveform models and NR.

A full readiness assessment should repeat this calculation source by source with the full LISA response and noise curve, calibrated analytic-inspiral truncation errors, NR resolution and waveform extraction error estimates, and an explicit analytic–NR parameter map in a common BMS frame. Such an assessment would identify which existing simulations are sufficient for a given LISA source and which factors set the limiting accuracy.

Acknowledgments

We thank the SXS Collaboration and the developers of `SpEC` and `SpECTRE` for the waveform catalogs and infrastructure on which this analysis is based. Computations for the catalog audit were performed on Mbot. This work is supported in part by the Sherman Fairchild Foundation, NSF grants PHY-2309211, PHY-2309231, and OAC-2513339, and NASA award 80NSSC26K0340 at Caltech

References

[1] Dongze Sun et al. "Hybridization-guided numerical-relativity requirements for LISA massive-black-hole binaries". to be submitted soon.

[2] Curt Cutler and Michele Vallisneri. "LISA detections of massive black hole inspirals: Parameter extraction errors due to inaccurate template waveforms". In: *Phys. Rev. D* 76 (2007), p. 104018. DOI: 10.1103/PhysRevD.76.104018. arXiv: 0707.2982 [gr-qc].

[3] Niayesh Afshordi et al. "Waveform Modelling for the Laser Interferometer Space Antenna". arXiv:2311.01300. Nov. 2023. arXiv: 2311.01300 [gr-qc].

[4] Geraint Pratten et al. "On the LISA science performance in observations of short-lived signals from massive black hole binary coalescences". In: *Phys. Rev. D* 107 (2023), p. 123026. arXiv: 2212.02572 [gr-qc].

[5] T. van der Steen et al. "The Doppler boosted LISA response to gravitational waves". In: (2025). arXiv: 2509.10038 [gr-qc].

[6] Lee Lindblom, Benjamin J. Owen, and Duncan A. Brown. "Model waveform accuracy standards for gravitational wave data analysis". In: *Phys. Rev. D* 78

(2008), p. 124020. DOI: 10.1103/PhysRevD.78.124020. arXiv: 0809.3844 [gr-qc].

[7] Michael Boyle et al. “The SXS Collaboration catalog of binary black hole simulations”. In: *Class. Quant. Grav.* 36.19 (2019), p. 195006. DOI: 10.1088/1361-6382/ab34e2. arXiv: 1904.04831 [gr-qc].

[8] Deborah Ferguson et al. “Assessing the readiness of numerical relativity for LISA and 3G detectors”. In: *Phys. Rev. D* 104.4 (2021), p. 044037. DOI: 10.1103/PhysRevD.104.044037. arXiv: 2006.04272 [gr-qc].

[9] Luc Blanchet. “Gravitational Radiation from Post-Newtonian Sources and Inspiralling Compact Binaries”. In: *Living Rev. Relativ.* 17 (2014), p. 2. DOI: 10.12942/lrr-2014-2. arXiv: 1310.1528 [gr-qc].

[10] Andrea Taracchini et al. “Effective-one-body model for black-hole binaries with generic mass ratios and spins”. In: *Phys. Rev. D* 89.6 (2014), p. 061502. DOI: 10.1103/PhysRevD.89.061502. arXiv: 1311.2544 [gr-qc].

[11] Leor Barack and Adam Pound. “Self-force and radiation reaction in general relativity”. In: *Rep. Prog. Phys.* 82.1 (2019), p. 016904. DOI: 10.1007/s41114-018-0017-5. arXiv: 1805.10385 [gr-qc].

[12] L. Santamaria et al. “Matching post-Newtonian and numerical relativity waveforms: Systematic errors and a new phenomenological model for non-precessing black hole binaries”. In: *Phys. Rev. D* 82 (2010), p. 064016. DOI: 10.1103/PhysRevD.82.064016. arXiv: 1005.3306 [gr-qc].

[13] Dongze Sun et al. “Optimizing post-Newtonian parameters and fixing the BMS frame for numerical-relativity waveform hybridizations”. In: *Phys. Rev. D* 110.10 (2024), p. 104076. DOI: 10.1103/PhysRevD.110.104076. arXiv: 2403.10278 [gr-qc].

[14] Keefe Mitman et al. “Length dependence of waveform mismatch: a caveat on waveform accuracy”. In: *arXiv e-prints* (Feb. 2025), arXiv:2502.14025. arXiv: 2502.14025 [gr-qc].

[15] Eric Poisson and Clifford M. Will. *Gravity: Newtonian, Post-Newtonian, Relativistic*. Cambridge University Press, 2014. DOI: 10.1017/CBO9781139507486.

[16] Jan Steinhoff. “Spin gauge symmetry in the action principle for classical relativistic particles”. In: *arXiv e-prints* (2015), arXiv:1501.04951. arXiv: 1501.04951 [gr-qc].

[17] Saul A. Teukolsky. “Perturbations of a rotating black hole. I. Fundamental equations for gravitational, electromagnetic, and neutrino-field perturbations”. In: *Astrophys. J.* 185 (1973), pp. 635–647. DOI: 10.1086/152444.

[18] Leor Barack and Amos Ori. “Gravitational self-force on a particle orbiting a Kerr black hole”. In: *Phys. Rev. Lett.* 90 (2003), p. 111101. DOI: 10.1103/PhysRevLett.90.111101. arXiv: gr-qc/0212103.

[19] H. Bondi, M. G. J. van der Burg, and A. W. K. Metzner. “Gravitational waves in general relativity. VII. Waves from axi-symmetric isolated systems”. In: *Proc. Roy. Soc. Lond. A* 269 (1962), pp. 21–52. DOI: 10.1098/rspa.1962.0161.

[20] R. K. Sachs. “Gravitational waves in general relativity. VIII. Waves in asymptotically flat space-time”. In: *Proc. Roy. Soc. Lond. A* 270 (1962), pp. 103–126. DOI: 10.1098/rspa.1962.0206.

[21] Keefe Mitman et al. “Fixing the BMS frame of numerical relativity waveforms”. In: *Phys. Rev. D* 104 (2021), p. 024051. DOI: 10.1103/PhysRevD.104.024051. arXiv: 2105.02300 [gr-qc].

[22] Keefe Mitman et al. “Fixing the BMS frame of numerical relativity waveforms with BMS charges”. In: *Phys. Rev. D* 106 (2022), p. 084029. DOI: 10.1103/PhysRevD.106.084029. arXiv: 2208.04356 [gr-qc].

[23] Mark A Scheel et al. “The SXS collaboration’s third catalog of binary black hole simulations”. In: *Classical and Quantum Gravity* 42.19 (Oct. 2025), p. 195017. ISSN: 1361-6382. DOI: 10.1088/1361-6382/adfd34. URL: http://dx.doi.org/10.1088/1361-6382/adfd34.

[24] Aasim Jan et al. “Accuracy limitations of existing numerical relativity waveforms on the data analysis of current and future ground-based detectors”. In: *Phys. Rev. D* 110.2 (2024), p. 024023. DOI: 10.1103/PhysRevD.110.024023. arXiv: 2312.10241 [gr-qc].

[25] Curt Cutler and Eanna E. Flanagan. “Gravitational waves from merging compact binaries: How accurately can one extract the binary’s parameters from the inspiral waveform?” In: *Phys. Rev. D* 49 (1994), pp. 2658–2697. DOI: 10.1103/PhysRevD.49.2658. arXiv: gr-qc/9402014.

[26] Serge Droz et al. “Gravitational waves from inspiraling compact binaries: Validity of the stationary-phase approximation to the Fourier transform”. In: *Phys. Rev. D* 59 (1999), p. 124016. DOI: 10.1103/PhysRevD.59.124016. arXiv: gr-qc/9901076.

[27] Lawrence E. Kidder. “Coalescing binary systems of compact objects to post-Newtonian 5/2 order. V. Spin effects”. In: *Phys. Rev. D* 52 (1995), pp. 821–847. DOI: 10.1103/PhysRevD.52.821. arXiv: gr-qc/9506022.

[28] P. Ajith et al. “A phenomenological template family for black-hole coalescence waveforms”. In: *Classical Quantum Gravity* 24 (2007), S689–S699. DOI: 10.1088/0264-9381/24/19/S31.

[29] Patricia Schmidt, Frank Ohme, and Mark Hannam. “Towards models of gravitational waveforms from generic binaries: II. Modelling precession effects with a single effective precession parameter”. In: *Phys. Rev. D* 91.2 (2015), p. 024043. DOI: 10.1103/PhysRevD.91.024043.

[30] Monica Colpi et al. “LISA Definition Study Report”. In: (2024). DOI: 10.48550/arXiv.2402.07571. arXiv: 2402.07571 [astro-ph.CO].

[31] Michael Boyle. “Transformations of asymptotic gravitational-wave data”. In: *Phys. Rev. D* 93.8 (2016), p. 084031. DOI: 10.1103/PhysRevD.93.084031. arXiv: 1509.00862 [gr-qc].

[32] Travis Robson, Neil J. Cornish, and Chang Liu. “The construction and use of LISA sensitivity curves”. In: *Classical Quantum Gravity* 36.10 (2019), p. 105011. DOI: 10.1088/1361-6382/ab1101.

[33] Michael Boyle et al. “The SXS collaboration catalog of binary black hole simulations”. In: *Classical Quantum Gravity* 36.19 (2019), p. 195006. DOI: 10.1088/1361-6382/ab34e2. arXiv: 1904.04831 [gr-qc].

[34] Dongze Sun and Leo C. Stein. *Parameter matching between horizon quasi-local and point-particle definitions at 1PN for quasi-circular and non spinning BBH systems in harmonic gauge*. 2025. arXiv: 2510.25618 [gr-qc]. URL: https://arxiv.org/abs/2510.25618.

Chapter 3

OPTIMIZING POST-NEWTONIAN PARAMETERS AND FIXING THE BMS FRAME FOR NUMERICAL-RELATIVITY WAVEFORM HYBRIDIZATIONS

Published as: Dongze Sun et al. "Optimizing post-Newtonian parameters and fixing the BMS frame for numerical-relativity waveform hybridizations". In: *Physical Review D* 110 (2024), p. 104076. DOI: 10.1103/PhysRevD.110.104076. arXiv: 2403.10278 [gr-qc].

Dongze Sun. *NRPNHybridization*. https://github.com/dongzesun/NRPNHybridization.

Abstract

Numerical relativity (NR) simulations of binary black holes provide precise waveforms, but are typically too computationally expensive to produce waveforms with enough orbits to cover the whole frequency band of gravitational-wave observatories. Accordingly, it is important to be able to hybridize NR waveforms with analytic, post-Newtonian (PN) waveforms, which are accurate during the early inspiral phase. We show that to build such hybrids, it is crucial to both fix the Bondi-Metzner-Sachs (BMS) frame of the NR waveforms to match that of PN theory, and optimize over the PN parameters to mitigate the error caused by the discrepancy between NR and PN parameters. We test such a hybridization procedure including all spin-weighted spherical harmonic modes with $|m| \leq \ell$ for $\ell \leq 8$, using 29 NR waveforms with mass ratios $q \leq 10$ and spin magnitudes $|\chi_1|, |\chi_2| \leq 0.8$. We find that for spin-aligned systems, the PN and NR waveforms agree very well. The difference is limited by the small nonzero orbital eccentricity of the NR waveforms, or equivalently by the lack of eccentric terms in the PN waveforms. To maintain full accuracy of the simulations, the matching window for spin-aligned systems should be at least 5 orbits long and end at least 15 orbits before merger. For precessing systems, the errors are larger than for spin-aligned cases. The errors are likely limited by the absence of precession-related spin-spin PN terms. Using $10^5\,M$ long NR waveforms, we find that there is no optimal choice of the matching window within this time span, because the hybridization result for precessing cases is always better if using earlier or longer matching windows. We provide the mean orbital frequency of the smallest

acceptable matching window as a function of the target error between the PN and NR waveforms and the black hole spins.

3.1 Introduction

Gravitational-wave (GW) astronomy has revealed previously unattainable details about the astrophysics of compact objects [3, 4, 5, 6, 7, 8, 9, 10, 11] and the behavior of gravity in extreme regimes [12, 13, 14], thanks to the collaboration of LIGO, Virgo, and KAGRA [15, 16, 17, 18]. To further advance the field, the next generation of ground-based detectors, such as the Einstein Telescope (ET) [19] and Cosmic Explorer (CE) [20], as well as the first-generation of space-based detectors, including LISA [21], TianQin [22], and Taiji [23], are currently under development. These detectors are expected to provide a significant increase in sensitivity and bandwidth, enabling the detection of GW signals at frequencies as low as 0.1 mHz [24, 25, 26].

To fully exploit the scientific potential of these gravitational-wave observations, it is essential to construct precise theoretical waveform templates. The most accurate waveform templates are obtained through numerical simulations of the full set of Einstein's equations of general relativity, which is known as numerical relativity (NR). However, NR simulations are typically too computationally expensive to produce waveforms with enough orbits to cover the whole frequency band that is detectable by gravitational-wave observatories. Alternatively, analytic models based on the post-Newtonian (PN) approximation are efficient at providing waveforms that cover the low-frequency band during the early inspiral phase of binary black hole (BBH) systems. However, PN waveforms are not accurate for the late inspiral and merger phases of BBH systems. Consequently, it is important to be able to attach a PN waveform to the beginning of an NR waveform, thus producing a *hybrid* waveform that is accurate for the entire frequency band of GW detectors.

Such hybridization procedures were developed, for example, in Refs. [27, 28, 29, 30, 31, 32]. These procedures attained mismatches of 10^{-4} between the hybrid and NR waveforms in the matching window (for $m \neq 0$ modes) for non-precessing systems [31], and between 10^{-2} and 10^{-1} (for $m \neq 0$ modes) for precessing systems [32]. However, these procedures have four major limitations: (1) They did not account for the $m = 0$ modes since their NR waveforms did not include the correct gravitational-wave memory contribution. (2) The NR waveforms used in these procedures were not in the same frame as the PN waveforms. Reference [33] showed that comparing CCE waveforms without fixing the gauge freedom can result in relative errors three orders of magnitude larger than if one first fixes such freedoms. And they also showed that comparing CCE waveforms after mapping them to the same BMS frame can achieve smaller errors than comparing the extrapolated waveforms. Furthermore, Ref. [33] successfully developed a hybrid procedure that incorporates memory-containing waveforms. (3) These procedures used NR values of masses and spins to compute the corresponding PN waveform. However, the mass and spin parameters are defined differently in PN than they are in NR, and hence the NR and PN parameters are expected to agree only in the limit of infinite binary separation, even for infinite-resolution NR and infinite-order PN. In addition, for finite-resolution NR and finite-order PN there are systematic errors in the mapping from parameters to waveforms. (4) Existing procedures are primarily applicable to spin-aligned or anti-aligned systems, such as binaries born from isolated stellar evolution [34, 35, 36]. The accuracy of hybridization for precessing systems is severely limited by the inaccurate methodology previously mentioned: the mismatch is on the order of 10^{-2} or higher [32]. Theoretical considerations [34, 36] and observational evidence [11, 37, 38] indicate that spins can be randomly oriented for binaries that form dynamically in dense environments, and even binaries formed in isolation can exhibit distinctive precessional dynamics. Therefore, it is crucial to develop accurate hybridization procedures that are valid for precessing systems.

One technique that enables the extraction of waveforms at null infinity is Cauchy-characteristic evolution (CCE) [39, 40, 41, 42, 43]. It uses a worldtube from the Cauchy evolution of the Einstein field equations as the inner boundary to a characteristic evolution along null rays. The gravitational information is propagated and evolved to future null infinity, so one can obtain waveforms in any desired gauge. Reference [33] has shown that by mapping the CCE waveform to the correct Bondi-Metzner-Sachs (BMS) frame, the NR waveform agrees much better with the PN waveform. A key advantage of the hybrid waveforms presented here is that we use CCE NR waveforms. By contrast, previous hybrid waveform models [27, 28, 29, 30, 31, 32] used NR waveforms that were computed at null infinity using an extrapolation technique [44] that does not have a well-defined BMS frame and does not yield the correct memory contribution.

In this work, we simultaneously optimize over the PN parameters and fix the BMS frame of NR waveforms to build hybrid waveforms, so that we can mitigate the error caused by the discrepancy between NR and PN parameters, and inaccurate BMS frame. This is depicted graphically in Fig. 3.1. The optimization and the

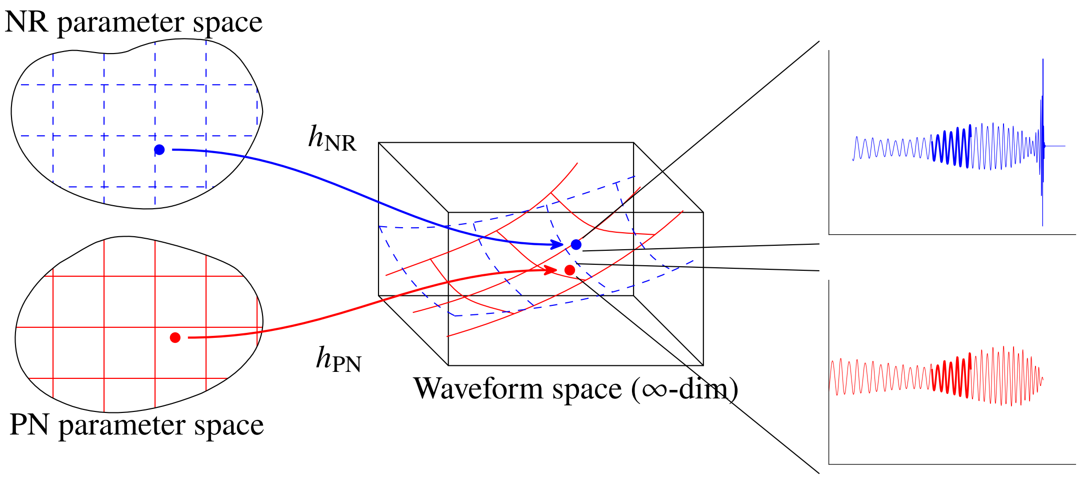

Figure 3.1: NR and PN parameter spaces are distinct because of the different gauges and different definitions of parameters used in PN and NR models. The maps into infinite-dimensional waveform space differ at each NR resolution and PN order. We optimize PN parameters and adjust the BMS frame to minimize the "vertical" difference transverse to the images of NR and PN parameter spaces.

fixing of the BMS frame, which includes the alignment of the rotation and time shift, are performed inside a time interval called a *matching window*. Because we use CCE and thus obtain the correct gravitational-wave memory, we are able to include all $-\ell \leq m \leq \ell$ for $\ell \leq 8$ spin-weighted spherical harmonic modes in the hybrid waveforms. We test the hybridization procedure using 29 NR waveforms from the SXS catalog [45] with mass ratios $q \leq 10$ and $|\chi_1|, |\chi_2| \leq 0.8$. The length of these waveforms ranges from 60 to over 100 orbits, making it possible to test the hybrid waveforms by comparing them to long NR waveforms at a very early stage. We find that for spin-aligned systems, we can reduce the PN–NR mismatches to the error caused by small non-zero eccentricities of the NR systems. We achieve a mismatch (in a 10-orbit long matching window ending 8000 M before merger) around two to three orders of magnitude smaller than previous models [27, 28, 29, 30, 31]. For precessing systems, we find that hybridization is likely limited by the absence of precession-related spin-spin PN terms, yielding mismatches one to two orders of magnitude smaller than previous models [32].

This paper is organized as follows. In Sec. 3.2, we introduce the PN and NR waveforms that we use to build the hybrid waveforms, and we discuss the freedoms in the physical parameters, 3D rotations and time shift, and further BMS frame parameters not previously considered. In Sec. 3.3, we explain why there are discrepancies between PN and NR parameters, and how we match the physical parameters and inertial frames between NR and PN waveforms. Following this, we present the complete procedure to build the hybrid waveforms in Sec. 3.4. In Sec. 3.5, we show the hybridization results as well as the improvement from PN parameters and BMS frame fixing compared with previous models, and we use the findings to more precisely compare the PN and NR waveforms. Sec. 3.6 analyzes the sources of error for spin-aligned and precessing systems. Additionally, based on our error analysis, we make recommendations for future surrogate models' matching window selection in Sec. 3.7. In Sec. 3.8, we provide a few closing remarks. We make the code used for this hybridization procedure publicly available in Ref. [2].

3.2 Waveforms

The complex strain $h = h_+ - i h_\times$ is decomposed into modes according to

$$h(u,\theta,\phi) = \sum_{\ell=2}^{\infty} \sum_{m=-\ell}^{\ell} h_{\ell m}(u)\ {}_{-2}Y_{\ell m}(\theta,\phi), \tag{3.1}$$

where $u \equiv t - r$ is the retarded time and ${}_{-2}Y_{\ell m}$ are the spin-weight -2 spherical harmonics. We model all the $-\ell \le m \le \ell$ modes for $\ell \le 8$.

Post-Newtonian waveforms

In this study, we use PN theory to describe the GW waveforms of BBHs in quasi-circular orbits during the early inspiral stage, and include GW memory contributions. Memory effects should be inherent in any correct PN formulation, but their importance can often be overlooked. In our case, we find that accounting for memory is crucial when comparing to NR waveforms which have memory (since memory effects inherently arise when directly solving Einstein's equations), and thus crucial for accurate hybridization.

For binding energy and flux, we include nonspinning terms that are complete to 3.5 PN order from [46], and also the 4 PN terms from [47]. We also include higher-order terms up to 6 PN from [48], but these terms are obtained in the EMRI limit. We include the spin-orbit terms up to 4 PN order from [49], spin-spin terms up to 3 PN order from [50], and 3.5 PN spin-cubed terms from [51] for the orbital phase.

For the precession of spins and the orbital angular momentum, we include spin-orbit terms up to 3.5 PN from [52], and spin-spin terms up to 4 PN from [50].

For mode amplitudes, we include terms up to 4 PN. The terms up to 3 PN are taken from [53], the 3.5 PN terms in the $(2,2)$ mode and $\ell = 3$ modes are taken from [54] and [55], respectively, and the 4 PN terms in $(2,2)$ mode are taken from [47]. We also include non-linear memory terms up to 3.5 PN [56, 33] for mode amplitudes, but they are only complete at 3 PN for non-spinning systems, and 2 PN for spinning systems. They are computed using the procedure outlined in Ref. [33].

We also generate the PN Moreschi supermomentum [57], which we will later use to fix the BMS frame of NR systems, as we will detail in Sec. 3.2. The Moreschi supermomentum modes are taken from [33], which has the leading order spin-spin and spin-orbit terms. We leave the effects of eccentric orbits for discussion in Sec. 3.6.

To produce the PN phase as a function of time, we use the TaylorT1 approximant. The difference between different PN approximants is anticipated to be at the same order with the PN truncation error, which is controlled by the PN truncation order, implying that switching PN approximants is unlikely to substantially reduce the hybridization error. The PN generation is implemented in the Python package `NRPNHybridization` [2].

There are 8 independent physical parameters in quasicircular PN theory: mass ratio q, total mass M, and two three-dimensional spin vectors χ_1 and χ_2. The remaining parameters are all gauge. There are 4 parameters for a time shift and SO(3) rotation, which were considered in previous hybridization work. We will determine the above 12 parameters by performing a 12D optimization. The rest of the BMS group includes a Lorentz boost (3 parameters), and a supertranslation (described below), which is given by a smooth real-valued function $\alpha(\theta, \phi)$ on the sphere. We band-limit α to $\ell \leq 8$ modes, and its (0,0) mode is already accounted for in the time shift above, so α contributes an additional $(\ell+1)^2 - 1 = 80$ real parameters. We will discuss how to determine these 80 parameters in the next subsection.

Numerical-relativity waveforms and BMS frames

It is worth noting that models of gravitational-wave emission are usually constructed in asymptotically flat spacetimes. Bondi, van der Burg, Metzner, and Sachs [58, 59, 60] demonstrated that the spacetime symmetry at the asymptotic boundary is the BMS group. This is comprised of the usual Lorentz transformations, as well as a set of generalized time and space translations referred to as "supertranslations," which can be interpreted as direction-dependent translations on the asymptotic boundary. Specifically, under a supertranslation $\alpha(\theta, \phi)$, the retarded-time coordinate $u \equiv t - r$ transforms as

$$u' = u - \alpha(\theta, \phi)\,. \tag{3.2}$$

These transformations are implemented in the `scri` python package [61], using the method described in Ref. [62].

Note that the BMS frame is defined at null infinity, but the outer boundary of NR simulations is set at a finite radius, which doesn't have the information from null infinity. So the NR BMS frame can not be specified arbitrarily when setting up the simulation, and therefore in practice an NR simulation (before any BMS frame fixing is done) is in some arbitrary uncontrolled BMS frame. Reference [63] emphasized the importance of having both PN and NR waveforms in the same BMS frame. We follow their procedure to map NR waveforms to the corresponding PN BMS frame. First, we determine the space translation and boost by minimizing the center-of-mass charge. We then calculate the supertranslations that map the $\ell \geq 2$ modes of the NR Moreschi supermomentum $\Psi_{\mathrm{M}}^{\mathrm{NR}}$ to the corresponding PN Moreschi supermomentum $\Psi_{\mathrm{M}}^{\mathrm{PN}}$, where Ψ_{M} is

$$\Psi_{\mathrm{M}} \equiv \Psi_2 + \sigma\dot{\bar{\sigma}} + \eth^2\bar{\sigma}, \tag{3.3}$$

with Ψ_2 being the Weyl scalar with spin-weight 0, σ the Newman-Penrose shear, and an overbar representing complex conjugation. For a quantity η of spin weight s, the spin-weight raising operator $\eth$ can be written as [64, 65]

$$\eth\eta = -\frac{1}{\sqrt{2}}(\sin\theta)^s\left(\frac{\partial}{\partial\theta} + \frac{i}{\sin\theta}\frac{\partial}{\partial\phi}\right)\left((\sin\theta)^{-s}\eta\right). \tag{3.4}$$

The mapping to the BMS frame is done using an iterative procedure [63, 33], as we explain in more detail below in Sec. 3.4.

We use NR waveforms that are computed using a Cauchy-characteristic evolution (CCE) [42, 43], for which the Cauchy evolution parts are performed using the Spectral Einstein Code (SpEC) [66], and the CCE computation is performed using the SpECTRE code [67]. CCE uses a worldtube from the Cauchy evolution of the Einstein field equations as the inner boundary of a characteristic evolution on a null foliation. The gravitational information is propagated and evolved to future null infinity. Note that Ψ_2 and σ required in Eq. (3.3) are calculated by the SpECTRE CCE code. Note that unlike CCE waveforms, extrapolated waveforms obtained using the methods described in Ref. [44] cannot be mapped to the PN BMS frame, because they do not have an accurate value of Ψ_2 for calculating the Moreschi supermomentum.

The NR waveforms that we use are from simulations in the SXS catalog [45, 68]. We plot the parameter space χ_p versus q in Fig. 3.2, where $\chi_p = \max\{\chi_{1\perp}, \frac{4+3q}{q(4q+3)}\chi_{2\perp}\}$

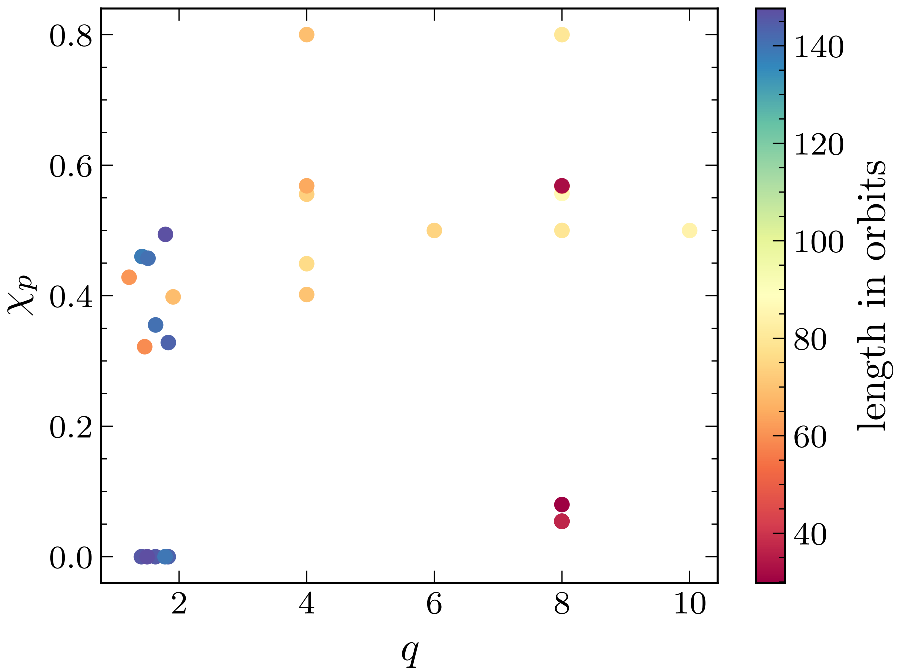

Figure 3.2: The parameter space of the NR simulations that we use. The color shows the length of the waveform in terms of orbits.

[69] and $\chi_{1,2\perp}$ is the magnitude of the projection in the orbital plane. They are systems SXS:BBH:1412–1416 and 2617–2640. Of these, SXS:BBH:1412–1416 and 2617-2621 are exceptionally long, spanning over 100 orbits. This extensive length enables us to evaluate the validity of hybridization at an early stage in the binary's inspiral. The mass ratio for both the SXS:BBH:1412–1416 and 2617-2635 systems falls within the range $1 < q < 10$. As for the SXS:BBH:2636–2640 systems, the mass ratios are approximately $q \approx 8$. The waveforms SXS:BBH:1412–1416 correspond to spin-aligned systems, while the other systems utilized in our study are precessing systems. The magnitudes of the spin parameters χ_1 and χ_2 are constrained as $|\chi_1|, |\chi_2| \leq 0.8$.

The 8 physical parameters in NR simulations, namely the masses m_1 and m_2 and dimensionless spin vectors $\boldsymbol{\chi}_1$ and $\boldsymbol{\chi}_2$, are measured quasi-locally on the apparent horizons of the BHs [68]. Therefore, the value of these quantities under this 'quasi-local' definition could differ from the PN mass and spin parameters that appear in PN expansions. This difference is accounted for in the matching procedure.

3.3 Matching PN and NR parameters

There are three reasons why we want to perform the optimization over all intrinsic parameters:

1. The definitions of PN parameters are not consistent with the NR definitions. The NR parameters are measured quasi-locally on the apparent horizon, as detailed in [68]. Meanwhile PN parameters are attributed to point particles, via asymptotic matching in "body zones", as explained in [70]. The difference between the PN and NR definitions should be small as we see in the optimization results, but perfect agreement between them is anticipated only at infinite separation, even for infinite-order PN and infinite-resolution NR. The leading order contribution to the difference is expected to be the binding energy between the two black holes, which appears at 1 PN order. Determining the exact relationship between PN and NR definitions requires solving for the apparent horizon in the PN metric and evaluating the parameters at the PN apparent horizon, which is beyond the scope of this paper. We are working on this issue as a separate project.

   The difference in parameter definitions is not an error or uncertainty, but a conventional discrepancy, thus it has no physical significance. For astrophysical parameter inference, it is recommended to quote PN parameters rather than NR, since these correspond to masses and spins infinitely far in the past.

2. Even if we used the same definitions of mass and spin quantities in PN and NR, the definitions are gauge dependent. Apparent horizon integrals used in NR are gauge dependent since apparent horizons are themselves slicing-dependent [71]. Meanwhile specifying a spin in PN requires a choice of spin supplementary condition (SSC), which is a type of gauge choice [72]. A choice of SSC also affects the definition of mass in PN. This gauge-dependence also applies to the total binary mass, which is distinct from the gauge-invariant ADM energy; these differ by the binding energy and the energy carried away by radiation.

3. Both PN and NR waveforms have systematic errors. The PN errors are mainly due to the truncation at a finite PN order, and the NR errors are mainly due to numerical truncation. The error is supposed to affect both the waveform and the parameters. As we will show in Sec. 3.5, the difference between the PN and NR parameters are at the same order as the residual between the strain modes. Therefore, there is no reason to force the difference between the PN and NR

> parameters to be zero, seeing as this would introduce more error in the strain and thus make the hybrid waveform less accurate. Given the finite length and finite resolution of the waveforms, the optimized parameters can compensate for the errors in the model and the unmodeled effects, to provide the best agreement and smoothest transition between the NR and PN waveforms.

Therefore, we must identify the proper PN parameters that correspond to the NR systems.

Here we are concerned with optimizing only 12 parameters: 8 PN parameters (q, M, χ_1 and χ_2) and 4 coordinate parameters that determine the SO(3) rotation and time translation. For technical reasons discussed in Sec. 3.4, we use a different method to determine the additional supertranslation and boost parameters. We will present the complete procedure to determine all the parameters in Sec. 3.4.

We determine these 12 parameters by minimizing the normalized L^2 difference over a chosen matching window between the fixed NR waveform $h^{\mathrm{NR}}(t)$ and the free PN waveform, $h^{\mathrm{PN}}(t;\vec{\lambda})$, where $\vec{\lambda}$ are the chosen parameters. We define a cost function $\mathcal{E}$ from the normalized L^2 difference between the waveforms,

$$\mathcal{E}[h^{\mathrm{NR}}, h^{\mathrm{PN}}] = \frac{1}{2}\frac{\sum_{\ell,m}\int_{t_1}^{t_2}\left|h^{\mathrm{NR}}_{\ell m}(t) - h^{\mathrm{PN}}_{\ell m}(t;\vec{\lambda})\right|^2 dt}{\sum_{\ell,m}\int_{t_1}^{t_2}\left|h^{\mathrm{NR}}_{\ell m}(t)\right|^2 dt}\,. \tag{3.5}$$

Here t_1 and t_2 are the start and end time of the matching window. $\mathcal{E}$ reduces to sphere-weighted average of the commonly used time-domain mismatch with a flat noise power spectral density (see Appendix C of [73]).

Unless otherwise specified, we typically use a matching window ending at $-8000\,M$ for precessing systems, and $-5000\,M$ for spin-aligned systems, for the purposes of illustration. We set $t = 0$ at the merger, where the merger is defined as the peak of the L^2 norm of the strain modes.

We use the nonlinear least squares method to perform the minimization.[1] However, it turns out that the cost function Eq. (3.5) has long and narrow valleys that cause the optimizer to run slowly. Fig. 3.3 shows two examples of the valleys in the cost function. The top plot shows an example of the dependence of the cost function on

[1] For the optimization, we use `scipy.optimize.least_squares` with the Trust Region Reflective algorithm [74, 75]. The tolerances are set to gtol = 10^{-8} and xtol, ftol = 3×10^{-15}. We use the NR value of the parameters as the initial guess. The gradient is computed numerically. We impose bounds on the optimization parameters, which we will discuss later in the text.

the x components of χ_1 and χ_2. We can see that the constraint on χ_1 is better than χ_2, although they still show some degeneracy between each other. Additionally, the figure on the bottom illustrates the cross section involving the time shift and the z component of the logarithm of the quaternion rotor that rotates the inertial frame. This figure shows the degeneracy between time and phase.

In order to mitigate these degeneracies and enhance the optimization process, we reparametrize the 12 parameters to diagonalize the valleys. First, we introduce new parameters x_1 to x_4 to describe the fractional change in PN mass ratio q, total mass M, and spin amplitudes compared to their NR counterparts; see Eq. (3.6). Then, note that the NR value of the spin vectors could be measured in a different Euclidean frame from the PN frame, which is also suggested by the degeneracy between χ_{1x} and χ_{2x} shown in the upper plot of Fig. 3.3. We therefore introduce the quaternion $\mathbf{Q}_1$ to describe the rotational transformation of the two spin vectors as a unified entity. This quaternion will have three degrees of freedom, which we parameterize as (x_5, x_6, x_7). One degree of freedom corresponds to a rotation *about* χ_1^{NR}, and thus has no effect on χ_1^{NR} itself. But if the two spins are not parallel, that degree of freedom can affect χ_2^{NR}. This leaves just a single degree of freedom representing the rotation of χ_2^{NR}, in a direction orthogonal to both χ_1^{NR} and χ_2^{NR}. This final rotation is encoded as another quaternion $\mathbf{Q}_2$ that depends on only one additional parameter x_8. Thus we have

$$\begin{aligned}
q &= x_1 q^{\mathrm{NR}}, \\
M &= x_2 M^{\mathrm{NR}}, \\
\chi_1 &= x_3 \mathbf{Q}_1 \chi_1^{\mathrm{NR}} \bar{\mathbf{Q}}_1, \\
\chi_2 &= x_4 \mathbf{Q}_2 \mathbf{Q}_1 \chi_2^{\mathrm{NR}} \bar{\mathbf{Q}}_1 \bar{\mathbf{Q}}_2, \\
\mathbf{Q}_1 &= \exp\left[(x_5, x_6, x_7)\right], \\
\mathbf{Q}_2 &= \exp\left[\frac{x_8}{2}\left(\widehat{\chi_1^{\mathrm{NR}} \times \chi_2^{\mathrm{NR}}}\right)\right],
\end{aligned} \tag{3.6}$$

where the bar represents the conjugate of a quaternion, and the hat over the cross product indicates that the result is normalized. “NR” superscripts denote the NR values of these quantities obtained at the reference time, which we typically set as the end time of the matching window. Here we use the standard quaternion notation, where the exponential of a 3-vector gives a unit quaternion [76].

We also need a quaternion $\mathbf{R}$, which describes an overall SO(3) rotation of the system,

$$\mathbf{R} = \exp\left[(x_9, x_{10}, x_{11}) + \frac{x_0}{2}\mathbf{\Omega}_{\mathrm{tot}}\right]. \tag{3.7}$$

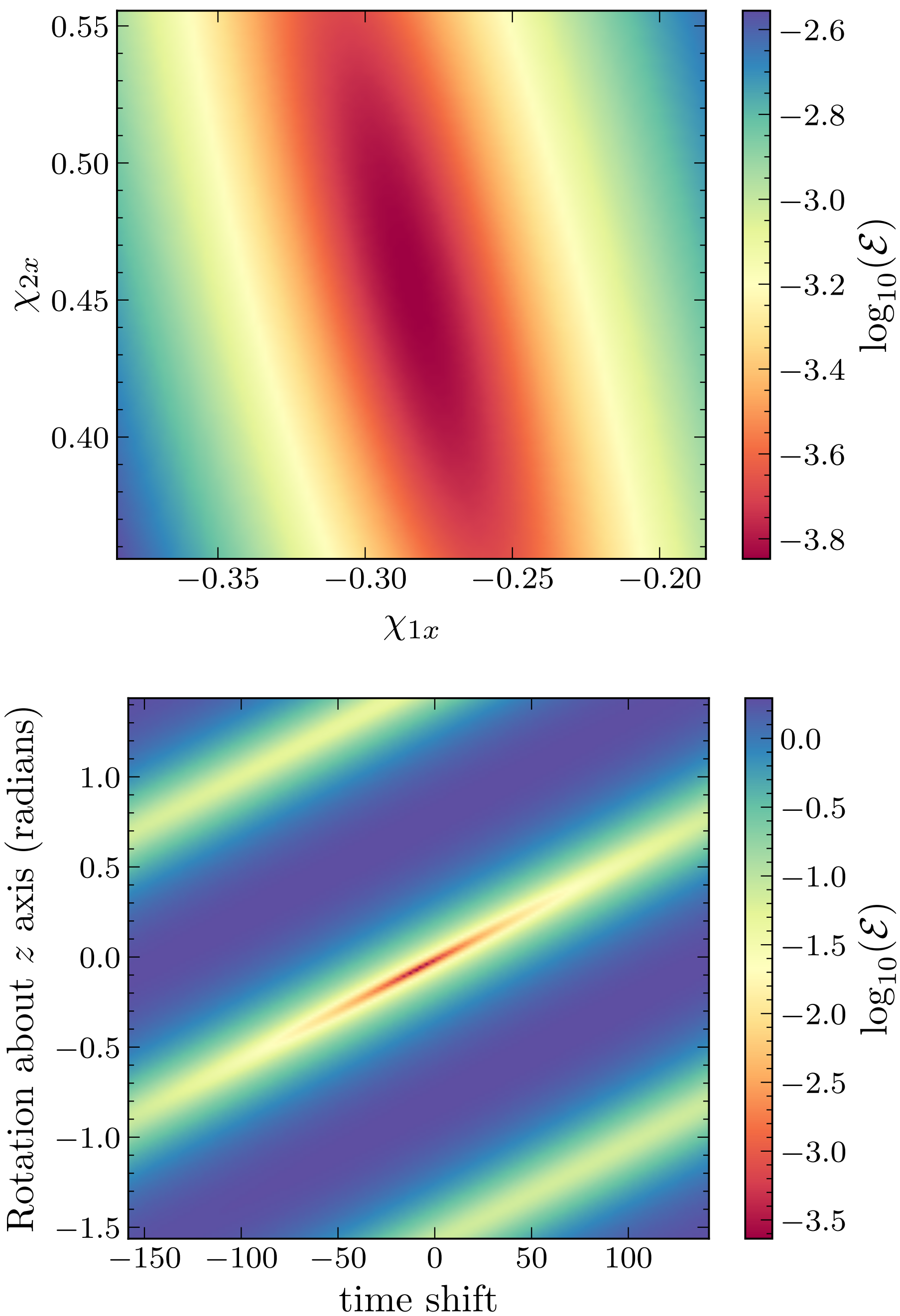

Figure 3.3: The profile of the cost function $\mathcal{E}$ with respect to parameters for system SXS:BBH:2617. The matching window is 20 orbits long, and ends 8000 M before merger. In each plot, the 10 other parameters are fixed to their best-fit values. The slanting long and narrow valleys show the degeneracy between these parameters, which can drastically slow down the optimization.

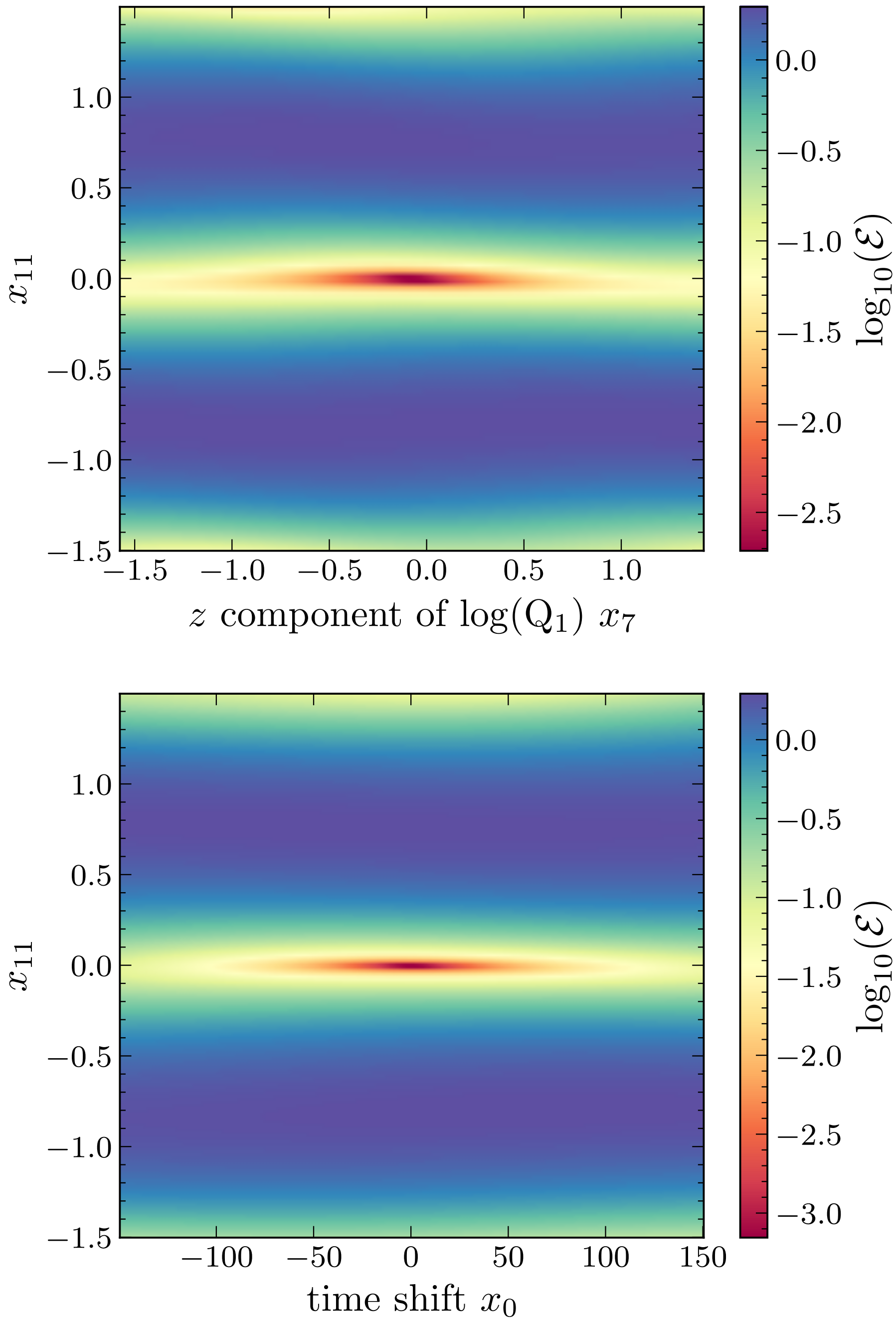

Figure 3.4: The profile of the cost function $\mathcal{E}$ with respect to the new parameters for system SXS:BBH:2617. The matching window is 20 orbits long, and ends at 8000 M before merger. In each plot, the 10 parameters that are not varied are fixed at the best-fit values. These new parameters are no longer degenerate. If the cost function has a narrow diagonal valley, as in Fig. 3.3, the optimizer tends to zigzag within the valley, leading to a significant slowdown in the optimization process. However, if the valley aligns with an axis, the optimizer can easily re-scale the axis, leading to more efficient optimization.

The $\frac{x_0}{2}\mathbf{\Omega}_{\rm tot}$ term in the quaternion rotor $\mathbf{R}$ is introduced to eliminate the degeneracy between time and phase shown in the bottom plot in Fig. 3.3. Here x_0 is the parameter that describes the time shift between the NR and PN systems, and $\mathbf{\Omega}_{\rm tot}$ is the total angular velocity measured at the reference time, which captures both orbital and precession contributions. $\mathbf{\Omega}_{\rm tot}$ is measured from the NR strain by defining it as the angular velocity of a rotating frame in which the time dependence of the waveform mode is minimized [76].

When performing the nonlinear least squares optimization, we impose bounds on the parameters defined in Eqs. (3.6) and (3.7). For x_{1-4}, the bounds are windows of size ±0.05, ±0.02, ±0.01 and ±0.01 around their respective initial guesses. For x_{5-11}, the range is $\pm\pi/4$, and $\pm 0.5\pi/\Omega_{\rm orb}$ for the time shift x_0.

Fig. 3.4 shows how the new reparameterization can diagonalize the valleys of the cost function and mitigate the degeneracies. This parametrization has been tested on many systems.

We test the optimization routine by using a PN waveform with known parameters as a proxy "NR" waveform, and adjusting the parameters of another PN waveform until the two waveforms match. In most cases, both the original PN parametrization and our new parametrization presented in Eq. (3.6) and Eq. (3.7) can recover the PN parameters to high accuracy and reduce the waveform differences to $\mathcal{E} \approx 10^{-15}$, as shown in Fig. 3.5. But for poor initial guesses, our new parametrization generally behaves better than the original PN parametrization, as shown in Fig. 3.6.

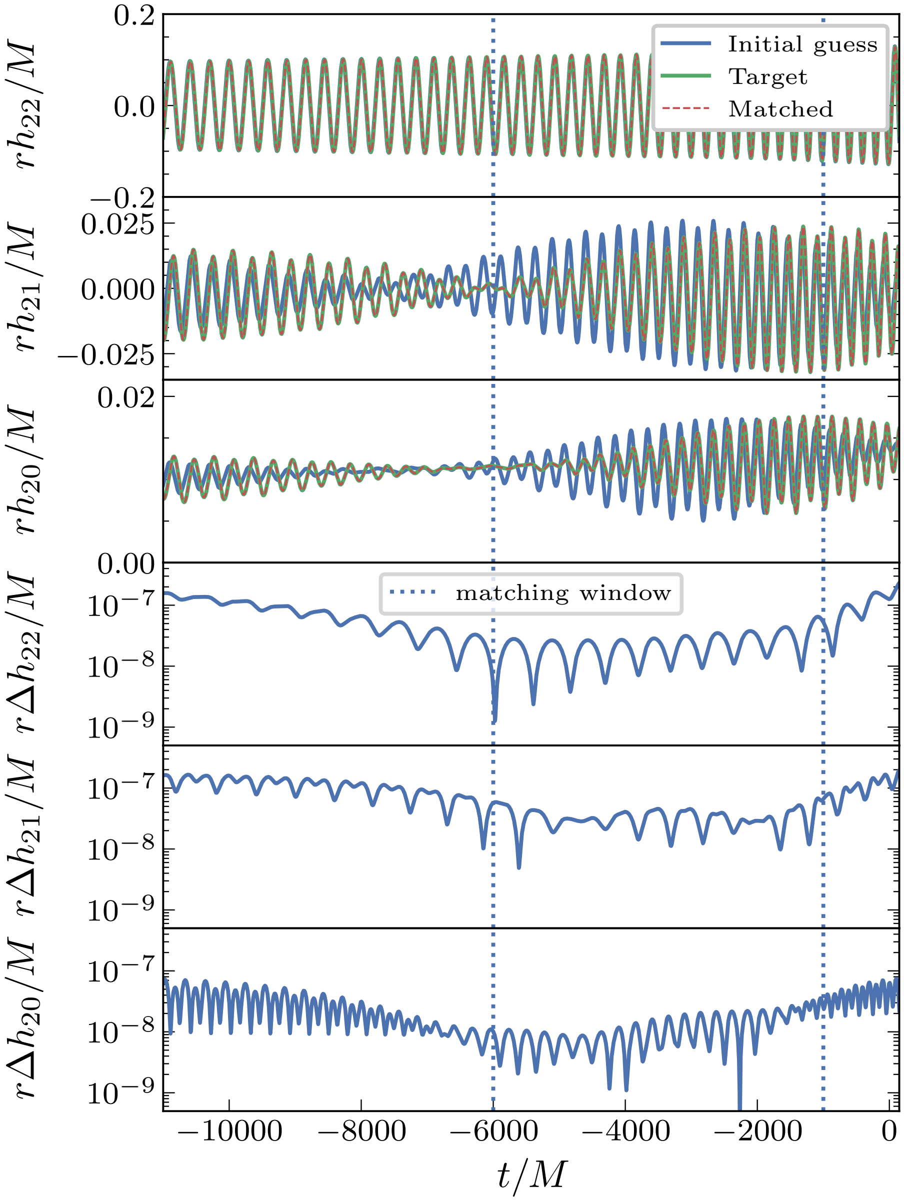

Figure 3.5: Strain and residual of two PN waveforms, for a test in which we match the two waveforms by varying the parameters of one of them. The target PN waveform has parameters $q = 1.5$, $M = 1.0$, $\chi_1 = (0.5, 0.2, 0.3)$, $\chi_2 = (0.1, 0.3, 0.4)$, and is rotated away by $\mathbf{R} = \exp(0.05, 0.02, 0.03)$ from the original frame in which the PN waveform is generated. The initial guess is $q = 1.65$, $M = 1.05$, $\chi_1 = (0.42, 0.24, 0.47)$, $\chi_2 = (0.01, 0.20, 0.41)$. The parameters obtained by the optimization are $q = 1.500004$, $M = 1.000005$, $\chi_1 = (0.10001, 0.200002, 0.30003)$, $\chi_2 = (0.399994, 0.09998, 0.20006)$. The matching window is the region between two vertical dotted lines, which is $5000\,M$ long.

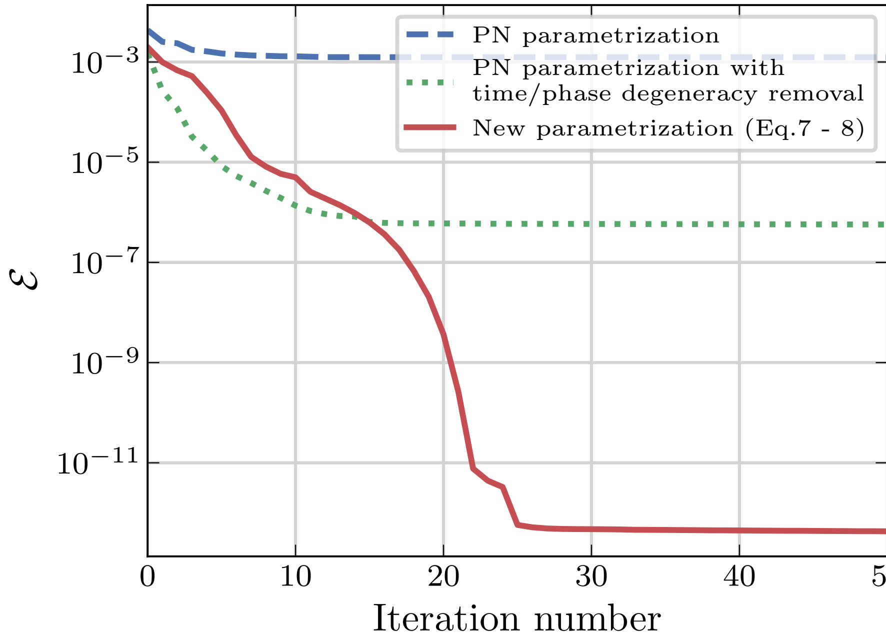

Figure 3.6: The convergence of different parametrization methods for a PN-PN matching test, in which we match the two waveforms by varying the parameters of one of them. The target PN waveform has parameters $q = 1.5$, $M = 1.0$, $\chi_1 = (0.5, 0.2, 0.3)$, $\chi_2 = (0.1, 0.3, 0.4)$, and is rotated away by $\mathbf{R} = \exp(0.0, 0.0, 0.05)$ from the original frame in which the PN waveform is generated. The initial guess is $q = 1.65$, $M = 1.05$, $\chi_1 = (0.42, 0.24, 0.47)$, $\chi_2 = (0.01, 0.20, 0.41)$. The matching window is $5000\,M$ long. The result using the new parametrization in Eqs. (3.6) and (3.7) is shown as the red curve, which converges much faster and better than the original PN parametrization, which is shown as the blue dashed curve. The green dotted curve also uses the original PN parametrization but incorporates the $\frac{x_0}{2}\mathbf{\Omega}_{\text{tot}}$ term in the frame rotor $\mathbf{R}$ defined in Eq. (3.7). In other words, it uses (x_0, q, M, χ_1 and χ_2) and (x_9 through x_{11}) as parameters. The green dotted curve shows better convergence than the blue dashed curve.

3.4 Hybridization procedure

In the previous section we described how we determine the PN parameters, the time offset, and the overall rotation of a PN waveform that we match to an NR waveform. However, we also need to account for differences in supertranslations and boosts between the NR and PN waveforms. While it is possible to add extra supertranslation parameters into the cost function defined in the previous section, we find it more efficient to account for all parameters (8 PN physical parameters, time shift, boost, rotation, and supertranslations) using the following iterative procedure:

1. Map the NR waveform to its superrest frame, which is defined as the frame in

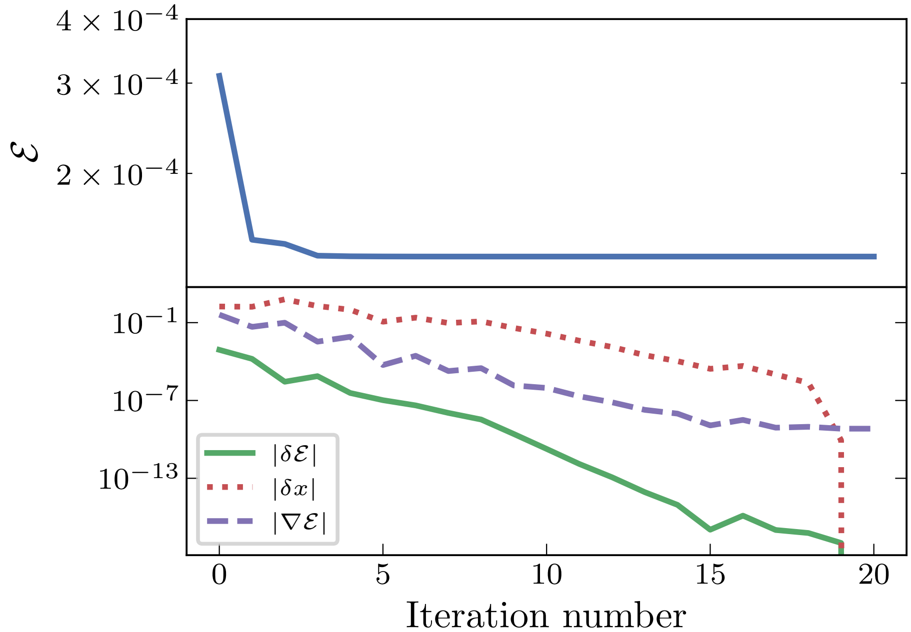

Figure 3.7: The convergence of the 12-D nonlinear least-squares optimization for system SXS:BBH:2617 in the second iteration of step 6 of the procedure in Sec. 3.4, using the parameters from the first iteration as the initial guess. The horizontal axis is the iteration number for the 12-D optimization. The end of the matching window is 5000 M before merger, and is 20 orbits long. The blue curve shows the value of the cost function, and the green solid and red dotted curves show the reduction of the function value and the norm of change in parameters after each iteration. The norm of the gradient of the cost function is shown in dashed purple.

which the Moreschi supermomentum is minimized [33]. The superrest frame is determined during inspiral at the middle of the matching window.

The original CCE waveforms are typically in an arbitrary BMS frame with large center-of-mass charge and supermomentum, resulting in significant oscillations in the strain mode amplitudes and orbital frequency. These irregularities introduce bias when determining the PN parameters. Mapping the NR waveform to its superrest frame reduces the effects caused by a large center-of-mass charge and supermomentum, mitigating biases and enabling a more accurate optimization of the PN parameters.

2. Set the $m = 0$ modes of the NR and PN waveforms to zero in their corotating frame.

   The $m = 0$ modes have the most memory contribution, and are thus more influenced by the supertranslations involved in the BMS frame transformation.

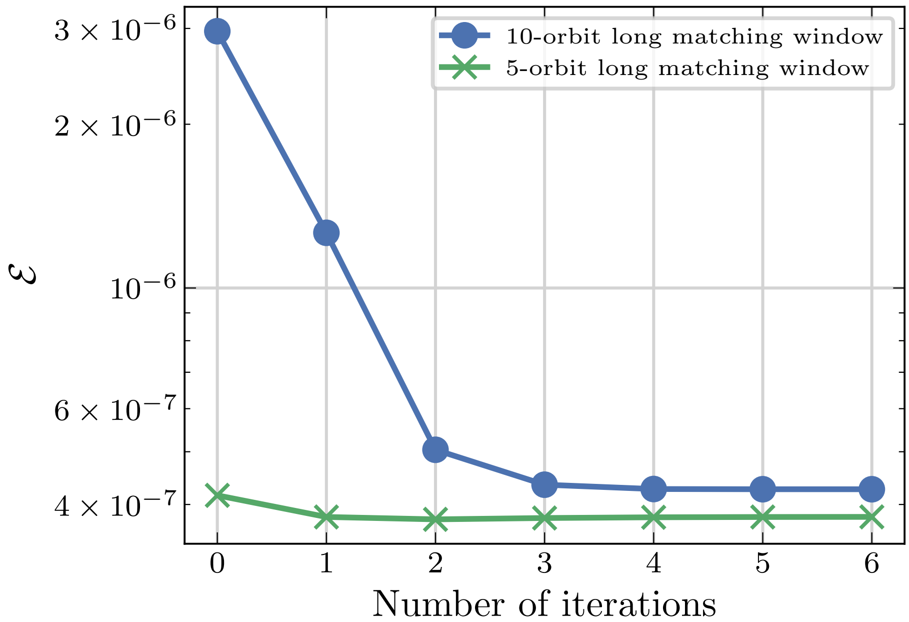

Figure 3.8: The convergence of iterations of step 6 of the procedure in Sec. 3.4 for system SXS:BBH:1414. The 0th iteration is step 3 of the procedure in Sec. 3.4, for which the NR waveform is mapped into the superrest frame, and for this iteration the error does not include the $m = 0$ modes since the value of the strain in these modes in the superrest frame does not agree with PN. For the other iterations, the NR waveform is mapped to the PN BMS frame, and the errors include the $\ell \leq 8$ modes. The blue curve uses a 10-orbit long matching window that ends $8000\,M$ before merger, and the green curve uses a 5-orbit long matching window that ends $2000\,M$ before merger. Both curves converge within 4 iterations. The cost function for the shorter matching window is smaller and converges less rapidly than the case with a longer matching window, likely because the short waveforms are being overfit. This overfitting is explored in Sec. 3.7.

Since the superrest frame of the NR system differs from the PN BMS frame, the strain modes in these two frames are expected to differ as well. This can also introduce bias when optimizing PN parameters. Therefore, we set $m = 0$ modes to zero in their corotating frame to exclude the principal memory contributions to the strain. Note that the $m = 0$ modes will be restored in step 4 and the steps thereafter.

3. Perform the 12D optimization described in the previous section to determine the 8 PN parameters, rotation, and time shift.

4. Now with the $m = 0$ modes of the original NR waveform included, map the original NR waveform to the BMS frame of the resulting PN system by applying

the supertranslations that map the NR Moreschi supermomentum to the PN Moreschi supermomentum, and also applying the boost that minimizes the center-of-mass charge. Note that the PN Moreschi supermomentum depends on the PN parameters, so the NR waveform obtained by this step depends on the current values of the PN parameters.

5. Again perform the 12D optimization, but using the NR waveform from step 4, including the $m = 0$ modes in the PN waveform.
6. Iterate steps 4 and 5 until the relative change in $\mathcal{E}$ is less than 10^{-2}.
7. Use a smooth stitching function to hybridize the PN and NR waveforms over the matching window.

Our stitching function is the smooth transition function

$$\tau(t) = \begin{cases} 0 & t < t_1, \\ \left\{1 + \exp\left[(t_2 - t_1)\left(\frac{1}{t-t_1} + \frac{1}{t-t_2}\right)\right]\right\}^{-1} & t_1 \leq t \leq t_2, \\ 1 & t_2 < t. \end{cases} \tag{3.8}$$

The hybridized waveform is then

$$h^{\text{Hyb}}_{\ell m}(t) = [1 - \tau(t)] h^{\text{PN}}_{\ell m}(t) + \tau(t) h^{\text{NR}}_{\text{BMS}\,\ell m}(t), \tag{3.9}$$

where h^{PN} is the PN waveform obtained with the given x_i parameters and $h^{\text{NR}}_{\text{BMS}}$ is the NR waveform in the adjusted BMS frame, as obtained in step 4 of the iterative procedure.

The convergence of the 12-D optimization is tested for the NR-PN hybridization case with comparable BH masses, as shown in Fig. 3.7. The optimization typically converges within tens of iterations.

The process of iteratively optimizing PN parameters and mapping the NR waveform to the resulting PN BMS frame demonstrates rapid convergence for cases with comparable BH masses, as illustrated in Fig. 3.8. In the case of shorter matching windows, the decrease in the cost function during each iteration is less pronounced compared to longer matching windows. This can be attributed to the limited information contained within shorter windows, which may result in overfitting. We will further address this problem in Sec. 3.7. The iteration process typically converges within 2–4 steps.

For cases with a larger mass ratio ($q \sim 8$), larger eccentricity ($e > 0.05$), or larger χ_p (> 0.5), both the 12-D optimization and the overall iterative procedure converge more slowly. For these cases, the 12-D optimization typically takes more than a hundred iterations, and the overall iterative procedure typically takes more than 10 iterations. This slowdown occurs because for systems with large mass ratios, the waveforms become less sensitive to the smaller black hole's properties. And for systems with larger χ_p or eccentricity, the PN and NR waveforms that we use become intrinsically different, as we will show in Sec. 3.6. These features make the optimization more challenging.

3.5 Results

Comparison between PN and NR waveforms

We present typical hybridization results for spin-aligned systems and precessing systems in Figs. 3.9 and 3.10. For the early inspiral stage, the PN and NR waveforms agree quite well, up to the systematic errors (eg., non-zero eccentricity of NR systems, absence of PN terms, etc.) that we will discuss in Sec. 3.6.

Apart from systematic errors in the early inspiral stage, we notice the PN failure thousands of M before merger as the differences between the NR and PN strain modes become much larger. We will be interested in the frequency at which the PN truncation error becomes larger than other systematic errors that affect our hybridization procedure. Later we will choose the matching window to end before this frequency, so that the PN truncation error has a negligible effect on the matching procedure compared to the other errors.

The PN expansion parameter is $v = (M\Omega_{\text{orb}})^{1/3}$, and each power of v counts for $\frac{1}{2}$PN order. PN waveforms that are complete up to N PN order have truncation errors at relative order $O\left(\Omega_{\text{orb}}^{(2N+1)/3}\right)$. Therefore, the frequency at which PN truncation error becomes dominant satisfies

$$\left(\text{Coefficient} \cdot \Omega_{\text{orb}}^{(2N+1)/3}\right)^2 \approx \mathcal{E}_{\text{sys}}, \tag{3.10}$$

where $\mathcal{E}_{\text{sys}}$ is the norm of differences induced by other systematic errors. The systematic errors include errors that can cause the differences between NR and PN beyond PN truncation. These may arise from numerical errors, eccentricities in NR binaries that are meant to be quasicircular, inaccuracies in PN parameters, imprecise

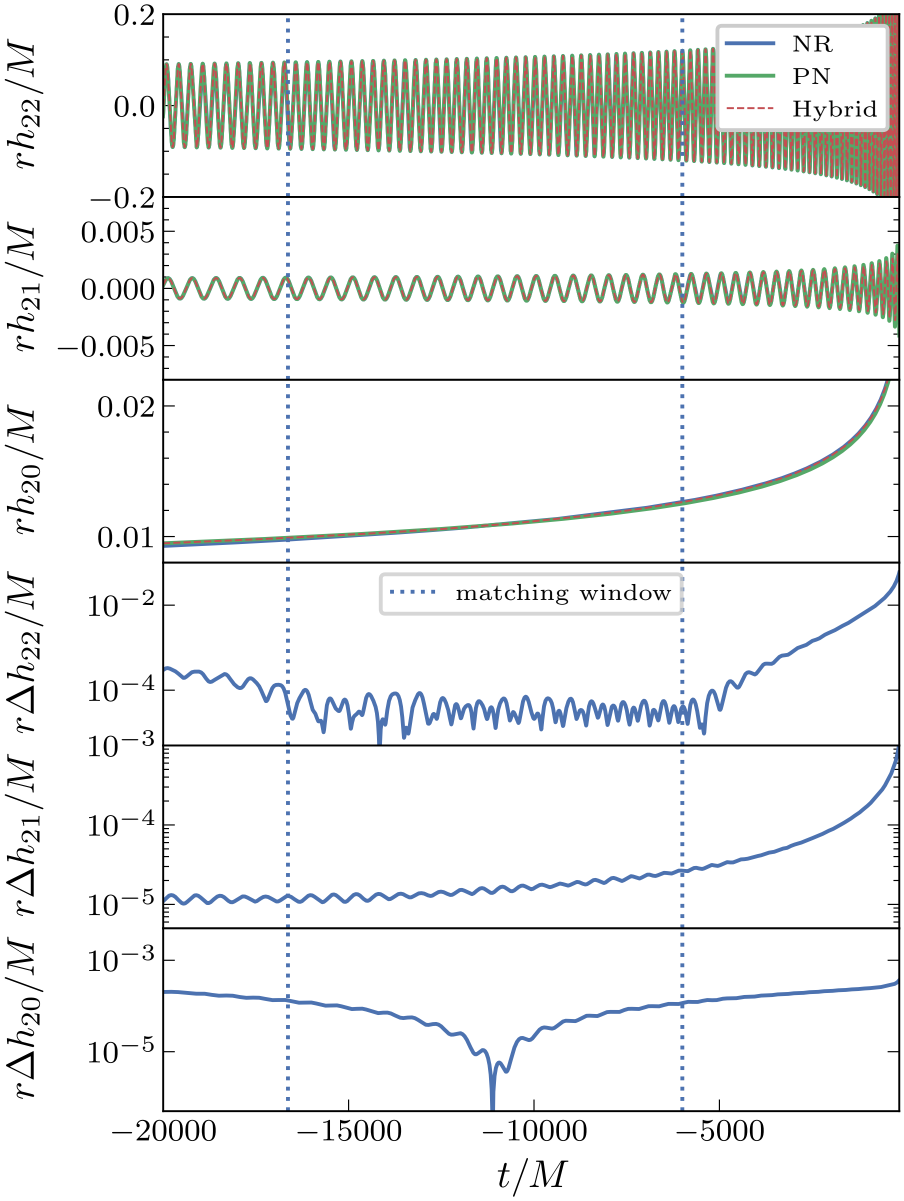

Figure 3.9: Strain and residual of the hybridized spin-aligned system SXS:BBH:1412. The matching window is the region between the two vertical dotted lines, which is 20 orbits long and ends at $-6000\,M$. The blue, green and red curves in the upper panel are the strain modes of the NR, PN and hybrid waveforms. The blue curves in the lower panel are the residuals between the NR and PN strain modes.

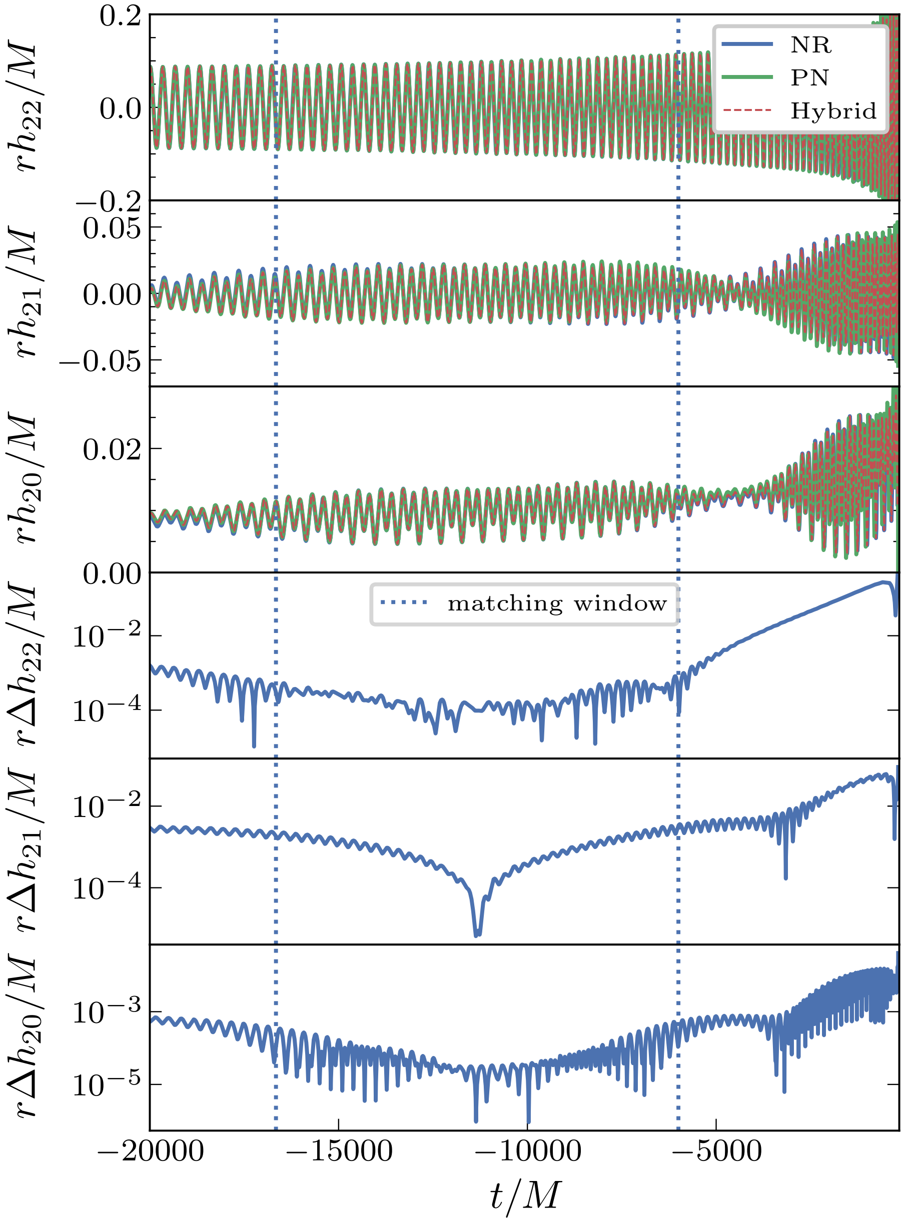

Figure 3.10: Strain and residual of the hybridized precessing system SXS:BBH:2619. The matching window is the region between the two vertical dotted lines, which is 20 orbits long and ends at $-6000\,M$. The blue, green and red curves in the upper panel are the strain modes of the NR, PN and hybrid waveforms. The blue curves in the lower panel are the residuals between the NR and PN strain modes.

BMS frame alignment, incomplete consideration of certain physical aspects in PN or NR models like high order spin interactions in PN, or inaccurate boundary conditions in NR, and more. We will explore further the systematic errors that limit our hybridization accuracy in Sec. 3.6.

Improvement from PN parameters and BMS frame fixing

In Fig. 3.11, we present the hybridization errors of 29 systems. The hybridization error plotted is the cost function in Eq. (3.5) computed within a 10-orbit matching window. However, only the brown markers in the figure represent errors computed using the full hybridization procedure described in Sec. 3.4. The other markers represent results obtained using only parts of the procedure, omitting some of the waveform modes, or using NR waveforms that are not obtained using CCE; these markers are included to illustrate the need for all parts of the procedure described in Sec. 3.4. For all the markers, the 4 parameters representing the 3D rotation and time shift between the PN and NR waveforms are optimized to obtain a minimal hybridization error. The triangular markers use extrapolated NR waveforms obtained using the methods described in [44], which lack the correct memory effect. The circular markers use CCE waveforms that include memory contributions and contain enough information to allow suitable BMS transformations. The blue triangular markers denote errors obtained from the extrapolated waveforms without adding supertranslations, and with the 8 PN parameters fixed to their corresponding NR values. The extrapolated waveforms get a different CoM-correction that is described in [77]. Because the extrapolated waveforms lack the correct memory terms, we include the green triangular markers, which are obtained by setting the $m = 0$ modes to zero in the NR corotating frame before hybridization, and then plotting the hybridization error of only the $m \neq 0$ modes. For the green triangular markers, the PN parameters are fixed to their corresponding NR values. The errors represented by the pink, purple, and brown circular markers include all modes including $m = 0$. The pink circular markers utilize CCE waveforms, but the NR waveforms are in their inspiral superrest frames, and the PN parameters are fixed to their corresponding NR values at the reference time. The purple circular markers map the NR waveforms to the corresponding PN BMS frame, but the PN parameters used in both the PN waveform and to define the PN BMS frame are the corresponding NR values of those parameters. Comparing the results in the superrest frame against those in the PN BMS frame (pink and purple circular markers), we observe that by fixing the BMS frame we can improve the error between PN and NR waveforms by 1 to 3 orders

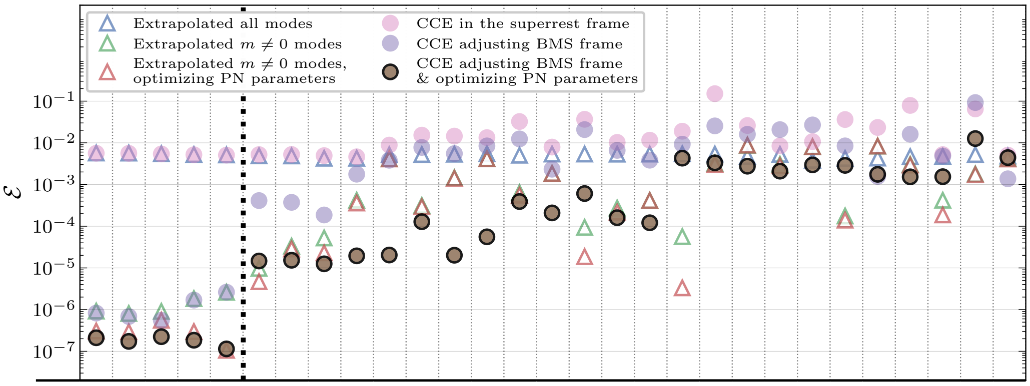

SXS ID	1415	1413	1412	1414	1416	2637	2640	2639	2638	2622	2619	2617	2623	2625	2624	2626	2620	2618	2621	2629	2627	2628	2632	2633	2635	2634	2636	2631	2630
χ_p	0.00	0.00	0.00	0.00	0.00	0.05	0.05	0.05	0.08	0.32	0.33	0.36	0.40	0.40	0.43	0.45	0.46	0.46	0.49	0.50	0.50	0.50	0.56	0.56	0.57	0.57	0.57	0.80	0.80
q	1.5	1.4	1.6	1.8	1.8	8.0	8.0	8.0	8.0	1.5	1.8	1.6	1.9	4.0	1.2	4.0	1.5	1.4	1.8	10.0	6.0	8.0	4.0	8.0	8.0	4.0	8.0	8.0	4.0
e	4.3e−5	1.0e−4	4.4e−4	1.6e−3	1.7e−3	3.7e−4	1.2e−4	7.0e−5	4.7e−4	2.2e−4	6.5e−5	2.0e−4	1.7e−4	2.4e−4	1.3e−4	1.4e−4	1.1e−4	6.8e−5	4.5e−4	3.9e−4	1.2e−4	1.2e−4	1.7e−4	1.7e−4	2.5e−4	1.2e−4	5.9e−4	7.5e−5	2.1e−4
$\Delta\phi$	0.07	0.01	0.01	0.03	0.03	0.02	0.03	0.03	0.06	2e−4	0.05	0.03	0.01	0.23	0.02	0.38	3e−3	2e−3	0.06	0.29	0.32	0.2	1.35	0.75	0.26	0.04	0.05	0.5	1.11

Figure 3.11: Hybridization errors in the matching window, Eq. (3.5), for different waveforms and for different methods of choosing PN parameters and matching the BMS frame. See text for details. All the errors are measured after adjusting the 3-D rotation and time shift. The BMS frame for extrapolated waveforms cannot be modified using the method described in this paper because those waveforms do not have an accurate value of Ψ_2 to calculate the Moreschi supermomentum. We only adjust the BMS frame for CCE waveforms. Systems on the left of the vertical dotted line are spin-aligned systems; systems on the right are precessing systems, and systems are ordered left to right by χ_p. The mass ratios for SXS:BBH:2617–2635 systems are $1 < q < 10$ and for SXS:BBH:2636–2640 systems are $q \approx 8$. The matching window is 10 orbits. For systems other than the SXS:BBH:2636–2640 systems, the matching window ends $8000\,M$ before merger. For the SXS:BBH:2636–2640 systems the matching window ends $5000\,M$ before merger because these systems are not long enough. The brown markers use the full hybridization procedure described in Sec. 3.4. e is the eccentricity measured from the trajectory at the NR reference time, and $\Delta\phi$ is the dephasing between the two highest resolution NR runs of the last 20 orbits before merger. It is important to recognize that this dephasing does not directly reflect the inaccuracy of the NR waveforms, as the NR parameters within the matching window for different Levs can deviate by 10^{-2}, given their evolution over nearly a hundred orbits prior to the matching window.

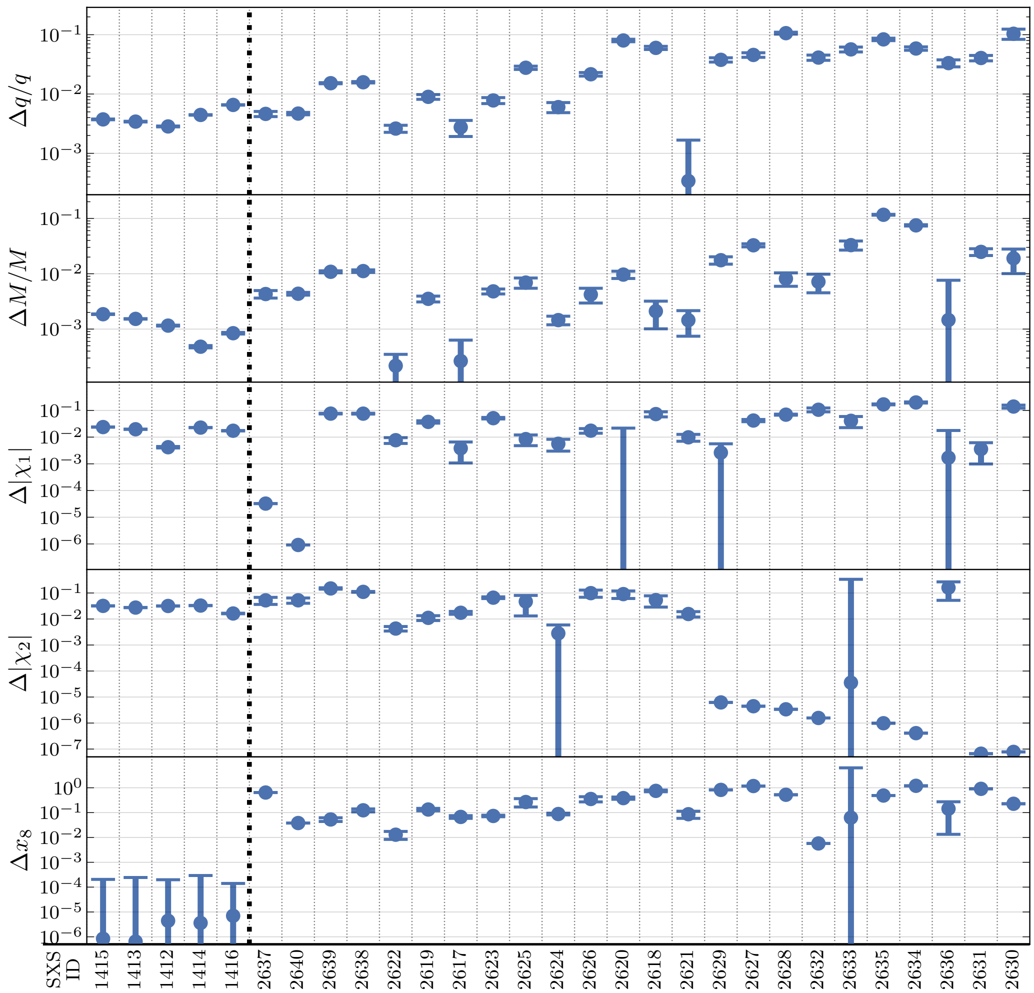

SXS ID	1415	1413	1412	1414	1416	2637	2640	2639	2638	2622	2619	2617	2623	2625	2624	2626	2620	2618	2621	2629	2627	2628	2632	2633	2635	2634	2636	2631	2630
χ_P	0.00	0.00	0.00	0.00	0.00	0.05	0.05	0.05	0.08	0.32	0.33	0.36	0.40	0.40	0.43	0.45	0.46	0.46	0.49	0.50	0.50	0.50	0.56	0.56	0.57	0.57	0.57	0.80	0.80
q	1.5	1.4	1.6	1.8	1.8	8.0	8.0	8.0	8.0	1.5	1.8	1.6	1.9	4.0	1.2	4.0	1.5	1.4	1.8	10.0	6.0	8.0	4.0	8.0	8.0	4.0	8.0	8.0	4.0
e	4.3e−5	1.0e−4	4.4e−4	1.6e−3	1.7e−3	3.7e−4	1.2e−4	7.0e−5	4.7e−4	2.2e−4	6.5e−5	2.0e−4	1.7e−4	2.4e−4	1.3e−4	1.4e−4	1.1e−4	6.8e−5	4.5e−4	3.9e−4	1.2e−4	1.2e−4	1.7e−4	1.7e−4	2.5e−4	1.2e−4	5.9e−4	7.5e−5	2.1e−4
$\Delta\phi$	0.07	0.01	0.01	0.03	0.03	0.02	0.03	0.03	0.06	2e−4	0.05	0.03	0.01	0.23	0.02	0.38	3e−3	2e−3	0.06	0.29	0.32	0.2	1.35	0.75	0.26	0.04	0.05	0.5	1.11

Figure 3.12: The differences in parameters between NR and PN for selected waveforms hybridized using the procedure of Sec. 3.4. Plotted ΔX is $|X_{\mathrm{NR}} - X_{\mathrm{PN}}|$ for selected parameters X. Systems on the left of the vertical dotted line are spin-aligned systems; systems on the right are precessing systems, and systems are ordered left to right by χ_p. The mass ratio for SXS:BBH:2617–2635 systems are $1 < q < 10$, for SXS:BBH:2636–2640 systems are $q \approx 8$. The error bars show the uncertainties of the optimization, and the markers show the best-fit value of the parameters.

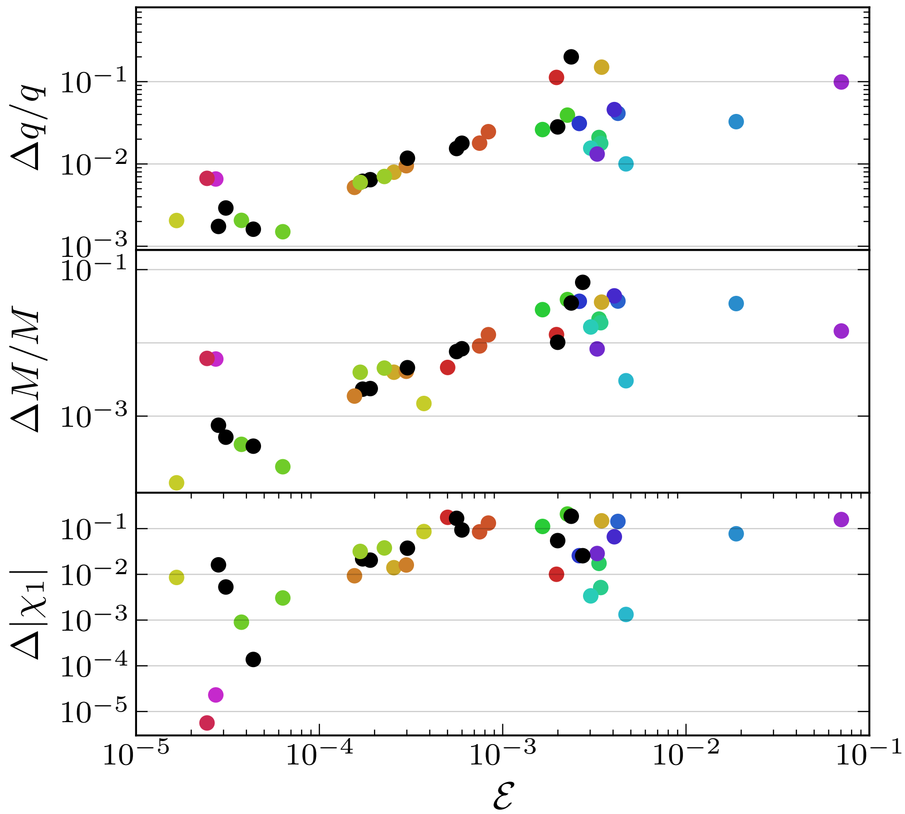

Figure 3.13: The differences in parameters between NR and PN with respect to $\mathcal{E}$ in a 10-orbit long matching window. Each color represents a different system. The points with the same color represent the same system with different matching windows. All the systems in this figure are precessing systems.

of magnitude. This indicates that CCE NR waveforms are usually in a BMS frame that differs from the PN BMS frame, and aligning the BMS frame is crucial when comparing or hybridizing two GW waveforms.

By optimizing PN parameters in addition to optimizing time shift and rotation, as shown in the red and brown, we further reduce $\mathcal{E}$ by 2 to 3 orders of magnitude for spin-aligned systems and up to 3 orders of magnitude for precessing systems. This suggests that the NR parameters at the reference time are different from the parameters that yield the best-matching PN waveform. Fig. 3.12 shows the difference in parameters for selected systems, using the full hybridization procedure described in Sec. 3.4, which corresponds to the brown markers in Fig. 3.11. We see that the fractional difference in mass ratio q between PN and NR is around 10^{-2}, the fractional difference in total mass M is around $10^{-3} \sim 10^{-2}$, and the absolute difference in spin magnitudes is around $10^{-2} \sim 10^{-1}$. Fig. 3.13 shows the correlation between the

PN/NR parameter difference and $\mathcal{E}$ in the matching window. Note that $\mathcal{E}$ is the L^2 error, so the residual in the strain is about $\mathcal{E}^{1/2}$, which is around the same order as the difference in the parameters, as expected.

Given that the best-fit PN parameters can be significantly different from the NR parameters in some cases, it is possible that the optimization over intrinsic PN parameters leads to overfitting. Missing PN terms or NR truncation errors can potentially be absorbed by this optimization, leading to an incorrect PN waveform getting attached to the NR waveform. While Fig. 3.11 does not capture this effect because it only shows the errors in the matching window, one can check this by comparing the errors between PN and NR in an earlier test window that was not included in the optimization. This will be done in Sec. 3.7.

3.6 Sources of error

In this section, we study the origin of the hybridization error. We have two goals in mind: first, we would like to better understand how to improve the hybridization procedure using current NR waveforms and currently known PN terms. Second, we would like to know whether the hybridization error is at present limited by our current NR waveforms or our knowledge of PN, so that we can understand what is needed in terms of NR or PN improvements to reduce hybridization errors in the future.

Spin-aligned systems

For spin-aligned systems, we can see from Fig. 3.11 and Fig. 3.14 that the error inside the matching window is on the order of 10^{-7}.

The blue curve in Fig. 3.14 shows $\mathcal{E}$ in a 15-orbit long matching window with a varying end time, and it has a local minimum when the angular velocity is around 0.012, or between 3000–8000 M before merger. The increase in hybridization error after the minimum, where the end time of the matching window gets closer to merger, corresponds to the expected late-time PN failure that we discussed in Sec. 3.5. We will show below that the increase in hybridization error before the minimum, where the matching window is moved earlier and thus farther from merger, is consistent with the effects of using an NR waveform with small but nonzero orbital eccentricity to hybridize with a PN waveform that assumes eccentricity is identically zero. The test window error (green curve) in Fig. 3.14 will be discussed later in Sec. 3.6.

The contribution of eccentricity to the leading order in PN quasi-Keplerian expansion

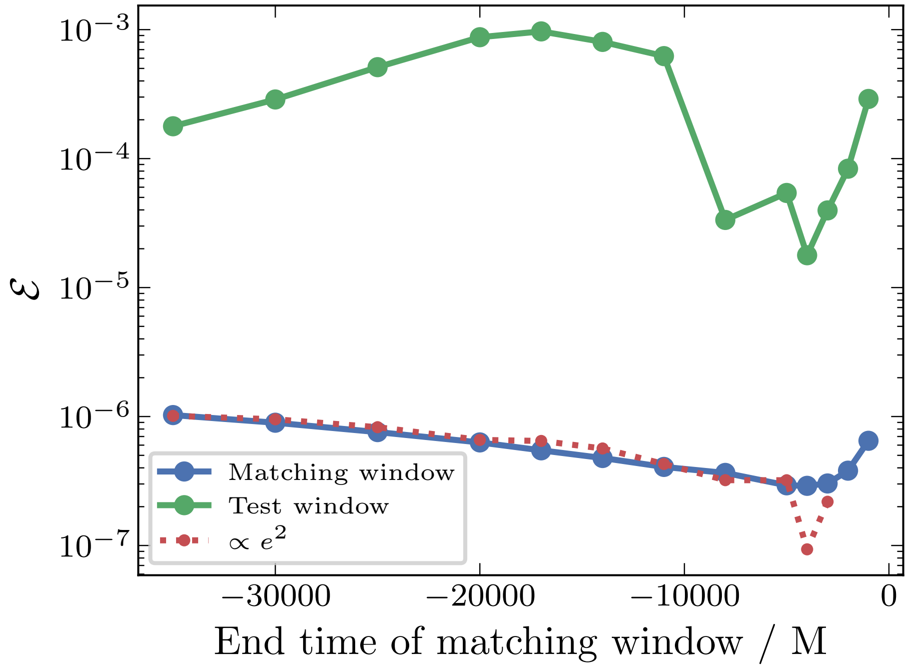

Figure 3.14: Hybridization error for different locations of the matching window for system SXS:BBH:1412. We vary the end time of the matching window, while keeping the matching window 15 orbits long. The test window is 10 orbits long, and the center (in number of orbits) of the test window is 30 orbits earlier than the center of the matching window. The red dotted curve shows the square of the eccentricity measured using `gw_eccentricity` [78] by the amplitude fitting method at the middle of the matching window multiplied by a factor of 15. The factor is obtained by varying the overall amplitude of the red curve until it overlays the blue curve.

is given by [79]

$$h^{22}_{\mathrm{Newt}} \propto 1 + e\left(\frac{1}{4}\exp(-\mathrm{i}\xi) + \frac{5}{4}\exp(\mathrm{i}\xi)\right), \tag{3.11}$$

where e is the time-evolving eccentricity parameter. The angle ξ is closely related to the mean anomaly, going through roughly 2π with each orbit. From Eq. (3.11) we can obtain the PN prediction of the L^2 normalized difference $\mathcal{E}_{\mathrm{sys}}$ between eccentric PN waveforms and non-eccentric PN waveforms in the limit of small eccentricity as

$$\mathcal{E}_{\mathrm{sys}} \propto e^2. \tag{3.12}$$

In Fig. 3.15 we plot $\mathcal{E}$ between PN and NR for 10 different systems. The error increases with the eccentricity, and is roughly consistent with the expected $\mathcal{E} \propto e^2$ behavior of Eq. (3.11).

In addition to examining the overall magnitude of $\mathcal{E}$ caused by eccentricity, we also examine the time evolution of eccentricity and its effect on $\mathcal{E}$. The time evolution of

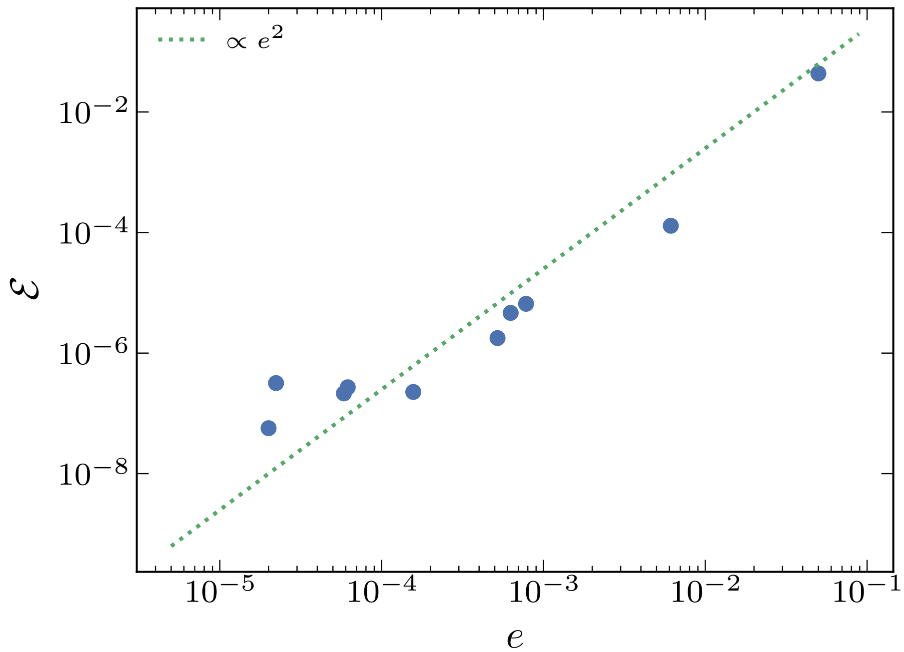

Figure 3.15: The L^2 normalized error $\mathcal{E}$ versus eccentricity e for 10 different systems: SXS:BBH:1412–1416, SXS:BBH:1153, 1164, 1165, 1168; and the additional system 3618. We include SXS:BBH:3618 for reference as a higher-eccentricity point ($e = 0.0496$). It is spin-aligned with $\chi_1 = \chi_2 = 0.6$ and $q = 1.0$, and will be added to the public SXS catalog soon. The end time of the matching window is $-5000\,M$, and the length of the matching window is 10 orbits. The green dotted curve is a quadratic fit to the plotted points.

eccentricity to leading order is given by [80]

$$e_t(\Omega_t) \approx e_0 \left(\frac{\Omega_0}{\Omega_t}\right)^{19/18}, \tag{3.13}$$

where Ω_t is the orbital frequency at time t, and Ω_0 is the orbital frequency at a fiducial time when the eccentricity is e_0. According to Eqs. (3.11) and (3.12), the oscillation amplitude of the norm of the $(2,2)$ mode should be proportional to $e \propto \Omega^{-19/18}$. We check the oscillation amplitude of the norms of the $(2,2)$, $(2,-2)$, $(2,1)$ and $(2,-1)$ modes for system SXS:BBH:1412. The oscillation amplitude is obtained by subtracting the individual mode's norm from its orbital average, which is obtained by applying a low-pass filter to the original mode. We find that the oscillation amplitudes of the norms of the above modes are proportional to $\Omega^{-19/18}$ and are thus consistent with eccentricity damping. The same argument applies to $\mathcal{E}$ within the matching window as we show in Fig. 3.14. Assuming that the change of e and Ω in the window is small, then $\mathcal{E} \propto e^2 \propto \Omega^{-19/9}$. The red dotted line is e^2 multiplied by a coefficient chosen to approximately agree with the matching window error (blue curve), where the eccentricity e is measured from the waveform amplitude fit of the $(2,2)$ mode using the package `gw_eccentricity` [78], and measurements are taken at the middle of the different matching windows. The value of $\mathcal{E}$ in the matching window (blue curve) agrees very well with the trend of e^2 (green curve), showing the expected effect of eccentricity damping.

We also remark, based on Eq. (3.11), that the eccentricity contribution oscillates at the same frequency as the orbital frequency, and is symmetric for positive and negative m. We therefore check the oscillation amplitudes of the norms of the $(2,2)$ and $(2,-2)$ modes for a system with a greater eccentricity, SXS:BBH:1168. The oscillation amplitudes and phase for these two modes are indeed the same, which is consistent with the above arguments for eccentricity.

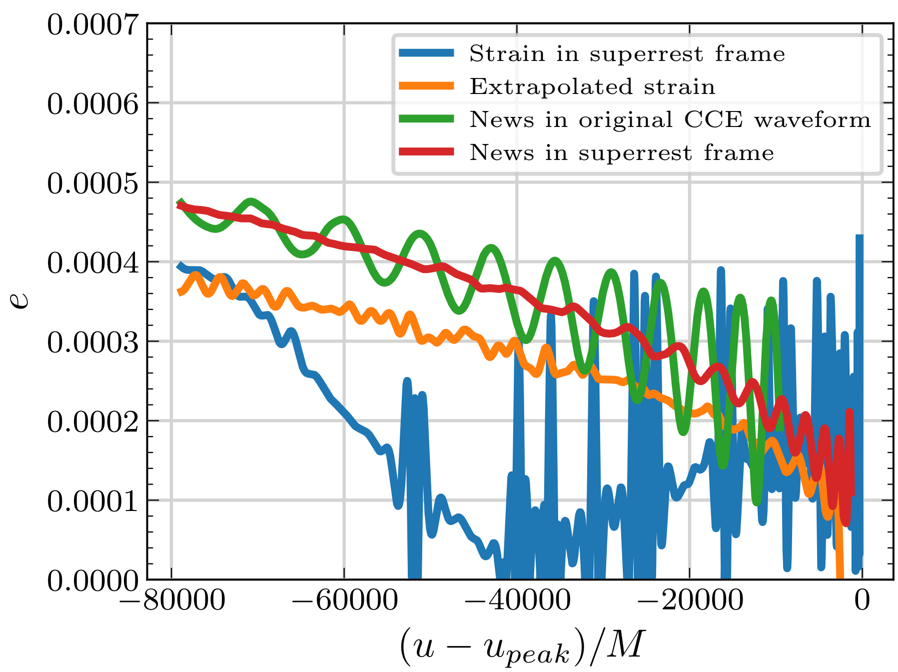

Figure 3.16: Measurement of eccentricity e from both strain and news (the time derivative of strain), and in different BMS frames, for system SXS:BBH:1412. When transforming to a superrest frame, the frame is determined from the middle of the inspiral.

On the basis of these arguments, one might assume that the hybridization error would be reduced if we included eccentricity and mean anomaly in our PN parameter optimization. However, by conducting such a 14-dimensional optimization in the superrest frame of the NR system, we found that the error couldn't be reduced further since the error generated by such a small eccentricity is overpowered by the error caused by the incorrect BMS frame. Fixing the BMS frame, however, is not a simple task when eccentricity is present, as both eccentricity and supertranslation can produce oscillations in the waveform mode amplitudes and the angular velocity. This degeneracy is depicted in Fig. 3.16, where we plot the eccentricity measurement in different BMS frames as a function of time. We can see by comparing the eccentricity measurement using a CCE waveform in the superrest frame (blue) and an extrapolated waveform (orange) that the measurement of eccentricity from the strain has a strong dependence on the method of obtaining the asymptotic waveform. The measurement of eccentricity from the Bondi news—the time derivative of the strain—is less dependent on the BMS frame, but there are still large oscillations with respect to the measurement time (green and red lines). Because of the degeneracy between supertranslations and eccentricity, including eccentricity in hybridization is nontrivial and we leave it for future work.

Precessing systems

In Fig. 3.17, we present the hybridization errors within the matching window for various precessing systems. The horizontal axis for the upper panel is the spin-precession parameter χ_p. Notably, these blue dots reveal a correlation between the hybridization error and the spin precession for each system.

To discern whether the error is caused by the numerical error of NR spin-precession or the absence of spin-precession terms in PN, it is important to recognize that the spin terms entering the PN expansion are the spin angular momentum $\boldsymbol{S}_i = \chi_i m_i^2$, rather than χ_p. To investigate this, in the lower panel we plot the hybridization error for the same systems against $S_\perp/M^2 = (S_{1\perp} + S_{2\perp})/M^2$ using two different NR simulations that are identical except for the resolution parameter "Lev" that determines the error tolerance of the simulation. Larger "Lev" means a smaller error tolerance, which translates into a more accurate (but more computationally expensive) NR simulation. The same Lev for all simulations used in this paper corresponds to the same tolerance for the adaptive-mesh-refinement algorithm. See the last paragraph of Sec. 2.1 in Ref. [68] for details. By comparing the results for Lev4 and Lev3 (green dots and red crosses), it is evident that the NR numerical error is not the limiting error source. The slope of the Lev4 L^2 norm error (green dots) is 3.8, implying that the slope of the absolute difference between PN and NR waveforms should be 1.9, since the residual is around the square root of $\mathcal{E}$. Note that the contribution of the missing PN precession-dependent spin-spin terms to the

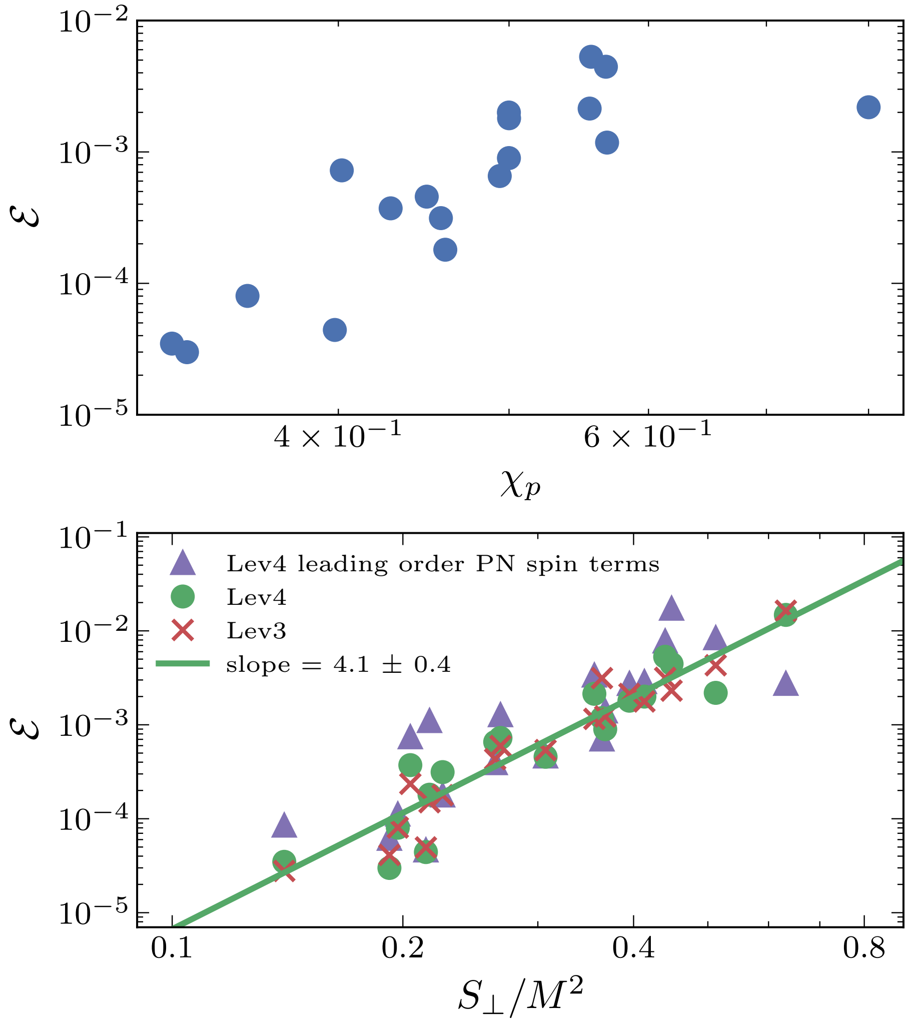

Figure 3.17: Hybridization error, Eq. (3.5), inside the matching window for precessing systems SXS:BBH:2617–2635. The horizontal axis is the spin-precession parameter χ_p for the upper panel, and $S_\perp/M^2$ for the lower panel. Here $\boldsymbol{S}_i = \chi_i m_i^2$ is the spin angular momentum, and $S_\perp$ is the magnitude of the projection in the orbital plane. Results are shown for two different choices of the resolution parameter "Lev" used to compute the NR simulation. Lev4 uses a finer tolerance for the adaptive-mesh-refinement algorithm than Lev3, so Lev4 has smaller numerical errors. The additional purple markers use only the leading order spin-spin and spin-orbit terms in both strain and Ψ_M for Lev4, whereas the other markers use all PN terms listed in Sec. 3.2, which have higher order terms in the strain, but the same terms in Ψ_{M}. The matching window is 10 orbits long, and the end time is 8000 M before merger.

waveform is expected to be proportional to $(S_\perp/M^2)^2$, so our result is consistent with those missing terms being the dominant source of error.

To verify consistency, we included results that only use the leading order spin-spin and spin-orbit terms in both the strain and Ψ_M for Lev4 (purple triangular markers). It is important to recognize that this comparison is not fully consistent, as the Lev4 scenario represented by green dots also includes the spin-spin and spin-orbit PN terms at only the leading order in Ψ_M, but has up to the next-to-next leading order in the strain. Nevertheless, there are still differences when using different terms in the strain at higher values of $S_\perp/M^2$. The slope for markers including only the leading order spin terms is 3.6 ± 0.6, suggesting that higher order PN spin terms might influence the hybridization error.

3.7 Choice of matching window

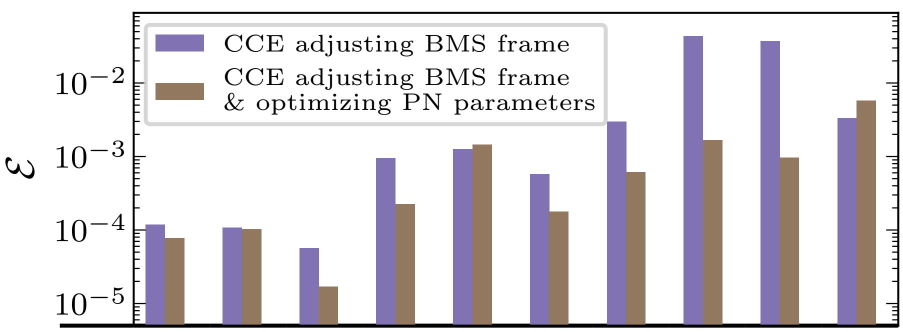

SXS ID	1415	1413	1412	1414	1416	2619	2617	2620	2618	2621
χ_p	0.00	0.00	0.00	0.00	0.00	0.33	0.36	0.46	0.46	0.49
q	1.5	1.4	1.6	1.8	1.8	1.8	1.6	1.5	1.4	1.8
e	4.3e−5	1.0e−4	4.4e−4	1.6e−3	1.7e−3	6.5e−5	2.0e−4	1.1e−4	6.8e−5	4.5e−4

Figure 3.18: Test window error for 10 long waveforms from Fig. 3.11. The center of the test window is 30 orbits earlier than the center of the matching window. The matching window is the same with Fig. 3.11. For most systems, the optimization over PN parameters can result in smaller error in both the matching window and the test window.

The matching window should be selected so that both PN and NR are valid there and agree with each other to an acceptable tolerance. We can estimate the matching window's end time by Eq. (3.10), which estimates the frequency at which PN becomes inaccurate at late times: When the left-hand side of this equation exceeds the right-hand side, the PN truncation error becomes dominant in the hybridization error, and this error grows polynomially with the orbital frequency as we get closer to merger. If the matching window is chosen earlier so that the left-hand side is smaller than the right-hand side, the hybridization error is then dominated by the remaining systematic errors that we are not able to eliminate for now.

However, Eq. (3.10) typically has undetermined coefficients, which depend on parameters of the system. In addition, Eq. (3.10) does not tell us how to determine the *length* of the matching window. In Secs. 3.7 and 3.7 below, we will describe our method of choosing the matching window, which is different for spin-aligned and precessing systems.

Recall that the hybridization method involves varying the PN parameters and frame parameters to minimize the PN-NR differences in the matching window. It is not appropriate to simply compare PN to NR in the window where the difference is optimized. To better evaluate how well we match PN and NR, we also compare PN-NR differences in a new window, called a *test window*, that is outside the matching window so that PN-NR differences are not minimized there, and that is earlier in time than the matching window so that both PN and NR should be valid there. The idea is that for a good choice of matching window, and for sufficiently accurate NR and PN waveforms, the PN-NR differences in the test window should also be small. But it's still expected that the differences in the test window is larger than the differences in the matching window, given that both PN and NR (waveforms and parameters) are not accurate and disagree with each other, as we explained in Sec. 3.3 and Sec. 3.5. Unless otherwise specified, the test window is chosen to be 10 orbits long, and the center of the test window (in number of orbits) is 30 orbits earlier than the center of the matching window.

We also show the test window error for 10 long waveforms in Fig. 3.18. By comparing the results with and without optimization over PN parameters (brown and purple columns), we can see that for most systems, the optimization over PN parameters can result in smaller error in the test window.

Spin-aligned systems

Fig. 3.14 shows how we determine the end time of the matching window for spin-aligned systems. In this figure, we fix the length of the matching window as 15 orbits long, and vary the end time of the matching window. We plot $\mathcal{E}$ in both the matching window and the test window as blue and green curves, respectively. We can see that there is an optimal choice for the end time of the matching window, which is about 3000 M to 8000 M before merger, where the errors in the matching and test windows show a minimum. For matching windows ending earlier than this optimum, the errors are larger because of larger eccentricity, as shown in Sec. 3.6. The slope of the matching window error (blue curve) before $-5000\,M$ agrees very well with eccentricity damping, which is shown as the red dotted curve. For matching windows ending later than the optimum, we get larger errors because PN breaks down at late times.

The other free parameter is the matching window's length. Generally speaking, the matching window should be as long as possible, provided that the numerical error of the NR waveform is less than the systematic error stated in Sec. 3.6. However, most current NR simulations are short, and long NR simulations are very expensive. If the NR waveform is too short to include sufficient data, the hybridization model will be invalid.

To find the minimal duration of the matching window, we fix the end time based on Fig. 3.14, and change the start time. We also use a test window to check the results. The position of the matching window and test window are shown in the upper panel of Fig. 3.19, and the hybridization errors in both windows are shown in the lower panel. The solid, dashed, and dotted curves in the lower panel show the errors using NR waveforms with different numerical resolution, labeled by "Lev" as in Sec. 3.6 above. We can see from the matching window errors (blue curves) that the NR numerical error does not significantly affect the hybridization error in the matching window. But when comparing the test window errors (green curves), we can see that they roughly converge to smaller values as we increase the resolution. This suggests that low-resolution NR simulations can accumulate numerical phase error over long periods of time. But note that the NR dephasing between the two highest Levs, $\Delta\phi$, does not directly reflect the inaccuracy of the NR waveforms, as the NR parameters within the matching window for different Levs can deviate by 10^{-2}, given their evolution over nearly a hundred orbits prior to the matching window. Consequently, the optimized PN parameters for various NR Levs also differ by 10^{-2}, allowing the PN waveform to

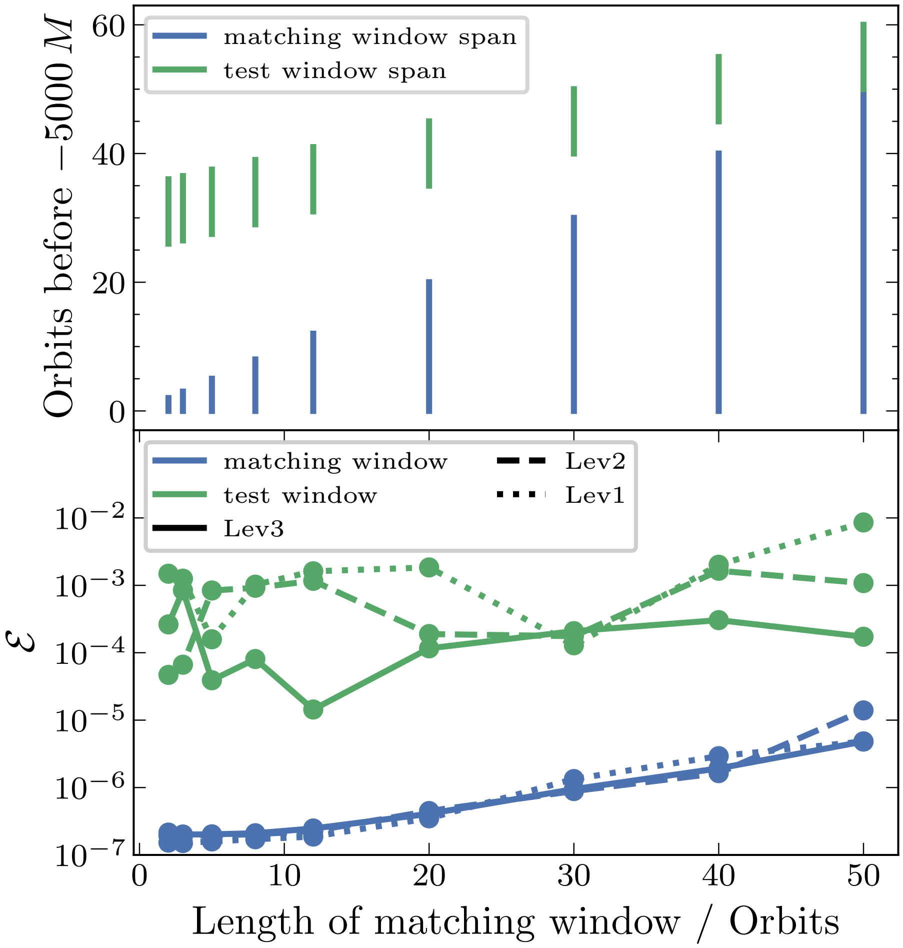

Figure 3.19: The hybridization error for different lengths of matching window for spin-aligned system SXS:BBH:1412. We fix the end time of the matching window to be 5000 M before merger. The test window is 10 orbits long, and the center of the test window (in number of orbits) is 30 orbits earlier than the center of the matching window. "Lev" labels the resolution of the NR simulations, as in Fig. 3.17.

agree better with their respective NR waveforms and partially compensating for the phase error. Assessing the adequacy of the current NR resolution for hybridization purposes requires performing the entire hybridization process using various NR Levs, as shown in Fig. 3.19. However, the conclusion depends on the precision and frequency band needed for these observations (specifically, the frequency band of the test window). We leave this for future work.

We can see from the Lev3 errors (solid green and blue curves) that the optimal length of matching window should be around 5 to 20 orbits. The shorter the matching window is, the less information it includes, and the larger the chance that the small

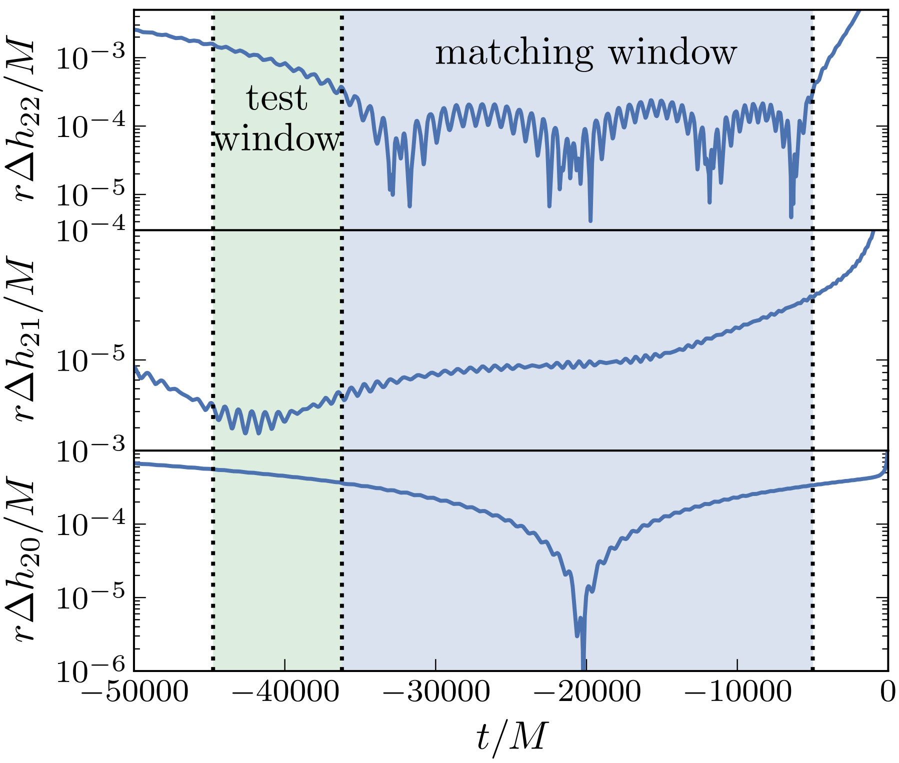

Figure 3.20: The residual of spin-aligned system SXS:BBH:1412 corresponding to the rightmost points for Lev3 in Fig. 3.19. The matching window is 50 orbits long and ends at 5000 M before merger, and the test window is 10 orbits long and immediately before the matching window. The error increases rapidly outside the matching window, so that the error in the test window is much larger than the error in the matching window. The error increases outside the matching window because of slight differences between the PN and NR waveforms. In this spin-aligned case, we use non-eccentric PN to hybridize with a slightly eccentric NR waveform. While we can minimize the error within the matching window, the inherent differences between the models prevent us from reducing the error outside.

error in the matching window is spurious; for very short matching windows (< 5 orbits) the test window errors (green curves) no longer converge and the Lev3 test window error (solid green curve) increases significantly. For longer matching windows (> 20 orbits), the Lev3 test window error (green solid curve) becomes flat and the matching window errors (blue curves) increase. This is because on the one hand, the start time of the matching window is earlier, where the NR eccentricity is larger, resulting in a larger error in the matching window, as shown by the blue curve in Fig. 3.14. On the other hand, a longer matching window leads to more accumulated phase error, potentially caused by both the disagreement between zero-eccentricity PN and small-but-finite-eccentricity NR, as well as insufficient NR resolution. In Fig. 3.20, we plot the residual corresponding to the rightmost points for Lev3 in Fig. 3.19. We can see that even if the matching window is long enough to be adjacent to the test window, we still cannot achieve good alignment between PN and NR outside the matching window. The error increases beyond the matching window because the PN and NR waveforms are inherently not identical. In this case of spin-aligned systems, we use a non-eccentric PN model to hybridize with NR waveforms that possess slight eccentricity. Given the inherent differences between the waveform models, it is not possible to reduce the error outside the matching window, even if we achieve minimal error within it.

For NR waveforms with different and small but nonzero eccentricities, the best location of the matching window could be slightly different. We can refer to Eq. (3.10) and Eq. (3.12). Error due to non-zero eccentricity and error from breakdown of PN are comparable when

$$\text{Coefficient} \cdot e^2 \approx \left(\text{Coefficient} \cdot \Omega_{\text{orb}}^{(2N+1)/3}\right)^2 . \tag{3.14}$$

In Fig. 3.14, the matching window error (blue curve) before $-8000\,M$ corresponds to the left-hand side, the matching window error after $-3000\,M$ corresponds to the RHS, and the region between $-8000\,M$ and $-3000\,M$ is where the two effects are comparable. For cases with different but small eccentricities, we expect the error curve after $-3000\,M$ to be similar to that in Fig. 3.14, and the curve before $-8000\,M$ to be parallel to the blue curve in Fig. 3.14, but with a vertical shift. Since the curve after $-3000\,M$ is steep and the curve before $-8000\,M$ is gradual, the point where the left and right part of the curve meet with each other (which is the best location for the matching window) is not very sensitive to the eccentricity of the system.

At the current state-of-the-art NR accuracy, and for $\mathcal{E}$ between PN and NR in the test window of $\sim 10^{-4}$, the minimal choice for a matching window for spin-aligned systems would be at least 5 orbits long and ending 3000 M before merger. This minimal choice will become longer and earlier if higher-accuracy hybrids are desired, and if the accuracy of the waveforms improves. Matching windows longer than 20 orbits or ending earlier than 8000 M are not beneficial given the current state of the art, but would be beneficial if the residual eccentricity of NR waveforms were decreased or if eccentric PN waveforms were used for hybridization and the potential degeneracy between eccentricity and supertranslations are properly handled.

Precessing systems

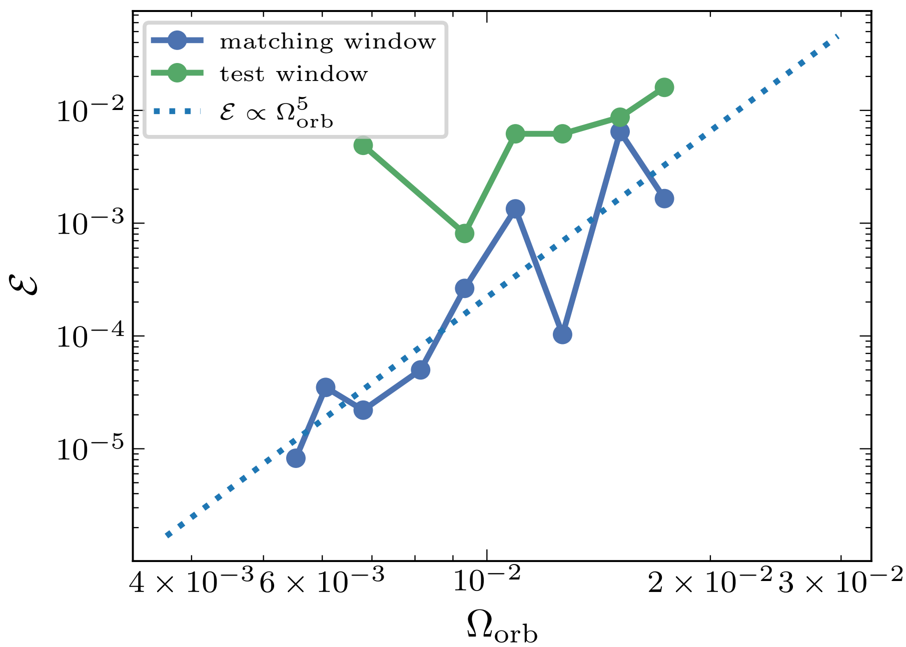

Figure 3.21: The L^2 normalized error $\mathcal{E}$ in the matching window as a function of orbital angular velocity for system SXS:BBH:2621. The matching window is 10 orbits long, but the end time of the matching window is varied, and the orbital angular velocity is the mean value over the matching window. The test window is 10 orbits long, and the center of the test window (in number of orbits) is 30 orbits earlier than the center of the matching window.

In Sec. 3.6, we established that the error in hybridizing precessing systems mainly results from the absence of higher-order PN spin terms. Because PN error decreases with smaller frequencies, we anticipate smaller hybridization errors at earlier times. To determine the best location of the matching window, we plot the hybridization error of system SXS:BBH:2621 in the matching window versus orbital angular velocity $\Omega_{\rm orb}$ in Fig. 3.21. This system has $\chi_p = 0.49$. Since the leading missing PN precession-related spin terms are expected to be $\propto (S_\perp/M^2)^\alpha v^\beta$, where $v = (\Omega_{\rm orb} M)^{1/3}$ is the PN expansion parameter, we can get the indices α and β by fitting the points in Fig. 3.17 and Fig. 3.21, respectively. Then we can get an empirical formula $\mathcal{E} \sim 3.6 \times 10^8 \times (S_\perp/M^2)^{4.1}\Omega_{\rm orb}^5$, or

$$\Omega_{\rm orb} \lesssim 0.012\mathcal{E}^{0.2}(S_\perp/M^2)^{-0.82}. \tag{3.15}$$

Once a required precision $\mathcal{E}$ for a 10-orbit long window is given, we can use Eq. (3.15) to determine the average orbital angular velocity of the matching window. From the average orbital angular velocity one can figure out the end time of the matching window. Note that both Figs. 3.17 and 3.21 use a 10-orbit long matching window, because it is short enough to avoid being dominated by long-term accumulated phase error, and also limits significant frequency changes within the window.

We also plot the predicted $\mathcal{E}$ given a 10-orbit window in terms of the end time of the matching window and $S_\perp/M^2$ in Fig. 3.22. Here we used leading order PN to substitute orbital angular velocity with time: $\nu(u - u_{\rm peak}) = \frac{5}{256}\Omega_{\rm orb}^{-8/3}$, where $\nu = m_1 m_2/(m_1 + m_2)^2$.

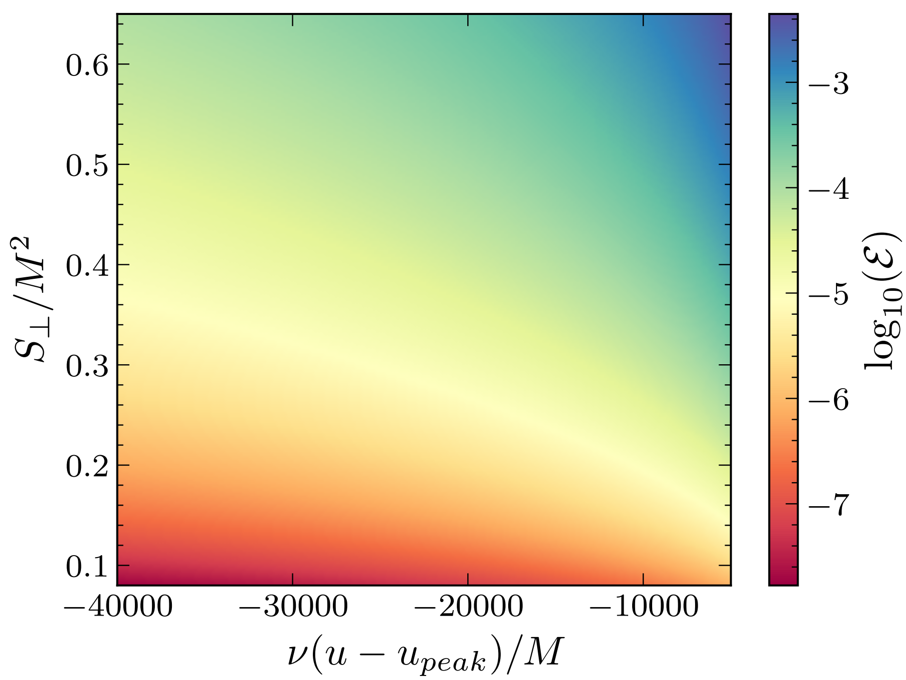

Figure 3.22: The predicted L^2 normalized error $\mathcal{E}$ for a 10-orbit matching window based on Eq. (3.15). The horizontal axis is the approximate center of the matching window, where $\nu = m_1 m_2/(m_1 + m_2)^2$, and u is the retarded time. The vertical axis is the maximum of the in-plane component of the two dimensionless spin momenta.

Determining the ideal matching window length for precessing systems through experiments is challenging, unlike the spin-aligned cases. This challenge arises because the recommended end time for the matching window is significantly earlier for systems with large spin. Consequently, generating a complete precession cycle before this end time is impractical using NR simulations. However, considering that the error is primarily governed by the PN spin terms, which diminish at earlier times (in contrast to errors stemming from non-zero eccentricity, which worsen at earlier times), it is anticipated that longer matching windows are more beneficial for precessing systems.

Short waveforms

Unfortunately, most of the NR waveforms in current catalogs are not long enough to meet the minimal criteria for a matching window discussed in Sec. 3.7. In this scenario, it is important to note that the optimized PN parameters and BMS frame computed by the hybridization procedure may be biased by the breakdown of PN. Additionally, there is a risk of overfitting when optimizing the PN parameters and inertial frames from too-small a matching window.

To better understand these issues, we simulate an "8000 M" waveform scenario. We set the start time of the matching window to be $-8000\,M$ and test the hybridization results using a 10-orbit long test window positioned between 30 and 40 orbits before $-8000\,M$. The results are shown in Fig. 3.23 and Fig. 3.24.

In Fig. 3.23, we display $\mathcal{E}$ for different lengths of the matching window for system SXS:BBH:2617 for this scenario. The matching window errors obtained using extrapolated waveforms (dotted lines) in the upper panel are independent of the length of the matching window because the error is dominated by the incorrect gravitational-wave memory in the extrapolated waveforms. The matching window errors obtained using CCE waveforms (solid lines) show that as the length of the matching window becomes shorter, the error in the matching window becomes smaller. However, by comparing the errors in the matching window and test window (upper and lower panels), we can see that smaller error in the matching window does not mean smaller error in the test window. To more intuitively show the relation between the error in the matching window and the test window, we gather all the data points from Fig. 3.23, and plot them again in Fig. 3.24. We can see that the errors in the test window and matching window show no unambiguous trend. This non-correlation of the matching and test window errors suggests that although we

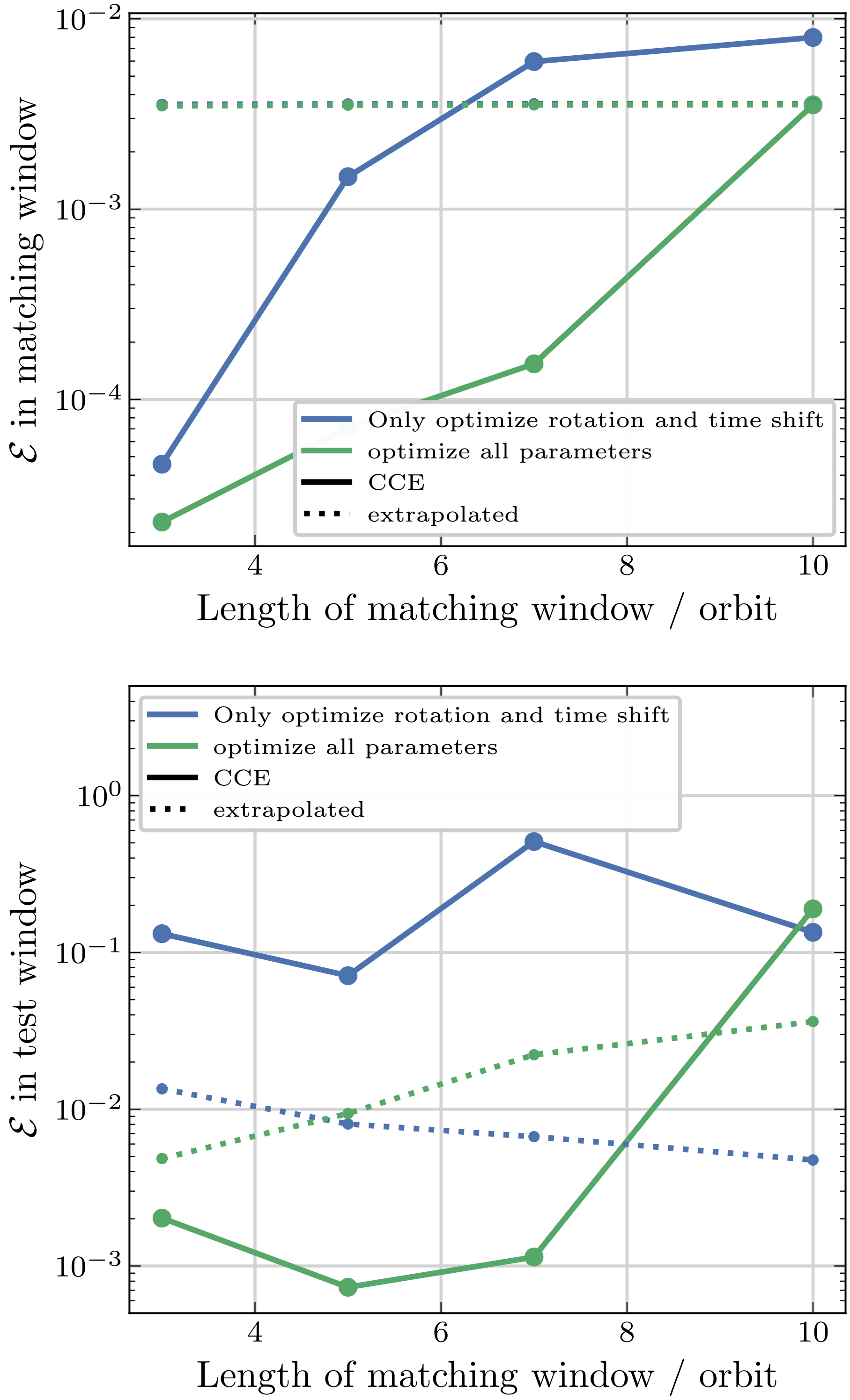

Figure 3.23: The L^2 normalized error $\mathcal{E}$ for different lengths of the matching window for system SXS:BBH:2617. The test window is between 30 and 40 orbits before $-8000\,M$. We fix the start time of the matching window to be 8000 M before merger. The upper and lower panel show $\mathcal{E}$ in the matching window and the test window, respectively. The dotted curves use extrapolated NR waveforms, while the solid curves use CCE NR waveforms. All the curves are obtained after adjusting the 3-D rotation and time shift, and all the curves using CCE waveforms are obtained after mapping to the PN BMS frame. In addition to the 3-D rotation and time shift, the green curves optimize all 12 parameters, which is the full hybridization procedure described in Sec. 3.4.

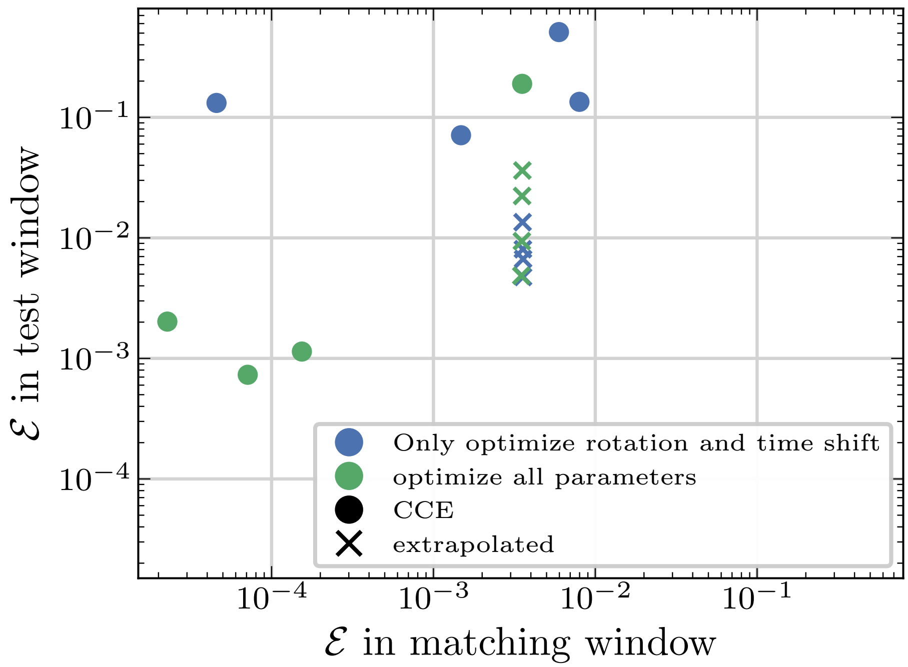

Figure 3.24: The L^2 normalized error $\mathcal{E}$ for different lengths of the matching window for system SXS:BBH:2617. The test window is between 30 and 40 orbits before $-8000\,M$. We fix the start time of the matching window to be 8000 M before merger. The crosses use extrapolated NR waveforms, while the dots use CCE NR waveforms. All the data are obtained after adjusting the 3-D rotation and time shift, and all the dots using CCE waveforms are obtained after mapping to the PN BMS frame. The blue and the green data points are the same data as the blue and green curves in Fig. 3.23. The extrapolated waveforms all have the same error in the matching window, because for those waveforms the matching window error is dominated by incorrect gravitational-wave memory.

can always get a small error in the matching window if the matching window is short, it is not gaining us more information about the PN parameters and BMS frame to improve the error in the test window.

So, if we do not have NR waveforms that are long enough to meet the criteria outlined in Sec. 3.7 and Sec. 3.7, the hybridization could be biased by the breakdown of PN and overfitting.

3.8 Conclusions

We provide a BBH waveform hybridization routine that includes every spin-weighted spherical harmonic mode with $-\ell \leq m \leq \ell$ for $\ell \leq 8$ as well as memory effects, and utilizes BMS frame fixing and PN parameter optimization. The L^2 normalized error

$\mathcal{E}$ between PN and NR waveforms in a 10-orbit *matching* window is roughly 10^{-7} for spin-aligned systems, and roughly 10^{-5} for precessing systems.

However, a more informative measure of the accuracy of a hybridized waveform is the PN-NR difference in a *test* window that is earlier than the matching window so that PN errors are small, and that does not overlap with the matching window so that we are not actively minimizing the PN-NR difference there. In a test window that is 10 orbits long and 30 orbits earlier than the matching window, we can reduce the normalized L^2 norm of PN-NR difference to less than $\sim 10^{-4}$ for spin-aligned systems, as shown by the solid green curve in Fig. 3.19. This corresponds to $\sim 10^{-2}$ residual between PN and NR waveforms in this interval. Again, we note that these numbers are not directly comparable to the frequency-domain mismatches used in GW data analysis, even assuming a flat noise curve, because the test and matching windows will not generally encompass the entire detectable waveform. At best, these numbers constitute lower bounds for the full mismatch. However, they do suggest that even for spin-aligned systems the results may be inadequate for high-SNR events in future detectors such as Cosmic Explorer and LISA.

For spin-aligned systems, the error in the test window can likely be decreased somewhat by using higher-accuracy NR waveforms, since the green curves in Fig. 3.19 are roughly decreasing with NR resolution. However, the error is ultimately limited by trying to match zero-eccentricity PN waveforms with small but non-zero eccentricity NR waveforms. To achieve test window differences much better than $\mathcal{E} \lesssim 10^{-4}$ for spin-aligned systems, it will be necessary to either reduce the residual eccentricity of the NR waveforms or to use an eccentric PN model for hybridization.

While we recommend optimizing the intrinsic PN parameters in addition to the BMS frame parameters, we find that this optimization can sometimes lead to fractional differences in mass ratio and spin up to $\sim 10^{-1}$ between NR and the best-fit PN waveform (see Fig. 3.12). This could arise from overfitting, where missing PN terms or NR truncation errors can be absorbed into the PN parameter optimization. This can be more significant for most current NR waveforms as they are typically much shorter than the ones considered here (see Sec. 3.7 for tests using NR waveforms starting $8000M$ before merger). As PN continues to improve and NR waveforms become longer, we expect these differences to decrease. In the meantime, caution is warranted when varying the intrinsic PN parameters for short NR waveforms.

In principle, if one had perfect and exactly quasi-circular NR waveforms, the matching window should be chosen as early as possible (to avoid matching at late times near merger where PN becomes inaccurate), and it should be chosen as long as possible (so that one can match over a longer stretch of data and thus obtain a better fit). For current NR waveforms, and for spin-aligned systems, we find that to achieve $\mathcal{E} \sim 10^{-4}$ differences in the test window, the matching window should be at least 5 orbits long and should end at least 3000 M before merger. While in principle a longer and earlier matching window should be better, we find that matching windows longer than 20 orbits or ending earlier than 8000 M are not beneficial because the error is then dominated by the nonzero eccentricity of the NR waveforms as described above. By using either smaller-eccentricity NR waveforms or employing eccentric PN, it should be possible to further improve hybridization by using longer and earlier matching windows.

Hybridization of precessing systems is much more difficult than spin-aligned systems, because the current PN waveforms for precessing systems are much less accurate than for spin-aligned systems. For precessing systems, the error in the hybrid is likely to be dominated by the lack of precession-related spin-spin terms in the PN model. Unlike the error caused by non-zero eccentricity, the error stemming from PN terms diminishes at earlier times. So there is no optimal choice of the matching window even in the entire 10^5 M span of the NR waveforms in the SXS catalog, and it always improves the hybridization by using matching windows as long and early as possible. We provide a formula, Eq. (3.15), and a plot, Fig. 3.22, as a guide for choosing a matching window for precessing hybrids. The recommended end time for the matching window is significantly earlier for systems with large spin.

It is possible that using the effective one-body (EOB) formalism [81] instead of PN could significantly affect the position and length of the matching window and decrease the requirement for long NR waveforms. However, to do so requires that one have Ψ_M in the EOB formalism to be able to fix the BMS freedoms, which is not currently the case. Furthermore, current EOB waveforms are calibrated using the extrapolated NR waveforms, which lack memory effects. We plan to explore how the hybridization procedure changes when using EOB waveforms trained on CCE waveforms in future work.

Acknowledgments

We thank Sizheng Ma, Nils Deppe, Qing Dai, Harald Pfeiffer and Aditya Vijaykumar for useful discussions. Computations for this work were performed on the Wheeler cluster at Caltech, which is supported by the Sherman Fairchild Foundation and by

Caltech, Resnick High Performance Computing (HPC) Cluster at the Caltech High Performance Computing Center, Frontera at the Texas Advanced Computing Center, and Urania HPC system at the Max Planck Computing and Data Facility. This work was supported in part by the Sherman Fairchild Foundation, by NSF Grants PHY-2207342 and OAC-2209655 at Cornell, and by NSF Grants PHY-2309211, PHY-2309231, and OAC-2209656 at Caltech. The work of L.C.S. was partially supported by NSF CAREER Award PHY-2047382 and a Sloan Foundation Research Fellowship. V.V. acknowledges support from NSF Grant No. PHY-2309301; UMass Dartmouth's Marine and Undersea Technology (MUST) Research Program funded by the Office of Naval Research (ONR) under Grant No. N00014-23-1-2141; and the European Union's Horizon 2020 research and innovation program under the Marie Sklodowska-Curie grant agreement No. 896869.

References

[1] Dongze Sun et al. "Optimizing post-Newtonian parameters and fixing the BMS frame for numerical-relativity waveform hybridizations". In: *Physical Review D* 110 (2024), p. 104076. DOI: 10.1103/PhysRevD.110.104076. arXiv: 2403.10278 [gr-qc].

[2] Dongze Sun. *NRPNHybridization*. https://github.com/dongzesun/NRPNHybridization.

[3] B. P. Abbott et al. "GW150914: The Advanced LIGO Detectors in the Era of First Discoveries". In: *Phys. Rev. Lett.* 116.13 (2016), p. 131103. DOI: 10.1103/PhysRevLett.116.131103. arXiv: 1602.03838 [gr-qc].

[4] B. P. Abbott et al. "Binary Black Hole Mergers in the first Advanced LIGO Observing Run". In: *Phys. Rev.* X6.4 (2016). [erratum: Phys. Rev.X8,no.3,039903(2018)], p. 041015. DOI: 10.1103/PhysRevX.6.041015, 10.1103/PhysRevX.8.039903. arXiv: 1606.04856 [gr-qc].

[5] B. P. Abbott et al. "GW150914: First results from the search for binary black hole coalescence with Advanced LIGO". In: *Phys. Rev.* D93.12 (2016), p. 122003. DOI: 10.1103/PhysRevD.93.122003. arXiv: 1602.03839 [gr-qc].

[6] B. P. Abbott et al. "Properties of the Binary Black Hole Merger GW150914". In: *Phys. Rev. Lett.* 116.24 (2016), p. 241102. DOI: 10.1103/PhysRevLett.116.241102. arXiv: 1602.03840 [gr-qc].

[7] Benjamin P. Abbott et al. "GW170817: Observation of Gravitational Waves from a Binary Neutron Star Inspiral". In: *Phys. Rev. Lett.* 119.16 (2017), p. 161101. DOI: 10.1103/PhysRevLett.119.161101. arXiv: 1710.05832 [gr-qc].

[8] B. P. Abbott et al. “Binary Black Hole Population Properties Inferred from the First and Second Observing Runs of Advanced LIGO and Advanced Virgo”. In: *Astrophys. J. Lett.* 882.2 (2019), p. L24. DOI: 10.3847/2041-8213/ab3800. arXiv: 1811.12940 [astro-ph.HE].

[9] R. Abbott et al. “GWTC-3: Compact Binary Coalescences Observed by LIGO and Virgo During the Second Part of the Third Observing Run”. In: (Nov. 2021). arXiv: 2111.03606 [gr-qc].

[10] R. Abbott et al. “GW190412: Observation of a Binary-Black-Hole Coalescence with Asymmetric Masses”. In: *Phys. Rev. D* 102.4 (2020), p. 043015. DOI: 10.1103/PhysRevD.102.043015. arXiv: 2004.08342 [astro-ph.HE].

[11] R. Abbott et al. “The population of merging compact binaries inferred using gravitational waves through GWTC-3”. In: (Nov. 2021). arXiv: 2111.03634 [astro-ph.HE].

[12] B. P. Abbott et al. “Tests of general relativity with GW150914”. In: *Phys. Rev. Lett.* 116.22 (2016). [Erratum: Phys. Rev. Lett.121,no.12,129902(2018)], p. 221101. DOI: 10.1103/PhysRevLett.116.221101. arXiv: 1602.03841 [gr-qc].

[13] B. P. Abbott et al. “Tests of General Relativity with the Binary Black Hole Signals from the LIGO-Virgo Catalog GWTC-1”. In: *Phys. Rev.* D100.10 (2019), p. 104036. DOI: 10.1103/PhysRevD.100.104036. arXiv: 1903.04467 [gr-qc].

[14] R. Abbott et al. “Tests of General Relativity with GWTC-3”. In: (Dec. 2021). arXiv: 2112.06861 [gr-qc].

[15] J. Aasi et al. “Advanced LIGO”. In: *Class. Quant. Grav.* 32 (2015), p. 074001. DOI: 10.1088/0264-9381/32/7/074001. arXiv: 1411.4547 [gr-qc].

[16] B. P. Abbott et al. “GWTC-1: A Gravitational-Wave Transient Catalog of Compact Binary Mergers Observed by LIGO and Virgo during the First and Second Observing Runs”. In: *Phys. Rev.* X9.3 (2019), p. 031040. DOI: 10.1103/PhysRevX.9.031040. arXiv: 1811.12907 [astro-ph.HE].

[17] F. Acernese et al. “Advanced Virgo: a second-generation interferometric gravitational wave detector”. In: *Class. Quant. Grav.* 32.2 (2015), p. 024001. DOI: 10.1088/0264-9381/32/2/024001. arXiv: 1408.3978 [gr-qc].

[18] T. Akutsu et al. “KAGRA: 2.5 Generation Interferometric Gravitational Wave Detector”. In: *Nature Astron.* 3.1 (2019), pp. 35–40. DOI: 10.1038/s41550-018-0658-y. arXiv: 1811.08079 [gr-qc].

[19] M. Punturo et al. “The Einstein Telescope: A third-generation gravitational wave observatory”. In: *Class. Quant. Grav.* 27 (2010), p. 194002. DOI: 10.1088/0264-9381/27/19/194002.

[20] David Reitze et al. "Cosmic Explorer: The U.S. Contribution to Gravitational-Wave Astronomy beyond LIGO". In: *Bull. Am. Astron. Soc.* 51 (2019), p. 035. arXiv: 1907.04833 [astro-ph.IM].

[21] Pau Amaro-Seoane et al. "eLISA/NGO: Astrophysics and cosmology in the gravitational-wave millihertz regime". In: *GW Notes* 6 (2013), pp. 4–110. arXiv: 1201.3621 [astro-ph.CO].

[22] Jun Luo et al. "TianQin: a space-borne gravitational wave detector". In: *Class. Quant. Grav.* 33.3 (2016), p. 035010. DOI: 10.1088/0264-9381/33/3/035010. arXiv: 1512.02076 [astro-ph.IM].

[23] Wen-Rui Hu and Yue-Liang Wu. "The Taiji Program in Space for gravitational wave physics and the nature of gravity". In: *Natl. Sci. Rev.* 4.5 (2017), pp. 685–686. DOI: 10.1093/nsr/nwx116.

[24] Michele Maggiore et al. "Science Case for the Einstein Telescope". In: *JCAP* 03 (2020), p. 050. DOI: 10.1088/1475-7516/2020/03/050. arXiv: 1912.02622 [astro-ph.CO].

[25] Pau Amaro-Seoane et al. "Low-frequency gravitational-wave science with eLISA/NGO". In: *Class. Quant. Grav.* 29 (2012). Ed. by Mark Hannam et al., p. 124016. DOI: 10.1088/0264-9381/29/12/124016. arXiv: 1202.0839 [gr-qc].

[26] M. Bailes, B.K. Berger, P.R. Brady, et al. "Gravitational-wave physics and astronomy in the 2020s and 2030s". In: *Nat Rev Phys* 3 (2021), pp. 344–366. URL: https://doi.org/10.1038/s42254-021-00303-8.

[27] L. Santamaria et al. "Matching post-Newtonian and numerical relativity waveforms: Systematic errors and a new phenomenological model for non-precessing black hole binaries". In: *Phys. Rev. D* 82 (2010), p. 064016. DOI: 10.1103/PhysRevD.82.064016. arXiv: 1005.3306 [gr-qc].

[28] Ilana MacDonald et al. "Suitability of post-Newtonian/numerical-relativity hybrid waveforms for gravitational wave detectors". In: *Class. Quant. Grav.* 28 (2011), p. 134002. DOI: 10.1088/0264-9381/28/13/134002. arXiv: 1102.5128 [gr-qc].

[29] Michael Boyle. "Uncertainty in hybrid gravitational waveforms: Optimizing initial orbital frequencies for binary black-hole simulations". In: *Phys. Rev.* D84 (2011), p. 064013. DOI: 10.1103/PhysRevD.84.064013. arXiv: 1103.5088 [gr-qc].

[30] Ilana MacDonald et al. "Suitability of hybrid gravitational waveforms for unequal-mass binaries". In: *Phys. Rev.* D87.2 (2013), p. 024009. DOI: 10.1103/PhysRevD.87.024009. arXiv: 1210.3007 [gr-qc].

[31] Vijay Varma et al. "Surrogate model of hybridized numerical relativity binary black hole waveforms". In: *Phys. Rev.* D99.6 (2019), p. 064045. DOI: 10.1103/PhysRevD.99.064045. arXiv: 1812.07865 [gr-qc].

[32] Jam Sadiq et al. "Hybrid waveforms for generic precessing binaries for gravitational-wave data analysis". In: *Phys. Rev. D* 102.2 (2020), p. 024012. DOI: 10.1103/PhysRevD.102.024012. arXiv: 2001.07109 [gr-qc].

[33] Keefe Mitman et al. "Fixing the BMS frame of numerical relativity waveforms with BMS charges". In: *Phys. Rev. D* 106.8 (2022), p. 084029. DOI: 10.1103/PhysRevD.106.084029. arXiv: 2208.04356 [gr-qc].

[34] Simone S. Bavera et al. "The origin of spin in binary black holes: Predicting the distributions of the main observables of Advanced LIGO". In: *Astron. Astrophys.* 635 (2020), A97. DOI: 10.1051/0004-6361/201936204. arXiv: 1906.12257 [astro-ph.HE].

[35] Linhao Ma and Jim Fuller. "Tidal Spin-up of Black Hole Progenitor Stars". In: *Astrophys. J.* 952.1 (2023), p. 53. DOI: 10.3847/1538-4357/acdb74. arXiv: 2305.08356 [astro-ph.HE].

[36] Davide Gerosa et al. "Spin orientations of merging black holes formed from the evolution of stellar binaries". In: *Phys. Rev.* D98.8 (2018), p. 084036. DOI: 10.1103/PhysRevD.98.084036. arXiv: 1808.02491 [astro-ph.HE].

[37] Vaibhav Tiwari, Stephen Fairhurst, and Mark Hannam. "Constraining black-hole spins with gravitational wave observations". In: *Astrophys. J.* 868.2 (2018), p. 140. DOI: 10.3847/1538-4357/aae8df. arXiv: 1809.01401 [gr-qc].

[38] Carl L. Rodriguez et al. "Illuminating Black Hole Binary Formation Channels with Spins in Advanced LIGO". In: *Astrophys. J. Lett.* 832.1 (2016), p. L2. DOI: 10.3847/2041-8205/832/1/L2. arXiv: 1609.05916 [astro-ph.HE].

[39] Nigel T. Bishop et al. "Cauchy-characteristic extraction in numerical relativity". In: *Phys. Rev.* D54 (1996), pp. 6153–6165. DOI: 10.1103/PhysRevD.54.6153. arXiv: gr-qc/9705033 [gr-qc].

[40] Jeffrey Winicour. "Characteristic Evolution and Matching". In: *Living Rev. Rel.* 12 (2009), p. 3. DOI: 10.12942/lrr-2009-3. arXiv: 0810.1903 [gr-qc].

[41] M. C. Babiuc, J. Winicour, and Y. Zlochower. "Binary Black Hole Waveform Extraction at Null Infinity". In: *Class. Quant. Grav.* 28 (2011). Ed. by Luis Lehner, Harald P. Pfeiffer, and E. Poisson, p. 134006. DOI: 10.1088/0264-9381/28/13/134006. arXiv: 1106.4841 [gr-qc].

[42] Jordan Moxon, Mark A. Scheel, and Saul A. Teukolsky. "Improved Cauchy-characteristic evolution system for high-precision numerical relativity waveforms". In: *Phys. Rev. D* 102.4 (2020), p. 044052. DOI: 10.1103/PhysRevD.102.044052. arXiv: 2007.01339 [gr-qc].

[43] Jordan Moxon et al. "SpECTRE Cauchy-characteristic evolution system for rapid, precise waveform extraction". In: *Phys. Rev. D* 107.6 (2023), p. 064013. DOI: 10.1103/PhysRevD.107.064013. arXiv: 2110.08635 [gr-qc].

[44] Michael Boyle and Abdul H. Mroue. “Extrapolating gravitational-wave data from numerical simulations”. In: *Phys. Rev.* D80 (2009), p. 124045. DOI: 10.1103/PhysRevD.80.124045. arXiv: 0905.3177 [gr-qc].

[45] SXS Collaboration. *The SXS Collaboration catalog of gravitational waveforms*. http://www.black-holes.org/waveforms.

[46] Luc Blanchet. “Gravitational Radiation from Post-Newtonian Sources and Inspiralling Compact Binaries”. In: *Living Rev. Relativ.* 17 (2014), p. 2. DOI: 10.12942/lrr-2014-2. arXiv: 1310.1528 [gr-qc].

[47] Luc Blanchet et al. “Gravitational-wave flux and quadrupole modes from quasicircular nonspinning compact binaries to the fourth post-Newtonian order”. In: *Phys. Rev. D* 108.6 (2023), p. 064041. DOI: 10.1103/PhysRevD.108.064041. arXiv: 2304.11186 [gr-qc].

[48] Ryuichi Fujita. “Gravitational Waves from a Particle in Circular Orbits around a Schwarzschild Black Hole to the 22nd Post-Newtonian Order”. In: *Prog. Theor. Phys.* 128 (2012), pp. 971–992. DOI: 10.1143/PTP.128.971. arXiv: 1211.5535 [gr-qc].

[49] Sylvain Marsat et al. “Next-to-leading tail-induced spin–orbit effects in the gravitational radiation flux of compact binaries”. In: *Class. Quant. Grav.* 31 (2014), p. 025023. DOI: 10.1088/0264-9381/31/2/025023. arXiv: 1307.6793 [gr-qc].

[50] Alejandro Bohé et al. “Quadratic-in-spin effects in the orbital dynamics and gravitational-wave energy flux of compact binaries at the 3PN order”. In: *Class. Quant. Grav.* 32.19 (2015), p. 195010. DOI: 10.1088/0264-9381/32/19/195010. arXiv: 1501.01529 [gr-qc].

[51] Sylvain Marsat. “Cubic order spin effects in the dynamics and gravitational wave energy flux of compact object binaries”. In: *Class. Quant. Grav.* 32.8 (2015), p. 085008. DOI: 10.1088/0264-9381/32/8/085008. arXiv: 1411.4118 [gr-qc].

[52] Alejandro Bohe et al. “Next-to-next-to-leading order spin-orbit effects in the near-zone metric and precession equations of compact binaries”. In: *Class. Quant. Grav.* 30 (2013), p. 075017. DOI: 10.1088/0264-9381/30/7/075017. arXiv: 1212.5520 [gr-qc].

[53] Luc Blanchet et al. “The Third post-Newtonian gravitational wave polarisations and associated spherical harmonic modes for inspiralling compact binaries in quasi-circular orbits”. In: *Class. Quant. Grav.* 25 (2008). [Erratum: Class.Quant.Grav. 29, 239501 (2012)], p. 165003. DOI: 10.1088/0264-9381/25/16/165003. arXiv: 0802.1249 [gr-qc].

[54] Guillaume Faye et al. “The third and a half post-Newtonian gravitational wave quadrupole mode for quasi-circular inspiralling compact binaries”. In: *Class. Quant. Grav.* 29 (2012), p. 175004. DOI: 10.1088/0264-9381/29/17/175004. arXiv: 1204.1043 [gr-qc].

[55] Guillaume Faye, Luc Blanchet, and Bala R. Iyer. "Non-linear multipole interactions and gravitational-wave octupole modes for inspiralling compact binaries to third-and-a-half post-Newtonian order". In: *Class. Quant. Grav.* 32.4 (2015), p. 045016. DOI: 10.1088/0264-9381/32/4/045016. arXiv: 1409.3546 [gr-qc].

[56] Marc Favata. "Post-Newtonian corrections to the gravitational-wave memory for quasicircular, inspiralling compact binaries". In: *Physical Review D* 80.2 (July 2009). ISSN: 1550-2368. DOI: 10.1103/physrevd.80.024002. URL: http://dx.doi.org/10.1103/PhysRevD.80.024002.

[57] O. M. Moreschi. "Supercenter of Mass System at Future Null Infinity". In: *Class. Quant. Grav.* 5 (1988), pp. 423–435. DOI: 10.1088/0264-9381/5/3/004.

[58] H. Bondi, M. G. J. van der Burg, and A. W. K. Metzner. "Gravitational waves in general relativity. VII. Waves from axi-symmetric isolated systems". In: *Proc. Roy. Soc. Lond. A* 269 (1962), pp. 21–52. DOI: 10.1098/rspa.1962.0161.

[59] R. K. Sachs. "Gravitational waves in general relativity. VIII. Waves in asymptotically flat space-time". In: *Proc. Roy. Soc. Lond. A* 270 (1962), pp. 103–126. DOI: 10.1098/rspa.1962.0206.

[60] R. Sachs. "Asymptotic symmetries in gravitational theory". In: *Phys. Rev.* 128 (1962), pp. 2851–2864. DOI: 10.1103/PhysRev.128.2851.

[61] Michael Boyle et al. *scri*. Version 2022.8.8. Nov. 2023. DOI: 10.5281/zenodo.4041971. URL: https://github.com/moble/scri.

[62] Michael Boyle. "Transformations of asymptotic gravitational-wave data". In: *Phys. Rev. D* 93.8 (2016), p. 084031. DOI: 10.1103/PhysRevD.93.084031. arXiv: 1509.00862 [gr-qc].

[63] Keefe Mitman et al. "Fixing the BMS frame of numerical relativity waveforms". In: *Phys. Rev. D* 104 (2021), p. 024051. DOI: 10.1103/PhysRevD.104.024051. arXiv: 2105.02300 [gr-qc].

[64] E. T. Newman and R. Penrose. "Note on the Bondi-Metzner-Sachs group". In: *J. Math. Phys.* 7 (1966), pp. 863–870. DOI: 10.1063/1.1931221.

[65] Michael Boyle. "How should spin-weighted spherical functions be defined?" In: *J. Math. Phys.* 57.9 (2016), p. 092504. DOI: 10.1063/1.4962723. arXiv: 1604.08140 [gr-qc].

[66] *The Spectral Einstein Code*. http://www.black-holes.org/SpEC.html.

[67] Nils Deppe et al. *SpECTRE v2023.05.16*. 10.5281/zenodo.7942177. Version 2023.05.16. May 2023. DOI: 10.5281/zenodo.7942177. URL: https://spectre-code.org.

[68] Michael Boyle et al. "The SXS Collaboration catalog of binary black hole simulations". In: *Class. Quant. Grav.* 36.19 (2019), p. 195006. DOI: 10.1088/1361-6382/ab34e2. arXiv: 1904.04831 [gr-qc].

[69] P. Schmidt, F. Ohme, and M. Hannam. "Towards models of gravitational waveforms from generic binaries II: Modelling precession effects with a single effective precession parameter". In: *Phys. Rev. D* 91.2 (2015), p. 024043. DOI: 10.1103/PhysRevD.91.024043. arXiv: 1408.1810 [gr-qc].

[70] Eric Poisson and Clifford M. Will. *Gravity: Newtonian, Post-Newtonian, Relativistic*. Cambridge University Press, 2014. DOI: 10.1017/CBO9781139507486.

[71] Thomas W. Baumgarte and Stuart L. Shapiro. *Numerical Relativity: Solving Einstein's Equations on the Computer*. Cambridge University Press, 2010. DOI: 10.1017/CBO9781139193344.

[72] Jan Steinhoff. "Spin gauge symmetry in the action principle for classical relativistic particles". In: *arXiv e-prints* (2015), arXiv:1501.04951. arXiv: 1501.04951 [gr-qc].

[73] Jonathan Blackman et al. "A Surrogate Model of Gravitational Waveforms from Numerical Relativity Simulations of Precessing Binary Black Hole Mergers". In: *Phys. Rev.* D95.10 (2017), p. 104023. DOI: 10.1103/PhysRevD.95.104023. arXiv: 1701.00550 [gr-qc].

[74] Pauli Virtanen et al. "SciPy 1.0: Fundamental Algorithms for Scientific Computing in Python". In: *Nature Methods* 17 (2020), pp. 261–272. DOI: 10.1038/s41592-019-0686-2.

[75] M. A. Branch, T. F. Coleman, and Y. Li. "A Subspace, Interior, and Conjugate Gradient Method for Large-Scale Bound-Constrained Minimization Problems". In: *SIAM Journal on Scientific Computing* 21.1 (1999), pp. 1–23.

[76] Michael Boyle. "Angular velocity of gravitational radiation from precessing binaries and the corotating frame". In: *Phys. Rev.* D87.10 (2013), p. 104006. DOI: 10.1103/PhysRevD.87.104006. arXiv: 1302.2919 [gr-qc].

[77] Charles J. Woodford, Michael Boyle, and Harald P. Pfeiffer. "Compact Binary Waveform Center-of-Mass Corrections". In: *Phys. Rev. D* 100.12 (2019), p. 124010. DOI: 10.1103/PhysRevD.100.124010. arXiv: 1904.04842 [gr-qc].

[78] Md Arif Shaikh et al. "Defining eccentricity for gravitational wave astronomy". In: (Feb. 2023). pypi.org/project/gw_eccentricity. arXiv: 2302.11257 [gr-qc].

[79] Michael Ebersold et al. "Gravitational-wave amplitudes for compact binaries in eccentric orbits at the third post-Newtonian order: Memory contributions". In: *Phys. Rev. D* 100.8 (2019), p. 084043. DOI: 10.1103/PhysRevD.100.084043. arXiv: 1906.06263 [gr-qc].

[80] Blake Moore et al. "Gravitational-wave phasing for low-eccentricity inspiralling compact binaries to 3PN order". In: *Phys. Rev. D* 93.12 (2016), p. 124061. DOI: 10.1103/PhysRevD.93.124061. arXiv: 1605.00304 [gr-qc].

[81] A. Buonanno and T. Damour. "Effective one-body approach to general relativistic two-body dynamics". In: *Physical Review D* 59.8 (Mar. 1999). ISSN: 1089-4918. DOI: 10.1103/physrevd.59.084006. URL: http://dx.doi.org/10.1103/PhysRevD.59.084006.

Part II

Strong-Field Matching

Chapter 4

PARAMETER MATCHING BETWEEN HORIZON QUASI-LOCAL AND POINT-PARTICLE DEFINITIONS AT 1PN FOR QUASI-CIRCULAR AND NON-SPINNING BBH SYSTEMS IN HARMONIC GAUGE

Published as: Dongze Sun and Leo C. Stein. "Parameter matching between horizon quasi-local and point-particle definitions at 1PN for quasi-circular and non spinning BBH systems in harmonic gauge". In: (2025). arXiv: 2510.25618 [gr-qc].

Abstract

We investigate how commonly used parameter definitions in Post-Newtonian (PN) theory compare with those from Numerical Relativity (NR) for binary black hole (BBH) systems. In NR, masses and spins of each companion are measured quasi-locally from apparent horizon (AH) geometry, whereas in PN they are attributes of point particles defined via asymptotic matching in body zones. Although these definitions coincide in the infinite-separation limit, they could differ by finite-separation corrections that matter for precision modeling. To quantify and control these effects, we constructed the leading-order map between quasi-local, horizon-based NR parameters and PN point-particle parameters in the harmonic gauge. To obtain this map, we perform asymptotic matching between each companion's inner zone metric and the PN two-body metric, and build a gauge-preserving diffeomorphism that maintains the harmonic gauge in the strong-field region. On a family of harmonic inertial time slices, we solve perturbatively for the AH and compute its quasi-local areal mass. This yields the leading-order matching between AH-based and point-particle parameter definitions in harmonic gauge. On a horizon-penetrating harmonic slicing, the AH quasi-local mass agrees with the PN point-particle mass at 1PN order. For generic harmonic slicings that deviate from horizon-penetrating by a 1PN-order perturbation, the AH mass differs from the PN mass by a corresponding 1PN correction. This parameter matching provides a bridge between PN and NR, enabling definition-consistent PN–NR hybrids and better-conditioned initial data and boundary condition for NR and Cauchy–Characteristic Evolution (CCE). The framework can be extend to spinning and mildly eccentric binaries and to real NR gauges beyond harmonic.

4.1 Introduction

Gravitational-wave astronomy is entering a new precision era with the arrival of next-generation observatories. Ground-based detectors such as Cosmic Explorer (CE) and the Einstein Telescope (ET), together with the space-based Laser Interferometer Space Antenna (LISA), will probe binary black hole coalescences with sensitivities far beyond current capabilities. These instruments will record long-duration signals with extremely high signal-to-noise ratios (SNRs) [2, 3], providing unprecedented access to the dynamics of compact binaries across the inspiral, merger, and ringdown. As statistical uncertainties on measured source parameters shrink in this high-SNR regime, the burden shifts to theory: waveform models must achieve accuracy levels such that systematic errors remain safely below statistical errors. This demand places renewed emphasis on the consistency of parameter definitions used across modeling frameworks. Even subtle mismatches—such as differences in how masses or spins are defined in post-Newtonian (PN) versus numerical relativity (NR) descriptions—can accumulate over thousands of inspiral cycles and bias astrophysical inference. Addressing this challenge requires a parameter-consistent bridge between PN and NR, ensuring that systematic differences in parameter definitions are carefully considered.

For an isolated system, one can define gauge-invariant global quantities such as the Arnowitt–Deser–Misner (ADM) mass and ADM angular momentum, which characterize the energy and angular momentum of the entire spacetime, including contributions from binding energy and gravitational radiation. However, in a dynamical binary black hole (BBH) spacetime with gravitational waves, it is generally ill-defined to decompose the ADM mass into "mass of hole 1" and "mass of hole 2" without additional structure. The difficulty lies in the fact that the self-energy of each black hole is inherently mixed with the system's binding energy and radiative energy, and any attempt to separate these pieces depends on a choice of gauge. NR typically adopts a gauge adapted to the evolution scheme (e.g. moving-puncture or generalized harmonic formulations), whereas post-Newtonian (PN) theory employs the harmonic gauge. Thus, while global quantities are unambiguously defined, the assignment of masses and spins to individual black holes in a binary is necessarily gauge-dependent, and PN and NR frameworks make different gauge choices in practice.

Apart from the gauge difference, PN and NR also use different definitions. In NR, each black hole's properties are measured quasi-locally from the geometry of its apparent horizon [4, 5]. Using techniques from the isolated/dynamical horizon framework [6, 7], one can define the individual mass and angular momentum of a black hole from surface integrals on the AH. Since the AH is slicing dependent, the individual mass and angular momentum are also slicing dependent, and they coincide with the ADM quantities only in the infinite-separation limit. As the black holes approach each other, each black hole's horizon mass incorporates effects of the companion's gravitational field. This indicates that the notion of "mass of an individual BH" in a binary is inherently scale-dependent, which agrees with the asymptotic mass at infinite separation, but differs at finite separations due to the presence of binding energy, tidal deformations, and radiations. The scale-dependent feature of the NR mass was observed in Ref. [8].

In post-Newtonian theory, one treats the black holes as point masses characterized by constant parameters mass and spin, and solves Einstein's equations as an expansion in v/c or $GM/(c^2 r)$ [9]. To rigorously connect this idealized point-mass description to an actual black hole, the PN point-mass parameters are defined via an asymptotic matching procedure [10]: the inner-zone metric near each object is asymptotically expanded in series of $1/r$, and matched in an overlap region (buffer zone) to the global PN metric for the binary system. In this way, the constant PN mass parameter is essentially the mass parameter of an isolated BH solution that would produce the same far-field. At infinite separation, this clearly coincides with each black hole's physical mass. However, at finite separation the matching can induce differences from NR, once the two metrics are self-consistently matched. Our aim is to quantify this difference at the leading post-Newtonian order.

Comparisons of PN and NR waveforms have indirectly noticed parameter discrepancies. Past efforts to hybridize PN and NR waveforms typically assumed that the masses and spins used in PN formulas could be taken directly from the NR horizon masses and spins read from the simulation [11, 12, 13, 14, 15, 16, 17]. This works well to leading order, but as modeling accuracy improved, it became evident that small mismatches in these parameters can visibly affect the waveform phasing. Recently, Ref. [18] demonstrated that allowing slight adjustments ("optimization") of the PN masses and spins away from the raw NR values yields markedly better PN–NR agreement in hybrid waveforms. In their study, the PN parameters that minimize the waveform mismatch differ systematically from the NR values. This finding suggests that PN and NR are using slightly different conventions for the masses and spins, reinforcing the need for a proper translation in between.

In this paper, we bridge this gap by deriving an analytic, leading-order parameter mapping between PN and NR definitions of mass for binary black holes. To do so, we need a spacetime metric that is valid in both inner zone near the horizon ($r \sim r_s \ll b$) and in the near zone where the PN two-body metric is valid ($r_s \ll r \ll \lambda$). Here b is the separation between the two black holes, r_s is the Schwarzschild radius of the companion black hole that we are interested in, and λ is the wavelength of the gravitational radiation.

Refs.[19] and [20, 21] pioneered an approach to build such global BBH metric, aiming to provide initial data for NR. Their metric is constructed by matched asymptotic expansions: they asymptotically matched a near zone PN metric to a tidally perturbed BH metric around each black hole in a buffer region where both approximations are valid. However, in their construction, the coordinates are not enforced to satisfy a single global consistent gauge condition, which can complicate our parameter matching because it's hard to define a time slice in a gauge consistent way.

We work entirely in the harmonic gauge for both the inner zone and near zone to ensure an apple-to-apple comparison without gauge ambiguities. We adopt harmonic gauge for simplicity, but this framework can be extended to gauges commonly used in NR, e.g., generalized harmonic formalism used in SpEC. The inner zone metric in the harmonic gauge is given by Ref. [22] in the comoving frame with respect to the black hole, which is an isolated BH solution plus tidal multipoles whose leading contributions scale as $O\left(M^3/b^3\right)$ – at relative 3PN order. Because our goal is a leading-order (1PN) parameter matching, we neglect these higher-order tidal pieces. The coordinate transformation between the comoving frame and inertial frame is constructed by enforcing the harmonic gauge through the strong field region, the boundary conditions for the gauge equations are provided by asymptotic matching with the PN metric in the buffer region. Applying this coordinate transformation places the inner zone metric and near zone metric in the same harmonic coordinate system.

We solve perturbatively for the AH on a group of harmonic inertial time slice and compute its quasi-local areal mass from the horizon geometry. We find that the AH areal mass generally differs from the PN mass at 1PN order under 1PN perturbations, but it reduces to the PN mass when the time slice is horizon penetrating. For a realistic NR orbital separation (e.g., 10 orbits before merger), if the time slice is not chosen properly near the black hole, the fractional mass difference $\delta m/m$ would be on the order of 10^{-2}, which is not negligible for the precision requirements of the next generation detectors.

Aligning the PN and NR parameter definitions through this matching has several important implications. First, it enables the construction of PN–NR waveform hybrids with consistent physical parameters, and it avoids the risk of overfitting that can bias the parameters. This should reduce systematic mismatches over long inspirals and give hybrids a more robust physical interpretation. Second, our results can inform the setup of NR initial conditions. Current NR simulations of BBHs often start from initial data specified by approximate methods (e.g. superposed BHs with PN or effective-one-body estimates for orbital parameters) and involve some iterations to achieve the desired masses and eccentricities after relaxation. With a PN–NR parameter mapping, one could choose the initial orbital separation and momenta such that the resulting horizon masses correspond to a given PN binary with parameters (m_1, m_2) at a certain post-Newtonian order. This would reduce the initial junk radiation and parameter drift, effectively providing better initial data that already incorporates the PN corrections at a given order. Additionally, our framework is formulated in a gauge consistent manner: we work in harmonic coordinates throughout. In future extensions, the approach can be generalized to other gauge choices by first solving for the coordinate transformation between harmonic coordinates and the desired coordinates, and then locating the AH under the desired slicing condition. The framework itself can also be straightforwardly extended to include black-hole spins and orbital eccentricity.

In this paper, we use lower-case Latin indices from the beginning of the alphabet to denote four-dimensional spacetime quantities, whereas lower-case Latin indices from the middle of the alphabet are spatial. We work in geometrized units with $G = c = 1$ throughout the paper.

The remainder of this paper is organized as follows. Sec. 4.2 reviews the definitions of mass in PN theory and in NR. Sec. 4.3 presents our asymptotic matching scheme performed in harmonic coordinates. Sec. 4.4 specifies the harmonic slicing conditions, and we propose a horizon penetrating harmonic slicing for BBH systems. In Sec. 4.5, we solve for the AH on the matched slice, extract the AH areal mass, and derive the leading-order parameter mapping. We quantify the magnitude of the correction for typical binary configurations. Finally, Sec. 4.6 concludes the paper with a summary of our key results and an outlook on extensions, including incorporating spins, eccentricities and exploring alternative gauges used in NR.

4.2 Mass Definitions in PN and NR

In this section, we review how mass is defined in the PN and in NR for non-spinning BBH systems, and we clarify how they can be different.

PN mass

In the PN approach, each compact object is idealized as a point particle characterized solely by a constant mass parameter m_A (and spin parameters for spinning case), with $A = 1, 2$ for a binary. The gravitational field produced by the point masses is obtained by solving Einstein's equations expanded in PN orders. In harmonic coordinates, where the perturbed metric $h^{ab} = \sqrt{-g}g^{ab} - \eta^{ab}$ (with η_{ab} the Minkowski metric) satisfies the harmonic gauge condition $\partial_b h^{ab} = 0$. The Einstein field equations in harmonic gauge take the form of inhomogeneous flat-space wave equations

$$\Box h^{ab} = 16\pi\tau^{ab} \tag{4.1}$$

where

$$\tau^{ab} = |g|T^{ab} + \frac{1}{16\pi}\Lambda^{ab}, \tag{4.2}$$

is the effective stress-energy pseudo-tensor of both matter and gravity. Here Λ^{ab} is the nonlinear gravitational source term (quadratic and higher in h) arising from self-interactions of the field (see Eq. (15) of [23] for full expression), and the stress-energy tensor for the points masses is given by

$$T^{ab}(t, \mathbf{x}) = \sum_{A=1}^{2} \frac{m_A u_A^a u_A^b}{\sqrt{-g^{cd}(t, \mathbf{y}_A) u_A^c u_A^d}} \frac{\delta^{(3)}[\mathbf{x} - \mathbf{y}_A(t)]}{\sqrt{-g}}, \tag{4.3}$$

where $\mathbf{y}_A(t)$ is the trajectory of body A and u_A^a is its 4-velocity. Then the field solution is given by

$$h^{ab} = 16\pi\Box_{\text{ret}}^{-1}\tau^{ab}, \tag{4.4}$$

where

$$(\Box_{\text{ret}}^{-1} f)(t, \mathbf{x}) = -\frac{1}{4\pi} \iiint \frac{d^3\mathbf{x}'}{|\mathbf{x} - \mathbf{x}'|} f(t - |\mathbf{x} - \mathbf{x}'|, \mathbf{x}'). \tag{4.5}$$

The PN mass parameters enter the field solutions through this integral.

Because point masses generate singular fields, all these local integrals in the PN iteration require a careful regularization procedure. Blanchet's MPM–PN scheme [24, 9] initially employed a Hadamard partie-finie regularization to handle the divergent self-field of each point mass. While Hadamard's method can yield the finite part of most integrals, it was found to break down at the 3PN level, leaving an undetermined constant in the equation of motion. The resolution of this problem came from using dimensional regularization, which is able to preserve the symmetries of the theory. In practice, one works in general d spatial dimensions (analytically continued away from $d = 3$) so that all integrals are convergent, and defines the physical theory by the limit $d \to 3$ by taking the finite part of any $1/(d-3)$ poles. It successfully fixed the cutoff ambiguity, yielding a fully self-consistent solution for point-mass binaries at high PN order, and with the mass parameters m_i unambiguously defined.

To rigorously connect this idealized point-mass description to an actual black hole, the PN point-mass parameters are defined alternatively via an asymptotic matching procedure in Poisson's approach [10]. Since the PN two-body metric is only valid in the region $r \gg r_\mathrm{s}$, and diverges near the point particle, they replace the singular point-particle with a perturbed black hole solution near the object ($r \ll d$, where d is the separation between two objects) in this object's comoving frame. Then they solve for the tidal moments of the perturbed black hole solution and the coordinate transformation between the comoving frame and the PN inertial frame by asymptotically expanding the both solutions in comoving frame in series of $1/r$, and matching the coefficients in an overlap region where both the two solutions are valid ($r_\mathrm{s} \ll r \ll d$). In this way, the constant PN mass parameter is essentially the mass parameter of an perturbed black hole that would produce the same far-field. At infinite separation or in the limit that the mass of the secondary object tends to zero, the PN mass clearly coincides with the black hole's Schwarzschild mass.

The horizon absorption of energy should in principle change the mass of each black hole. PN handles this horizon absorption by absorbing it into the definition of binding energy E_b. In this definition, the PN ADM mass is given by

$$E_\mathrm{ADM} = m_1 + m_2 + E_b, \tag{4.6}$$

and E_b evolves according to the balance law

$$\frac{dE_b}{dt} = -\left(F_\infty + F_{H,1} + F_{H,2}\right), \tag{4.7}$$

where F_∞ and $F_{H,i}$ are the energy flux to null infinity and the flux into the horizons, respectively. In this way, the mass parameters entering the PN expressions are kept as constants.

NR mass

In NR, a black hole's mass is often defined quasi-locally on each time slice using its apparent horizon (AH) – a marginally outer trapped surface. For a non-spinning hole, the quasi-local (irreducible) mass is given by the AH areal mass

$$m = \sqrt{\frac{A}{16\pi}}, \tag{4.8}$$

where A is the area of the AH of black hole. This quantity is geometrically invariant on the slice, but it is slicing dependent because the AH itself depends on the chosen time slicing. By contrast, the event horizon (EH) is a global and gauge invariant null surface, so as the irreducible mass defined from the area of EH. However, the EH cannot be determined without knowledge of the entire spacetime evolution, so in practice, the EH based masses is impractical during a simulation. Consequently, NR uses AH based, quasi-local measurements which depends only on local variables on a given time slice. The slicing dependence of AH introduces an intrinsic ambiguity, thus the NR quasi-local masses extracted from the AHs need not coincide with the point-particle masses used in PN theory. Accordingly, any direct comparison between NR and PN requires an explicit, gauge-consistent parameter translation.

4.3 Constructing global metric

In this section we construct the global metric using the matched–asymptotic framework [25, 22]. We enforce the harmonic gauge $\partial_a(\sqrt{-g}g^{ab}) = 0$ in the strong field region, so that the global metric and the coordinate transformations are valid and gauge-preserving through the horizon. We work to leading post-Newtonian order (1PN), and we neglect tidal multipoles whose leading contributions enter at relative 3PN.

Region setup and notations

Consider a binary with component labels $A = 1, 2$, PN parameters m_A, PN trajectories and velocities $\mathbf{y}_A(t)$ and $\mathbf{v}_A(t)$, and separation b. We introduce the usual PN expansion parameter $v = |\mathbf{v_1} - \mathbf{v_2}| \ll 1$. For non-spinning and quasi-circular case, $v^2 = (m_1 + m_2)/b$ at leading order. We also have $\partial_t v_1 \sim O(1/b^2) \sim O(v^4)$, and $\partial_t b \sim O(v^6)$, so we treat them as constants at 1PN order.

Following Ref. [20], we divide the global 4-manifold as two inner zones of the black holes ($r_A \ll b$), a near zone ($m_A \ll r_A \ll \lambda$), and a far zone ($r_A \gg \lambda$), as shown in Fig. 4.1. Here λ is the wavelength of gravitational radiation, and $r_A = |\mathbf{x} - \mathbf{y_A}| = \sqrt{\delta_{ij}(x^i - y^i_A)(x^j - y^j_A)} \equiv ((x_A - y_A)(x_A - y_A))$. Here we use (ab) to denote the dot product of spatial vectors. We use $n^i_A = (x^i - y^i_A)/r_A$ to denote the normal vector in r_A direction. We raise and lower indices of the spatial vector n^i_A and v^i_A with the Euclidean metric δ_{ij}.

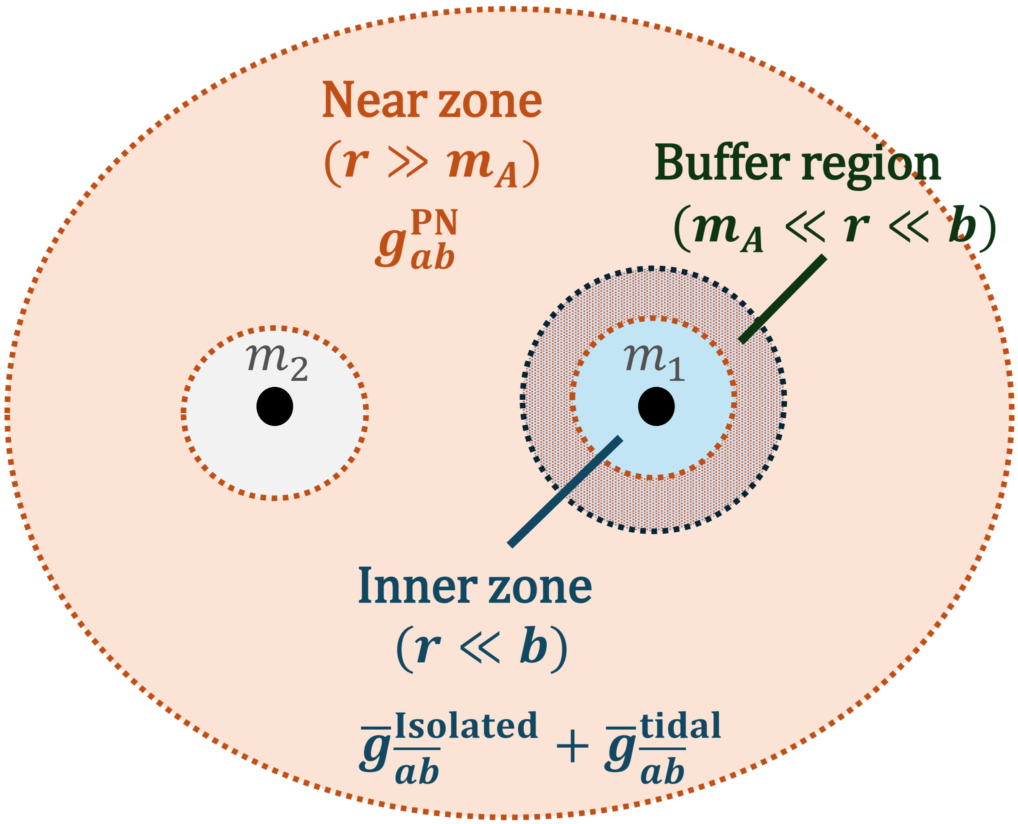

Figure 4.1: A schematic diagram showing the domain setup and symbols.

We are only interested in the inner zone, where the metric is given as a non-rotating black hole in the harmonic coordinates in the black hole's comoving frame, and the near zone, where the metric is given by the PN two-body metric in the inertial frame. In order to match the inner zone metric with the near zone metric, we use a buffer region where both descriptions are valid ($m_A \ll r_A \ll b$).

We use the following notation: we use a bar $\bar{}$ to denote coordinates or indices in the comoving frame, and coordinates or indices without the bar are in the inertial frame. We use superscript or subscript H for harmonic coordinates, KS for Kerr-Schild coordinates, and CS for Cook-Scheel coordinates.

Inner zone metric

In the inner zone of black hole 1, we start from a Kerr-Schild Cartesian coordinate system $\bar{x}^{\bar{a}}_{\mathrm{KS}} = \left(\bar{t}_{\mathrm{KS}}, \bar{x}^{\bar{i}}_{\mathrm{KS}}\right)$. The metric there is taken as an isolated black hole solution plus tidal multipoles [22]. The latter start at $\mathcal{O}\left(M^3/b^3\right)$, which are at relative 3PN and are consistently neglected for a leading 1PN mass matching. Thus in the inner zone we retain only the monopolar field of mass parameter m_1^{IZ}, which is to be related to the PN parameter m_1 by the asymptotic matching.

The inner zone metric of black hole 1 in the Kerr-Schild Cartesian coordinate at 1PN order is

$$\begin{aligned}
g^{\mathrm{KS}}_{\bar{0}\bar{0}} &= -1 + \frac{2m_1^{\mathrm{IZ}}}{\bar{r}_1^{\mathrm{KS}}}, \\
g^{\mathrm{KS}}_{\bar{0}\bar{i}} &= \frac{2m_1^{\mathrm{IZ}}}{\bar{r}_1^{\mathrm{KS}}} \bar{n}^{\mathrm{KS}}_{1\bar{i}}, \\
g^{\mathrm{KS}}_{\bar{i}\bar{j}} &= \delta_{\bar{i}\bar{j}} + \frac{2m_1^{\mathrm{IZ}}}{\bar{r}_1^{\mathrm{KS}}} \bar{n}^{\mathrm{KS}}_{1\bar{i}} \bar{n}^{\mathrm{KS}}_{1\bar{j}}.
\end{aligned} \tag{4.9}$$

Here $\bar{r}_1^{\mathrm{KS}} = (\bar{x}_{\mathrm{KS}}\bar{x}_{\mathrm{KS}})$, and $\bar{n}^{\bar{i}}_{1\mathrm{KS}} = \bar{x}^{\bar{i}}_{\mathrm{KS}}/\bar{r}_1^{\mathrm{KS}}$.

Near zone metric

In the near zone, the metric can be described by the PN two-body metric in the barycentric harmonic coordinates $x^a_{\mathrm{H}} = \left(t_{\mathrm{H}}, x^i_{\mathrm{H}}\right)$ in the inertial frame. Since our inner zone comoving frame metric is accurate to 2.5PN, we will use the 2.5PN two-body metric to reach the same accuracy in the buffer region. The 2.5PN metric is given by [26]. We substitute $1/r_{2\mathrm{H}} = 1/b + O(v^4)$, keep terms up to $O(v^2)$, and truncate the metric to $O(m_1^2/r_{1\mathrm{H}}^2)$ order, which is sufficient for our asymptotic matching purpose. The results reads

$$\begin{aligned}
g^{\mathrm{H}}_{00} =& -1 + \frac{2m_2}{b} + \frac{m_1}{r_{1\mathrm{H}}}\left(2 - (n_{1\mathrm{H}}v_1)^2 + 4v_1^2 - \frac{6m_2}{b}\right) \\
&+ \frac{m_1^2}{r_{1\mathrm{H}}^2}\left(-2 + 3(n_{1\mathrm{H}}v_1)^2 - v_1^2 + \frac{8m_2}{b}\right) \\
&+ O\left(\frac{m_1^3}{r_{1\mathrm{H}}^3}, v^3\right), \\
g^{\mathrm{H}}_{0i} =& -4\frac{m_1}{r_{1\mathrm{H}}}v_{1i} + \frac{m_1^2}{r_{1\mathrm{H}}^2}\left(v_{1i} - (n_{1\mathrm{H}}v_1)n^{\mathrm{H}}_{1i}\right) \\
&+ O\left(\frac{m_1^3}{r_{1\mathrm{H}}^3}, v^3\right), \\
g^{\mathrm{H}}_{ij} =& \left[1 + \frac{2m_2}{b} + \frac{m_1}{r_{1\mathrm{H}}}\left(2 - (n_{1\mathrm{H}}v_1)^2 + \frac{2m_2}{b}\right)\right. \\
&\left.+ \frac{m_1^2}{r_{1\mathrm{H}}^2}\right]\delta_{ij} + \frac{4m_1}{r_{1\mathrm{H}}}v_{1i}v_{1j} + \frac{m_1^2}{r_{1\mathrm{H}}^2}n^{\mathrm{H}}_{1i}n^{\mathrm{H}}_{1j} \\
&+ O\left(\frac{m_1^2}{r_{1\mathrm{H}}^2}, v^3\right).
\end{aligned} \tag{4.10}$$

Note that g^{H}_{ij} is not complete at $\mathcal{O}\left(\frac{m_1^2}{r_{1\mathrm{H}}^2}\right)$ order.

Coordinate transformation

Before we match the parameters, it's important to express the inner zone and near zone metrics to the same frame. Ref. [27] proposed a coordinate transformation between the comoving frame and inertial frame by inserting the PN trajectory of the black hole, but this approach generally does not preserve the desired gauge. Ref. [25] presents a general coordinate transformation by asymptotic matching with the PN metric in the buffer region. It preserves the harmonic gauge in the weak field region where the metric is flat, but the gauge preserving feature doesn't extend to the strong field region near the horizon. We construct the coordinate transformation by enforcing the harmonic gauge through the strong field region, and the boundary conditions for the gauge equations are provided by asymptotic matching with the PN metric in the buffer region.

We parameterize the coordinate transformation as

$$\begin{aligned} \bar{t}_{\mathrm{KS}} &= t_{\mathrm{H}} + \xi^0(t_{\mathrm{H}}, x^i_{\mathrm{H}}), \\ \left(1 - \frac{m_1^{\mathrm{IZ}}}{\bar{r}_{1\mathrm{KS}}}\right)\bar{x}^{\bar{i}}_{\mathrm{KS}} &= x^i_{\mathrm{H}} - y^i_A + \xi^i(t_{\mathrm{H}}, x^i_{\mathrm{H}}), \end{aligned} \tag{4.11}$$

here the $\left(1 - \frac{m_1^{\mathrm{IZ}}}{\bar{r}_{1\mathrm{KS}}}\right)$ factor is introduced to bring the comoving Kerr-Schild coordinates to a comoving harmonic coordinates. We further expand ξ^0 as

$$\xi^0(t_{\mathrm{H}}, x^i_{\mathrm{H}}) = \mathcal{A}(t_{\mathrm{H}}) - ((x_{\mathrm{H}} - y_A)v_1) + \kappa(t_{\mathrm{H}}, x^i_{\mathrm{H}}). \tag{4.12}$$

The first two terms are introduced to keep the trajectory, and the third term is introduced to preserve the harmonic gauge. We have $\dot{\mathcal{A}} \sim \xi^i \sim \mathcal{O}(v^2)$, and $\kappa \sim \mathcal{O}(1)$.

Substituting Eq. (4.12) into Eq. (4.11), we can solve for the inverse transformation as

$$\begin{aligned} t_{\mathrm{H}} =& \bar{t}_{\mathrm{KS}} - \mathcal{A}(\bar{t}_{\mathrm{KS}}) + \left[1 - \dot{\mathcal{A}}(\bar{t}_{\mathrm{KS}})\right] \\ &\cdot \left[\left(1 - \frac{m_1^{\mathrm{IZ}}}{\bar{r}_{1\mathrm{KS}}}\right)(\bar{x}_{\mathrm{KS}} v_1) - K(\bar{t}_{\mathrm{KS}}, \bar{x}^{\bar{i}}_{\mathrm{KS}})\right], \\ x^i_{\mathrm{H}} =& \left(1 - \frac{m_1^{\mathrm{IZ}}}{\bar{r}_{1\mathrm{KS}}}\right)\bar{x}^{\bar{i}}_{\mathrm{KS}} + y^i_A \\ &- \xi^i\left(\bar{t}_{\mathrm{KS}}, \left(1 - \frac{m_1^{\mathrm{IZ}}}{\bar{r}_{1\mathrm{KS}}}\right)\bar{x}^{\bar{i}}_{\mathrm{KS}}\right), \end{aligned} \tag{4.13}$$

where $K(\bar{t}_{\rm KS}, \bar{x}^{\bar{i}}_{\rm KS}) \equiv \kappa\left(t_{\rm H}(\bar{t}_{\rm KS}, \bar{x}^{\bar{i}}_{\rm KS}), x^i_{\rm H}(\bar{t}_{\rm KS}, \bar{x}^{\bar{i}}_{\rm KS})\right)$. Eq. (4.11) and Eq. (4.13) also gives the transformation of $\bar{r}_{1\rm KS}$ and $\bar{n}^{\bar{i}}_{1\rm KS}$ as

$$\begin{aligned}\bar{r}_{1\rm KS} =& r_{1\rm H} + (n_{1\rm H}\xi) + m_1,\\ \bar{n}^{\bar{i}}_{1\rm KS} =& \left[1 - \frac{(n_{1\rm H}\xi)}{r_{1\rm H}}\right] n^i_{1\rm H} + \frac{\xi^i}{r_{1\rm H}}.\end{aligned} \tag{4.14}$$

The harmonic condition reads

$$g^{\bar{a}\bar{b}}_{\rm KS}\left(\partial_{\bar{a}}\partial_{\bar{b}}x^c_{\rm H} - \Gamma^{\bar{d}}_{{\rm KS}\bar{a}\bar{b}}\partial_{\bar{d}}x^c_{\rm H}\right) = 0. \tag{4.15}$$

Substituting Eq. (4.13), we get

$$\begin{aligned}\bar{\nabla}^2 K - &\frac{2m_1^{\rm IZ}}{\bar{r}_{1\rm KS}}\bar{n}^{\bar{i}}_{1\rm KS}\bar{n}^{\bar{j}}_{1\rm KS}\partial_{\bar{i}}\partial_{\bar{j}}K\\ &- \frac{2m_1^{\rm IZ}}{\bar{r}^2_{1\rm KS}}\left(1 + \bar{n}^{\bar{i}}_{1\rm KS}\partial_{\bar{i}}K\right) = \mathcal{O}(v^3),\end{aligned} \tag{4.16}$$

$$\left(1 - \frac{m_1^{\rm IZ}}{\bar{r}_{1\rm KS}}\right)\bar{\nabla}^2\xi^k - \frac{m_1^{\rm IZ}}{\bar{r}_{1\rm KS}}\bar{n}^{\bar{i}}_{1\rm KS}\bar{n}^{\bar{j}}_{1\rm KS}\partial_{\bar{i}}\partial_{\bar{j}}\xi^k = \mathcal{O}(v^3), \tag{4.17}$$

where ∇^2 is the flat Laplacian. We can further decompose ξ^i as

$$\xi^i(t_{\rm H}, x^j_{\rm H}) = B(t_{\rm H}, x^j_{\rm H})n^i_{1\rm H} + D(t_{\rm H}, x^j_{\rm H})v^i_1, \tag{4.18}$$

then we substitute it into Eq. (4.15) to get

$$\bar{\nabla}^2 B - \frac{m_1^{\rm IZ}}{\bar{r}_{1\rm KS}}\bar{n}^{\bar{i}}_{1\rm KS}\bar{n}^{\bar{j}}_{1\rm KS}\partial_{\bar{i}}\partial_{\bar{j}}B - \frac{2B}{\bar{r}^2_{1\rm KS}} = \mathcal{O}(v^3), \tag{4.19}$$

$$\begin{aligned}&\frac{2B}{\bar{r}^2_{1\rm KS}}\left(v_1\bar{n}_{1\rm KS}\right) - \frac{2v_1^{\bar{i}}\partial_{\bar{i}}B}{\bar{r}_{1\rm KS}} + \frac{m_1^{\rm IZ}}{\bar{r}_{1\rm KS}}\left(v_1\bar{n}_{1\rm KS}\right)\bar{n}^{\bar{i}}_{1\rm KS}\bar{n}^{\bar{j}}_{1\rm KS}\partial_{\bar{i}}\partial_{\bar{j}}B + \bar{n}^{\bar{i}}_{1\rm KS}v_1^{\bar{j}}\partial_{\bar{i}}\partial_{\bar{j}}B + \frac{2\left(v_1\bar{n}_{1\rm KS}\right)\bar{n}^{\bar{i}}_{1\rm KS}\partial_{\bar{i}}B}{\bar{r}_{1\rm KS}} - v_1^{\bar{i}}v_1^{\bar{j}}\partial_{\bar{i}}\partial\\ &+ \frac{m_1^{\rm IZ}v_1^2}{\bar{r}_{1\rm KS}}\bar{n}^{\bar{i}}_{1\rm KS}\bar{n}^{\bar{j}}_{1\rm KS}\partial_{\bar{i}}\partial_{\bar{j}}D = \mathcal{O}(v^4).\end{aligned} \tag{4.20}$$

The harmonic condition Eq. (4.15) does not constrain $\mathcal{A}$ at 1PN order, so we will need to get information of $\mathcal{A}$ and acquire boundary conditions for K, B and D by asymptotically matching the inner zone metric with the PN near zone metric in the buffer region.

Asymptotic matching

In order to asymptotically match the inner zone metric with the PN near zone metric, we first need to transform the inner zone metric to the inertial frame in the harmonic coordinates

$$g^{\mathrm{H}}_{ab}(t_{\mathrm{H}}, x^j_{\mathrm{H}}) = g^{\mathrm{KS}}_{\bar{c}\bar{d}} \frac{\partial \bar{x}^{\bar{c}}_{\mathrm{KS}}}{\partial x^a_{\mathrm{H}}} \frac{\partial \bar{x}^{\bar{d}}_{\mathrm{KS}}}{\partial x^b_{\mathrm{H}}}. \tag{4.21}$$

The Jacobian is given by Eq. (4.11) and Eq. (4.13) as

$$\begin{aligned}
\partial^{\bar{0}}_0 =& 1 + \dot{\mathcal{A}} + v_1^2 + \partial_t \kappa - v_1^i \partial_i \kappa, \\
\partial^{\bar{0}}_i =& - v_{1i} + \partial_i \kappa, \\
\partial^{\bar{i}}_0 =& - \left(1 + \frac{m_1^{\mathrm{IZ}}}{r_{1\mathrm{H}}}\right) v_1^i + \frac{m_1^{\mathrm{IZ}}}{r_{1\mathrm{H}}} (v_1 n_{1\mathrm{H}}) n^i_{1\mathrm{H}}, \\
\partial^{\bar{i}}_j =& \left[1 + \frac{B}{r_{1\mathrm{H}}} + \frac{m_1^{\mathrm{IZ}}}{r_{1\mathrm{H}}} \left(1 - \frac{(v_1 n_{1\mathrm{H}}) D}{r_{1\mathrm{H}}}\right)\right] \delta^i_j \\
&+ n^i_{1\mathrm{H}} \partial_j B - \frac{m_1^{\mathrm{IZ}} (v_1 n_{1\mathrm{H}})}{r_{1\mathrm{H}}} n^i_{1\mathrm{H}} \partial_j D \\
&+ \left(1 + \frac{m_1^{\mathrm{IZ}}}{r_{1\mathrm{H}}}\right) v_1^i \partial_j D + \left[-\frac{B}{r_{1\mathrm{H}}}\right. \\
&\left.+ \frac{2 m_1^{\mathrm{IZ}} (v_1 n_{1\mathrm{H}}) D}{r^2_{1\mathrm{H}}} - \frac{m_1^{\mathrm{IZ}}}{r_{1\mathrm{H}}} \left(1 - \frac{(v_1 n_{1\mathrm{H}}) D}{r_{1\mathrm{H}}}\right)\right] n^i_{1\mathrm{H}} n^{\mathrm{H}}_{1j} \\
&- \frac{m_1^{\mathrm{IZ}} D}{r^2_{1\mathrm{H}}} \left(n^i_{1\mathrm{H}} v_{1j} + v_1^i n^{\mathrm{H}}_{1j}\right).
\end{aligned} \tag{4.22}$$

We apply the Jacobian and Eq. (4.14) to the inner zone metric Eq. (4.9), and expand the results in series of $1/r_{1\mathrm{H}}$, and keep the terms up to the second order. The full transformed metric is very lengthy, so we will just give the useful parts. The δ_{ij} component of the transformed metric reads

$$\begin{aligned}
g^{\mathrm{H}(\delta)}_{ij} =& 1 + \frac{2 m_1^{\mathrm{IZ}} + 2B}{r_{1\mathrm{H}}} \\
&+ \frac{m^2_{1\mathrm{IZ}} + 2 m_1^{\mathrm{IZ}} B + B^2 - 2 m_1^{\mathrm{IZ}} D (n_{1\mathrm{H}} v_1)}{r^2_{1\mathrm{H}}} \\
&+ O\left(\frac{m_1^3}{r^3_{1\mathrm{H}}}, v^3\right).
\end{aligned} \tag{4.23}$$

By comparing with Eq. (4.10), we immediately get

$$m_1^{\mathrm{IZ}} = m_1, \quad B \doteq \frac{m_2}{b} r_{1\mathrm{H}}, \quad D \doteq \frac{1}{2} r_{1\mathrm{H}} (v_1 n_{1\mathrm{H}}), \tag{4.24}$$

where $\doteq$ denotes equality in the buffer region (boundary condition). For B, the boundary condition is spherically symmetric, so we look for a spherical symmetric solution to Eq. (4.19). The general spherical symmetric solution is

$$B = \beta_1 r_{1\text{H}} + \beta_2 \left(-1 - \frac{r_{1\text{H}}}{r_{1\text{H}} - m1} + \frac{2r_{1\text{H}}}{m_1} \ln \frac{r_{1\text{H}}}{r_{1\text{H}} - m_1} \right), \tag{4.25}$$

where the second term scales like $O(m_1^2/r_{1\text{H}}^2)$, so it can not be constrained by the current 2.5PN metric whose spatial components are not complete at $O(m_1^2/r_{1\text{H}}^2)$ order. So we will choose $\beta_1 = m2/d$, and $\beta_2 = 0$. This gives

$$B = \frac{m_2}{b} r_{1\text{H}}. \tag{4.26}$$

Eq. (4.20) can then be simplified by substituting B, which gives

$$\nabla^2 D - \frac{m_1^{\text{IZ}}}{\bar{r}_{1\text{KS}}} \bar{n}^{\bar{i}}_{1\text{KS}} \bar{n}^{\bar{j}}_{1\text{KS}} \partial_{\bar{i}} \partial_{\bar{j}} D = O(v^3). \tag{4.27}$$

Based on the boundary condition Eq. (4.24), we look for a $l = 1$ solution. The general $l = 1$ solution can be written as

$$D = (\delta_1 + \delta_2 r_{1\text{H}})(n_{1\text{H}} u), \tag{4.28}$$

where $\mathbf{u}$ is a constant vector. The boundary condition Eq. (4.24) gives $\delta_1 = 0, \delta_2 = \frac{1}{2}$, and $\mathbf{u} = \mathbf{v_1}$. So we have

$$D = \frac{1}{2} r_{1\text{H}} (v_1 n_{1\text{H}}). \tag{4.29}$$

To simplify the matching for κ and $\mathcal{A}$, we first study the gauge constraint Eq. (4.16). This equation is independent of $\bar{t}_{\text{KS}}$, so we can decompose K as $K(\bar{t}_{\text{KS}}, \bar{x}^{\bar{i}}_{\text{KS}}) = K_1(\bar{t}_{\text{KS}}) K_2(\bar{x}^{\bar{i}}_{\text{KS}})$. Given that both the inner zone metric and near zone metric have no explicit dependence on time, and that $K_1(\bar{t}_{\text{KS}})$ enters directly in the Jacobian Eq. (4.22), then $K_1(\bar{t}_{\text{KS}})$ must be constant. So $K = K(\bar{x}^{\bar{i}}_{\text{KS}})$. For simplicity, we first look for a spherical symmetric solution to Eq. (4.16). The general solution is

$$K = 2m_1 \ln \frac{\bar{r}_{1\text{KS}} - 2m_1}{k_1} + k_2 \ln \frac{\bar{r}_{1\text{KS}} - 2m_1}{\bar{r}_{1\text{KS}}}, \tag{4.30}$$

where the k_1 coefficient is just an arbitrary constant time shift, so we can choose it to be $2m_1$ to make the unit correct. We substitute the coordinate transformation Eq. (4.14) into ansatz Eq. (4.30) to get the ansatz for κ

$$\begin{aligned} \kappa =& 2m_1 \ln \frac{r_{1\text{H}} \left(1 + \frac{m_2}{b} + \frac{1}{2}(n_{1\text{H}} v_1)\right) - m_1}{2m_1} \\ &+ k_2 \ln \frac{r_{1\text{H}} - 2m_1 \left(1 - \frac{m_2}{b} - \frac{1}{2}(n_{1\text{H}} v_1)\right)}{r_{1\text{H}}}, \end{aligned} \tag{4.31}$$

and then substitute the κ along with Eq. (4.26) and Eq. (4.29) into the transformed metric Eq. (4.21). The $O(1)$ coefficient of the tt component is

$$g_{ij}^{\mathrm{H}(O(1))} = -1 - 2\dot{\mathcal{A}} - v_1^2. \tag{4.32}$$

Comparing it with the tt component of Eq. (4.10), we have

$$\dot{\mathcal{A}} = -\frac{1}{2}v_1^2 - \frac{m_2}{b}. \tag{4.33}$$

Then the $O(m_1^2/r_{1\mathrm{H}}^2)$ coefficient of the tt component reduces to

$$\begin{aligned} g_{ij}^{\mathrm{H}(O(m_1^2/r_{1\mathrm{H}}^2))} =& \frac{m_1^2}{r_{1\mathrm{H}}^2}\left(-2 + 2k_2(n_{1\mathrm{H}}v_1)\right. \\ & \left. +3(n_{1\mathrm{H}}v_1)^2 - v_1^2 + \frac{8m_2}{b}\right). \end{aligned} \tag{4.34}$$

Comparing with the Eq. (4.10), we have $k_2 = 0$. So

$$\kappa = 2m_1 \ln \frac{r_{1\mathrm{H}}\left[1 + \frac{m_2}{b} + \frac{1}{2}(n_{1\mathrm{H}}v_1)\right] - m_1}{2m_1}. \tag{4.35}$$

We use $B, D, \dot{\mathcal{A}}$ and κ from Eq. (4.26), Eq. (4.29), Eq. (4.33) and Eq. (4.35) to transform the inner zone metric Eq. (4.9), the results agrees exactly with the near zone metric Eq. (4.10) for the available orders in $m_1/r_{1\mathrm{H}}$ up to $O(v^2)$. This suggests that the $l > 0$ modes of K vanishes at 1PN order, which agrees our spherical symmetric ansatz Eq. (4.30).

In conclusion, the harmonic gauge-preserving coordinate transformation from the PN inertial frame to the comoving Kerr-Schild coordinate is given by

$$\begin{aligned} \bar{t}_{\mathrm{KS}} =& \left(1 - \frac{1}{2}v_1^2 - \frac{m_2}{b}\right)t_{\mathrm{H}} - ((x_{\mathrm{H}} - y_A)v_1) \\ & + 2m_1 \ln \frac{r_{1\mathrm{H}}\left[1 + \frac{m_2}{b} + \frac{1}{2}(n_{1\mathrm{H}}v_1)\right] - m_1}{2m_1}, \\ \bar{x}_{\mathrm{KS}}^{\bar{i}} =& \left[1 + \frac{m_1}{r_{1\mathrm{H}}}\left(1 - \frac{m_2}{b} - \frac{1}{2}(n_{1\mathrm{H}}v_1)\right)\right] \\ & \left[\left(1 + \frac{m_2}{b}\right)\left(x_{\mathrm{H}}^i - y_A^i\right) + \frac{1}{2}r_{1\mathrm{H}}(n_{1\mathrm{H}_{v_1}})v_1^i\right], \\ \bar{r}_{1\mathrm{KS}} =& r_{1\mathrm{H}}\left(1 + \frac{1}{2}(n_{1\mathrm{H}}v_1)^2 + \frac{m_2}{b}\right) + m_1, \\ \bar{n}_{1\mathrm{KS}}^{\bar{i}} =& \left(1 - \frac{1}{2}(n_{1\mathrm{H}}v_1)^2\right)n_{1\mathrm{H}}^i + \frac{1}{2}(n_{1\mathrm{H}}v_1)v_1^i. \end{aligned} \tag{4.36}$$

The inverse transformation is

$$\begin{aligned}
t_{\mathrm{H}} &= \left(1+\frac{1}{2}v_1^2+\frac{m_2}{b}\right)\left[\bar{t}_{\mathrm{KS}}+(\bar{r}_{1\mathrm{KS}}-m_1)\,(\bar{n}_{\mathrm{KS}}v_1)\right.\\
&\quad \left.-2m_1\ln\frac{\bar{r}_{1\mathrm{KS}}-2m_1}{2m_1}\right],\\
x_{\mathrm{H}}^i &= (\bar{r}_{1\mathrm{KS}}-m_1)\left[\left(1-\frac{m_2}{b}\right)\bar{n}_{1\mathrm{KS}}^{\bar{i}}-\frac{1}{2}\,(\bar{n}_{\mathrm{KS}}v_1)\,v_1^i\right]\\
&\quad +y_A^i,\\
r_{1\mathrm{H}} &= \left(1-\frac{1}{2}(\bar{n}_{1\mathrm{KS}}v_1)^2-\frac{m_2}{b}\right)(\bar{r}_{1\mathrm{KS}}-m_1)\,,\\
n_{1\mathrm{H}}^i &= \left(1+\frac{1}{2}(\bar{n}_{1\mathrm{KS}}v_1)^2\right)\bar{n}_{1\mathrm{KS}}^{\bar{i}}-\frac{1}{2}(\bar{n}_{\mathrm{KS}}v_1)v_1^i.
\end{aligned} \tag{4.37}$$

4.4 Slicing condition

The apparent horizon is slicing dependent, but the slicing conditions that satisfy the harmonic condition is not unique. We can add any function $F(\bar{t}_{\mathrm{KS}},\bar{x}_{\mathrm{KS}}^{\bar{i}})$ to the harmonic time t_{H} in Eq. (4.37) as long as F satisfies the harmonic condition Eq. (4.15). For simplicity, we focus on the static case, so $F=F(\bar{x}_{1\mathrm{KS}}^{\bar{i}})$. Putting it into Eq. (4.15), we get

$$\bar{\nabla}^2 F-\frac{2m_1}{\bar{r}_{1\mathrm{KS}}}\bar{n}_{1\mathrm{KS}}^{\bar{i}}\bar{n}_{1\mathrm{KS}}^{\bar{j}}\partial_{\bar{i}}\partial_{\bar{j}}F-\frac{2m_1}{\bar{r}_{1\mathrm{KS}}^2}\bar{n}_{1\mathrm{KS}}^{\bar{i}}\partial_{\bar{i}}F=0. \tag{4.38}$$

The general spherically symmetric solution is

$$F=f_1\ln\frac{\bar{r}_{1\mathrm{KS}}-2m_1}{\bar{r}_{1\mathrm{KS}}}+f_2, \tag{4.39}$$

where f_2 is just an arbitrary constant time shift that we are setting to zero.

We note that when

$$f_1=2m_1\left(1+\frac{1}{2}v_1^2+\frac{m_2}{b}\right), \tag{4.40}$$

the harmonic time slice becomes

$$\begin{aligned}
t_{\mathrm{CS}} &= \left(1+\frac{1}{2}v_1^2+\frac{m_2}{b}\right)\left[\bar{t}_{\mathrm{KS}}+(\bar{r}_{1\mathrm{KS}}-m_1)\,(\bar{n}_{\mathrm{KS}}v_1)\right.\\
&\quad \left.+2m_1\ln\frac{2m_1}{\bar{r}_{1\mathrm{KS}}}\right]=const.,
\end{aligned} \tag{4.41}$$

which is regular through the horizon. This is the generalized case of the Cook-Scheel slicing [28], which is the unique harmonic and horizon penetrating slicing for an isolated single black hole.

To study the dependence of the AH quasi-local mass on the slicing condition, we perturb the generalized Cook-Scheel slicing condition in Eq. (4.41) by setting $f_1 = 2m_1\left(1+\frac{1}{2}v_1^2+\frac{m_2}{b}\right) - 2m_1\delta v^2$. The slicing condition then becomes

$$\begin{aligned} T = &\left(1+\frac{1}{2}v_1^2+\frac{m_2}{b}\right)\left[\bar{t}_{\mathrm{KS}} + (\bar{r}_{1\mathrm{KS}} - m_1)\,(\bar{n}_{\mathrm{KS}} v_1)\right.\\ &\left. + 2m_1 \ln\frac{2m_1}{\bar{r}_{1\mathrm{KS}}}\right] - 2m_1\delta v^2 \ln\frac{\bar{r}_{1\mathrm{KS}} - 2m_1}{\bar{r}_{1\mathrm{KS}}} = const.. \end{aligned} \tag{4.42}$$

We will solve perturbatively for the AH on this slicing condition and compute its quasi-local areal mass from the horizon geometry in the next section.

4.5 AH quasi-local mass

The apparent horizon of a black hole is defined as an outer marginally trapped surface on a given time slice. It is a closed 2-surface whose outgoing null normal has zero expansion. If one combines the AH on each time slice into a 3-dimensional surface, this worldtube will depend on the slicing. As we will see, this slicing dependent feature of the AH will bring ambiguity into the quasi-local mass defined from the AH geometry.

Finding the apparent horizon

Here we solve for the AH on the given time slice $T = const.$ in Eq. (4.42). The future-pointing unit timelike normal to this time slice is given by

$$\tau_a = -\alpha D_a T, \tag{4.43}$$

where D_a is the covariant derivative with respect to the 4-metric g_{ab}, and

$$\alpha = (-g^{ab} D_a T D_b T)^{-1/2}. \tag{4.44}$$

The induced 3-metric on this time slice is given by

$$g^{(3)}_{ab} = g_{ab} + \tau_a \tau_b. \tag{4.45}$$

Let s^a be the unit outward pointing normal to the AH 2-surface in this time slice, so that

$$s^a \tau_a = 0, \quad s^a s_a = 1, \quad \tau^a \tau_a = -1, \tag{4.46}$$

then the 2-metric on the AH 2-surface is

$$g^{(2)}_{ab} = g_{ab} + \tau_a \tau_b - s_a s_b, \tag{4.47}$$

and

$$k^a = \frac{1}{\sqrt{2}}(\tau^a + s^a) \tag{4.48}$$

is the future-pointing null geodesic congruence whose projection on the 3D time slice is orthogonal to the AH 2-surface. Note that k^a is only defined on the AH 2-surface, its extension away from the 2-surface is not defined. The AH is defined by the vanishing of expansion on the 2-surface, which is

$$\Theta \equiv g^{(2)ab} D_a k_b = 0. \tag{4.49}$$

Since the covariant derivative of k_a is projected onto the 2-surface by $g^{(2)ab}$, no knowledge of the extension of k^a away from the 2-surface is required. Only if k^a is affinely parametrized, i.e., $k^a D_a k^b = 0$ in the neighborhood of the 2-surface, Eq. (4.49) reduces to $D_a k^a = 0$.

Note that $\tau^a D_b \tau_a = 0$ and $s^a D_b s_a = 0$ from Eq. (4.46), Eq. (4.49) can be simplified as

$$\Theta = \frac{1}{\sqrt{2}} \left[g^{ab} D_a(\tau_b + s_b) + \tau^a \tau^b D_a s_b - s^a s^b D_a \tau_b \right] = 0. \tag{4.50}$$

We will use this equation for the remaining calculations.

In order to get s^a, we parametrize the AH 2-surface in the comoving Kerr-Schild coordinates by

$$\begin{aligned} \mathcal{R} =& \bar{r}_{1\mathrm{KS}} - 2m_1 - R(\bar{\theta}, \bar{\phi}) \\ =& \bar{r}_{1\mathrm{KS}} - 2m_1 - \sum_{\bar{l},\bar{m}} \bar{R}_{\bar{l}\bar{m}} Y^{\bar{l}\bar{m}}(\bar{\theta}, \bar{\phi}) = 0, \end{aligned} \tag{4.51}$$

with $(\bar{\theta}, \bar{\phi})$ defined by

$$\bar{x}^{\bar{i}}_{\mathrm{KS}} = \bar{r}_{1\mathrm{KS}} \left(\sin(\bar{\theta}) \cos(\bar{\phi}), \sin(\bar{\theta}) \sin(\bar{\phi}), \cos(\bar{\phi}) \right). \tag{4.52}$$

Here $\bar{R}_{\bar{l}\bar{m}} \sim O(v^2)$, given that we are on a time slice that is perturbed from the horizon-penetrating one by $O(v^2)$. Then we have

$$s^a = \frac{g^{(3)ab} D_b \mathcal{R}}{\sqrt{g^{(3)cd} D_c \mathcal{R} D_d \mathcal{R}}}. \tag{4.53}$$

Eq. (4.50) is a scalar equation which does not transform under coordinate transformations, so we solve it in the comoving Kerr-Schild coordinates, which simplifies the calculation significantly compared with working in the inertial harmonic coordinates.

We substitute the slicing Eq. (4.42) and the comoving metric Eq. (4.9) into Eq. (4.50), project it onto $\bar{l}, \bar{m}$ modes, and truncate terms to $O(v^2)$ and $O(R)$, we obtain

$$\begin{aligned}\bar{R}_{\bar{0}\bar{0}} &= -\sqrt{\pi} m_1 \delta v^2 + O(v^3),\\ \bar{R}_{\bar{l}>0,\bar{m}} &= O(v^3),\end{aligned} \tag{4.54}$$

so the AH is given by

$$\bar{r}_{1\mathrm{KS}} = 2m_1 - \frac{m_1}{2}\delta v^2. \tag{4.55}$$

For the horizon penetrating slicing, i.e., $\delta = 0$, the AH reduces to the Kerr-Schild horizon at $\bar{r}_{1\mathrm{KS}} = 2m_1$.

Quasi-local mass

The AH quasi-local mass is defined from the area of the AH by Eq. (4.8). The AH area A is given by

$$A = \int_0^{2\pi} d\bar{\phi} \int_0^{\pi} d\bar{\theta} \sqrt{g^{(2)}_{\bar{\theta}\bar{\theta}} g^{(2)}_{\bar{\phi}\bar{\phi}} - g^{(2)2}_{\bar{\theta}\bar{\phi}}}, \tag{4.56}$$

where

$$g^{(2)}_{\bar{\theta}i\bar{\theta}j} = g^{(2)}_{\bar{a}\bar{b}} \partial_{\bar{\theta}i} \bar{x}^{\bar{a}}_{1\mathrm{KS}} \partial_{\bar{\theta}j} \bar{x}^{\bar{b}}_{1\mathrm{KS}}. \tag{4.57}$$

Note that from Eq. (4.42), we have $\bar{t}_{\mathrm{KS}} = const. - (\bar{r}_{1\mathrm{KS}} - m_1)(\bar{n}_{\mathrm{KS}} v_1) + \ldots$, so the Jacobian is

$$\begin{aligned}\partial_{\bar{\theta}} \bar{x}^{\bar{a}} =& \bar{r}_{1\mathrm{KS}} \Big((1 - \frac{m_1}{\bar{r}_{1\mathrm{KS}}}) v_1 \cos(\bar{\theta}) \sin(\bar{\phi}), \cos(\bar{\theta}) \cos(\bar{\phi}),\\ & \cos(\bar{\theta}) \sin(\bar{\phi}), -\sin(\bar{\theta}) \Big),\\ \partial_{\bar{\phi}} \bar{x}^{\bar{a}} =& \bar{r}_{1\mathrm{KS}} \Big((1 - \frac{m_1}{\bar{r}_{1\mathrm{KS}}}) v_1 \sin(\bar{\theta}) \cos(\bar{\phi}), -\sin(\bar{\theta}) \sin(\bar{\phi}),\\ & \sin(\bar{\theta}) \cos(\bar{\phi}), 0 \Big).\end{aligned} \tag{4.58}$$

Substituting the AH Eq. (4.55) and the 2-metric Eq. (4.47), we get the AH quasi-local mass from Eq. (4.8) as

$$m_1^{\mathrm{AH}} = m_1 \left(1 - \frac{1}{4}\delta v^2\right). \tag{4.59}$$

For the horizon penetrating slicing, i.e., $\delta = 0$, the AH quasi-local mass agrees with the PN mass at 1PN order. But for a general harmonic slicing condition that is perturbed from the horizon penetrating one by 1PN order at $O(v^2)$, the AH quasi-local mass is also perturbed from the PN mass by $O(v^2)$. For a realistic NR orbital separation (e.g., 10 orbits before merger), $O(v^2)$ would be on the order of 10^{-2}, which is not negligible for the precision requirements of the next generation detectors.

4.6 Conclusions

We have provided a gauge-consistent bridge between apparent horizon quasi-local and PN point-particle parameter definitions for non-spinning, quasi-circular BBH systems at leading PN order, working entirely in harmonic gauge. By constructing a harmonic and gauge-preserving map between the inner zone black hole metric and the near zone PN two-body metric, we constructed a global harmonic metric for BBH, and we generalized the Cook-Scheel harmonic horizon penetrating slicing to the BBH case. We located the apparent horizon on harmonic time slices, and derived the leading order relation between the AH areal mass and the PN mass parameter at 1PN order. We find that on a horizon penetrating harmonic slicing (the generalized Cook–Scheel slice), the AH quasi-local mass agrees with the PN point-particle mass at 1PN order. For generic harmonic slicings that deviate from the horizon penetrating condition by an $O(v^2)$ perturbation, the AH mass differs from the PN mass by a fractional amount $\frac{\Delta m_1}{m_1} = -\frac{1}{4}\delta v^2$. For typical orbital velocities at realistic NR separations (e.g., 10 orbits before merger), this amounts to $O(10^{-2})$ corrections, which is not negligible at the precision demanded by next generation detectors.

Our work neglected tidal multipoles entering at relative 3PN, and restricted to non-spinning, quasi-circular binaries. Some natural extensions would include: (i) incorporating spin and eccentricity to obtain mappings for both mass and angular momentum; (ii) adding leading tidal effects and extend to higher PN orders; (iii) translating the mapping from harmonic to gauges more commonly used in NR (e.g., damped harmonic in SpEC) via explicit coordinate transforms that preserves the new gauge.

Extending the matching procedure to the actual NR gauges would enable PN–NR waveform hybridizations to be performed with parameter consistent inputs, reducing the need for ad-hoc optimization of PN masses to fit NR and thereby decreasing the risk of parameter bias over long inspirals. It also suggests a practical prescription for NR initial data by starting from a global gauge-consistent metric that is accurate to a given PN order, which could potentially mitigate junk radiation and parameter drift during the early evolution.

Acknowledgments

We thank Saul Teukolsky, Mark Scheel, and Qing Dai for useful discussions. This work was supported in part by the Sherman Fairchild Foundation, by NSF Grants PHY-

2309211, PHY-2309231, and OAC-2209656 at Caltech. Computational resources for this work were supported by Qing Dai.

References

[1] Dongze Sun and Leo C. Stein. "Parameter matching between horizon quasi-local and point-particle definitions at 1PN for quasi-circular and non spinning BBH systems in harmonic gauge". In: (2025). arXiv: 2510.25618 [gr-qc].

[2] Niayesh Afshordi et al. "Waveform Modelling for the Laser Interferometer Space Antenna". arXiv:2311.01300. Nov. 2023. arXiv: 2311.01300 [gr-qc].

[3] Enrico Barausse et al. "Massive Black Hole Merger Rates: The Effect of Kiloparsec Separation Wandering and Supernova Feedback". In: *Astrophys. J.* 904.1 (2020), p. 16. DOI: 10.3847/1538-4357/abba7f. arXiv: 2006.03065 [astro-ph.GA].

[4] Michael Boyle et al. "The SXS collaboration catalog of binary black hole simulations". In: *Classical and Quantum Gravity* 36.19 (Sept. 2019), p. 195006. DOI: 10.1088/1361-6382/ab34e2. URL: https://dx.doi.org/10.1088/1361-6382/ab34e2.

[5] Mark A. Scheel et al. *The SXS Collaboration's third catalog of binary black hole simulations*. 2025. arXiv: 2505.13378 [gr-qc]. URL: https://arxiv.org/abs/2505.13378.

[6] Abhay Ashtekar and Badri Krishnan. "Dynamical horizons and their properties". In: *Phys. Rev.* D68 (2003), p. 104030. DOI: 10.1103/PhysRevD.68.104030. arXiv: gr-qc/0308033 [gr-qc].

[7] Abhay Ashtekar and Badri Krishnan. "Isolated and Dynamical Horizons and Their Applications". In: *Living Reviews in Relativity* 7.1 (Dec. 2004). ISSN: 1433-8351. DOI: 10.12942/lrr-2004-10. URL: http://dx.doi.org/10.12942/lrr-2004-10.

[8] Daniel Pook-Kolb et al. "Existence and stability of marginally trapped surfaces in black-hole spacetimes". In: *Physical Review D* 99.6 (Mar. 2019). ISSN: 2470-0029. DOI: 10.1103/physrevd.99.064005. URL: http://dx.doi.org/10.1103/PhysRevD.99.064005.

[9] Luc Blanchet. "Post-Newtonian theory for gravitational waves". In: *Living Reviews in Relativity* 27.1 (July 2024). ISSN: 1433-8351. DOI: 10.1007/s41114-024-00050-z. URL: http://dx.doi.org/10.1007/s41114-024-00050-z.

[10] Eric Poisson and Clifford M. Will. *Gravity: Newtonian, Post-Newtonian, Relativistic*. Cambridge University Press, 2014. DOI: 10.1017/CBO9781139507486.

[11] L. Santamaria et al. "Matching post-Newtonian and numerical relativity waveforms: Systematic errors and a new phenomenological model for non-precessing black hole binaries". In: *Phys. Rev. D* 82 (2010), p. 064016. DOI: 10.1103/PhysRevD.82.064016. arXiv: 1005.3306 [gr-qc].

[12] Ilana MacDonald et al. "Suitability of post-Newtonian/numerical-relativity hybrid waveforms for gravitational wave detectors". In: *Class. Quant. Grav.* 28 (2011), p. 134002. DOI: 10.1088/0264-9381/28/13/134002. arXiv: 1102.5128 [gr-qc].

[13] Michael Boyle. "Uncertainty in hybrid gravitational waveforms: Optimizing initial orbital frequencies for binary black-hole simulations". In: *Phys. Rev.* D84 (2011), p. 064013. DOI: 10.1103/PhysRevD.84.064013. arXiv: 1103.5088 [gr-qc].

[14] Ilana MacDonald et al. "Suitability of hybrid gravitational waveforms for unequal-mass binaries". In: *Phys. Rev.* D87.2 (2013), p. 024009. DOI: 10.1103/PhysRevD.87.024009. arXiv: 1210.3007 [gr-qc].

[15] Vijay Varma et al. "Surrogate model of hybridized numerical relativity binary black hole waveforms". In: *Phys. Rev.* D99.6 (2019), p. 064045. DOI: 10.1103/PhysRevD.99.064045. arXiv: 1812.07865 [gr-qc].

[16] Jam Sadiq et al. "Hybrid waveforms for generic precessing binaries for gravitational-wave data analysis". In: *Phys. Rev. D* 102.2 (2020), p. 024012. DOI: 10.1103/PhysRevD.102.024012. arXiv: 2001.07109 [gr-qc].

[17] Jooheon Yoo et al. "Numerical relativity surrogate model with memory effects and post-Newtonian hybridization". In: *Physical Review D* 108.6 (Sept. 2023). ISSN: 2470-0029. DOI: 10.1103/physrevd.108.064027. URL: http://dx.doi.org/10.1103/PhysRevD.108.064027.

[18] Dongze Sun et al. "Optimizing post-Newtonian parameters and fixing the BMS frame for numerical-relativity waveform hybridizations". In: *Phys. Rev. D* 110 (10 Nov. 2024), p. 104076. DOI: 10.1103/PhysRevD.110.104076. URL: https://link.aps.org/doi/10.1103/PhysRevD.110.104076.

[19] Kashif Alvi. "Note on ingoing coordinates for binary black holes". In: *Physical Review D* 67.10 (May 2003). ISSN: 1089-4918. DOI: 10.1103/physrevd.67.104006. URL: http://dx.doi.org/10.1103/PhysRevD.67.104006.

[20] Nicolás Yunes et al. "Binary black hole initial data from matched asymptotic expansions". In: *Physical Review D* 74.10 (Nov. 2006). ISSN: 1550-2368. DOI: 10.1103/physrevd.74.104011. URL: http://dx.doi.org/10.1103/PhysRevD.74.104011.

[21] Nicolás Yunes and Wolfgang Tichy. "Improved initial data for black hole binaries by asymptotic matching of post-Newtonian and perturbed black hole solutions". In: *Physical Review D* 74.6 (Sept. 2006). ISSN: 1550-2368. DOI: 10.1103/physrevd.74.064013. URL: http://dx.doi.org/10.1103/PhysRevD.74.064013.

[22] Stephanne Taylor and Eric Poisson. "Nonrotating black hole in a post-Newtonian tidal environment". In: *Physical Review D* 78.8 (Oct. 2008). ISSN: 1550-2368. DOI: 10.1103/physrevd.78.084016. URL: http://dx.doi.org/10.1103/PhysRevD.78.084016.

[23] Luc Blanchet. "Gravitational Radiation from Post-Newtonian Sources and Inspiralling Compact Binaries". In: *Living Reviews in Relativity* 5.1 (Apr. 2002). ISSN: 1433-8351. DOI: 10.12942/lrr-2002-3. URL: http://dx.doi.org/10.12942/lrr-2002-3.

[24] Luc Blanchet. "Gravitational Radiation from Post-Newtonian Sources and Inspiralling Compact Binaries". In: *Living Reviews in Relativity* 17.1 (Feb. 2014). DOI: 10.12942/lrr-2014-2. URL: https://doi.org/10.12942%2Flrr-2014-2.

[25] S KOPEIKIN and I VLASOV. "Parametrized post-Newtonian theory of reference frames, multipolar expansions and equations of motion in the N-body problem". In: *Physics Reports* 400.4–6 (Nov. 2004), pp. 209–318. ISSN: 0370-1573. DOI: 10.1016/j.physrep.2004.08.004. URL: http://dx.doi.org/10.1016/j.physrep.2004.08.004.

[26] Luc Blanchet, Guillaume Faye, and Bénédicte Ponsot. "Gravitational field and equations of motion of compact binaries to 5/2 post-Newtonian order". In: *Physical Review D* 58.12 (Oct. 1998). ISSN: 1089-4918. DOI: 10.1103/physrevd.58.124002. URL: http://dx.doi.org/10.1103/PhysRevD.58.124002.

[27] Luciano Combi et al. "Superposed metric for spinning black hole binaries approaching merger". In: *Physical Review D* 104.4 (Aug. 2021). ISSN: 2470-0029. DOI: 10.1103/physrevd.104.044041. URL: http://dx.doi.org/10.1103/PhysRevD.104.044041.

[28] Gregory B. Cook and Mark A. Scheel. "Well-behaved harmonic time slices of a charged, rotating, boosted black hole". In: *Phys. Rev. D* 56 (8 Oct. 1997), pp. 4775–4781. DOI: 10.1103/PhysRevD.56.4775. URL: https://link.aps.org/doi/10.1103/PhysRevD.56.4775.

Chapter 5

STRONG-FIELD MATCHING FOR PN–BHPT–NR PARAMETER MAPS IN BINARY BLACK HOLES

To be submitted as: Dongze Sun et al. "Strong-Field Matching for PN–BHPT–NR Parameter Maps in Binary Black Holes". to be submitted soon.

Abstract

Accurate long-duration gravitational-wave models for massive black-hole binaries require a consistent connection between post-Newtonian (PN) theory, numerical relativity (NR), and black-hole perturbation theory (BHPT). The usual waveform-level alignment of PN and NR data does not by itself determine how masses, spins, coordinates, slicing, and gauge are identified across the two descriptions. This finite-separation relation is important for high-SNR LISA sources, where fractional parameter shifts at the 10^{-4}–10^{-3} level can enter the waveform-accuracy budget. We develop the NR-side strong-field component of a PN–BHPT–NR parameter map, using the local BHPT/Kerr–Schild description as the bridge between the PN point-particle mass and the NR strong-field geometry. Starting from NR data in inertial damped-harmonic coordinates, we determine a gauge-preserving coordinate transformation to a local comoving Kerr–Schild (KS) frame by solving the generalized-harmonic coordinate equations with the NR gauge source. In the quasi-stationary approximation this gives an elliptic coordinate solve on a single time slice, supplemented by a monopole mass parameter calibration. For an equal-mass binary at coordinate separation $b = 80M$, the procedure removes the dominant monopole mass residual, gives a converged local mass $m_{\mathrm{KS}} \simeq 0.50049M$, and leaves residuals at the expected tidal scale. This provides a gauge-consistent way to connect NR simulations with BHPT. Together with the established PN–BHPT matching, this NR–BHPT matching enables a PN–NR parameter map for gauge- and parameter-consistent hybrid waveforms.

5.1 Introduction

Gravitational waves from binary black holes encode the geometry and dynamics of strongly curved spacetime. Ground-based detectors have already measured many stellar-mass mergers, and space-based detectors such as LISA are expected to observe massive black-hole binaries with long inspirals and large signal-to-noise ratios [2, 3, 4]. The modeling requirement for such sources is stringent because a small phase, amplitude, or gauge inconsistency can accumulate over many cycles and produce a waveform error that is distinguishable at high signal-to-noise ratio [5, 6]. This accuracy requirement motivates waveform models assembled from complementary descriptions of binary-black-hole dynamics. The relevant theoretical problem is therefore to assemble a single waveform model whose pieces use compatible definitions of time, mass, spin, center, and asymptotic frame.

PN theory, NR, and BHPT provide complementary descriptions of the binary spacetime across the inspiral, merger, ringdown, and local strong-field regions. Post-Newtonian (PN) theory gives analytic control of the weak-field, slow-motion inspiral and supplies long waveforms at large separation [7, 8]. Numerical relativity (NR) solves the full nonlinear problem through late inspiral, merger, and ringdown, with computational costs that limit the length and parameter-space density of available simulations [9, 10, 11]. Black-hole perturbation theory (BHPT) describes fields on a black-hole background and is applicable both in the local neighborhood of each member of a widely separated binary and in the ringdown of the remnant [12, 13, 14, 15, 16, 17]. A complete waveform model must therefore combine information from PN theory, NR, and BHPT for different regimes.

Waveform hybridization is the standard way to combine analytic inspiral waveforms with NR late-time waveforms. In its simplest form, one aligns the PN and NR waveforms over a time or frequency window, then joins the PN inspiral to the NR late inspiral, merger, and ringdown [18, 19, 20, 21]. This window-based construction is essential, but it is not a complete spacetime matching. The alignment can involve time shifts, phase shifts, rotations, boosts, supertranslations, and sometimes intrinsic-parameter adjustments. A fit that minimizes waveform differences in a finite window can absorb coordinate or parameter inconsistencies into these freedoms, mixing physical parameter shifts with gauge choices. The resulting hybrid can have a small matching-window residual and still carry a biased inspiral phase, an inconsistent local black-hole frame, or an incorrect source-parameter interpretation.

The parameter problem is especially important. In PN theory, the individual masses and spins are parameters of effective point-particle sources, defined through the matching and regularization conventions of the PN expansion [7, 8]. In NR, the masses and spins used to label a simulation are usually quasi-local horizon quantities, computed from apparent-horizon areas and approximate rotational vector fields [22, 23, 24]. These definitions agree in the isolated infinite-separation limit, but at finite separation they need not be identical because the horizon is embedded in a gauge-dependent slice and is distorted by the companion.

These differences are numerically small but potentially observable at LISA accuracy. Existing PN–NR waveform studies have found that optimizing the PN parameters can improve agreement, with representative preferred shifts of order 10^{-3} in mass and 10^{-2} in spin for some aligned-spin cases [21]. A fractional mass shift at the 10^{-3} level is already large compared with the accuracy scale relevant for high-SNR LISA sources. A separate analytic matching calculation in harmonic gauge showed that the horizon quasi-local mass agrees with the PN point-particle mass at 1PN order for horizon-penetrating slicings, and that horizon-avoiding harmonic slicings produce a 1PN quasi-local mass shift [25]. At this level, the hybridization error includes PN truncation error, NR numerical error, and the error introduced by aligning two descriptions that may use different coordinates, different time slicings, different asymptotic BMS frames, and different definitions of the same intrinsic parameters. A spacetime parameter map explains which PN masses and spins correspond to the horizon quantities measured in the NR simulation, leaving the waveform fit to determine the asymptotic alignment freedoms.

A parameter-consistent hybrid waveform should be derived from a spacetime matching problem. The PN near-zone metric and the NR metric must be related by explicit coordinate transformations, gauge relations, and parameter maps. NR is valid through the strong-field region, whereas the PN metric is accurate only in the near zone away from the horizons and does not resolve the black-hole interior or apparent-horizon geometry. BHPT is the natural strong-field bridge between PN and NR. In the local frame that comoves with the black hole, it represents the neighborhood of each black hole as a perturbed single-hole spacetime with local parameters and external tidal fields. Matching PN to this inner-zone BHPT description relates the PN point-particle parameters to the BHPT background parameters, while matching NR to the BHPT description relates the quasi-local NR parameters to BHPT background parameters. The resulting PN–BHPT–NR matching provides a geometric prescription for identifying masses, spins, residual gauge freedoms, and local frames before constructing the final waveform hybrid.

To construct the PN–BHPT–NR matching, we find the coordinate transformation from the global inertial frame used by PN or NR to the local comoving frame used by the inner-zone black-hole metric. This transformation must preserve the chosen gauge through the strong-field region, so that the transformed inner-zone metric can be compared consistently with PN or NR data in the region where the descriptions overlap. In the generalized-harmonic formulation, this requirement becomes a wave-map equation for the coordinate functions, with a gauge source H^a specifying the target gauge [9]. This gauge-preserving coordinate transformation identifies the local Kerr–Schild mass and frame associated with the selected black hole in the NR spacetime, so that these quantities can be compared with the corresponding parameters obtained by PN–BHPT matching. The present paper constructs this NR–BHPT side of the parameter map; the PN–BHPT side is supplied by matched-asymptotic PN calculations of tidally perturbed black holes.

5.2 PN–NR matching and BHPT as a strong-field bridge

A natural first-principles strategy for PN–NR parameter matching would be to construct a spacetime metric in a PN frame, impose a gauge and slicing condition analogous to the NR one, compute the apparent horizons in that spacetime, and compare the resulting quasi-local masses and spins with the values measured in NR. Its obstruction is that the PN metric is a near-zone expansion that is valid far from each black hole, $r_A \gg m_A$, so the apparent-horizon region must be supplied by an inner-zone description.

The PN side of this bridge has already been established by matched-asymptotic calculations. Taylor and Poisson matched a tidally perturbed nonrotating black-hole metric to a PN external spacetime and showed that the black hole is represented in the PN metric by a monopole mass, while the matching determines the coordinate transformation between the barycentric PN frame and the local black-hole frame [26]. Later extensions determined the PN tidal moments at the first post-Newtonian order [27]. Together with the 3PN effacement structure of compact-binary dynamics [7], these results fix the PN–BHPT identification of the nonspinning black-hole mass parameter to the order needed for the present PN–BHPT–NR parameter map. The remaining task addressed here is the NR–BHPT strong-field matching: identifying the local BHPT/Kerr–Schild mass and coordinate transformation selected by the NR spacetime.

BHPT supplies the inner-zone strong-field metric, as shown in Fig. 5.1. Near black hole A, the binary spacetime can be written as

$$g_{ab}^{\mathrm{IZ}} = g_{ab}^{\mathrm{BH}}(\lambda_{\mathrm{BHPT}}) + h_{ab}^{\mathrm{tidal}}, \tag{5.1}$$

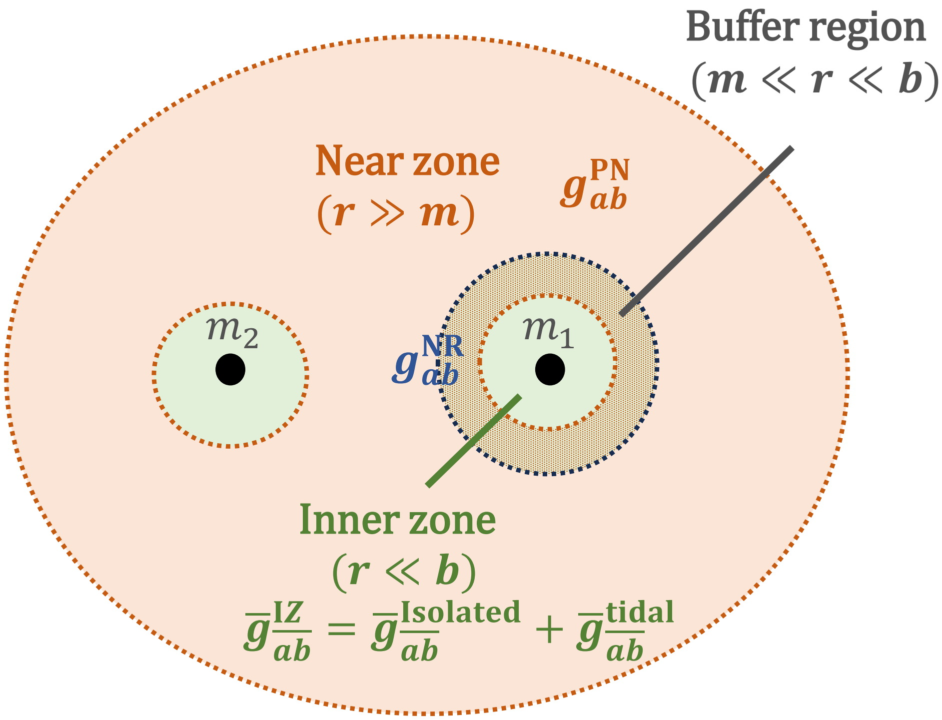

Figure 5.1: Schematic matching regions for a binary black-hole spacetime. PN theory describes the weak-field near zone and supplies long inspiral information; NR describes the nonlinear binary spacetime, including the strong-field neighborhoods of the horizons; BHPT describes the local inner zone of each black hole as a perturbed KS background. The present construction solves the NR–BHPT strong-field matching problem in one inner zone, providing the NR-side component of the PN–BHPT–NR parameter map.

where g_{ab}^{BH} is an isolated black-hole background with local parameters λ_{BHPT}, and h_{ab}^{tidal} is generated by the companion. This description is valid for radii small compared with the binary separation, $r_A \ll b$. The PN near-zone metric and the inner-zone BHPT metric overlap in the buffer region

$$m_A \ll r_A \ll b, \tag{5.2}$$

where both can be expanded and matched. In the same local region, the NR metric is also available, up to numerical and boundary errors. The BHPT description therefore supplies the common local language

$$\lambda_{\mathrm{PN}} \longleftrightarrow \lambda_{\mathrm{BHPT}} \longleftrightarrow \lambda_{\mathrm{NR}}, \tag{5.3}$$

through which PN point-particle parameters and NR quasi-local horizon parameters can be related.

To connect this bridge, the coordinate transformation between the inertial binary frame and the local comoving black-hole frame must be fixed. In the generalized-harmonic formulation this transformation is determined by the gauge condition. If the global coordinates are treated as scalar fields on the local comoving spacetime, they satisfy a wave-map equation of the form

$$\Box x^a = H^a, \tag{5.4}$$

where H^a is the gauge source of the target PN or NR coordinate system. The role of this equation is to extend the matching from the buffer region into the strong field while preserving the chosen gauge. In the NR problem studied here, H^a is supplied by the damped-harmonic [28, 29] NR data on the inertial grid [30], and must be evaluated at the points selected by the current coordinate map.

5.3 Coordinate transformations and conventions

The full coordinate transformation is built in three stages: a shift and rotation from inertial NR coordinates to a hole-centered corotating frame, a finite-dimensional affine pre-transformation that captures the leading boost and dilation freedoms, and a residual gauge-preserving coordinate transformation solved using the gauge condition. We use four coordinate systems. Inertial NR coordinates are denoted by

$$x^a_{\rm inert} = (x^0_{\rm inert}, x^i_{\rm inert}). \tag{5.5}$$

A shifted corotating BH-centered coordinate system is denoted by

$$x^a_{\rm corot} = (x^0_{\rm corot}, x^i_{\rm corot}), \tag{5.6}$$

with

$$x^0_{\rm corot} = x^0_{\rm inert}, \tag{5.7}$$

$$x^i_{\rm corot} = R^i{}_j(x^0_{\rm inert})\,[x^j_{\rm inert} - C^j(x^0_{\rm inert})]. \tag{5.8}$$

Here $C^i(x^0_{\rm inert})$ is the BH center in the inertial simulation frame and $R^i{}_j$ rotates inertial spatial vectors into the corotating frame.

The next coordinate transformation is a low-dimensional affine pre-transformation from $x^a_{\rm corot}$ to an optimized comoving coordinate frame. We denote its output by $x^a_{\rm comov}$:

$$x^a_{\rm comov} = \Lambda^a{}_b\, x^b_{\rm corot}. \tag{5.9}$$

The final residual coordinate transformation used to pull back the NR data is represented on a spherical-shell domain with Kerr–Schild-like coordinates

$$x^a_{\mathrm{KS}} = (x^0_{\mathrm{KS}}, x^i_{\mathrm{KS}}), \qquad r = |x_{\mathrm{KS}}|, \qquad n^i = x^i_{\mathrm{KS}}/r, \tag{5.10}$$

and is written

$$x^a_{\mathrm{comov}}(x_{\mathrm{KS}}) = x^a_{\mathrm{KS}} + \xi^a(x_{\mathrm{KS}}). \tag{5.11}$$

The residual field ξ^a is the primary unknown to be solved by the gauge condition.

Affine pre-transformation

The affine pre-transformation used in this work maps selected-hole-centered corotating coordinates to the comoving coordinates used before the residual solve:

$$x^a_{\mathrm{comov}} = \Lambda^a{}_b\, x^b_{\mathrm{corot}}. \tag{5.12}$$

The matrix $\Lambda^a{}_b$ is optimized at each iteration by minimizing the mismatch between the final transformed NR metric and the Kerr–Schild target on the outer matching boundary. The parametrization is chosen to cover the relevant affine freedoms. We write

$$\Lambda^0{}_0 = \lambda_{\mathrm{time}}, \tag{5.13}$$

$$\Lambda^0{}_i = \beta_i, \tag{5.14}$$

$$\Lambda^i{}_0 = 0, \tag{5.15}$$

$$\Lambda^i{}_j = \lambda_{\mathrm{space}}\, \delta^i{}_j + \sigma^i{}_j, \qquad \sigma_{ij} = \sigma_{ji}, \qquad \sigma^i{}_i = 0, \tag{5.16}$$

with λ_{time} and λ_{space} incorporating the time dilation and space contraction due to the boost and the companion's gravity field, β_i incorporating the boost freedom, and σ_{ij} incorporating the space distortion. No freely optimized antisymmetric spatial rotation is included. A purely spatial rotation of the target Schwarzschild Kerr–Schild coordinates is a coordinate convention rather than a physical matching degree of freedom, and allowing an arbitrary rotation gives the optimizer a poorly constrained direction. The space-time affine block is set to zero, $\Lambda^i{}_0 = 0$. This does not remove the physical freedom, instead, that freedom is carried by the separate field $\partial_0\xi^a$, described below. Allowing both a free $\Lambda^i{}_0$ and a free $\partial_0\xi^i$ creates a degeneracy.

5.4 Elliptic equation for the residual map

The core matching equation is the generalized-harmonic coordinate condition Eq. (5.4) written in the target Kerr–Schild frame:

$$\Box_{\mathrm{KS}} x^a_{\mathrm{comov}} = H^a_{\mathrm{comov}} + O\!\left(\frac{m_2 R^2_{\mathrm{out}}}{b^3}, \xi^0 \partial_0 H^a_{\mathrm{comov}}\right). \tag{5.17}$$

Here H^a_{comov} is the gauge source of the BBH data after the inertial-to-corotating and pre-transformation maps have been applied. Explicitly,

$$\begin{aligned} H^a_{\text{comov}} &= \Box_{\text{comov}} x^a_{\text{comov}} \\ &= \frac{\partial x^a_{\text{comov}}}{\partial x^b_{\text{inert}}} H^b_{\text{inert}} + g^{bc}_{\text{inert}} \partial_b \partial_c x^a_{\text{comov}}, \end{aligned} \tag{5.18}$$

with all quantities evaluated on the NR solution and then expressed in the comoving coordinates. Equation (5.17) is the statement, up to the displayed tidal and quasi-stationary errors, that the coordinate functions $x^a_{\text{comov}}(x_{\text{KS}})$ should have the same wave-gauge source, but expressed on the Kerr–Schild-like coordinates.

For a nonspinning black hole of mass m, the Schwarzschild Kerr–Schild metric is

$$g^{\text{KS}}_{ab} = \eta_{ab} + \frac{2m}{r} \ell_a \ell_b, \tag{5.19}$$

$$\ell_a = (1, n_i), \qquad n_i = \delta_{ij} x^j_{\text{KS}} / r. \tag{5.20}$$

The determinant is $\det g^{\text{KS}} = -1$. For a quasi-stationary scalar $f(x_{\text{KS}})$, the Kerr–Schild wave operator reduces to

$$\Box_{\text{KS}} f = \left(\delta^{ij} - \frac{2m}{r} n^i n^j \right) \partial_i \partial_j f - \frac{2m}{r^2} n^i \partial_i f + \frac{2m}{r^2} \partial_0 f. \tag{5.21}$$

The last term is the stationary contribution from the g^{i0}_{KS} cross term. It is not a second time derivative. It is therefore retained even when the time dependence of the fields themselves is neglected.

It is useful to define the spatial elliptic operator

$$\mathcal{L}^{(m)}_{\text{KS}} f \equiv \left(\delta^{ij} - \frac{2m}{r} n^i n^j \right) \partial_i \partial_j f - \frac{2m}{r^2} n^i \partial_i f. \tag{5.22}$$

In spherical form,

$$\mathcal{L}^{(m)}_{\text{KS}} f = \left(1 - \frac{2m}{r} \right) \partial_r^2 f + \frac{2}{r} \left(1 - \frac{m}{r} \right) \partial_r f + \frac{1}{r^2} \Delta_{\mathbb{S}^2} f. \tag{5.23}$$

The coefficient of $\partial_r^2 f$ vanishes at $r = 2m$.

Substituting $x^a_{\text{comov}} = x^a_{\text{KS}} + \xi^a$ into Eq. (5.17) gives

$$\mathcal{L}^{(m)}_{\text{KS}} \xi^a = S^a + \mathcal{O}\left(\frac{m_2 R^2_{\text{out}}}{b^3}, \xi^0 \partial_0 H^a_{\text{comov}} \right), \tag{5.24}$$

and

$$\mathcal{L}^{(m)}_{\rm KS}\partial_0\xi^a = O\left(\frac{m_2 R^2_{\rm out}}{b^3}, \xi^0\partial_0 H^a_{\rm comov}\right), \tag{5.25}$$

where

$$S^a \equiv H^a_{\rm comov} - \Box_{\rm KS} x^a_{\rm KS} - \frac{2m}{r^2}\partial_0\xi^a. \tag{5.26}$$

With the convention above,

$$\Box_{\rm KS} x^0_{\rm KS} = \frac{2m}{r^2}, \tag{5.27}$$

$$\Box_{\rm KS} x^i_{\rm KS} = -\frac{2m}{r^2} n^i. \tag{5.28}$$

Equations (5.24)–(5.28) are the equations that determine the residual coordinate transformation.

The present operator is the single-hole Kerr–Schild operator. Therefore it omits the companion's tidal correction to the principal part. On a shell with outer radius $R_{\rm out}$, the neglected companion-induced metric correction scales as $m_2 R^2_{\rm out}/b^3$. For the numerical test below, with $m_2 = 0.5M$, $R_{\rm out} = 3M$, and $b = 80M$, this estimate gives $m_2 R^2_{\rm out}/b^3 \simeq 8.8 \times 10^{-6}$. The quasi-stationary treatment also neglects changes of the gauge source across the time shift, of size $\xi^0\partial_0 H^a_{\rm comov}$. For a well-separated companion, the leading physical omission is quadrupolar and should primarily enter the $\ell = 2$ sector. The discrepancy in the mass parameter only enters the $\ell = 0$ mode and therefore can be seprated from the neglected tidal effects.

5.5 Horizon-regular inner boundary condition

The inner boundary condition is fixed by regularity at the Kerr–Schild horizon. The spatial operator in Eq. (5.24) is elliptic for $r > 2m$, but its radial principal coefficient vanishes at $r = 2m$, as shown explicitly in Eq. (5.23). At the horizon the equation therefore becomes degenerate: it no longer determines $\partial_r^2\xi^a$ as an independent regular quantity. Equivalently, the local solution contains a regular branch and a singular branch, and the outer boundary data alone do not select which branch is realized. The inner boundary condition is the condition that selects the branch for which the coordinate functions extend smoothly through the future horizon. The resulting coordinates are horizon penetrating in the same sense as Kerr–Schild coordinates.

In the numerical solve the excision boundary is placed slightly outside the horizon,

$$r_{\rm in} = 2m + \epsilon, \qquad \epsilon = 10^{-6}. \tag{5.29}$$

For each component of ξ^a, assume the horizon-regular branch has a Taylor expansion

$$\xi^a = \xi^a_0 + (r - 2m)\xi^a_1 + O[(r - 2m)^2]. \tag{5.30}$$

Since the coefficient of $\partial_r^2 \xi^a$ in Eq. (5.23) vanishes at $r = 2m$, the leading horizon equation gives

$$\frac{1}{2m}\xi^a_1 + \frac{1}{(2m)^2}\Delta_{\mathbb{S}^2}\xi^a_0 = S^a\big|_{r=2m}. \tag{5.31}$$

Equivalently, the regular branch satisfies the Robin condition

$$\begin{aligned}\left[\partial_r \xi^a + \frac{1}{2m}\Delta_{\mathbb{S}^2}\xi^a\right]_{r=r_{\rm in}} &= 2m\, S^a\big|_{r=r_{\rm in}} \\ &\quad + O\left(\frac{m_2 R^2_{\rm out}}{b^3}, \epsilon, \xi^0 \partial_0 H^a_{\rm comov}\right).\end{aligned} \tag{5.32}$$

The $O(\epsilon)$ term enters because the condition is imposed at $r_{\rm in} = 2m + \epsilon$ instead of exactly at the degenerate surface. This condition removes the singular horizon branch and selects the horizon-penetrating coordinate solution. In the isolated Kerr–Schild limit it reduces to the single-hole regularity relation. In the binary problem the source S^a contains the transformed NR gauge source $H^a_{\rm comov}$, so the companion and the numerical gauge enter the regularity condition through the same gauge equation that defines the bulk transformation.

The $\partial_0 \xi^a$ field obeys the corresponding regularity condition obtained by applying the same horizon-branch selection. With the time dependence of the gauge source neglected at the order of the quasi-stationary solve, this gives

$$\begin{aligned}&\left[\partial_r \partial_0 \xi^a + \frac{1}{2m}\Delta_{\mathbb{S}^2}\partial_0\xi^a\right]_{r=r_{\rm in}} \\ &\qquad = O\left(\frac{m_2 R^2_{\rm out}}{b^3}, \epsilon, \xi^0 \partial_0 H^a_{\rm comov}\right).\end{aligned} \tag{5.33}$$

The remaining freedom in ξ^a and $\partial_0 \xi^a$ is fixed by the outer boundary data.

5.6 Outer boundary surface and angular relabeling

Identify the outer surface

The outer boundary is tied to a geometric surface in the NR spacetime. For a chosen KS outer radius $R_{\rm out}$ and mass parameter m, we identify the corresponding physical two-surface by the scalar condition

$$K_{\rm NR}(x^i_{\rm surf}) = K_{\rm KS}(R_{\rm out}; m) = \frac{48m^2}{R^6_{\rm out}}, \tag{5.34}$$

where $K_{\rm NR}$ is the Kretschmann scalar of the NR metric after the pre-transformation to the local comoving frame. The surface is represented as a star-shaped surface around the selected hole,

$$x^i_{\rm surf}(n) = C^i + \rho(n)n^i, \qquad n \in \mathbb{S}^2. \tag{5.35}$$

Angular gauge

Equation (5.34) fixes the physical two-surface. It does not fix the angular correspondence between a Kerr–Schild direction $n^i = x^i_{\rm KS}/R_{\rm out}$ and a point on that surface. This residual angular-label freedom is irrelevant for an exactly spherical isolated hole, but it affects the boundary data for the volume solve when the solution is not spherically symmetric.

We fix this freedom with relabeling of angular coordinates on the surface generated by a scalar function $\alpha(n)$ on the unit sphere. The general tangent displacement of the angular label is

$$\delta n^i = \nabla^i_{\mathbb{S}^2}\alpha = \left(\delta^{ij} - n^i n^j\right)\partial_j \alpha, \tag{5.36}$$

$$n^i_{\rm rel} = \frac{n^i + \delta n^i}{|n + \delta n|}, \tag{5.37}$$

so that $n_i \delta n^i \equiv 0$. The relabeling acts before the scalar surface is evaluated:

$$x^i_{\rm surf}(n) \longrightarrow x^i_{\rm surf}(n_{\rm rel}) = C^i + \rho(n_{\rm rel})n^i_{\rm rel}. \tag{5.38}$$

Thus the operation changes the correspondence between Kerr–Schild angular directions and points on the same K = const surface and does not apply an additional physical displacement to the surface.

The scalar α is fixed by requiring the labeled surface to have no area dipole in the pulled-back local geometry. This condition follows from the target geometry that a K = const surface of the non-spinning KS metric is spherically symmetric, so its area dipole vanishes. For the NR surface, define the induced two-metric on the surface

$$h_{AB} = \gamma_{ij}(x_{\rm surf})\partial_A x^i_{\rm surf}\,\partial_B x^j_{\rm surf}, \tag{5.39}$$

where γ_{ij} is the transformed spatial metric on the current matching slice. The area dipole and its linear response to an electric-parity relabeling are

$$M_i = \int_{\mathbb{S}^2} n_i \sqrt{\det h_{AB}}\, \mathrm{d}\Omega, \tag{5.40}$$

$$C_{ij} = \int_{\mathbb{S}^2} \sqrt{\det h_{AB}}\left(\delta_{ij} - n_i n_j\right) \mathrm{d}\Omega. \tag{5.41}$$

We use only the $\ell = 1$ part of the relabeling,

$$\delta\alpha(n) = A_i n^i, \tag{5.42}$$

because higher angular relabelings are degenerate with the physical tidal deformation of the matching surface that we are neglecting here. For this $\ell = 1$ correction, $\partial_i \delta\alpha = A_i$, and the linearized zero-dipole condition gives

$$C_{ij}\, A_j = M_i. \tag{5.43}$$

The scalar relabeling is updated incrementally,

$$\alpha_{\rm new}(n) = \alpha_{\rm old}(n) + \lambda\, \delta\alpha(n), \qquad 0 < \lambda \le 1, \tag{5.44}$$

so that the already-fixed dipole gauge is retained while only the residual area dipole is corrected.

Outer boundary condition for ξ^a

After the surface and its angular labeling have been fixed, the spatial outer Dirichlet data for the coordinate solve are

$$\xi^i\big|_{R_{\rm out}} = x^i_{\rm surf,comov}(n_{\rm rel}) - R_{\rm out} n^i, \tag{5.45}$$

where $x^i_{\rm surf,comov}$ denotes the relabeled scalar surface expressed in the local comoving frame. The time component of the coordinate value is free up to a constant shift; we fix this freedom by setting it to zero,

$$\xi^0\big|_{R_{\rm out}} = 0. \tag{5.46}$$

Outer boundary condition for $\partial_0 \xi^a$

The outer boundary data for $\partial_0 \xi^a$ are chosen so that the transformed time components of the metric match the non-spinning KS target on the same labeled surface. Define

$$E^a{}_i \equiv \partial_i x^a_{\rm comov} = \delta^a_i + \partial_i \xi^a, \tag{5.47}$$

and let $g^{\rm comov}_{ab}$ be the metric after applying the pre-transformation and the spatial residual map, but before applying the current $\partial_0 \xi^a$ correction. The target time vector

$$u^a \equiv \partial_0 x^a_{\rm comov}$$

is determined algebraically from

$$g^{\rm comov}_{ab} u^a E^b{}_i = g^{\rm KS}_{0i} = \frac{2m}{r} n_i, \tag{5.48}$$

$$g^{\rm comov}_{ab} u^a u^b = g^{\rm KS}_{00} = -1 + \frac{2m}{r}. \tag{5.49}$$

Equivalently, with

$$\gamma_{ij} = g^{\mathrm{comov}}_{ab} E^a{}_i E^b{}_j, \tag{5.50}$$

and with N^a the future-directed unit normal satisfying

$$g^{\mathrm{comov}}_{ab} N^a E^b{}_i = 0, \qquad g^{\mathrm{comov}}_{ab} N^a N^b = -1, \tag{5.51}$$

the future-directed solution is

$$u^a = E^a{}_i \gamma^{ij} g^{\mathrm{KS}}_{0j} + \sqrt{\gamma^{ij} g^{\mathrm{KS}}_{0i} g^{\mathrm{KS}}_{0j} - g^{\mathrm{KS}}_{00}}\, N^a. \tag{5.52}$$

The Dirichlet data for $\partial_0 \xi^a$ are therefore

$$\partial_0 \xi^a \big|_{R_{\mathrm{out}}} = u^a - \delta^a_0. \tag{5.53}$$

5.7 Mass update from monopolar residuals

After transforming the NR metric into the local comoving KS frame using the solved ξ^a, the monopolar mode of the residual is dominated by a mass offset. For non-spinning Kerr–Schild,

$$g^{\mathrm{KS}}_{00} = -1 + \frac{2m}{r}, \tag{5.54}$$

$$g^{\mathrm{KS}}_{rr} = 1 + \frac{2m}{r}. \tag{5.55}$$

Therefore the $\ell = 0$ residuals are fit separately to

$$\langle \Delta g_{00} \rangle (r) = c_{00} + \frac{2\delta m_{00}}{r}, \tag{5.56}$$

$$\langle \Delta g_{rr} \rangle (r) = c_{rr} + \frac{2\delta m_{rr}}{r}. \tag{5.57}$$

The constants c_{00} and c_{rr} are included because residual gauge and interpolation offsets can generate an approximately radius-independent monopole. The fitted mass offsets are therefore not forced to absorb every constant residual.

At each iteration, we update the KS mass parameter that appears in the target metric (5.19), the elliptic operator (5.22)–(5.23), the source term (5.26), the scalar outer surface (5.34), the horizon-regular inner conditions (5.32)–(5.33), and the time-component outer matching conditions (5.48)–(5.49). The update is defined by the monopole fit to the g_{00} residual,

$$m^{(n)} = m^{(n-1)} + \delta m^{(n-1)}_{00}, \tag{5.58}$$

where $\delta m_{00}^{(n-1)}$ is obtained from the $n-1$th iteration of Eq. (5.56). We do not use δm_{rr} from Eq. (5.57) to update the mass because the radial metric component is more strongly contaminated by the companion tidal field, whose even-parity contribution contains terms growing as r^2 across the matching shell. On a finite radial interval this tidal structure is not cleanly separated from the monopole model in Eq. (5.57), and it can make the inferred δm_{rr} very noisy. We therefore use g_{rr} only as a diagnostic of the monopole residual, while the mass used in the next coordinate solve is updated with δm_{00}.

5.8 Iterative matching procedure

The pre-transformation $\Lambda^a{}_b$, the residual coordinate transformation ξ^a, the local mass parameter m, the angular relabeling of the outer surface α, and the transformed gauge source H_a in the KS coordinates are determined by a fixed-point iteration. At iteration n, the current values of m, $\Lambda^a{}_b$, and the angular relabeling α define the local comoving frame and the $K = \text{const}$ outer surface. The NR gauge source is then transformed according to Eq. (5.18) and evaluated on the current approximation to the coordinate transformation.

The residual coordinate functions ξ^a are first obtained from Eq. (5.24), with source (5.26), the horizon-regular inner condition (5.32), and the outer data (5.45)–(5.46). This step fixes the spatial embedding of the KS shell into the local comoving NR geometry, up to the tidal and quasi-stationary errors.

The time-derivative part of the same coordinate map, $\partial_0\xi^a$, is then obtained from Eq. (5.25), with the regular inner condition (5.33). Its outer boundary data are computed from the metric after applying the pre-transformation and the spatial residual map, but before applying the current $\partial_0\xi^a$ correction. The algebraic matching conditions (5.48)–(5.49) determine the target time vector u^a, and Eq. (5.53) gives the corresponding Dirichlet data.

After ξ^a and $\partial_0\xi^a$ have been solved, the NR metric is transformed to the KS coordinate and compared with the target non-spinning KS metric. The area dipole of the pulled-back $K = \text{const}$ surface updates the angular relabeling through Eqs. (5.40)–(5.44). The affine map $\Lambda^a{}_b$ is updated by minimizing the outer-boundary metric mismatch within the parametrization (5.13)–(5.16). The mass parameter is updated with Eq. (5.58). These updated quantities define the next evaluation of H^a_{comov}, the next outer surface, and the next residual transformation solve.

The iteration is stopped when the low-order quantities that determine the map have stabilized, including the affine map, the area-gauge relabeling, the mass update, and the volume fields ξ^a and $\partial_0\xi^a$.

5.9 Numerical setup and results

Numerical setup

We test the construction on an equal-mass, nonspinning, quasi-circular NR binary evolved with SpECTRE [31, 32, 33] at coordinate separation $b = 80M$. The matching is performed on the slice $x^0 = 500M$, after the initial junk radiation has left the near-hole region and the gauge has reached a slowly varying state. Figure 5.2 shows the constant-Kretschmann surface used as the outer matching surface, plotted in the NR inertial coordinates. This surface fixes the physical two-surface on which the local KS description is matched to the binary spacetime.

The same slice provides a diagnostic for the quasi-stationary approximation used in the elliptic reduction of the gauge equation. The neglected source term in Eq. (5.24) is controlled by $\xi^0\partial_0 H^a_{\text{comov}}$. Figure 5.3 shows $\partial_0 H^a_{\text{corot}}$, evaluated from the NR gauge source in the corotating frame. Combining this with the computed magnitude of ξ^0 gives $\xi^0\partial_0 H^a_{\text{corot}} \sim 10^{-6}$ throughout the matching domain at $x^0 = 500M$. This is about an order of magnitude below the companion-tidal estimate $m_2 R^2_{\text{out}}/b^3 \simeq 8.8 \times 10^{-6}$ for the present $b = 80M$, $R_{\text{out}} = 3M$ solve, supporting the error hierarchy assumed in Eq. (5.24).

Convergence of the iterative matching

In this test, the first stage of the iteration is performed at fixed KS mass. Through iteration 012 we set $m = 0.5M$, where M is the total binary mass. This fixed-mass stage allows the affine map, the residual coordinate transformation and the time-derivative part of the coordinate map, and the angular relabeling to settle before the monopole mass calibration is fed back into the operator and boundary conditions. Starting with iteration 013, the mass update is turned on: the fitted δm_{00} from the $\ell = 0$ residual of g_{00} is added to the mass used in the Kerr–Schild target metric, the operator $\mathcal{L}^{(m)}_{\text{KS}}$, the horizon radius, and the boundary conditions.

Figure 5.4 shows the convergence of the matching iteration on the $y = z = 0$ line. The initial iterations remove the large mismatch produced by the starting map. By iteration 012 the metric and scalar residuals have stabilized at fixed $m = 0.5M$, but the residuals still contain a monopolar mass offset. After the mass feedback is activated at iteration 013, the Kretschmann residual is reduced to the finite-separation residual scale shown in Fig. 5.4 and the subsequent curves nearly overlap. The

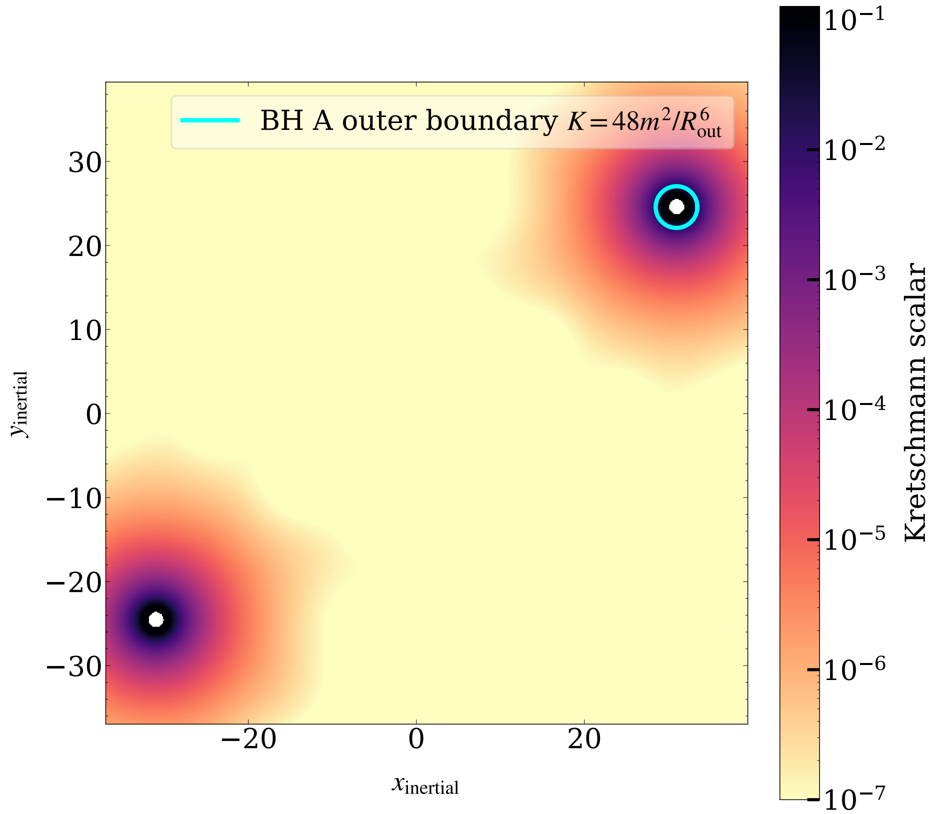

Figure 5.2: Constant-Kretschmann outer matching surface for the $b = 80M$ equal-mass, nonspinning SpECTRE test, shown in NR inertial coordinates.

remaining residuals are smooth across the matching domain and are dominated by the nonmonopolar structure expected from the companion field and residual finite-separation errors.

Figure 5.5 shows the residual multipoles before and after the monopole mass update is enabled. In Iteration 012 the KS mass is still fixed at its initial value $m = 0.5M$. The largest low-order contribution is the $\ell = 0$ residual, which is the expected signature of a small mismatch between the mass parameter used in the KS target and the mass selected by the transformed NR geometry. The $\ell = 2$ contribution in Δg_{rr} has the radial behavior and magnitude expected for the leading $m_2 r^2/b^3$ quadrupolar tidal field of the companion. It is therefore not used to define the mass update.

Starting at Iteration 013, the mass appearing in the operator and boundary conditions is updated from the $\ell = 0$ residual of Δg_{00}. By Iteration 024 the monopole residual is greatly reduced, as shown in Fig. 5.6, while the remaining dominant modes are quadrupolar tidal modes. This behavior is consistent with the purpose of the local matching: the algorithm removes monopole mass error and low-order coordinate

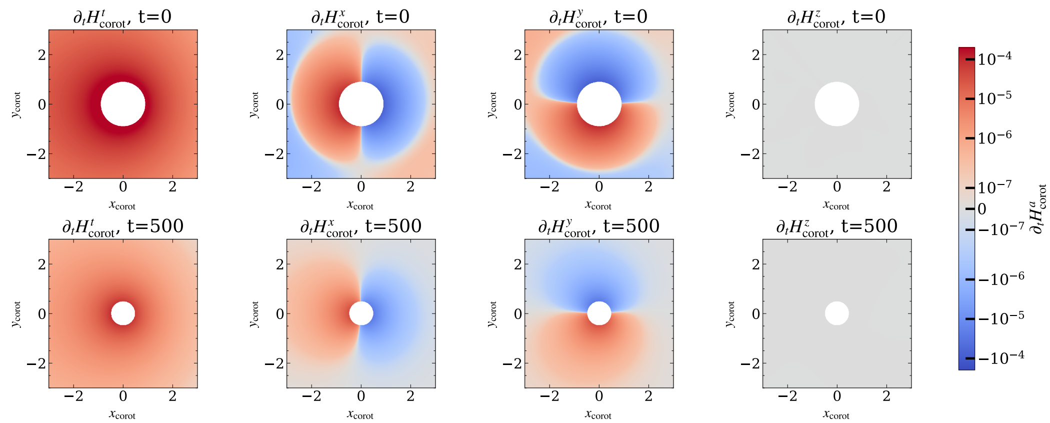

Figure 5.3: Time derivative of the NR gauge source on the $x^0 = 500M$ slice, evaluated in the corotating frame. Together with the computed ξ^0, this diagnostic shows that the neglected term $\xi^0 \partial_0 H^a_{\rm comov}$ is of order 10^{-6} in the matching domain.

artifacts, while leaving the companion tidal field as the leading physical difference between the transformed NR metric and the single-hole KS background.

Mass matching

The mass calibration gives an independent check that the monopole residual is separated from the tidal content. Figure 5.6 shows the mass correction δm_{00} obtained from the $\ell = 0$ residual of g_{00}. During iterations 0–12, the KS mass is held fixed at $m = 0.5M$, so δm_{00} is only a diagnostic. It decreases rapidly during the first few iterations and then reaches a nearly constant offset, indicating that the remaining $\ell = 0$ residual is a true mass mismatch in the chosen KS background. Beginning at iteration 13, the update $m^{(n+1)} = m^{(n)} + \delta m^{(n)}_{00}$ is applied to the mass entering $\mathcal{L}^{(m)}_{\rm KS}$, the boundary conditions, and the KS target metric. The fitted correction then converges to the 10^{-6} level. This scale is below the leading missing tidal contribution in the present $b = 80M$ test, showing that the $\ell = 0$ fit from g_{00} is not significantly contaminated by the quadrupolar tidal residual, which appears primarily in the $\ell = 2$ sector.

Figure 5.7 shows the corresponding KS mass used by the matching solve. The mass converges to $m_{\rm KS} \simeq 0.50049M$, which differs from the NR horizon mass $0.5004M$ by a fractional offset $\simeq 2 \times 10^{-4}$. Figure 5.8 shows the final fractional mass correction for equal-mass nonspinning binaries at different separations. The fitted offset grows as the holes are brought closer together, from $|\Delta m|/m \simeq 2 \times 10^{-4}$ at $b = 80M$ to $|\Delta m|/m \simeq 10^{-3}$ at $b = 20M$. This behavior is consistent with a finite-separation effect in the relation between the local KS/BHPT mass parameter and the nominal

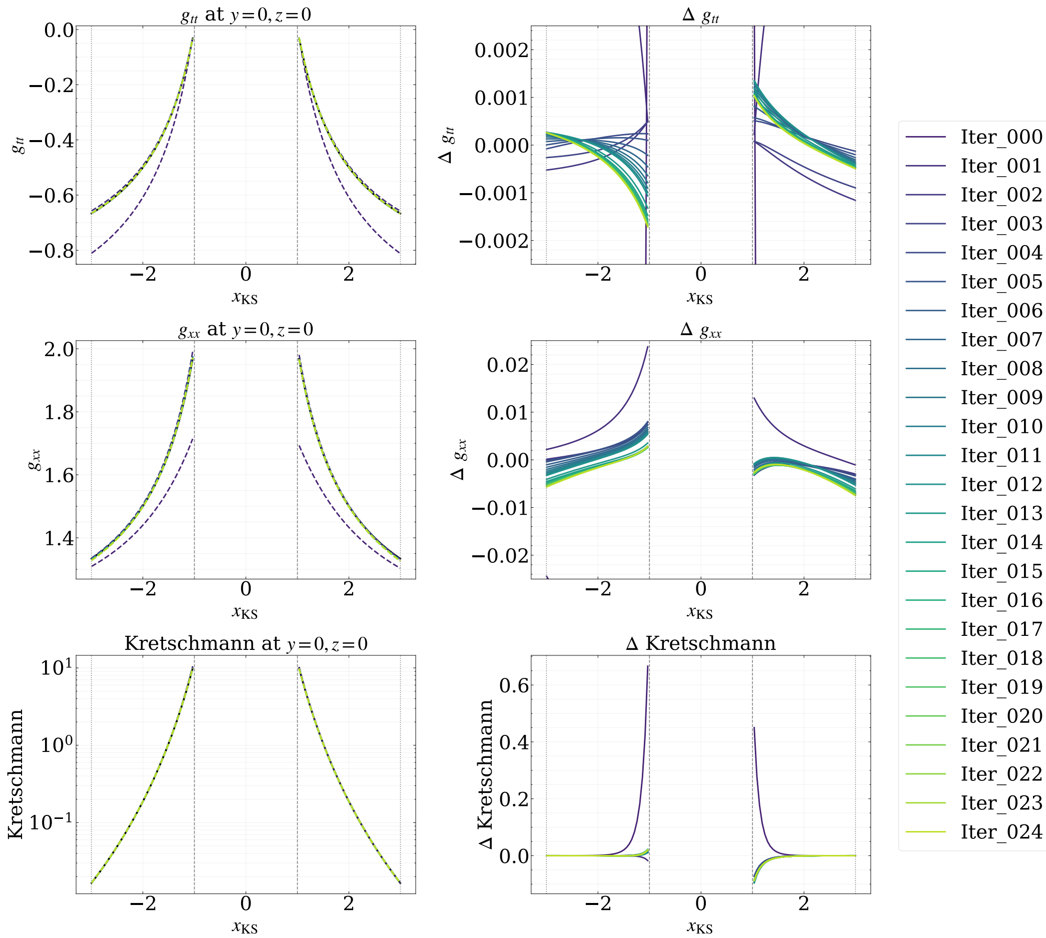

Figure 5.4: Convergence of the local matching iteration on the line $y = z = 0$. The left column shows the pulled-back metric components g_{00}, g_{xx}, and the Kretschmann scalar K, compared with the Schwarzschild Kerr–Schild target. The right column shows the corresponding residuals. The excised region lies between the two inner vertical lines, and the outer matching radius is $R_{\text{out}} = 3M$. The mass is held fixed at $m = 0.5M$ through iteration 012. Beginning with iteration 013, the mass inferred from the $\ell = 0$ residual of g_{00} is fed back into the Kerr–Schild target, the elliptic operator, and the boundary conditions. The post-update curves show that the monopole mass calibration removes the dominant scalar offset while leaving the expected nonmonopolar finite-separation residuals.

NR mass. This offset is larger than the LISA-motivated parameter-accuracy scale considered in this work. The result shows that the local mass entering the strong-field BHPT description is a gauge- and matching-dependent quantity that must be determined consistently with the coordinate transformation and parameter map.

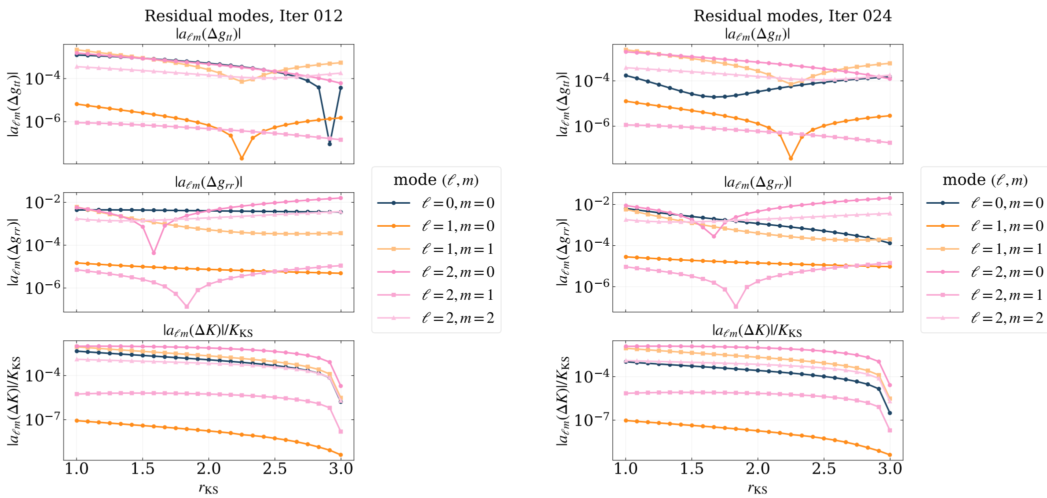

(a) Iteration 012.

(b) Iteration 024.

Figure 5.5: Spherical-harmonic amplitudes of the transformed-metric residuals on coordinate spheres in the local KS frame. The panels show the modes of Δg_{00}, Δg_{rr}, and $\Delta K/K_{\mathrm{KS}}$, where K is the Kretschmann scalar. Up to Iteration 012 the KS mass is held fixed at $m = 0.5M$. The monopole mass update is enabled starting at Iteration 013, and the Iteration 024 residuals show the result after the mass calibration has converged.

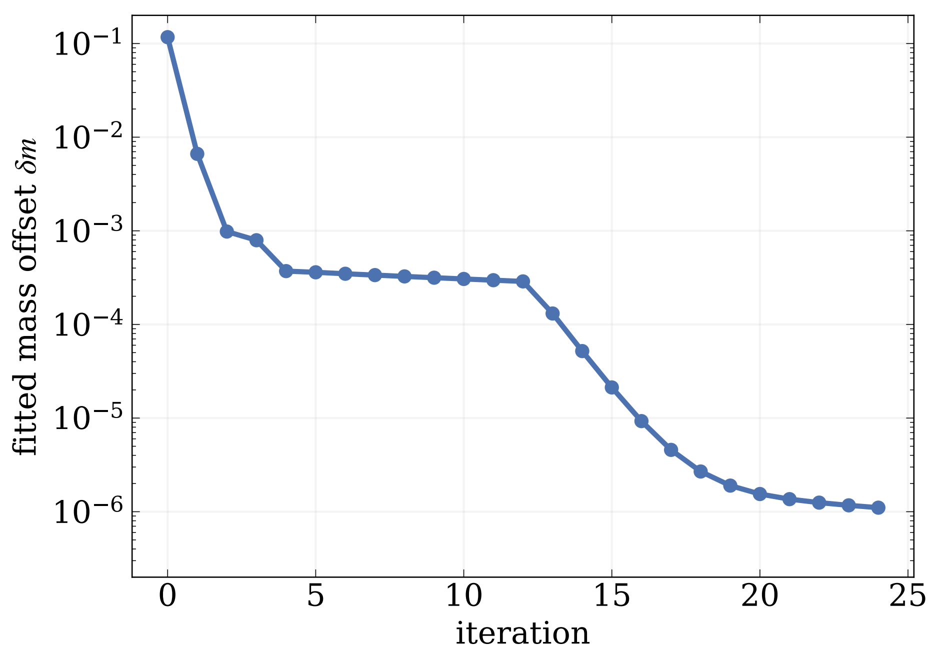

Figure 5.6: Mass correction δm_{00} fitted from the sphere-averaged residual of g_{00}. The KS mass is held fixed through iteration 12, so the early plateau measures the monopole mismatch of the fixed-mass solve. After the mass update is activated at iteration 13, the correction decreases to the 10^{-6} level.

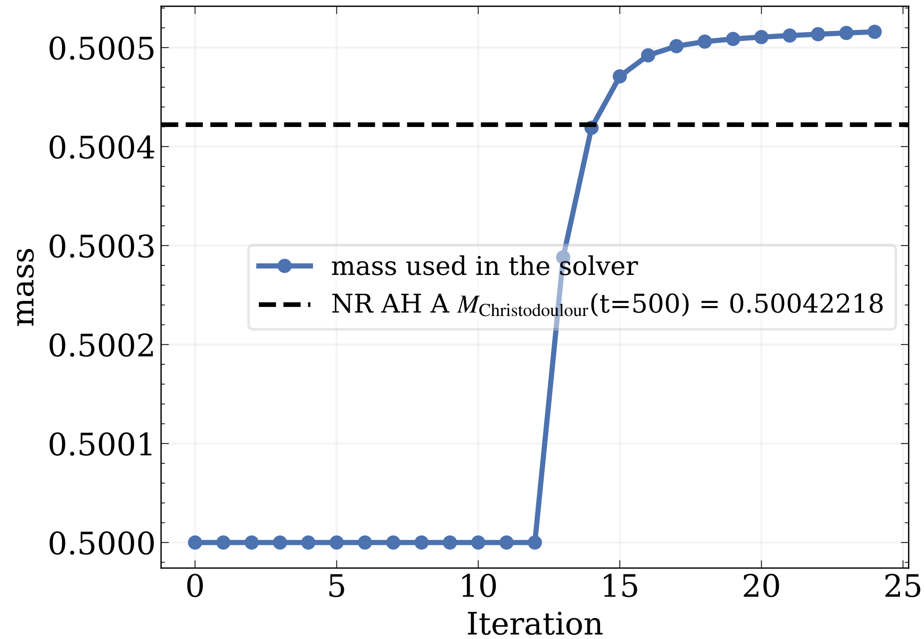

Figure 5.7: KS mass m used in the coordinate operator, boundary conditions, and target metric. The mass is fixed to $0.5M$ through iteration 12. Once the monopole update is activated, the mass converges to $m_{\mathrm{KS}} \simeq 0.50049M$, corresponding to a fractional offset $\simeq 1.8 \times 10^{-4}$.

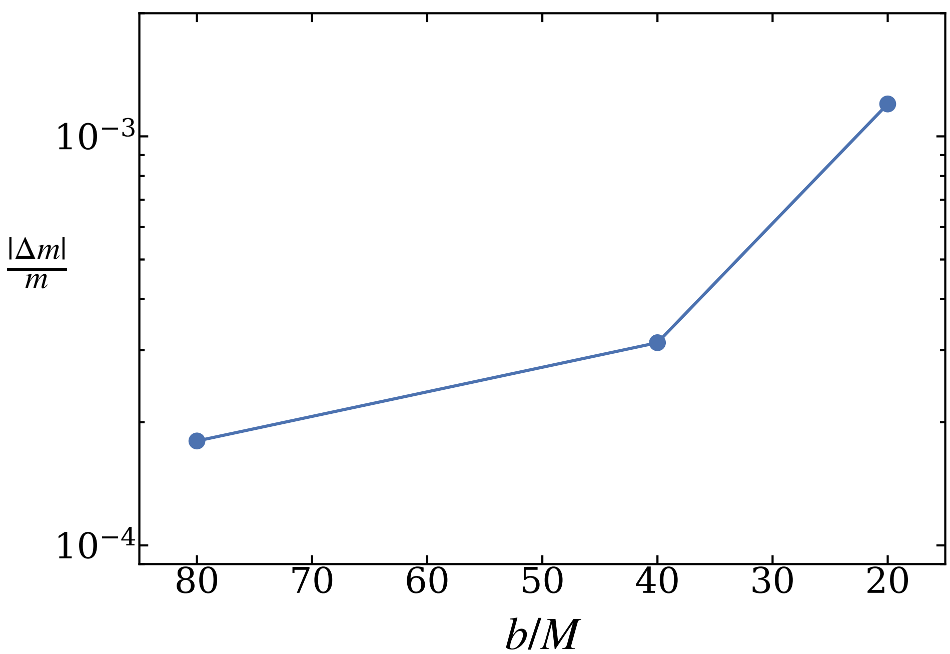

Figure 5.8: Final fractional mass offset $|\Delta m|/m$ obtained from the monopole part of Δg_{00} as a function of binary separation b/M. The offset decreases at larger separation, as expected for a finite-separation correction to the identification between the nominal NR mass and the local KS/BHPT mass parameter.

5.10 Conclusions

We have constructed the NR–BHPT strong-field matching component of a PN–BHPT–NR parameter map. Starting from an NR binary spacetime in inertial damped-harmonic coordinates, the method builds a local comoving Kerr–Schild frame around one black hole by solving the generalized-harmonic coordinate equations with the NR gauge source. The output is a gauge-preserving coordinate transformation and a local KS mass parameter that can be compared with the PN-side mass supplied by matched-asymptotic PN–BHPT calculations.

In the quasi-stationary approximation, the gauge equations reduce to an elliptic system on one time slice. The residual coordinate transformation ξ^a is solved with the single-hole Kerr–Schild operator $\mathcal{L}_{\rm KS}^{(m)}$, the inner boundary condition selects the horizon-regular branch at $r = 2m + \epsilon$, and the outer boundary is tied to a constant-Kretschmann matching surface. The angular relabeling, affine pre-transformation, and mass update are then determined from the area dipole and from metric and curvature residuals.

For the equal-mass, nonspinning SpECTRE test at $b = 80M$, $R_{\rm out} = 3M$, and $x^0 = 500M$, the quasi-stationary source term satisfies $\xi^0 \partial_0 H^a_{\rm comov} \sim 10^{-6}$, about an order of magnitude below the companion-tidal estimate $m_2 R_{\rm out}^2/b^3 \simeq 8.8 \times 10^{-6}$. The fixed-mass iterations leave a clear $\ell = 0$ residual, which identifies a local mass mismatch. Updating the KS mass with the $\ell = 0$ residual of g_{00} drives the inferred correction to the 10^{-6} level and leaves the quadrupolar $\ell = 2$ residuals as the leading difference between the transformed NR metric and the single-hole KS target. The converged value $m_{\rm KS} \simeq 0.50049M$ differs from the NR horizon mass $0.5004M$ by a fractional offset $\simeq 1.8 \times 10^{-4}$. ctional mass correction for equal-mass nonspinning binaries at different separations. The fitted offset grows as the holes are brought closer together, from $|\Delta m|/m \simeq 2 \times 10^{-4}$ at $b = 80M$ to $|\Delta m|/m \simeq 10^{-3}$ at $b = 20M$. This behavior is consistent with a finite-separation effect in the relation between the local KS/BHPT mass parameter and the nominal NR mass. This offset is large enough to be relevant for LISA-accuracy massive-black-hole-binary waveform modeling and illustrates why the local strong-field mass should be determined through a coordinate- and gauge-consistent matching calculation.

The present calculation has controlled limitations. It uses a nonspinning single-hole KS target, a single time slice, a quasi-stationary elliptic reduction, and a single-hole principal operator that omits the companion's tidal correction. The observed residual hierarchy is consistent with these approximations: the monopole residual is removed by the mass update, while the remaining dominant residuals occur in the quadrupolar sector expected from the omitted companion field. This behavior supports the use of the construction as the NR-side strong-field input to a complete PN–BHPT–NR parameter map.

Future directions

The immediate next step is to close the full PN–BHPT–NR loop. On the PN side, matched-asymptotic calculations identify the nonspinning black-hole monopole and its local coordinate transformation in the PN overlap region [26, 27]; on the NR side, the present work determines the local KS/BHPT mass and coordinate transformation selected by the NR spacetime. Combining these two pieces gives a direct PN–NR parameter map through BHPT. This map should be tested in waveform hybridization by fixing the intrinsic PN parameters from the strong-field matching and using the asymptotic waveform fit only for time, phase, rotation, boost, and BMS-frame alignment. Such a test requires long, accurate NR simulations with early-inspiral data and PN models whose eccentricity matches the residual eccentricity of the NR run.

The second direction is to generalize the strong-field matching from a nonspinning KS target to generic binary configurations. For spinning binaries, the local target should be a perturbed Kerr geometry in horizon-penetrating coordinates, and the parameter map must determine the local mass, spin magnitude, spin direction, tetrad or frame convention, and spin-dependent gauge terms. For eccentric and precessing binaries, the coordinate transformation must include time-dependent orbital kinematics and a rotating local frame while maintaining a clean separation between physical precession, gauge rotation, and angular relabeling of the matching surface. These extensions would make the method applicable to generic NR catalogs and to the massive-black-hole binaries expected for LISA.

The third direction is to use the same local frames for merger-ringdown and extreme-mass-ratio applications. In merger-ringdown studies, the strong-field coordinate transformation can place NR volume data in a local BHPT frame for projection onto quasinormal-mode bases, providing a bulk diagnostic of QNM excitation, nonlinear mode coupling, and the onset of the perturbative regime [15, 34, 35]. For extreme-mass-ratio inspirals, the method suggests a spatial-hybrid construction in which BHPT describes the small body's local strong-field neighborhood, a numerical or analytic spacetime supplies the outer region, and a gauge-preserving coordinate transformation joins the two descriptions.

These directions keep the same central structure: coordinate transformations fix gauge-preserving identifications of spacetime points, strong-field matching fixes the local BHPT frame around each black hole, and parameter maps translate between PN point-particle parameters, BHPT background parameters, NR horizon quantities, and observational source parameters. Treating these three ingredients separately gives a controlled route to precision waveform modeling for high-SNR gravitational-wave observations.

Acknowledgments

We thank the SpECTRE and SXS communities for the numerical infrastructure on which this work builds. This work is supported in part by the Sherman Fairchild Foundation, NSF grants PHY-2309211, PHY-2309231, and OAC-2513339, and NASA award 80NSSC26K0340 at Caltech. The computations were performed on the Mbot cluster at Cornell.

References

[1] Dongze Sun et al. "Strong-Field Matching for PN–BHPT–NR Parameter Maps in Binary Black Holes". to be submitted soon.

[2] Pau Amaro-Seoane et al. "Laser Interferometer Space Antenna". In: (2017). LISA mission proposal. DOI: 10.48550/arXiv.1702.00786. arXiv: 1702.00786 [astro-ph.IM].

[3] Monica Colpi et al. "LISA Definition Study Report". In: (2024). arXiv: 2402.07571 [astro-ph.CO].

[4] Niayesh Afshordi et al. "Waveform modelling for the Laser Interferometer Space Antenna". In: *Living Reviews in Relativity* 28.1 (2025), p. 9. DOI: 10.1007/s41114-025-00056-1. arXiv: 2311.01300 [gr-qc].

[5] Lee Lindblom, John G. Baker, and Benjamin J. Owen. "Improved time-domain accuracy standards for model gravitational waveforms". In: *Physical Review D* 82 (2010), p. 084020. DOI: 10.1103/PhysRevD.82.084020.

[6] Lee Lindblom, Benjamin J. Owen, and Duncan A. Brown. "Model waveform accuracy standards for gravitational-wave data analysis". In: *Physical Review D* 78 (2008), p. 124020. DOI: 10.1103/PhysRevD.78.124020.

[7] Luc Blanchet. "Gravitational Radiation from Post-Newtonian Sources and Inspiralling Compact Binaries". In: *Living Reviews in Relativity* 17 (2014), p. 2. DOI: 10.12942/lrr-2014-2. arXiv: 1310.1528 [gr-qc].

[8] Eric Poisson and Clifford M. Will. *Gravity: Newtonian, Post-Newtonian, Relativistic*. Cambridge University Press, 2014. DOI: 10.1017/CBO9781139507486.

[9] Frans Pretorius. "Evolution of Binary Black-Hole Spacetimes". In: *Physical Review Letters* 95.12 (2005), p. 121101. DOI: 10.1103/PhysRevLett.95.121101. arXiv: gr-qc/0507014.

[10] Joan Centrella et al. "Black-hole binaries, gravitational waves, and numerical relativity". In: *Reviews of Modern Physics* 82 (2010), pp. 3069–3119. DOI: 10.1103/RevModPhys.82.3069. arXiv: 1010.5260 [gr-qc].

[11] Abdul H. Mroue et al. "Catalog of 174 Binary Black Hole Simulations for Gravitational Wave Astronomy". In: *Physical Review Letters* 111.24 (2013), p. 241104. DOI: 10.1103/PhysRevLett.111.241104. arXiv: 1304.6077 [gr-qc].

[12] Tullio Regge and John A. Wheeler. "Stability of a Schwarzschild Singularity". In: *Physical Review* 108.4 (1957), pp. 1063–1069. DOI: 10.1103/PhysRev.108.1063.

[13] Frank J. Zerilli. "Effective potential for even-parity Regge-Wheeler gravitational perturbation equations". In: *Physical Review Letters* 24.13 (1970), pp. 737–738. DOI: 10.1103/PhysRevLett.24.737.

[14] Saul A. Teukolsky. "Perturbations of a Rotating Black Hole. I. Fundamental Equations for Gravitational, Electromagnetic, and Neutrino-Field Perturbations". In: *The Astrophysical Journal* 185 (1973), pp. 635–648. DOI: 10.1086/152444.

[15] Emanuele Berti, Vitor Cardoso, and Andrei O. Starinets. "Quasinormal modes of black holes and black branes". In: *Classical and Quantum Gravity* 26.16 (2009), p. 163001. DOI: 10.1088/0264-9381/26/16/163001. arXiv: 0905.2975 [gr-qc].

[16] Eric Poisson, Adam Pound, and Ian Vega. "The Motion of Point Particles in Curved Spacetime". In: *Living Reviews in Relativity* 14 (2011), p. 7. DOI: 10.12942/lrr-2011-7. arXiv: 1102.0529 [gr-qc].

[17] Leor Barack and Adam Pound. "Self-force and radiation reaction in general relativity". In: *Reports on Progress in Physics* 82.1 (2019), p. 016904. DOI: 10.1088/1361-6633/aae552. arXiv: 1805.10385 [gr-qc].

[18] P. Ajith et al. "Phenomenological template family for black-hole coalescence waveforms". In: *Classical and Quantum Gravity* 24.19 (2007), S689–S700. DOI: 10.1088/0264-9381/24/19/S31. arXiv: 0704.3764 [gr-qc].

[19] Ilana MacDonald et al. "Suitability of post-Newtonian/numerical-relativity hybrid waveforms for gravitational wave detectors". In: *Classical and Quantum Gravity* 28.13 (2011), p. 134002. DOI: 10.1088/0264-9381/28/13/134002. arXiv: 1102.5128 [gr-qc].

[20] Frank Ohme. "Analytical meets numerical relativity: status of complete gravitational waveform models for binary black holes". In: *Classical and Quantum Gravity* 29.12 (2012), p. 124002. DOI: 10.1088/0264-9381/29/12/124002. arXiv: 1111.3737 [gr-qc].

[21] Dongze Sun et al. "Optimizing post-Newtonian parameters and fixing the BMS frame for numerical-relativity waveform hybridizations". In: *Physical Review D* 110 (2024), p. 104076. DOI: 10.1103/PhysRevD.110.104076. arXiv: 2403.10278 [gr-qc].

[22] Olaf Dreyer et al. "Introduction to isolated horizons in numerical relativity". In: *Phys. Rev. D* 67 (2003), p. 024018. DOI: 10.1103/PhysRevD.67.024018. arXiv: gr-qc/0206008.

[23] Abhay Ashtekar and Badri Krishnan. "Isolated and dynamical horizons and their applications". In: *Living Reviews in Relativity* 7 (2004), p. 10. DOI: 10.12942/lrr-2004-10. arXiv: gr-qc/0407042.

[24] Gregory B. Cook and Bernard F. Whiting. "Approximate Killing vectors on S^2". In: *Physical Review D* 76.4 (2007), p. 041501. DOI: 10.1103/PhysRevD.76.041501. arXiv: 0706.0199 [gr-qc].

[25] Dongze Sun and Leo C. Stein. "Parameter matching between horizon quasi-local and point-particle definitions at 1PN for quasi-circular and non spinning BBH systems in harmonic gauge". In: (2025). arXiv: 2510.25618 [gr-qc].

[26] Stephanne Taylor and Eric Poisson. "Nonrotating black hole in a post-Newtonian tidal environment". In: *Phys. Rev. D* 78 (2008), p. 084016. DOI: 10.1103/PhysRevD.78.084016. arXiv: 0806.3052 [gr-qc].

[27] Eric Poisson and Eamonn Corrigan. "Nonrotating black hole in a post-Newtonian tidal environment II". In: *Phys. Rev. D* 97 (2018), p. 124048. DOI: 10.1103/PhysRevD.97.124048. arXiv: 1804.01848 [gr-qc].

[28] Lee Lindblom and Béla Szilágyi. "An Improved Gauge Driver for the Generalized Harmonic Einstein System". In: *Phys. Rev. D* 80 (2009), p. 084019. DOI: 10.1103/PhysRevD.80.084019. arXiv: 0904.4873 [gr-qc].

[29] Béla Szilágyi, Lee Lindblom, and Mark A. Scheel. "Simulations of Binary Black Hole Mergers Using Spectral Methods". In: *Phys. Rev. D* 80 (2009), p. 124010. DOI: 10.1103/PhysRevD.80.124010. arXiv: 0909.3557 [gr-qc].

[30] Vijay Varma and Mark A. Scheel. "Constructing a Boosted, Spinning Black Hole in the Damped Harmonic Gauge". In: *Phys. Rev. D* 98 (2018), p. 084032. DOI: 10.1103/PhysRevD.98.084032. arXiv: 1808.07490 [gr-qc].

[31] Lawrence E. Kidder et al. "SpECTRE: A Task-based Discontinuous Galerkin Code for Relativistic Astrophysics". In: *Journal of Computational Physics* 335 (2017), pp. 84–114. DOI: 10.1016/j.jcp.2016.12.059. arXiv: 1609.00098 [astro-ph.HE].

[32] Nils L. Vu et al. “A Scalable Elliptic Solver with Task-based Parallelism for the SpECTRE Numerical Relativity Code”. In: *Phys. Rev. D* 105 (2022), p. 084027. DOI: 10.1103/PhysRevD.105.084027. arXiv: 2111.06767 [gr-qc].

[33] Geoffrey Lovelace et al. “Simulating Binary Black Hole Mergers Using Discontinuous Galerkin Methods”. In: *Class. Quantum Grav.* 42 (2025), p. 035001. DOI: 10.1088/1361-6382/ad9f19. arXiv: 2410.00265 [gr-qc].

[34] Emanuele Berti, Kent Yagi, and Nicolás Yunes. “Extreme Gravity Tests with Gravitational Waves from Compact Binary Coalescences: I. Inspiral-Merger”. In: *General Relativity and Gravitation* 50.4 (2018), p. 46. DOI: 10.1007/s10714-018-2362-8. arXiv: 1801.03208 [gr-qc].

[35] Mark Ho-Yeuk Cheung et al. “Extracting linear and nonlinear quasinormal modes from black hole merger simulations”. In: *Physical Review D* 109.4 (2024), p. 044069. DOI: 10.1103/PhysRevD.109.044069. arXiv: 2310.04489 [gr-qc].

Part III

Applications, Infrastructure, and Outlook

Chapter 6

CONVERGENCE OF POST-NEWTONIAN THEORY FOR QUASI-CIRCULAR NON-PRECESSING COMPARABLE-MASS-RATIO BINARY BLACK HOLES

Published as: Dongze Sun et al. "Convergence of post-Newtonian for quasi-circular non-precessing comparable mass ratios BBHs". In: (May 2026). arXiv: 2605.20562 [gr-qc].

Abstract

Post-Newtonian (PN) theory provides the analytic foundation for modeling the early inspiral of binary black holes. However, as an asymptotic series, successive PN orders do not necessarily continue to improve agreement with the full nonlinear dynamics. While this has been explored in the extreme-mass-ratio limit, comparable-mass systems most relevant to current observations have not been benchmarked as systematically at high PN order. We study the convergence of the PN series for non-spinning and quasi-circular systems by comparing the PN energy flux at future null infinity to a long, high-accuracy numerical relativity (NR) simulation. To enable a gauge-consistent comparison, we place both descriptions in the same BMS frame and calibrate the intrinsic PN parameters by fitting to the NR waveform in the early inspiral. We find that for orbital velocities $v \lesssim 0.45$, higher PN orders continue to reduce the PN–NR flux discrepancy, with (incomplete) 6PN providing the best agreement among the orders considered. The improvement with PN order is non-monotonic with local extrema around 2.5PN and 4PN. This implies that the optimal truncation order of the PN series cannot be identified from the first local minimum in the energy flux residuals, contrary to suggestions in earlier work. As v approaches ~ 0.5 near the innermost circular orbit, higher PN orders no longer improve the agreement between NR and PN, indicating a loss of convergence. These results motivate continued high-order PN calculations and clarify the NR accuracy needed to validate them.

6.1 Introduction

Numerical relativity (NR) simulations of binary black hole mergers provide highly accurate gravitational waveforms, but their computational cost typically limits them to the late inspiral and merger-ringdown phases. To model the complete inspiral-merger-ringdown signal spanning the frequency bands of current gravitational-wave detectors, it is necessary to hybridize NR waveforms with analytic post-Newtonian (PN) waveforms, which accurately describe the early inspiral [2, 3, 4, 5, 6, 7]. Constructing reliable hybrid waveforms is non-trivial: it requires fixing the Bondi-Metzner-Sachs (BMS) frame of the NR waveforms to match the PN BMS frame [8, 9, 10] and adjusting the PN intrinsic parameters to account for the discrepancy between the PN and NR parameter definitions [10, 11]. More fundamentally, the validity of such hybrid models depends critically on (1) understanding the regime where PN theory provides a reliable approximation and where it breaks down, and (2) knowing how accurate NR needs to be, in order for hybridization to be justified.

Post-Newtonian theory is an asymptotic approximation to General Relativity in the orbital velocity v/c (or equivalently in GM/rc^2) [12]. Unlike convergent Taylor series, asymptotic series need not converge as more terms are added; beyond an optimal truncation order, additional terms in fact degrade rather than improve the approximation (for a pedagogical example, see [13, Ch. 3.5] as well as [14, Sec. IIE]). The optimal truncation order of the PN series is velocity-dependent. At lower velocities (smaller v/c), the optimal truncation order is higher and one can achieve better accuracy (i.e. approximate the full non-linear evolution as predicted by General Relativity better). Whereas at higher velocities approaching merger, the optimal truncation order is lower and the approximation becomes inherently less accurate. This raises a crucial question for gravitational-wave modeling: have we already reached the optimal PN order for current applications, or does pushing to higher orders still yield improvements? And related, if such improvements can be made, how accurate will our NR models need to be for cross-validation?

Determining the optimal truncation order of an asymptotic series ideally requires knowledge of both the exact solution and all terms in the expansion. In the absence of either, one can still assess convergence by using an alternative high-accuracy approximation as a benchmark. For binary black holes, previous studies have investigated PN convergence in the extreme-mass-ratio (EMR) limit, where black hole perturbation theory provides highly accurate predictions that can serve as such a benchmark. To ensure meaningful comparisons between different approximation schemes, which may employ different coordinate systems and gauge choices, these studies have focused on quantities such as the gravitational-wave energy flux at null infinity, which is invariant up to boosts and BMS supertranslations. Early work by

Simone, Poisson and Will [15] computed the energy flux for head-on black hole collisions using both PN theory and black hole perturbation theory. Their results revealed slow PN convergence; a feature later confirmed by high-order perturbative calculations that are characterized by rapidly growing coefficients in successive powers of v/c [16, 17]. This work was followed up for quasi-circular EMR binaries in [18]. Subsequent studies by Yunes and Berti [14] improved upon these comparisons, and the analysis was revisited by Sago, Fujita and Nakano in [19] when higher-order PN results in the EMR limit became available.

Here, we revisit this question in a regime where PN theory is expected to perform better: comparable mass systems [20]. With increasingly accurate numerical evolutions of compact binaries now available, it is time to re-examine these convergence questions using the improved knowledge of the "true" numerical evolution of the system. This expands upon early comparisons between PN and long NR waveforms initiated in [21].

In this paper, when we refer to the "convergence" of the PN expansion, we do not mean convergence in the strict mathematical sense of an infinite series. Rather, we study the behavior of the finite sequence of currently known PN truncations for a specific observable, the energy flux at future null infinity, using NR as a benchmark. More precisely, at fixed v, we ask whether the PN–NR discrepancy decreases as additional PN terms are included. Since the PN expansion is asymptotic, such improvement need not persist to arbitrarily high order, and may eventually reverse beyond an optimal truncation order. Moreover, this behavior is quantity-dependent: different gauge-invariant observables can exhibit different large-order behavior, so the conclusions of this paper apply specifically to the energy flux.

By comparing the PN and NR energy fluxes after placing both descriptions in the same BMS frame, with the frame transformations computed from the strain and Moreschi supermomentum [22], we find that, perhaps unsurprisingly, we have not yet saturated the utility of higher-order PN terms for gravitational-wave form modeling. Importantly, our analysis reveals that the optimal truncation order of the PN series cannot be identified from the first local minimum in the energy flux residuals, contrary to suggestions in earlier work [14].

Nonetheless, at $v \lesssim 0.32$, or roughly 5 orbits before merger, the error in the incomplete 6PN approximation falls below the NR error. This suggests that, when constructing PN–NR hybrids with the current NR accuracy, the NR portion of the waveform need not extend deep into the inspiral.

The outline of our paper is as follows. In Sec. 6.2, we describe the NR and PN waveforms used in this work, the computation of the energy flux, and the procedure for placing the two descriptions in a common BMS frame while fitting the PN intrinsic parameters. In Sec. 6.3, we present the PN–NR energy-flux comparison, analyze the convergence behavior of the PN series at different orbital velocities, and study the dependence of our results on the choice of matching window. In Sec. 6.4, we discuss the implications of these results for waveform modeling and summarize possible directions for future work. Throughout, we work in geometrized units with $G = c = 1$.

6.2 Method

In this section, we describe the high-accuracy NR waveform for a comparable-mass, non-precessing binary that will serve as our "reference" waveform. We will compute the resulting energy flux and compare this to PN results. In order to determine which PN parameters to use to compare to the NR simulation, we employ the hybridization framework introduced in Ref. [10]. This allows us to make a meaningful comparison by ensuring that both results are in the same Bondi–Metzner–Sachs (BMS) frame and that the PN parameters best match the NR result.

NR waveform and energy flux

We use a NR waveform computed using Cauchy-characteristic evolution (CCE) [23, 24] as the reference waveform. The Cauchy evolution is performed using the Spectral Einstein Code (SpEC) [25] and the CCE evolution is performed using the SpECTRE code [26]. The resulting waveform is given directly at future null infinity $\mathcal{I}^+$, along with the Bondi news, shear, and Weyl scalars.

We use the system SXS:BBH:2265 from the public SXS catalog [27, 28, 29] for comparison with PN. This system is the longest non-spinning and quasi-circular simulation in the SXS catalog to date, which has over 60 orbits available before merger. This choice allows comparison with the PN series at relatively small orbital velocities. The system has total mass $M = 1$ and mass ratio $q = 3$, based on the NR quasi-local measurement on apparent horizons [28]. The system is quasi-circular, but has a small residual eccentricity on the order of 10^{-5}.

The NR energy flux at $\mathcal{I}^+$ is calculated from the strain $h = h_+ - ih_\times$ based on [30]

$$\dot{E}_\infty = \oint_{\mathcal{I}^+} \frac{r^2}{16\pi} |\dot{h}|^2 d\Omega \,. \tag{6.1}$$

We will compute the energy flux as a function of the orbital velocity, $\dot{E}_\infty(v)$. The NR orbital velocity parameter is defined as $v \equiv (GM\Omega)^{1/3}$, where the orbital frequency Ω is measured from wave-zone data after BMS frame fixing (frame fixing is discussed below in Sec. 6.2).[1] The orbital frequency is defined as the frequency of a rotating frame in which the time-dependence of gravitational waves is minimized [32]; or equivalently, the frequency for a helical vector field $\partial_t + \Omega\partial_\phi$ that is closest to being a Killing symmetry [33]. The NR energy flux and orbital angular velocity are calculated using the `scri` package [34].

PN waveform and energy flux

For the PN waveforms, we also consider quasi-circular, non-spinning binaries characterized by the total mass M and mass ratio $q = m_1/m_2 \geq 1$. The orbital dynamics and gravitational-wave phase are modeled using the TaylorT1 approximant. In this approach, one writes the binary's binding energy E, gravitational-wave energy flux to null infinity $\dot{E}_\infty$ and into the horizon $\dot{E}_{\rm H}$ as PN series in the orbital velocity $v = (GM\Omega)^{1/3}$. The binary's phase evolution is found by numerically integrating the energy-balance equation

$$\frac{dv}{dt} = -\frac{\dot{E}_\infty + \dot{E}_{\rm H}}{M dE/dv}. \tag{6.2}$$

Non-spinning contributions to E and $\dot{E}_\infty$ for quasi-circular BBHs are complete through 4.5PN order [35, 36, 37, 38]. We include all the complete terms, supplemented by higher-order terms known in the EMR limit [16] up to 6PN. We include $\dot{E}_{\rm H}$ up to 4PN from Ref. [39].

For a consistent comparison between the NR and PN energy flux, we need to know which PN parameters to use to compare to the NR result and to ensure that the BMS frame of the NR and PN setting is the same. For instance, for the PN flux, one cannot simply use the same numerical values for M and q as in the NR simulation, because the definition of the NR masses and PN masses have a very different origin. The NR masses are measured quasi-locally from the apparent horizon, while the PN masses are attributes of point particles defined via asymptotic matching in body zones. To address these issues, we use the hybridization method from [10] (more

[1] The far-zone frequency Ω differs from the frequency that near-zone observers measure, denoted ω. The far-zone frequency is approximately $\Omega \approx \Omega_{2,2}/2$, where $\Omega_{2,2}$ is the instantaneous frequency of the $(2,2)$ mode – clearly linked to asymptotic observers. This leads to the two distinct PN expansion parameters, $x \equiv (GM\Omega/c^3)^{2/3}$ and $y \equiv (GM\omega/c^3)^{2/3}$, which differ at 4PN and higher orders. See [31] for more discussion.

details below). This method requires a comparison at the level of the waveform. The result of this method is an NR waveform in the same BMS frame as the PN setting (up to numerical error) and a PN waveform with the PN parameters such that this waveform matches the NR waveform in the early phase. Once the PN parameters are determined, we can directly use the PN energy flux formulas to compute the energy flux and compare this to the NR energy flux (without the need to use the PN waveform itself to compute the PN energy flux). Thus, as a first step, we need an accurate description of the PN gravitational-wave strain modes h_{lm}.

For quasi-circular non-spinning binaries, the oscillatory waveform modes are complete through 3.5PN order, while the dominant $(2,2)$ mode is known through 4PN [40, 41, 42, 43, 44, 45, 46]. In our implementation, all oscillatory modes are included through 3 PN order, the $(2,2)$ mode is included through 4PN, the $(3,1)$ and $(3,3)$ modes are included through 3.5 PN order, and the non-oscillatory $m = 0$ modes are included through 3PN [44]. The 3.5PN extension of the memory [47] is not included, but its impact on the present flux comparison should be negligible because memory is non-oscillatory, thus it only contributes to the flux through its time derivative at 5PN. These modes are then used to compute the asymptotic Poincaré charges associated with the PN waveform at $\mathcal{I}^+$. Those charges enter our frame-fixing procedure, where we align the PN and NR descriptions in the same asymptotic frame before comparing their energy fluxes.

The PN evolution including the above E, $\dot{E}_\infty$, $\dot{E}_\mathrm{H}$ and strain mode terms are implemented in the code [48], which derives from the code `GWFrames` [32].

Comparing NR and PN energy flux

The energy flux at $\mathcal{I}^+$ is invariant under rotations, but not under boosts, spatial translations, or proper BMS supertranslations. These transformations change the labeling of the constant-retarded-time cross sections of $\mathcal{I}^+$, and hence modify the flux as a function of retarded time. To make meaningful comparisons between PN and NR, we must map the NR system into the PN frame. We therefore place both descriptions in a common BMS frame and, in practice, we choose the PN BMS frame as our reference, since it has simple initial conditions as $u \to -\infty$, where u is the retarded time along $\mathcal{I}^+$. Following Ref. [8], we determine the boost that maps the NR center-of-mass charge to the PN center-of-mass charge and apply this boost to the NR waveform. Operationally, the boost is found from the average time derivative of the center-of-mass charge. The BMS supertranslations are computed by

Model	NR	PN
q	3.0001	2.9896 ± 0.0002
M	1.00000	0.99899 ± 0.00006

Table 6.1: The intrinsic parameters for the NR and PN systems. The quoted uncertainties are 1σ fit errors estimated from the numerical Jacobian of the residual at the minimum [49, Secs. 15.5–15.6].

mapping the NR Moreschi supermomentum to the analytically-known PN Moreschi supermomentum, as detailed in Refs. [8, 10].

Even in the same frame, the NR and PN system have different intrinsic parameters due to different parameter definitions and truncation errors (numerical truncation for NR, and finite truncation in powers of v in PN). Following Ref. [10], we therefore treat the PN intrinsic parameters as fit parameters and determine them by minimizing the fractional L^2 error in the waveforms. In other words, we minimize the cost function

$$\mathcal{E}[h^{\rm NR}, h^{\rm PN}] = \frac{1}{2}\frac{\sum_{\ell,m}\int_{t_1}^{t_2}\left|h_{\ell m}^{\rm NR}(t) - h_{\ell m}^{\rm PN}(t;\vec{\lambda})\right|^2 dt}{\sum_{\ell,m}\int_{t_1}^{t_2}\left|h_{\ell m}^{\rm NR}(t)\right|^2 dt}, \tag{6.3}$$

where $\vec{\lambda}$ includes the intrinsic parameters M and q, and a time shift Δt, and a frame rotation $\Delta\phi$. We include all $-\ell \leq m \leq \ell$ for $\ell \leq 8$ spin-weighted spherical harmonic modes in the cost function. The cost function is evaluated in a "matching window" during the early inspiral. Our default matching window is 5 orbits long and begins just after the junk radiation has left the system. We also explore alternative matching windows to probe the robustness of our conclusions, as detailed in Sec. 6.3.

The determination of the boost, spatial translations, supertranslations and the fit of the intrinsic parameters are performed iteratively. Starting from NR values as an initial guess, we alternate between updating the boost, spatial translations and supertranslations (and boosting, spatially translating and supertranslating the NR waveform into the PN frame) and updating the PN parameters $\vec{\lambda}$, until the cost function $\mathcal{E}$ converges with a fractional change smaller than 10^{-2}. The final best-fit physical parameters are summarized in Tab. 6.1. We do not list the fitting parameters that are pure gauge (rotation, boost, time shift, spatial translation, and 77 proper supertranslation parameters).

Given the large number of (mostly gauge) fit parameters, one might worry about overfitting. In practice, however, we fit only two physical PN parameters, (M, q), and effectively at a single reference value of v. The flux comparison is then performed over a wide range of v, providing a nontrivial check against overfitting; see [10] for a more systematic study.

After mapping both PN and NR to the same frame and performing the parameter optimization, we compute the NR energy flux and orbital velocity v as discussed in Sec. 6.2. The NR energy flux computed this way provides our best approximation to the "true" energy flux of a comparable-mass, quasi-circular, non-spinning binary. To compare PN against NR, we then evaluate the PN energy flux at the NR orbital velocity v, at a variety of PN orders.

Finally, we emphasize that both the frame-fixing and parameter-fitting procedures rely on the PN strain, which is currently complete only through 4PN order. We used phase evolution at 6PN and strain at 4PN for frame fixing and parameter fitting. As a result, PN–NR comparisons of the energy flux at higher PN orders (> 4) do not consistently incorporate the corresponding higher-order corrections in the strain and should be interpreted with some caution. Nevertheless, existing evidence suggests that the difference between PN and NR is dominated by differences in the phase evolution rather than by inaccuracies in the strain amplitudes [50], so the impact of using strain modes truncated at 4 PN on our higher-order PN comparisons should be subdominant.

6.3 Results

In Fig. 6.1 we show the differences between the PN and NR energy flux as a function of the orbital velocity v for several PN truncation orders. For reference, we have also included the total NR energy flux in black (dotted). To quantify the small-v behavior, we fit each PN curve in the range $0.22 \leq v \leq 0.3$ (between the vertical dashed lines) using a simple linear ansatz $\log(\Delta\dot{E}) = k\log(v) + b$, and extract the power-law slope k. Since the PN energy flux contains an overall v^{10} factor, the correction at PN order N is expected to scale as v^{10+2N}, thus the PN truncation error should be asymptotic to $\sim v^{10+2N+1}$. The fitted slopes below 6PN in Fig. 6.1 are roughly consistent with this expectation, confirming that we are indeed probing the PN truncation error in this regime. Although the $v \to 0$ asymptotics predict definite slopes, the differences between analytical slopes and numerically fitted slopes should not be alarming given our modest values of $0.22 \leq v \leq 0.3$ and non-trivial frame-fixing and parameter-fitting procedures.

For $v \lesssim 0.45$, the 6PN approximation systematically yields the smallest energy flux difference with respect to NR, indicating that the PN series is still improving the

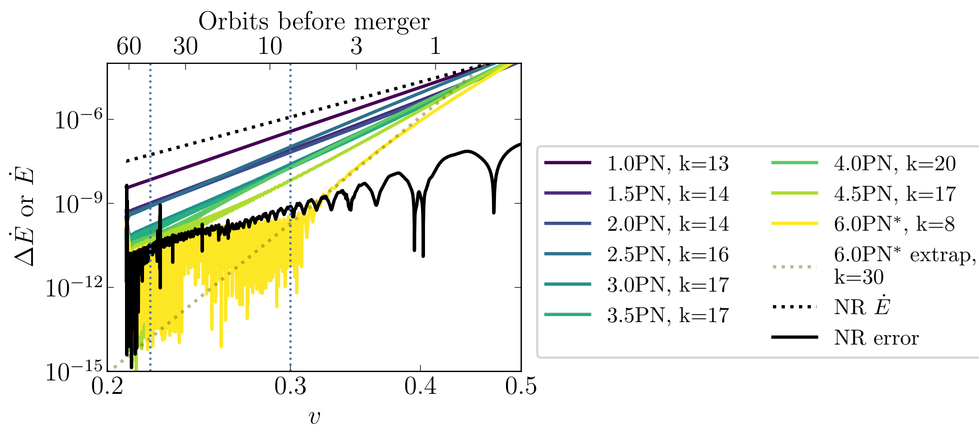

Figure 6.1: Solid colored curves: differences in energy flux $\Delta\dot{E}$ between NR and different PN order. Dotted black: the NR $\dot{E}$ from the highest resolution. Solid black: $\Delta\dot{E}$ between two highest NR resolutions after they are mapped to the same BMS frame, which measures the NR truncation error. Dotted brown line: the extrapolated 6PN $\dot{E}$, fitted in the region $0.32 \le v \le 0.4$. The slope k (rounded to the nearest integer in the legend) for the solid colored lines are fitted in the region $0.22 \le v \le 0.3$, which is the region between the two vertical dotted lines. The PN systems are frame-fixed in a 5-orbit matching window starting $v = 0.21$, or around 60 orbits before merger (shortly after the junk radiation left the system).

* The 6PN energy fluxes are not complete and we have only included the known results in the EMR limit.

PN–NR discrepancy up to (at least) 6PN in this velocity range. That being said, we expect PN to break down near the innermost circular orbit (ICO), which is known at 4PN for equal-mass non-spinning systems to be at $v \sim 0.47$ [51]. We see that as v approaches 0.5, all PN orders' energy differences cluster together, and the 6PN curve no longer improves the agreement between PN and NR. This signals the loss of convergence of the PN expansion near the ICO.

Note that the 6PN curve in Fig. 6.1 exhibits large oscillations for $v \lesssim 0.32$, which obscures the clean power-law PN truncation error we expect at small v. These oscillations are caused by the NR truncation error, as their magnitude aligns with the NR truncation error shown in the black curve. To estimate the underlying PN truncation error, we therefore extrapolate the 6PN fit obtained in the range $0.32 \le v \le 0.4$ down to $0.2 \le v \le 0.32$, shown as the brown dotted line in Fig. 6.1. The slope of this extrapolated line is much larger than the expected $10 + 2N + 1 = 23$, suggesting that the missing higher order PN terms become dominant in the region $0.32 \le v \le 0.4$. Despite this caveat, if we take this extrapolation seriously, this indicates that at $v = 0.2$, the 6PN flux is accurate at the level of 10^{-15}, comparable to double machine precision. In this regime, truly testing 6PN would therefore require

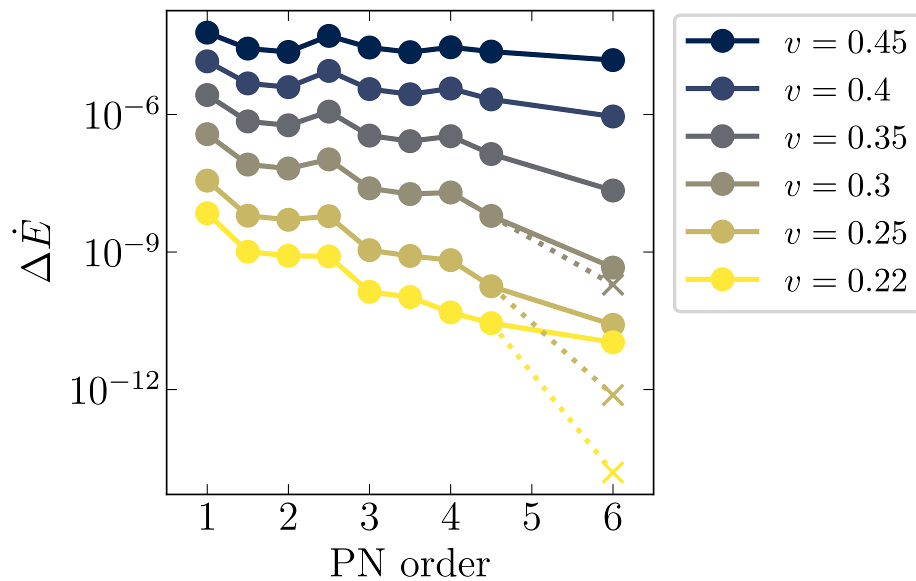

Figure 6.2: The energy flux residual $\Delta\dot{E}$ between different PN orders and NR at some v values, with respect to the PN truncation orders. These are vertical slices of Fig. 6.1 at different v. The cross markers appearing at 6PN are the extrapolated data from the dotted brown line of Fig. 6.1.

NR simulations with much higher accuracy. Accordingly, pushing the non-spinning flux beyond 6PN is unlikely to yield measurable gains for present or upcoming detectors, while extending high-order PN results to spinning and eccentric binaries should be more beneficial in practice.

To better visualize the behavior at fixed orbital velocities, Fig. 6.2 shows the energy flux difference as a function of PN order for several constant-v slices. For $v \lesssim 0.45$, the residuals generally decrease with PN order. The rate at which the residuals decrease is larger for smaller v, again indicating convergence. However, the decrease is not monotonic, as there are local extrema around 2.5PN and 4PN. This non-monotonic pattern implies that choosing an "optimal" truncation order based solely on the first change in monotonicity of the residuals, as suggested in Ref. [14], is not appropriate for PN series. While the asymptotic nature of PN series implies an optimal truncation order exists—beyond which higher-order terms worsen the approximation—this plot clearly shows that the optimal order cannot be determined from the first local minimum in energy flux difference. This also puts into question the related "region of validity" definition in [14].

We have checked the robustness of our conclusions against the choice of hybridization window. Our default matching window is 5 orbits long and begins just after the junk radiation has left the system at $v = 0.21$. Using a shorter 3-orbit window, or shifting the 5-orbit window within the early inspiral between $0.22 \leq v \leq 0.3$ leads to very similar PN–NR energy flux differences. By contrast, a much longer 15-orbit window produces noticeably different results. Over such a long interval the evolution of v is no longer negligible. The alignment must then compromise between the (slightly) different $v(t)$ evolutions of PN and NR over a broad range of v, rather than enforcing agreement at an effectively fixed v. Consequently, the two descriptions can end the matching window at slightly different values of v. The inferred $\Delta\dot{E}$ then reflects not only PN truncation error but also this accumulated misalignment in v, which biases the flux comparison.

6.4 Discussion and conclusions

We investigated the convergence properties of the post-Newtonian approximation by comparing the energy flux $\dot{E}_\infty(v)$ from high-order PN calculations against a high-accuracy numerical relativity simulation of a non-spinning, quasi-circular binary black hole system with mass ratio $q = 3$. Our analysis uses a hybridization framework that ensures both the PN and NR systems are mapped to the same BMS frame and that the PN intrinsic parameters are optimally matched to the NR evolution [10].

Our results demonstrate that, for the energy flux and across the currently available PN orders, the discrepancy between PN and NR predictions continues to decrease through at least 6PN order for orbital velocities $v \lesssim 0.45$. In this regime, each successive PN order systematically reduces the disagreement with NR, but the improvement with PN order is not necessarily monotonic. The energy flux differences scale approximately as the expected power law $\Delta\dot{E} \sim v^{10+2N+1}$ for truncation at PN order N. The improvement with PN order breaks down as v approaches ~ 0.5 near the ICO, where all PN orders cluster together and higher-order terms no longer improve agreement with NR.

Importantly, our analysis reveals that the optimal truncation order of the PN series cannot be identified from the first local minimum in the energy flux residuals, contrary to suggestions in earlier work [14]. We observe non-monotonic improvement between PN and NR with local extrema around 2.5PN and 4PN, indicating that the asymptotic nature of the PN expansion is more subtle than a simple monotonic approach to optimal truncation.

We further show that at $v \lesssim 0.32$, or roughly 5 orbits before merger, the error in the incomplete 6PN approximation falls below the NR error. This suggests that, when constructing PN–NR hybrids for accurate waveform modeling, the NR portion of the waveform need not extend deep into the inspiral of quasi-circular black hole binaries. This of course assumes that, at earlier times, the missing terms at 5, 5.5, and 6PN do not reverse the general trends we observed.[2]

A striking result emerges when we extrapolate the incomplete 6PN behavior to lower velocities: at $v \approx 0.2$, the 6PN approximation seems to achieve accuracy at the level of $\sim 10^{-15}$ in the energy flux. Entertaining this extrapolation, this suggests that to meaningfully test 6PN theory or to justify hybridization with 6PN waveforms at such low velocities would therefore require NR simulations with fractional accuracy approaching 10^{-15}—comparable to double machine precision. This represents a formidable challenge that pushes well beyond the capabilities of current NR codes. In this sense, pushing the non-spinning flux beyond 6PN is unlikely to produce observable gains for present or near-future detectors, whereas extending high-order PN information to spinning and eccentric systems may yield greater practical benefits.

These results have practical implications for gravitational-wave astronomy. Current waveform models for LIGO-Virgo-KAGRA observations typically employ PN approximations at 3.5PN or 4PN order. Our findings indicate that pushing to higher PN orders – 5PN and incomplete 6PN –could yield measurable improvements in waveform accuracy, especially for signals that span the early inspiral regime where $v \lesssim 0.4$. This will be all the more important for future observations in which we expect to see longer duration signals. However, realizing these improvements requires not only the analytical calculation of higher-order PN terms but also sufficiently accurate NR simulations to properly calibrate and validate the resulting hybrid waveforms.

Future directions

Several extensions of this work would be valuable. First, our current analysis relies on an optimization-based approach to match PN and NR parameters, minimizing the waveform mismatch over a chosen hybridization window. While this approach is effective, it carries the risk of overfitting the PN parameters to compensate for modeling errors rather than capturing genuine physical agreement. We plan to develop

[2]A complete calculation of the (point-mass) 5PN contributions would of course be particularly valuable for tidal deformability inference, since the leading adiabatic tidal effects enter the phasing at 5PN order and are therefore degenerate with any unknown point-mass terms at the same order. If the point-mass 5PN terms are not fully known, any mismatch at 5PN can bias the tidal signal, directly limiting how cleanly Love numbers can be extracted from waveform data.

alternative matching procedures based on first-principle parameter mappings—for instance, relating the PN point-particle masses to NR quasi-local horizon masses through well-defined theoretical prescriptions [11]. Such an approach would provide a more robust foundation for PN–NR comparisons and reduce sensitivity to the choice of matching window.

Second, our present study focuses on non-spinning, quasi-circular binaries. Extending this analysis to more general systems—including spinning and eccentric configurations—represents an important next step. For spinning systems, understanding PN convergence becomes more complex due to the richer parameter space and the interplay between orbital and spin dynamics. Recent advances in high-order spin-dependent PN calculations [52, 53, 54] and improvements in NR accuracy for spinning systems [29, 55] now make such comparisons feasible. Similarly, eccentric binary simulations have matured considerably, and eccentric PN theory has been developed to high orders in some limits (although more developments here are certainly welcome). Systematic PN–NR comparisons for eccentric systems would both benchmark the eccentric PN approximation and probe if the convergence properties we observe for circular orbits persist when eccentricity is present.

However, extending these comparisons to eccentric systems is substantially more challenging. In this work, we took advantage of the fact that at fixed (M, q), the time evolution of a quasicircular non-spinning BBH naturally runs through a range of values of v, which we can take as the asymptotic expansion parameter. By contrast, in eccentric systems, the instantaneous relative orbital velocity v is not a suitable expansion parameter—binaries with different semimajor axis and eccentricity (a, e) can attain the same v at different orbital phases between pericenter and apocenter. A more appropriate choice is the mean motion n, leading to the expansion parameter $x \equiv (GMKn/c^3)^{2/3}$ which reduces to $x \to v^2/c^2$ in the quasicircular limit (here $2\pi K$ gives the advance of pericenter per radial orbit). An individual eccentric inspiral then traces only a single path through (x, e) space. By contrast, a quasicircular inspiral sweeps across the entire one-dimensional range of v. Demonstrating convergence with eccentricity will therefore require a family of binaries covering initial eccentricities $0 \le e < 1$.

These extensions would serve the dual purpose of benchmarking PN theory against NR in broader regions of parameter space while simultaneously using high-order PN results to validate and test the accuracy of state-of-the-art NR simulations. As NR and PN methods continue to improve in tandem, such cross-validation becomes increasingly valuable for ensuring the reliability of gravitational-wave models across the full parameter space relevant for current and future detectors.

Acknowledgments

We would like to thank the organizers of the workshop "Mathematical Methods for the General Relativistic Two-body Problem" at the Institute for Mathematical Sciences (IMS) at the National University of Singapore (NUS), which provided the environment that stimulated this idea. We would also like to thank D. Trestini for valuable feedback on an earlier version of this manuscript. The work at Caltech was supported in part by the Sherman Fairchild Foundation, and by NSF Grants PHY-2309211, PHY-2309231, and OAC-2513339, and NASA award 80NSSC26K0340. Computations for this work were performed on the Resnick High Performance Computing (HPC) Cluster at the Caltech High Performance Computing Center. This research was conducted while BB was visiting the Okinawa Institute of Science and Technology (OIST) through the Theoretical Sciences Visiting Program (TSVP). L.C.S. was supported in part by NSF CAREER award PHY–2047382 and a Sloan Foundation Research Fellowship.

References

[1] Dongze Sun et al. "Convergence of post-Newtonian for quasi-circular non-precessing comparable mass ratios BBHs". In: (May 2026). arXiv: 2605.20562 [gr-qc].

[2] L. Santamaria et al. "Matching post-Newtonian and numerical relativity waveforms: Systematic errors and a new phenomenological model for non-precessing black hole binaries". In: *Phys. Rev. D* 82 (2010), p. 064016. DOI: 10.1103/PhysRevD.82.064016. arXiv: 1005.3306 [gr-qc].

[3] Ilana MacDonald et al. "Suitability of post-Newtonian/numerical-relativity hybrid waveforms for gravitational wave detectors". In: *Class. Quant. Grav.* 28 (2011), p. 134002. DOI: 10.1088/0264-9381/28/13/134002. arXiv: 1102.5128 [gr-qc].

[4] Michael Boyle. "Uncertainty in hybrid gravitational waveforms: Optimizing initial orbital frequencies for binary black-hole simulations". In: *Phys. Rev.* D84 (2011), p. 064013. DOI: 10.1103/PhysRevD.84.064013. arXiv: 1103.5088 [gr-qc].

[5] Ilana MacDonald et al. "Suitability of hybrid gravitational waveforms for unequal-mass binaries". In: *Phys. Rev.* D87.2 (2013), p. 024009. DOI: 10.1103/PhysRevD.87.024009. arXiv: 1210.3007 [gr-qc].

[6] Vijay Varma et al. "Surrogate model of hybridized numerical relativity binary black hole waveforms". In: *Phys. Rev.* D99.6 (2019), p. 064045. DOI: 10.1103/PhysRevD.99.064045. arXiv: 1812.07865 [gr-qc].

[7] Jam Sadiq et al. "Hybrid waveforms for generic precessing binaries for gravitational-wave data analysis". In: *Phys. Rev. D* 102.2 (2020), p. 024012. DOI: 10.1103/PhysRevD.102.024012. arXiv: 2001.07109 [gr-qc].

[8] Keefe Mitman et al. "Fixing the BMS frame of numerical relativity waveforms with BMS charges". In: *Phys. Rev. D* 106.8 (2022), p. 084029. DOI: 10.1103/PhysRevD.106.084029. arXiv: 2208.04356 [gr-qc].

[9] Jooheon Yoo et al. "Numerical relativity surrogate model with memory effects and post-Newtonian hybridization". In: *Phys. Rev. D* 108.6 (2023), p. 064027. DOI: 10.1103/PhysRevD.108.064027. arXiv: 2306.03148 [gr-qc].

[10] Dongze Sun et al. "Optimizing post-Newtonian parameters and fixing the BMS frame for numerical-relativity waveform hybridizations". In: *Phys. Rev. D* 110.10 (2024), p. 104076. DOI: 10.1103/PhysRevD.110.104076. arXiv: 2403.10278 [gr-qc].

[11] Dongze Sun and Leo C. Stein. "Parameter matching between horizon quasi-local and point-particle definitions at 1PN for quasi-circular and non spinning BBH systems in harmonic gauge". In: (Oct. 2025). arXiv: 2510.25618 [gr-qc].

[12] T. Futamase and Bernard F. Schutz. "Newtonian and post-Newtonian approximations are asymptotic to general relativity". In: *Phys. Rev. D* 28.10 (1983), p. 2363. DOI: 10.1103/PhysRevD.28.2363.

[13] C.M. Bender and S.A. Orszag. *Advanced Mathematical Methods for Scientists and Engineers: Asymptotic Methods and Perturbation Theory*. Advanced Mathematical Methods for Scientists and Engineers. Springer, 1999. ISBN: 9780387989310.

[14] Nicolas Yunes and Emanuele Berti. "Accuracy of the post-Newtonian approximation: Optimal asymptotic expansion for quasicircular, extreme-mass ratio inspirals". In: *Phys. Rev. D* 77 (2008). [Erratum: Phys.Rev.D 83, 109901 (2011)], p. 124006. DOI: 10.1103/PhysRevD.77.124006. arXiv: 0803.1853 [gr-qc].

[15] Liliana E. Simone, Eric Poisson, and Clifford M. Will. "Headon collision of compact objects in general relativity: Comparison of postNewtonian and perturbation approaches". In: *Phys. Rev. D* 52 (1995), pp. 4481–4496. DOI: 10.1103/PhysRevD.52.4481. arXiv: gr-qc/9506080.

[16] Ryuichi Fujita. "Gravitational Waves from a Particle in Circular Orbits around a Schwarzschild Black Hole to the 22nd Post-Newtonian Order". In: *Prog. Theor. Phys.* 128 (2012), pp. 971–992. DOI: 10.1143/PTP.128.971. arXiv: 1211.5535 [gr-qc].

[17] Ryuichi Fujita. “Gravitational Waves from a Particle in Circular Orbits around a Rotating Black Hole to the 11th Post-Newtonian Order”. In: *PTEP* 2015.3 (2015), 033E01. DOI: 10.1093/ptep/ptv012. arXiv: 1412.5689 [gr-qc].

[18] Eric Poisson. “Gravitational radiation from a particle in circular orbit around a black hole. 6. Accuracy of the postNewtonian expansion”. In: *Phys. Rev. D* 52 (1995). [Addendum: Phys.Rev.D 55, 7980–7981 (1997)], pp. 5719–5723. DOI: 10.1103/PhysRevD.52.5719. arXiv: gr-qc/9505030.

[19] Norichika Sago, Ryuichi Fujita, and Hiroyuki Nakano. “Accuracy of the Post-Newtonian Approximation for Extreme-Mass Ratio Inspirals from Black-hole Perturbation Approach”. In: *Phys. Rev. D* 93.10 (2016), p. 104023. DOI: 10.1103/PhysRevD.93.104023. arXiv: 1601.02174 [gr-qc].

[20] Thibault Damour. “The general relativistic two body problem”. In: (Dec. 2013). arXiv: 1312.3505 [gr-qc].

[21] Michael Boyle et al. “High-accuracy comparison of numerical relativity simulations with post-Newtonian expansions”. In: *Phys. Rev.* D76 (2007), p. 124038. DOI: 10.1103/PhysRevD.76.124038. arXiv: 0710.0158 [gr-qc].

[22] O. M. Moreschi. “Supercenter of Mass System at Future Null Infinity”. In: *Class. Quant. Grav.* 5 (1988), pp. 423–435. DOI: 10.1088/0264-9381/5/3/004.

[23] Jordan Moxon, Mark A. Scheel, and Saul A. Teukolsky. “Improved Cauchy-characteristic evolution system for high-precision numerical relativity waveforms”. In: *Phys. Rev. D* 102.4 (2020), p. 044052. DOI: 10.1103/PhysRevD.102.044052. arXiv: 2007.01339 [gr-qc].

[24] Jordan Moxon et al. “SpECTRE Cauchy-characteristic evolution system for rapid, precise waveform extraction”. In: *Phys. Rev. D* 107.6 (2023), p. 064013. DOI: 10.1103/PhysRevD.107.064013. arXiv: 2110.08635 [gr-qc].

[25] *The Spectral Einstein Code*. http://www.black-holes.org/SpEC.html.

[26] Nils Deppe et al. *SpECTRE v2023.05.16*. 10.5281/zenodo.7942177. Version 2023.05.16. May 2023. DOI: 10.5281/zenodo.7942177. URL: https://spectre-code.org.

[27] SXS Collaboration. *The SXS Collaboration catalog of gravitational waveforms*. http://www.black-holes.org/waveforms.

[28] Michael Boyle et al. “The SXS Collaboration catalog of binary black hole simulations”. In: *Class. Quant. Grav.* 36.19 (2019), p. 195006. DOI: 10.1088/1361-6382/ab34e2. arXiv: 1904.04831 [gr-qc].

[29] Mark A. Scheel et al. “The SXS collaboration’s third catalog of binary black hole simulations”. In: *Class. Quant. Grav.* 42.19 (2025), p. 195017. DOI: 10.1088/1361-6382/adfd34. arXiv: 2505.13378 [gr-qc].

[30] Milton Ruiz et al. "Multipole expansions for energy and momenta carried by gravitational waves". In: *Gen. Rel. Grav.* 40 (2008), p. 2467. DOI: 10.1007/s10714-007-0570-8. arXiv: 0707.4654 [gr-qc].

[31] David Trestini. "Schott term in the binding energy for compact binaries on circular orbits at fourth post-Newtonian order". In: *Phys. Rev. D* 112.2 (2025), p. 024076. DOI: 10.1103/lsbb-sv45. arXiv: 2504.13245 [gr-qc].

[32] Michael Boyle. "Angular velocity of gravitational radiation from precessing binaries and the corotating frame". In: *Phys. Rev.* D87.10 (2013), p. 104006. DOI: 10.1103/PhysRevD.87.104006. arXiv: 1302.2919 [gr-qc].

[33] Aniket Khairnar, Leo C. Stein, and Michael Boyle. "Approximate helical symmetry in compact binaries". In: *Phys. Rev. D* 111.2 (2025), p. 024072. DOI: 10.1103/PhysRevD.111.024072. arXiv: 2410.16373 [gr-qc].

[34] Michael Boyle et al. *scri*. Version 2022.8.8. Nov. 2023. DOI: 10.5281/zenodo.4041971. URL: https://github.com/moble/scri.

[35] Thibault Damour, Piotr Jaranowski, and Gerhard Schäfer. "Nonlocal-in-time action for the fourth post-Newtonian conservative dynamics of two-body systems". In: *Phys. Rev. D* 89.6 (2014), p. 064058. DOI: 10.1103/PhysRevD.89.064058. arXiv: 1401.4548 [gr-qc].

[36] Laura Bernard et al. "Center-of-Mass Equations of Motion and Conserved Integrals of Compact Binary Systems at the Fourth Post-Newtonian Order". In: *Phys. Rev. D* 97.4 (2018), p. 044037. DOI: 10.1103/PhysRevD.97.044037. arXiv: 1711.00283 [gr-qc].

[37] Luc Blanchet. "Gravitational Radiation from Post-Newtonian Sources and Inspiralling Compact Binaries". In: *Living Rev. Relativ.* 17 (2014), p. 2. DOI: 10.12942/lrr-2014-2. arXiv: 1310.1528 [gr-qc].

[38] Luc Blanchet et al. "Gravitational-Wave Phasing of Quasicircular Compact Binary Systems to the Fourth-and-a-Half Post-Newtonian Order". In: *Phys. Rev. Lett.* 131.12 (2023), p. 121402. DOI: 10.1103/PhysRevLett.131.121402. arXiv: 2304.11185 [gr-qc].

[39] Kashif Alvi. "Energy and angular momentum flow into a black hole in a binary". In: *Phys. Rev. D* 64 (2001), p. 104020. DOI: 10.1103/PhysRevD.64.104020. arXiv: gr-qc/0107080.

[40] Luc Blanchet et al. "The Third post-Newtonian gravitational wave polarisations and associated spherical harmonic modes for inspiralling compact binaries in quasi-circular orbits". In: *Class. Quant. Grav.* 25 (2008). [Erratum: Class.Quant.Grav. 29, 239501 (2012)], p. 165003. DOI: 10.1088/0264-9381/25/16/165003. arXiv: 0802.1249 [gr-qc].

[41] Guillaume Faye et al. "The third and a half post-Newtonian gravitational wave quadrupole mode for quasi-circular inspiralling compact binaries". In: *Class. Quant. Grav.* 29 (2012), p. 175004. DOI: 10.1088/0264-9381/29/17/175004. arXiv: 1204.1043 [gr-qc].

[42] Guillaume Faye, Luc Blanchet, and Bala R. Iyer. "Non-linear multipole interactions and gravitational-wave octupole modes for inspiralling compact binaries to third-and-a-half post-Newtonian order". In: *Class. Quant. Grav.* 32.4 (2015), p. 045016. DOI: 10.1088/0264-9381/32/4/045016. arXiv: 1409.3546 [gr-qc].

[43] Luc Blanchet et al. "Gravitational-wave flux and quadrupole modes from quasicircular nonspinning compact binaries to the fourth post-Newtonian order". In: *Phys. Rev. D* 108.6 (2023), p. 064041. DOI: 10.1103/PhysRevD.108.064041. arXiv: 2304.11186 [gr-qc].

[44] Marc Favata. "Post-Newtonian corrections to the gravitational-wave memory for quasi-circular, inspiralling compact binaries". In: *Phys. Rev. D* 80 (2009), p. 024002. DOI: 10.1103/PhysRevD.80.024002. arXiv: 0812.0069 [gr-qc].

[45] Quentin Henry, Guillaume Faye, and Luc Blanchet. "The current-type quadrupole moment and gravitational-wave mode $(\ell, \mathrm{m}) = (2, 1)$ of compact binary systems at the third post-Newtonian order". In: *Class. Quant. Grav.* 38.18 (2021), p. 185004. DOI: 10.1088/1361-6382/ac1850. arXiv: 2105.10876 [gr-qc].

[46] Quentin Henry. "Complete gravitational-waveform amplitude modes for quasicircular compact binaries to the 3.5PN order". In: *Phys. Rev. D* 107.4 (2023), p. 044057. DOI: 10.1103/PhysRevD.107.044057. arXiv: 2210.15602 [gr-qc].

[47] Kevin Cunningham et al. "Gravitational memory: new results from post-Newtonian and self-force theory". In: *Class. Quant. Grav.* 42.13 (2025). [Addendum: Class.Quant.Grav. 42, 199401 (2025)], p. 135009. DOI: 10.1088/1361-6382/adbc3d. arXiv: 2410.23950 [gr-qc].

[48] Dongze Sun. *NRPNHybridization*. https://github.com/dongzesun/NRPNHybridization.

[49] William H. Press et al. *Numerical Recipes: The Art of Scientific Computing*. 3rd ed. Cambridge University Press, 2007.

[50] Keefe Mitman et al. "Length dependence of waveform mismatch: a caveat on waveform accuracy". In: *arXiv e-prints* (Feb. 2025), arXiv:2502.14025. arXiv: 2502.14025 [gr-qc].

[51] Luc Blanchet, David Langlois, and Etienne Ligout. "Innermost stable circular orbit of arbitrary-mass compact binaries at fourth post-Newtonian order". In: *Phys. Rev. D* 112.6 (2025), p. 064025. DOI: 10.1103/mtv7-lkv8. arXiv: 2505.01278 [gr-qc].

[52] Gihyuk Cho, Rafael A. Porto, and Zixin Yang. "Gravitational radiation from inspiralling compact objects: Spin effects to the fourth post-Newtonian order". In: *Phys. Rev. D* 106.10 (2022), p. L101501. DOI: 10.1103/PhysRevD.106.L101501. arXiv: 2201.05138 [gr-qc].

[53] Mohammed Khalil. "Gravitational spin-orbit dynamics at the fifth-and-a-half post-Newtonian order". In: *Phys. Rev. D* 104.12 (2021), p. 124015. DOI: 10.1103/PhysRevD.104.124015. arXiv: 2110.12813 [gr-qc].

[54] Jung-Wook Kim, Michèle Levi, and Zhewei Yin. "Quadratic-in-spin interactions at fifth post-Newtonian order probe new physics". In: *Phys. Lett. B* 834 (2022), p. 137410. DOI: 10.1016/j.physletb.2022.137410. arXiv: 2112.01509 [hep-th].

[55] Deborah Ferguson et al. "Second MAYA catalog of binary black hole numerical relativity waveforms". In: *Phys. Rev. D* 112.4 (2025), p. 044043. DOI: 10.1103/gk7x-9cds. arXiv: 2309.00262 [gr-qc].

Chapter 7

GAUGE BOUNDARY CONDITIONS TO MITIGATE CENTER-OF-MASS DRIFT IN BBH SIMULATIONS

Published as: Dongze Sun et al. “Gauge Boundary conditions to mitigate center-of-mass drift in BBH simulations”. In: *Physical Review D* 113 (2026), p. 044016. DOI: 10.1103/b1cd-qysb. arXiv: 2510.25465 [gr-qc].

Abstract

Long-term numerical relativity (NR) simulations of binary black hole (BBH) systems in the Spectral Einstein Code (SpEC) code exhibit an unexpected exponential drift of the center-of-mass (CoM) away from the simulation's origin. In our work, we analyze this phenomenon and demonstrate that it is not a physical effect but rather a manifestation of a gauge artifact. The origin of this drift is the reflection of the gauge waves off the outer boundary of the computational domain. These reflections are introduced by inaccuracies in the gauge boundary condition, specifically, the application of the Sommerfeld condition to the time derivative of the gauge fields. Such an approach fails to completely suppress or correctly absorb the outgoing modes, thereby generating artificial feedback into the simulation. To mitigate this problem, we introduce a modified boundary condition that incorporates an explicit CoM correction source term designed to counteract the CoM motion. Our numerical experiments, performed with the SpEC code, reveal that this new boundary treatment reduces the CoM drift by several orders of magnitude compared to the standard implementation, and does not introduce any unwanted physical artifacts.

7.1 Introduction

Numerical relativity (NR) provides the most accurate solution for the dynamics and gravitational-wave emission of binary black holes (BBHs). The first stable BBH evolutions were obtained by Pretorius [2] in the generalized-harmonic formulation, followed soon after by the moving-puncture breakthroughs of Campanelli et al. [3] and Baker et al. [4]. These NR results play a crucial role in understanding the dynamics of these astrophysical phenomena, and the behavior of gravity in extreme regimes [5, 6, 7].

Despite major successes, long-duration NR simulations remain sensitive to how the artificial outer boundary is treated. In generalized-harmonic (GH) evolutions with the Spectral Einstein Code (SpEC) [8], an exponential drift of the BBH system's coordinate center-of-mass (CoM) has been consistently observed [9]. Fig. 7.1 illustrates this drift, which is a steadily increasing displacement of the CoM from the coordinate origin over time. It is unclear whether this boundary issue would occur for moving-puncture/BSSN codes; unlike SpEC, these codes generally place the boundary very far out so that it is causally disconnected over the simulation time [10, 11, 12, 13].

To uncover the cause of this spurious CoM behavior, Ref. [9] manipulated the outer boundary radius and observed that the exponential growth rate, denoted by σ, decreases monotonically with increasing boundary distance as $\sigma \propto 1/R^{1.45}$. This sensitivity to the boundary location strongly indicates that the drift is related to a coupling between the evolving fields and the computational boundary. This effect makes it infeasible to conduct long-term NR simulations with small outer boundary radii. To prevent the drift from affecting the simulation and waveform extraction, the outer boundary is typically set at radii on the order of $10^3\,M$ [14], where M is the total mass of the system. Although such large boundaries mitigate the drift, they also come with an increase in computational expense. Therefore, it is imperative to thoroughly investigate and address this issue to enable more efficient long-term NR simulations.

In our study, we probe this effect and find that the CoM drift is predominantly a gauge effect arising from the reflection of gauge waves off the outer boundary. These reflections are caused by the imperfect non-reflective Sommerfeld boundary condition applied to the time derivative of the gauge variables. Essentially, while the Sommerfeld condition is non-reflective for $l = 0$ outgoing radiation modes, any nonzero displacement of the CoM will generate higher-order outgoing radiation modes that can be reflected by the Sommerfeld condition. These reflected waves caused by the Sommerfeld condition then propel the CoM with exponential acceleration. Since the Sommerfeld condition is only imposed on the gauge degrees of freedom of the fields, the physical CoM defined from global Poincaré charges [15, 16, 17] is not affected and does not exhibit exponential drift, as we will show in Sec. 7.2.

Motivated by these insights, we propose an improved boundary treatment that mitigates the CoM drift. We add an additional CoM correction source term to the boundary condition. This term is formulated to effectively dampen the CoM velocity or realign the CoM with the coordinate origin. Numerical tests using our modified boundary condition demonstrate a significant reduction in the drift amplitude, by several orders of magnitude relative to the original setup. Thus, our modification not only clarifies the origin of the CoM drift but also provides a practical solution for performing long-term BBH simulations with smaller outer boundary radii and reduced computational cost.

In this paper, we use lower-case Latin indices from the beginning of the alphabet to denote four-dimensional spacetime quantities, whereas lower-case Latin indices from the middle of the alphabet are spatial. The coordinate CoM is defined using the Newtonian formula as

$$\mathbf{r_s} = \frac{m_1\mathbf{r_1} + m_2\mathbf{r_2}}{m_1 + m_2}, \tag{7.1}$$

where $\mathbf{r_1}$ and $\mathbf{r_2}$ are the coordinates of the center of the two black holes, which are defined as the surface-area weighted average of the location of the apparent horizons [14].

The remainder of this paper is organized as follows. In Sec. 7.2, we show that the CoM drift is a gauge effect by inspecting the physical charges. In Sec. 7.3, we review the Sommerfeld gauge boundary condition that is used in SpEC, and we discuss why this boundary condition leads to the exponential drift of the CoM. In Sec. 7.4, we derive the equation of motion of the CoM under given gauge boundary conditions. Following this, we present the new boundary conditions that significantly damp the CoM drift in Sec. 7.5. And we show that the gauge boundary conditions do not affect the resulting gauge-fixed waveform in Sec. 7.6. In Sec. 7.7, we discuss the potential of using higher-order boundary conditions, gauge constraint damping boundary condition, NR-post-Minkowskian matching, or Cauchy-Characteristic matching (CCM) as potential alternative solutions to address the CoM drift. In Sec. 7.8, we provide a few closing remarks. The BBH simulations used in this paper are performed by the SpEC code [8].

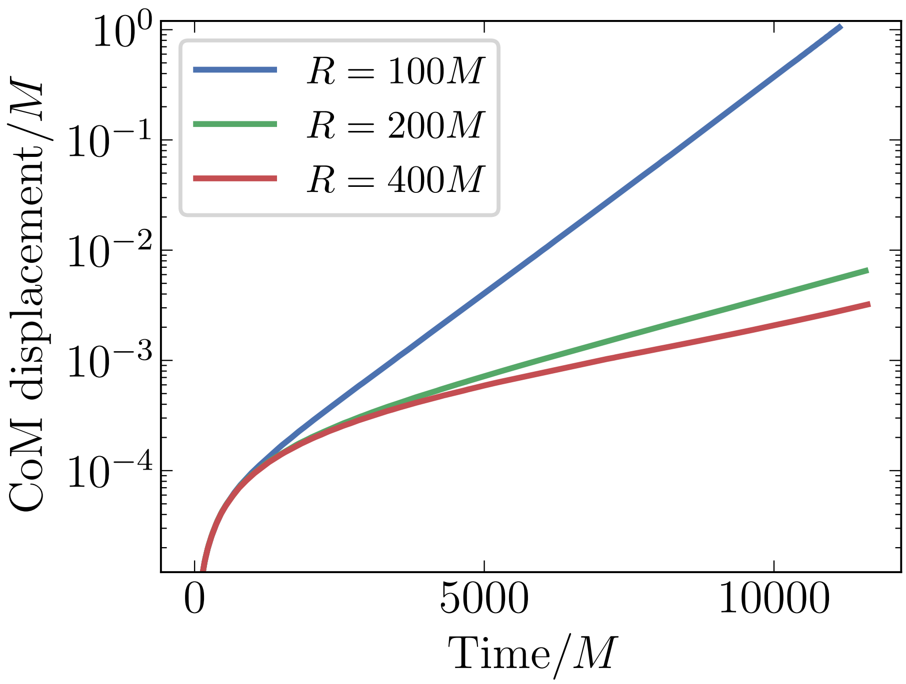

Figure 7.1: The CoM displacement from the origin for different outer boundary radii. The system is equal mass and non-spinning.

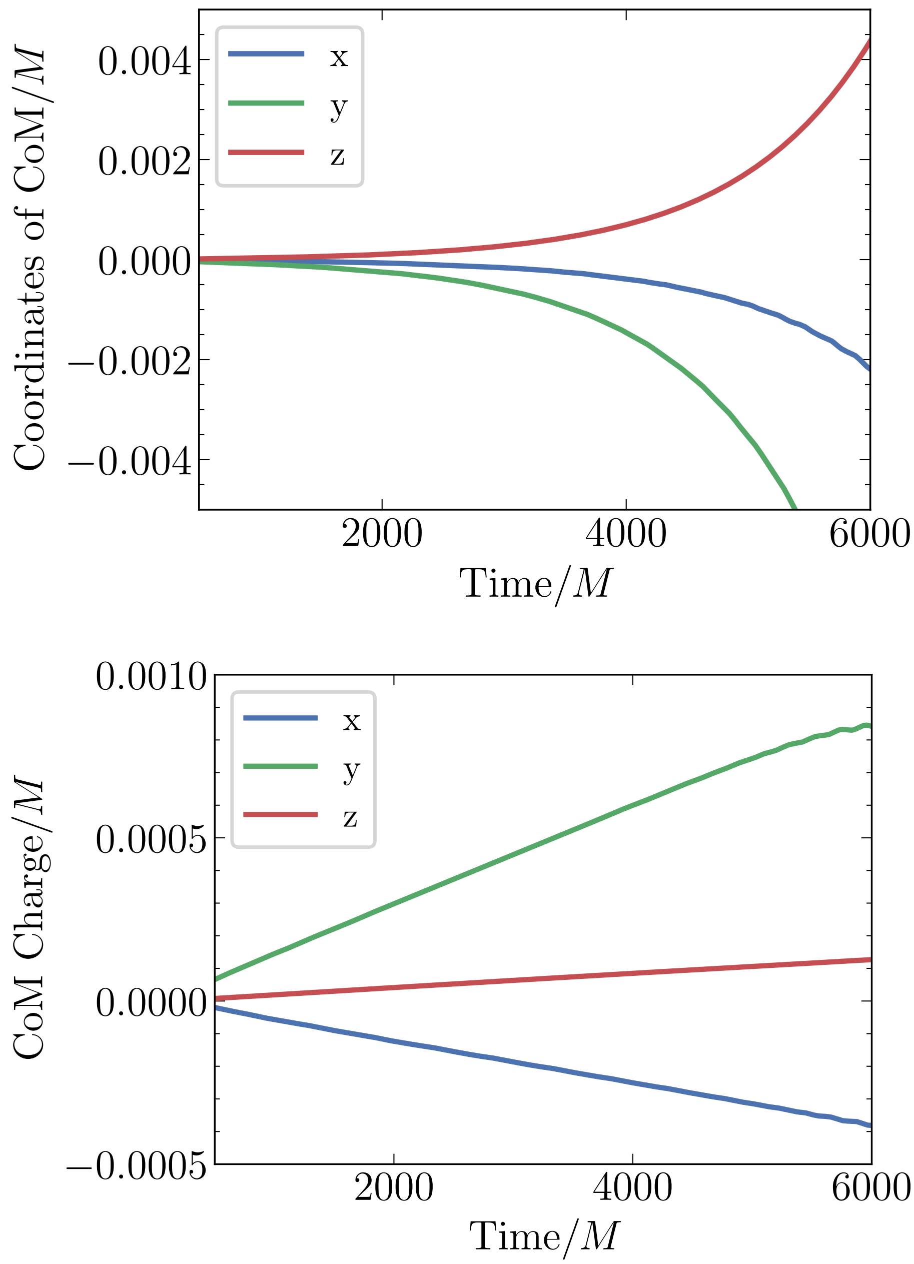

Figure 7.2: The upper panel shows the evolution of CoM coordinates and the lower panel shows their corresponding CoM charge. The outer boundary radius is set as 100 M.

7.2 CoM drift as a gauge effect

To identify whether the CoM drift is a physical or gauge effect, we inspect the Poincaré charges that are associated with the global conserved physical quantities. These charges are gauge-invariant up to the well-understood Bondi-van der Burg-Metzner-Sachs (BMS) group freedom [18, 19, 20]. We will address the BMS frame ambiguity in Sec. 7.6. The Poincaré charges are given by the integral of the Bondi mass aspect m_{B}, the Lorentz aspect N, and the energy moment aspect E over the celestial two-sphere (future null infinity $\mathscr{I}^+$ from the source) [20]. These functions are given in the Moreschi-Boyle convention [21, 17, 22] using the Bondi-Sachs coordinates $\{u, r, \theta^A\}$ as

$$\begin{aligned} m_{\mathrm{B}}(u,\theta^A) &\equiv -\mathrm{Re}\left[\Psi_2 + \sigma\dot{\bar{\sigma}}\right], \\ N(u,\theta^A) &\equiv -\left(\Psi_1 + \sigma\eth\bar{\sigma} + u\eth m + \frac{1}{2}\eth(\sigma\bar{\sigma})\right), \\ E(u,\theta^A) &\equiv N + u\eth m \\ &= -\left(\Psi_1 + \sigma\eth\bar{\sigma} + \frac{1}{2}\eth(\sigma\bar{\sigma})\right). \end{aligned} \tag{7.2}$$

Here Ψ_i are the Weyl scalars, σ is the Newman-Penrose shear, and an overbar represents complex conjugation. For a quantity η of spin weight s, the spin-weight raising operator $\eth$ can be written as [23, 24]

$$\eth\eta = -\frac{1}{\sqrt{2}}(\sin\theta)^s\left(\frac{\partial}{\partial\theta} + \frac{i}{\sin\theta}\frac{\partial}{\partial\phi}\right)((\sin\theta)^{-s}\eta)\,. \tag{7.3}$$

With these functions defined at $\mathscr{I}^+$, we then have the energy–momentum charge and complex dipole moment defined as

$$\begin{aligned} P^a &= \frac{1}{4\pi}\int_{\mathscr{I}^+} n^a m_{\mathrm{B}}\, d\Omega, \\ D^a + iJ^a &= \frac{1}{4\pi}\int_{\mathscr{I}^+} \bar{\eth} n^a E\, d\Omega, \end{aligned} \tag{7.4}$$

where $n^a = (1, \sin\theta\cos\phi, \sin\theta\cos\phi, \cos\theta)$. Here the real part D defines the gauge-independent mass dipole, and the imaginary part J defines the angular momentum.

A gauge-independent measurement of the CoM displacement, i.e., the CoM charge, can be defined as the mass dipole D scaled by the total energy P^0 [15, 16, 17]:

$$G^i \equiv \frac{D^i}{P^0}. \tag{7.5}$$

To carry out this check, we use Cauchy-characteristic evolution (CCE) to extract the Weyl scalars and σ at $\mathscr{I}^+$ [25, 26]. The Cauchy evolution parts are performed using the SpEC code [8], and the CCE computations are performed using the SpECTRE Code [27]. CCE uses a worldtube from the Cauchy evolution of the Einstein field equations as the inner boundary to a characteristic evolution on a null foliation. The gravitational information is evolved to future null infinity, so one can extract Weyl scalars there unambiguously from any Cauchy evolution.

Fig. 7.2 shows the evolution of CoM coordinates alongside the corresponding CoM charges of an equal-mass and non-spinning system. The CoM charges are computed using the `scri` package [28]. The CoM charges in each direction shown in the lower panel are considerably smaller than the corresponding CoM coordinates shown in the upper panel, and they do not exhibit exponential growth. This is strong evidence that the exponential CoM drift primarily arises as a gauge effect caused by inaccuracies in the gauge boundary conditions, rather than a genuine physical motion.

7.3 Sommerfeld boundary condition

In this section, we first review the gauge boundary condition used in the SpEC code, and then use a propagating scalar wave as a toy model to show how reflections can be generated by this boundary condition.

Gauge boundary condition in SpEC

The gauge boundary condition used in SpEC is the Sommerfeld non-reflective boundary condition [29, 30]. The Sommerfeld boundary condition acts on a general propagating tensor wave Ψ as

$$L\Psi \doteq 0, \tag{7.6}$$

where

$$L = \partial_t + \partial_r + \frac{1}{r}, \tag{7.7}$$

and $\doteq$ denotes equality at the boundary.

For gravitational waves, the spacetime metric can be approximately decomposed as a background part $g^{(\mathrm{B})}_{ab}$ that changes "adiabatically", and a propagating wave part h_{ab}:

$$g_{ab} = g^{(\mathrm{B})}_{ab} + h_{ab}. \tag{7.8}$$

The Sommerfeld boundary condition should then act like

$$Lh_{ab} \doteq 0. \tag{7.9}$$

The use of approximations for $g_{ab}^{(\mathrm{B})}$ may introduce inaccuracies in the boundary condition, leading to junk reflections within the simulation domain. To address this issue, we can further refine the boundary condition by taking a time derivative, thus removing the ambiguity in $g_{ab}^{(\mathrm{B})}$, resulting in

$$\partial_t \left(L g_{ab}\right) \doteq 0. \tag{7.10}$$

In SpEC, the Einstein equations are solved using the generalized harmonic (GH) formalism, with the gauge condition given by

$$\nabla^c \nabla_c x^a = H^a, \tag{7.11}$$

where H^a are the gauge source functions. In the GH formalism, the Einstein equations can be written in first-order form [31] by introducing the derivatives of g_{ab} as additional variables $\Phi_{iab} \equiv \partial_i g_{ab}$ and $\Pi_{ab} \equiv -t^c \partial_c g_{ab}$, where t^c is the future directed unit normal to the t = constant hypersurfaces. The gauge boundary condition is imposed on the incoming characteristic field, given by

$$u_{ab}^{1-} = \Pi_{ab} - n^i \Phi_{iab} - \gamma_2 g_{ab}, \tag{7.12}$$

where n^i is the outward-pointing spatial normal vector to the outer boundary, and γ_2 is introduced to damp the constraint violation $\partial_i g_{ab} - \Phi_{iab}$. The ingoing and outgoing null vectors are given by $k^a = \frac{1}{\sqrt{2}}\left(t^a - n^a\right)$ and $l^a = \frac{1}{\sqrt{2}}\left(t^a + n^a\right)$. In this notation, if we assume the background metric to be either constant or changes "adiabatically", i.e., $\partial_t g_{ab}^{\mathrm{B}} \sim \frac{v}{c} \partial_t h_{ab}$, where v is the coordinate velocity of the BH and $v/c \ll 1$, and h_{ab} is a spherical wave, then the Sommerfeld gauge boundary condition reads approximately as

$$P_{ab}^{\mathrm{G}cd} d_t \left[u_{cd}^{1-} + \left(\gamma_2 - \frac{1}{r}\right) g_{cd}\right] \doteq 0. \tag{7.13}$$

Here $P_{ab}^{\mathrm{G}cd} = \left[k_a k_b l^{(c} + k_a \delta_b^{(c} + k_b \delta_a^{(c}\right] l^{d)}$ is the projection operator that removes the four constraint-preserving degrees of freedom corresponding to the incoming constraint fields and two physical degrees of freedom that correspond to backscattered gravitational waves. This leaves four degrees of freedom that correspond to the gauge part of the field, which determine the lapse and shift (see [30] for more details). Here $d_t u$ is the incoming characteristic projection of $\partial_t u$, as defined in Ref. [31]: If the fundamental fields are u^α and the characteristic fields are $u^{\hat{\alpha}} \equiv e^{\hat{\alpha}}{}_\beta u^\beta$ where Greek letters label each field and $e^{\hat{\alpha}}{}_\beta$ are the characteristic eigenvectors, then $d_t u^{\hat{\alpha}} \equiv e^{\hat{\alpha}}{}_\beta \partial_t u^\beta$.

Reflection from the boundary condition

To understand how the CoM drift is coupled with the outer boundary condition, we first consider a scalar wave in 3-dimensional flat space as a toy model:

$$\psi_{\ell mk}(r,\theta,\phi,t) = e^{ikt}\Big(h_\ell^{(1)}(k|\mathbf{r}-\mathbf{r_s}|)Y_\ell^m(\theta,\phi) + \sum_{\ell',m'}\rho^\ell_{\ell'm'}h_{\ell'}^{(2)}(k|\mathbf{r}-\mathbf{r_s}|)Y_{\ell'}^{m'}(\theta,\phi)\Big), \quad (7.14)$$

where $h^{(1)}, h^{(2)}$ are spherical Hankel functions that correspond to the outgoing and ingoing waves, $\rho^\ell_{\ell'm'}$ are the reflection coefficients, and $\mathbf{r_s}$ is the location of the source.

We impose the Sommerfeld boundary condition Eq. (7.6) on this scalar field, and calculate $\rho^\ell_{\ell'm'}$ for $0 \le \ell \le 3$, $\ell' = \ell$ and $m' = 0$. In Fig. 7.3, we show the results as a function of the distance of the source from the origin, r_s, normalized by the outer boundary radius R. We can see that the Sommerfeld boundary condition is only perfectly non-reflective for the $\ell = 0$ mode for a source located at the origin ($r_s = 0$). When the source is positioned away from the origin ($r_s > 0$), there will be mode mixing and the Sommerfeld boundary condition is not non-reflective anymore. As we shall show below in Sec. 7.4, this reflection of the gauge wave leads to the drift of the CoM observed in BBH simulations.

This leads us to generalize the Sommerfeld boundary condition in Eq. (7.6) by introducing a parameter $\mathbf{r_0}$. The radial coordinate r is modified to $|\mathbf{r}-\mathbf{r_0}|$, in order to eliminate the reflections of $\ell \neq 0$ modes

$$L(\mathbf{r_0})\psi \doteq 0, \quad (7.15)$$

where

$$L(\mathbf{r_0}) = \partial_t + \partial_{|\mathbf{r}-\mathbf{r_0}|} + \frac{1}{|\mathbf{r}-\mathbf{r_0}|}. \quad (7.16)$$

$L(0)\psi \doteq 0$ corresponds to the original Sommerfeld boundary condition.

To show how the introduced parameter $\mathbf{r_0}$ works, we consider a spherical wave sourced at $\mathbf{r_s}$ instead of the origin,

$$\psi(\mathbf{r},t) = \frac{1}{|\mathbf{r}-\mathbf{r_s}|}\left(e^{ik(|\mathbf{r}-\mathbf{r}_s|-t)} + \rho e^{-ik(|\mathbf{r}-\mathbf{r}_s|+t)}\right), \quad (7.17)$$

which has nonzero ℓ modes with respect to the origin. In this case we can adjust the $\mathbf{r_0}$ parameter in Eq. (7.16) to shift the boundary condition with respect to the source, effectively eliminating reflected waves. Fig. 7.4 illustrates the reflection

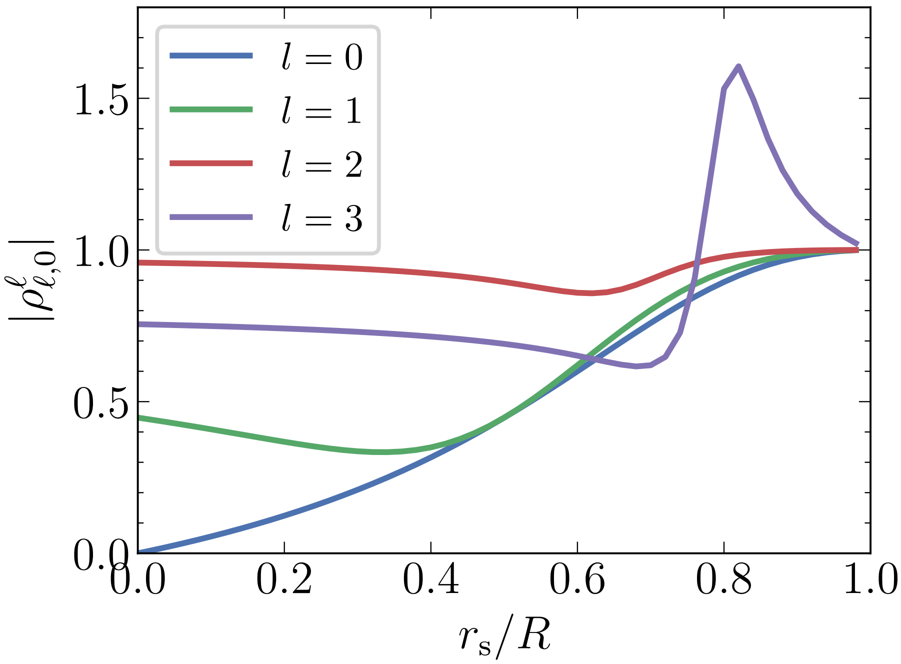

Figure 7.3: Reflection coefficient $|\rho^{\ell}_{\ell' m'}|$ for different ℓ. Given $m' = 0, \ell' = \ell, k = 1, t = 0, \theta = \phi = 0$.

coefficient ρ as a function of $\mathbf{r_0}$. Notably, when $\mathbf{r_0} = \mathbf{r_s}$, the boundary condition becomes non-reflective, demonstrating its efficacy in preventing wave reflections.

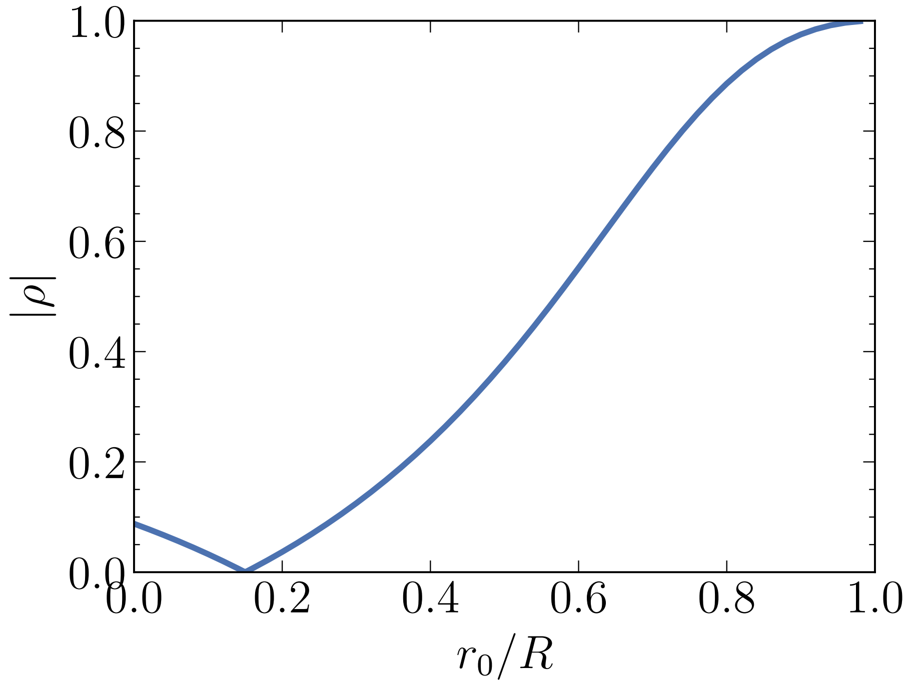

Figure 7.4: Reflection coefficient $|\rho|$ for a spherical wave whose source is localized at $\mathbf{r_s}/R = 0.15$, with $k = 1, t = 0, \theta = \phi = 0$.

7.4 CoM dynamics

In this section we will derive the leading-order equation of motion for the CoM under the interaction with the outer boundary gauge reflection. The derivation will only focus on the leading-order effects.

We use the following notation: $\mathbf{r_s}$ is the location of the CoM. $\mathbf{R}$ is the field point on the outer boundary, and $\mathbf{x_1}$ and $\mathbf{x_2}$ are the locations of the black holes. We assume $\mathrm{r_s} \ll r_{12} = |\mathbf{x_1} - \mathbf{x_2}| \ll R$, and $\mathrm{r_s} \ll 1/k$, where k is the wavenumber of the metric perturbation. The setup is shown in the schematic diagram in Fig. 7.5. The metric perturbation in the region near the outer boundary ($r \sim R \gg r_{12}$) can be written as the summation of outgoing and ingoing waves

$$\begin{aligned} h_{ab}(\mathbf{r},t) &= h_{ab}^{\text{outgoing}}(\mathbf{r},t) + h_{ab}^{\text{ingoing}}(\mathbf{r},t) \\ &= \left(f_{ab}^{\text{out}}(\theta,\phi) \frac{e^{ik|\mathbf{r}-\mathbf{r_s}|}}{|\mathbf{r}-\mathbf{r_s}|} + f_{ab}^{\text{in}}(\theta,\phi) \sum_{\ell'} \rho_{\ell'} h_{\ell'}^{(2)}(kr) \right) e^{-ikt} \\ &\qquad + O\left(\frac{1}{R^2}\right). \end{aligned} \tag{7.18}$$

Near the outer boundary, the quantity $h_{\ell'}^{(2)}(kr)$ behaves like $e^{-ikr}/r^{\ell+1}$, so we will

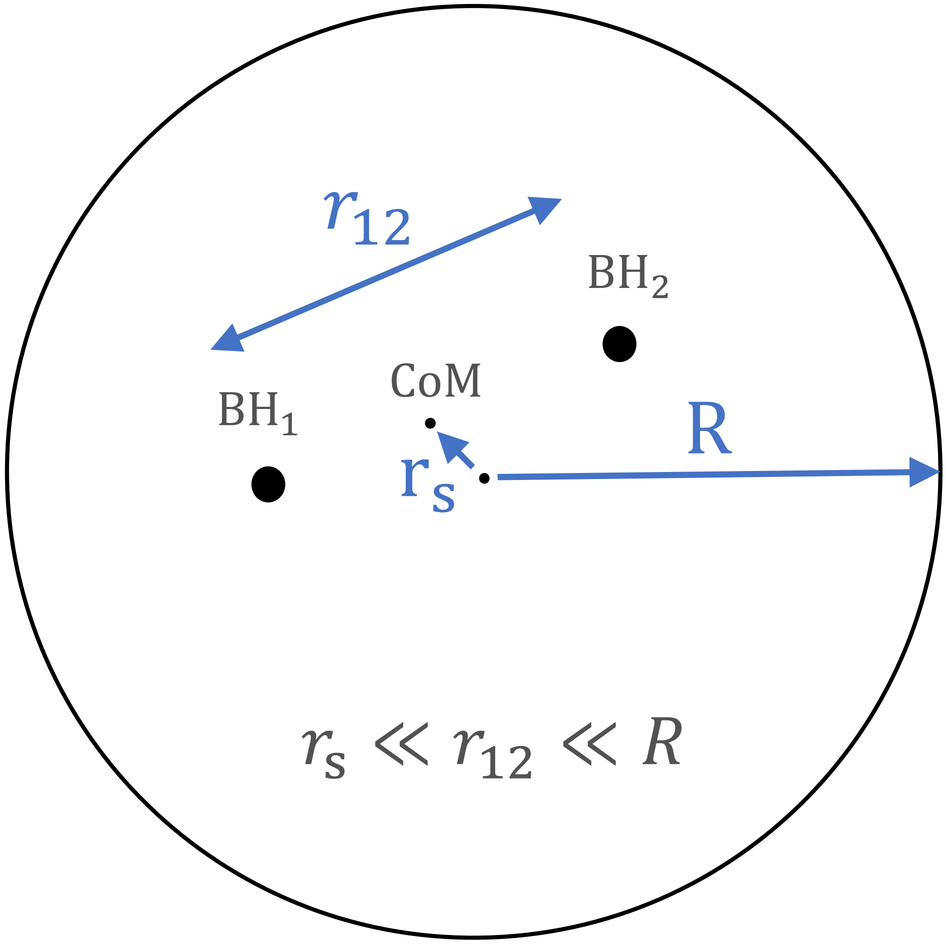

Figure 7.5: A schematic diagram showing the domain setup and symbols.

only focus on the dominant $\ell = 0$ reflected mode. Substituting the Sommerfeld boundary condition Eq. (7.9), we obtain

$$\rho_0 = \frac{\hat{\mathbf{R}} \cdot \mathbf{r_s}}{2R^2} e^{2ikR} + O\left(\frac{r_s^2}{R^2}\right). \tag{7.19}$$

The ingoing perturbation is then given by

$$h_{ab}^{\text{ingoing}}(\mathbf{r}, t) = f_{ab}^{\text{in}}(\theta, \phi) \frac{\hat{\mathbf{r}} \cdot \mathbf{r_s}}{2R^2} \frac{e^{ik(2R-r-t)}}{r} + O\left(\frac{r_s^2}{R^3}\right). \tag{7.20}$$

The momentum flux carried by a gravitational perturbation on the outer boundary is given by the integral of the Landau–Lifshitz pseudotensor on the outer boundary

$$\frac{dP^i}{dt} = -\int_{r=R} t_{\text{LL}}^{ij} \hat{r}_j r^2 d\Omega, \tag{7.21}$$

where

$$
\begin{aligned}
t_{\mathrm{LL}}^{ij} = \frac{1}{16\pi(-g)} \Big[& \partial_a \left(\sqrt{-g} g^{ij}\right) \partial_b \left(\sqrt{-g} g^{ab}\right) - \partial_a \left(\sqrt{-g} g^{ia}\right) \partial_b \left(\sqrt{-g} g^{jb}\right) \\
& + \frac{1}{2} g^{ij} g_{ab} \partial_c \left(\sqrt{-g} g^{ad}\right) \partial_d \left(\sqrt{-g} g^{bc}\right) + g_{ab} g^{cd} \partial_c \left(\sqrt{-g} g^{ia}\right) \partial_d \left(\sqrt{-g} g^{jb}\right) \\
& - \left(g^{ia} g_{bc} \partial_d \left(\sqrt{-g} g^{jc}\right) \partial_a \left(\sqrt{-g} g^{bd}\right) + g^{ja} g_{bc} \partial_d \left(\sqrt{-g} g^{ic}\right) \partial_a \left(\sqrt{-g} g^{bd}\right)\right) \\
& + \frac{1}{8} \left(2 g^{ia} g^{jb} - g^{ij} g^{ab}\right) \left(2 g_{cd} g_{ef} - g_{de} g_{cf}\right) \partial_a \left(\sqrt{-g} g^{cf}\right) \partial_b \left(\sqrt{-g} g^{de}\right) \Big]
\end{aligned}
\tag{7.22}
$$

is quadratic in the first derivatives of the metric. Using the decomposition

$$
g_{ab} = g_{ab}^{(\mathrm{B})} + h_{ab}^{\mathrm{outgoing}} + h_{ab}^{\mathrm{ingoing}}, \tag{7.23}
$$

the terms in the outer boundary integral in Eq. (7.21) that involve only $g_{ab}^{(\mathrm{B})}$ and $h_{ab}^{\mathrm{outgoing}}$ drop out, because they are even functions with respect to the source when time-averaged over orbits, while $\hat{r}$ is odd, therefore their product is odd and integrates to zero over the boundary. So the leading-order non-vanishing result of the integral Eq. (7.21) comes from terms involving the product of $\partial_a g_{bc}^{(\mathrm{B})}$ and $\partial_a h_{bc}^{\mathrm{ingoing}}$. The terms involving the product of $\partial_a h_{bc}^{\mathrm{outgoing}}$ and $\partial_a h_{bc}^{\mathrm{ingoing}}$ are on the order of $O(h^2)$, so we will ignore them in the leading-order calculation.

In the region near the outer boundary ($r \sim R \gg r_{12}$), the background metric can be described using the post-Newtonian (PN) approximation [32, 33]

$$
\begin{aligned}
g_{00}^{(\mathrm{B})} &= -1 + \frac{2Gm_1}{c^2 r_1} + O\left(\frac{1}{c^4}\right) + 1 \leftrightarrow 2, \\
g_{0i}^{(\mathrm{B})} &= -\frac{4m_1}{c^3 r_1} v_1^i + O\left(\frac{1}{c^5}\right) + 1 \leftrightarrow 2, \\
g_{ij}^{(\mathrm{B})} &= \left(1 + \frac{2Gm_1}{c^2 r_1}\right) \delta_{ij} + O\left(\frac{1}{c^4}\right) + 1 \leftrightarrow 2.
\end{aligned}
\tag{7.24}
$$

So we have $\partial_a g_{bc}^{(\mathrm{B})} \sim 1/R^2 + O(v/R^2)$. And from Eq. (7.20), we have $\partial_a h_{bc}^{\mathrm{ingoing}} \sim (\hat{\mathbf{R}} \cdot r_{\mathrm{s}})/R^3 + O(r_{\mathrm{s}}^2/R^4)$. Thus Eq. (7.21) gives $dP^i/dt \sim r_{\mathrm{s}}^i/R^3$ at leading order. This leads us to the CoM equation of motion:

$$
\ddot{\mathbf{r}}_{\mathrm{s}(t)} - \frac{a}{R^3} \mathbf{r}_{\mathrm{s}(t_{\mathrm{ret}})} = 0, \tag{7.25}
$$

where a is a dimensionless coefficient that collects the numerical factors from the leading-order evaluation of the outer boundary Landau-Lifshitz momentum flux, after keeping only the dominant $\partial g^{(\mathrm{B})} \partial h^{\mathrm{ingoing}}$ contribution. Here, the momentum flux takes the value at a retarded time $t_{\rm ret} \approx t - 2R$. For $t \gg R$, the solution is given by

$$\mathbf{r}_{\rm s}(t) = \mathbf{A} \exp\left(\frac{\sqrt{a}}{R^{3/2}} t\right). \tag{7.26}$$

The solution with a positive a is consistent with [9], whose results showed the exponential growth rate $\sigma \propto R^{-1.45}$, as shown in Fig. 7.1. In this leading order model the binary parameters primarily set the magnitude of the flux rather than its parity structure, so we do not expect the sign of the coefficient a to change with binary parameters.

We emphasize that the mechanism underlying Eq. (7.25) requires the outer boundary to be causally connected with the source (i.e., that reflected gauge perturbations can return on a timescale $\sim 2R$). If instead the outer boundary is placed sufficiently far out that the evolution time satisfies $t_{\rm evol} \lesssim 2R$, the feedback loop is effectively absent.

7.5 Modified boundary conditions

Having understood how the Sommerfeld boundary condition in Eq. (7.15) leads to exponential drift of the CoM, we now use Eq. (7.16) to modify the boundary condition to control the gauge reflection and the CoM drift. The parameter $\mathbf{r_0}$ is introduced as a source term in the boundary condition. Following the derivation in Sec. 7.4, we obtain the equation of motion for the CoM under Eq. (7.16)

$$\ddot{\mathbf{r}}_{\mathrm{s}(t)} + \frac{a}{R^3}\left(\mathbf{r_0} - \mathbf{r}_{\rm s}\right)_{(t_{\rm ret})} = 0. \tag{7.27}$$

For $t \gg R$, the second term can be linearly expanded as

$$\ddot{\mathbf{r}}_{\rm s} - \frac{2b}{R^2}\left(\dot{\mathbf{r}}_{\mathbf{0}} - \dot{\mathbf{r}}_{\rm s}\right) + \frac{a}{R^3}\left(\mathbf{r_0} - \mathbf{r}_{\rm s}\right) = 0, \tag{7.28}$$

where $b = (t - t_{\rm ret})/(2R)$.

We approximately treat b as a constant parameter, given that the location of the outer boundary doesn't change significantly during the simulation, i.e., $\Delta R/R \ll 1$. Then we can treat the CoM coordinate quantities (i.e., $\mathbf{r}_{\rm s}$, $\dot{\mathbf{r}}_{\rm s}$ and $\ddot{\mathbf{r}}_{\rm s}$) as measured at the time when the boundary condition is imposed, rather than at the retarded time.

One possible approach to control the drift is to allow the auxiliary parameter $\mathbf{r_0}$ above to depend on $\mathbf{r}_{\rm s}$, $\dot{\mathbf{r}}_{\rm s}$ and t in a way that ensures the solution to Eq. (7.28) does not exhibit exponential growth. In the following, we consider two specific forms of such dependence.

Example 1

We take a simple case as an example. Consider $\mathbf{r_0} = \lambda \mathbf{r}_\mathrm{s}$, where λ is a free parameter. Substituting into the CoM equation of motion Eq. (7.28), we get

$$\ddot{\mathbf{r}}_\mathrm{s} - 2\sigma\dot{\mathbf{r}}_\mathrm{s} + \omega^2\mathbf{r}_\mathrm{s} = 0, \tag{7.29}$$

where

$$\sigma = b\frac{(\lambda - 1)}{R^2}, \quad \omega = \sqrt{a}\frac{(\lambda - 1)^{1/2}}{R^{1.5}}. \tag{7.30}$$

For the limit $R \gg r_\mathrm{s}$ and $t \gg 1$, the equation gives

$$\mathbf{r}_\mathrm{s} = \begin{cases} \mathbf{A}e^{|\omega| t} & (\lambda < 1), \\ \mathbf{A}e^{\sigma t}\sin(\omega t + \phi_0) & (\lambda > 1). \end{cases} \tag{7.31}$$

In terms of the incoming characteristic field, the boundary condition Eq. (7.16) reads

$$\begin{aligned} P^{\mathrm{G}cd}_{ab} d_t \Bigg[u^{1-}_{cd} + \left(n^i - \frac{r^i - \lambda r^i_\mathrm{s}}{|\mathbf{r} - \mathbf{r_s}|} \right) \Phi_{icd} \\ + \left(\gamma_2 - \frac{1}{|\mathbf{r} - \lambda\mathbf{r_s}|} \right) g_{cd} \Bigg] \doteq 0. \end{aligned} \tag{7.32}$$

To test the model, we perform simulations of equal-mass and non-spinning system with different outer boundary radii R and free parameter λ. The initial separation is $19\,M$ and the merger time is around $11000\,M$. The simulation results exhibit strong agreement with the model fitting based on Eq. (7.31), as shown in Figure 7.6. By fitting the growth rate σ and frequency ω from Eq. (7.30) and (7.31) to the NR results for different λ, we obtain the parameters $a = 0.54$ and $b = 0.64$, which are independent of λ. The parameter b is greater than a due to the GR time lag.

To further test this model, we consider the growth rate $\sigma = 0.64(\lambda - 1)/R^2$. According to this formulation, when $(\lambda - 1) \sim R^2$, the growth rate is expected to be independent of R. We plot the CoM drift for different R and λ in Fig. 7.7. The observed results indeed agree with the anticipated behavior.

Eq. (7.31) shows that the growth rate of the solution is always positive, regardless of the value of the free parameter λ. One way to decelerate the CoM is to introduce an additional term involving $\dot{\mathbf{r}}_\mathrm{s}$ in the equation of motion, Eq. (7.29), to act as a damping term.

To do this, we introduce an additional velocity term to Eq. (7.16):

$$L(\mathbf{r_0}, \dot{\mathbf{r}}_\mathrm{s}, \mu) = \partial_t + \partial_{|\mathbf{r} - \mathbf{r_0}|} + \frac{1}{|\mathbf{r} - \mathbf{r_0}|} + \mu \mathbf{n} \cdot \dot{\mathbf{r}}_\mathrm{s}, \tag{7.33}$$

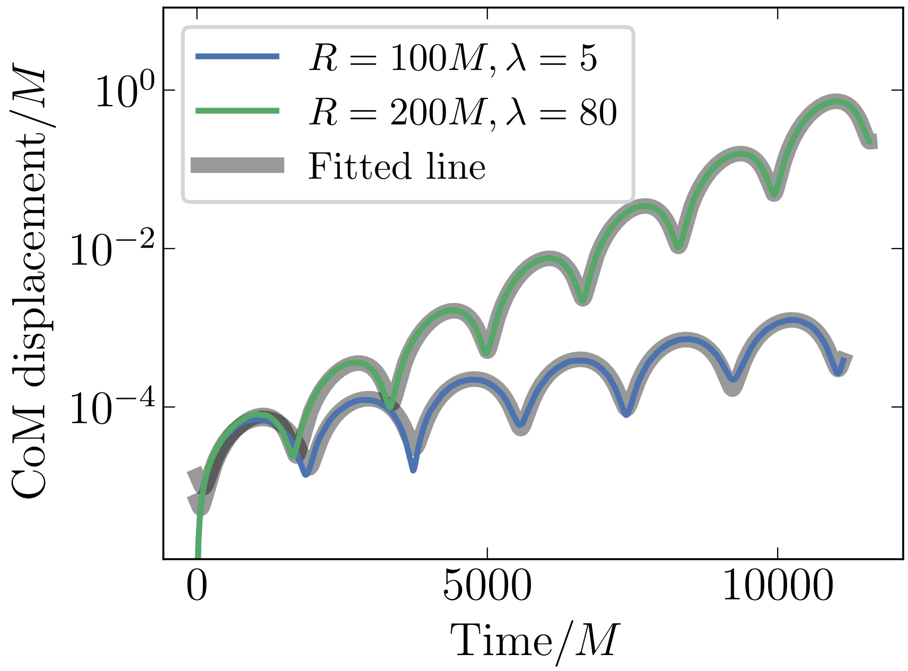

Figure 7.6: The green and blue lines are the results for $R = 100\,M, \lambda = 5$ and $R = 200\,M, \lambda = 80$, respectively, under gauge boundary condition Eq. (7.32). The wider gray lines are there fits. The system is equal-mass and non-spinning. The initial separation is $19\,M$ and the merger time is around $11000\,M$.

where $\mathbf{n}$ represents the outward-pointing normal vector to the outer boundary, and μ is a parameter. With this modification, the boundary condition, expressed in terms of the incoming characteristic field, becomes:

$$\begin{aligned} P^{\mathrm{G}cd}_{ab} d_t \Bigg[u^{1-}_{cd} + \left(n^i - \frac{r^i - \lambda r^i_{\mathrm{s}}}{|\mathbf{r} - \lambda \mathbf{r_s}|} \right) \Phi_{icd} \\ + \left(\gamma_2 - \frac{1}{|\mathbf{r} - \lambda \mathbf{r_s}|} \right) g_{cd} - \mu \frac{r^i - r^i_{\mathrm{s}}}{|\mathbf{r} - \lambda \mathbf{r_s}|} \dot{r}^i_{\mathrm{s}} \Bigg] \doteq 0. \end{aligned} \tag{7.34}$$

Here r_s and its time derivative are evaluated at the same coordinate time that the boundary condition is imposed. The post-Newtonian equation of motion of the CoM under this new boundary condition is then

$$(1 - 2b\mu R)\, \ddot{\mathbf{r}}_{\mathrm{s}} + (\mu - 2\sigma)\, \dot{\mathbf{r}}_{\mathrm{s}} + \omega^2 \mathbf{r}_{\mathrm{s}} = 0, \tag{7.35}$$

where b is the dimensionless retarded time parameter introduced in Eq. (7.28). For this equation to exhibit damping behavior, the parameter μ must satisfy the following conditions:

$$\begin{cases} (\mu - 2\sigma)^2 < 4\omega^2 (1 - 2b\mu R), \\ 2\sigma < \mu < \frac{1}{2bR}. \end{cases} \tag{7.36}$$

As a good choice, we can set

$$\mu \equiv \omega + 2\sigma. \tag{7.37}$$

Now the only remaining free parameter is λ. As discussed in Sec. 7.4, we can set $(\lambda - 1) \sim R^2$ so that the growth or damping rate becomes independent of the outer boundary radius. For $(\lambda - 1) = (R/100)^2$, the corresponding results are displayed in Fig. 7.8. This demonstrates the effectiveness of the modified boundary condition in damping the CoM drift.

An alternative way to introduce CoM damping for Eq. (7.29) without introducing an additional damping term like Eq. (7.33) is to use $\mathbf{r_0}$ in the boundary condition only when the CoM is accelerating. Namely,

$$\mathbf{r_0} = \begin{cases} \lambda \mathbf{r}_{\mathrm{s}} & (\ddot{\mathbf{r}}_{\mathrm{s}} \cdot \dot{\mathbf{r}}_{\mathrm{s}} \geq 0), \\ 0 & (\ddot{\mathbf{r}}_{\mathrm{s}} \cdot \dot{\mathbf{r}}_{\mathrm{s}} < 0). \end{cases} \tag{7.38}$$

The result for this approach is shown in Fig. 7.9, where we increased the initial separation to 29 M and the merger time to around 50000 M to show the long term behavior, since the oscillation time scale is longer than the previous cases. This approach is more robust than Eq. (7.33) because it has fewer parameters.

Example 2

Now we consider $\mathbf{r_0} = \mathbf{r}_{\mathrm{s}} + \eta R \dot{\mathbf{r}}_{\mathrm{s}}$, where η is a free parameter. The boundary condition expressed in terms of the incoming characteristic field then reads

$$\begin{aligned} P^{\mathrm{G}cd}_{ab} d_t \Bigg[u^{1-}_{cd} &+ \left(n^i - \frac{r^i - r^i_{\mathrm{s}} - \eta R \dot{r}^i_{\mathrm{s}}}{|\mathbf{r} - \mathbf{r_s} - \eta R \dot{\mathbf{r}}_{\mathrm{s}}|} \right) \Phi_{icd} \\ &+ \left(\gamma_2 - \frac{1}{|\mathbf{r} - \mathbf{r_s} - \eta R \dot{\mathbf{r}}_{\mathrm{s}}|} \right) g_{cd} \Bigg] \doteq 0. \end{aligned} \tag{7.39}$$

Then the CoM equation of motion Eq. (7.28) becomes

$$\alpha \ddot{\mathbf{r}}_{\mathrm{s}} + \beta \dot{\mathbf{r}}_{\mathrm{s}} = 0, \tag{7.40}$$

where

$$\alpha = 1 - \frac{2b\eta}{R}, \quad \beta = \frac{a\eta}{R^2}. \tag{7.41}$$

The equation gives

$$\mathbf{r}_{\mathrm{s}} = \mathbf{c_1} - \mathbf{c_2} e^{-\alpha t/\beta}, \tag{7.42}$$

where $\mathbf{c_1}$ and $\mathbf{c_2}$ are constants determined by the initial conditions. Eq. (7.42) guarantees a damping solution as long as $\alpha > 0$. We plot the CoM drift and velocity under this gauge boundary condition in Fig. 7.10. This approach avoids the oscillation of CoM around the coordinate origin, but the damping rate of the CoM drift is smaller than the other example.

General system

The results obtained so far are specific to equal-mass non-spinning systems. In more general cases with non-equal masses and spin precession, the Newtonian measurement of CoM can exhibit circular motion in addition to the linear drift, as indicated by the blue curve in Fig. 7.11. However, in the new gauge boundary condition, Eq. (7.16) or (7.33), we require the orbit-averaged drift coordinate and drift velocity as $\mathbf{r}_\mathrm{s}$ and $\dot{\mathbf{r}}_\mathrm{s}$, rather than the quantities associated with the circular motion. So we average the CoM coordinate and velocity over that last available orbit during the simulation, and take the averaged quantities $\langle \mathbf{r}_\mathrm{s} \rangle$ and $\langle \dot{\mathbf{r}}_\mathrm{s} \rangle$ in the boundary condition. Here $\langle f \rangle = \frac{\int_{t_0}^{t} f(t')dt'}{t-t_0}$, where t_0 is found by maximizing the dot product $\mathbf{r}_{12}(t) \cdot \mathbf{r}_{12}(t_0)$ over a time window $[t - 3\pi/\Omega, t - \pi/\Omega]$, with Ω being the orbital angular velocity.

As an illustration, we take the boundary condition Eq. (7.16) with Eq. (7.38). We use a system with mass ratio $q = 1$ and dimensionless spin parameters $\chi_1 = (0.1, 0.2, 0.3)$ and $\chi_2 = (0.2, 0.4, 0.1)$. The initial separation is 29 M and the merger time is around 65000 M. The resulting trajectory is shown as the green curve in Fig. 7.11, the vectorial displacement of the CoM under the new BC is shown in Fig. 7.12, and the overall CoM drifting is shown in Fig. 7.13. The surge of the CoM velocity near merger is expected and physical: it is the kick due to the asymmetry of the BBH system. Testing shows that this approach is effective for mass ratio q up to 8 and spin $|\chi_{1,2}|$ up to 0.8.

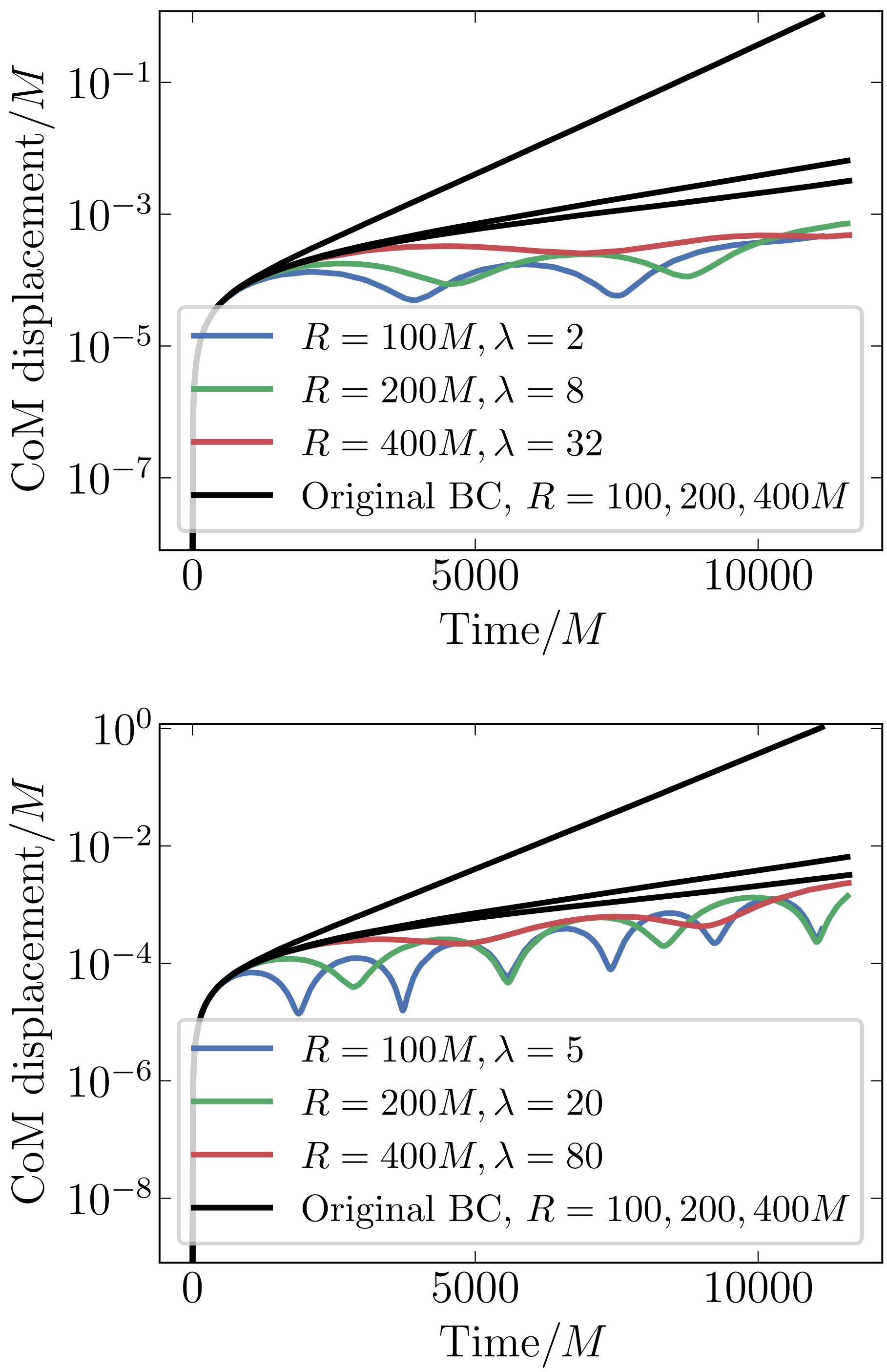

Figure 7.7: Different results with similar $(\lambda - 1)/R^2$ ratio under gauge boundary condition Eq. (7.32). The system is equal-mass and non-spinning. The initial separation is $19\,M$ and the merger time is around $11000\,M$.

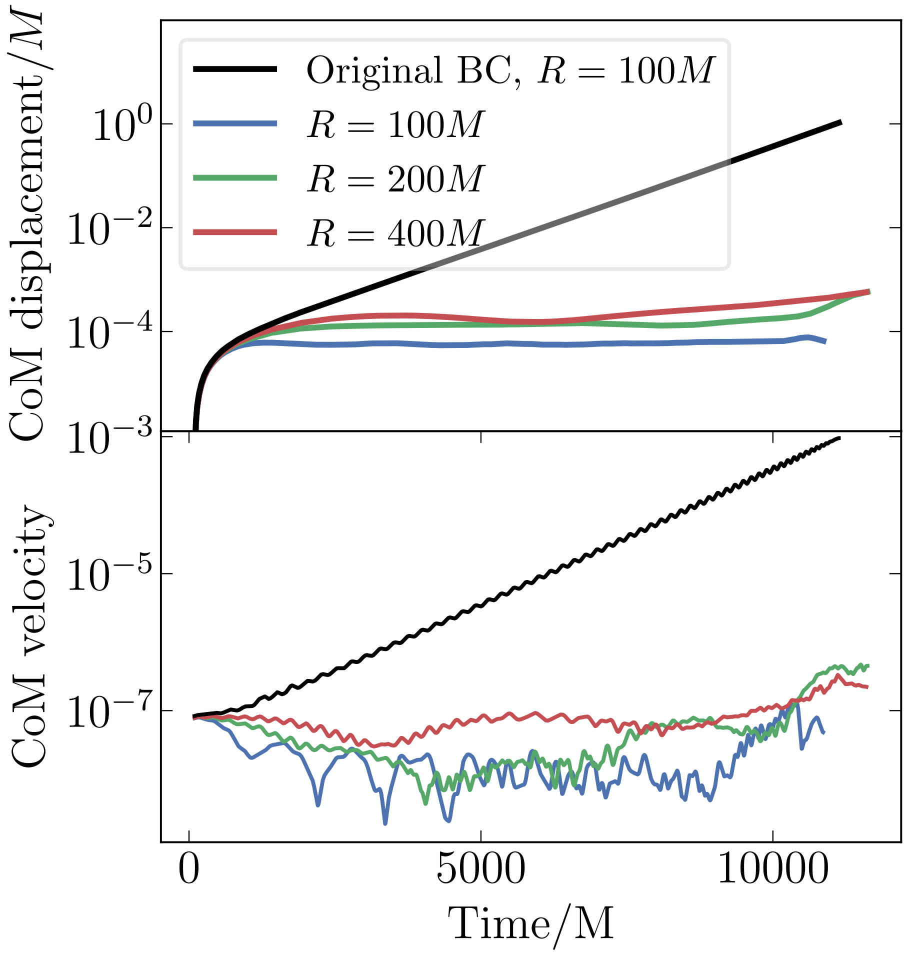

Figure 7.8: CoM drift and velocity under the gauge boundary condition Eq. (7.34) with $\lambda = 1 + (R/100)^2$. The upper panel shows the CoM drift and the lower panel shows the CoM velocities. The black curves are the results obtained using the original Sommerfeld boundary condition, and the other curves are results with the new boundary condition for $R = 100M, 200M$ and $400M$. The system is equal-mass and non-spinning. The initial separation is $19\,M$ and the merger time is around $11000\,M$.

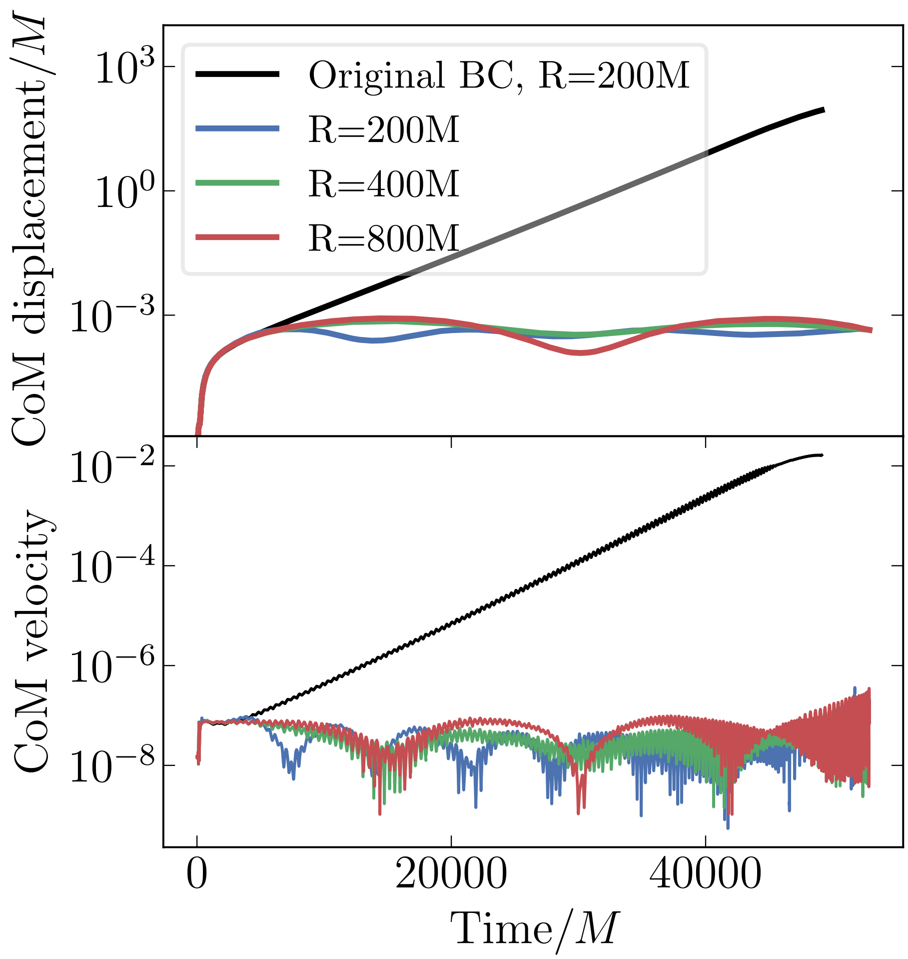

Figure 7.9: CoM drift and velocity under gauge boundary condition Eq. (7.32) with $\mathbf{r_0}$ specified by Eq. (7.38), where $\lambda = 1 + (R/100)^2$. The upper panel shows the CoM drift and the lower panel shows the CoM velocities. The black curves are the results obtained using the original Sommerfeld boundary condition, and other curves are results under the new boundary condition for $R = 200M, 400M$ and $800M$. The system is equal-mass and non-spinning. The initial separation is 29 M and the merger time is around 50000 M.

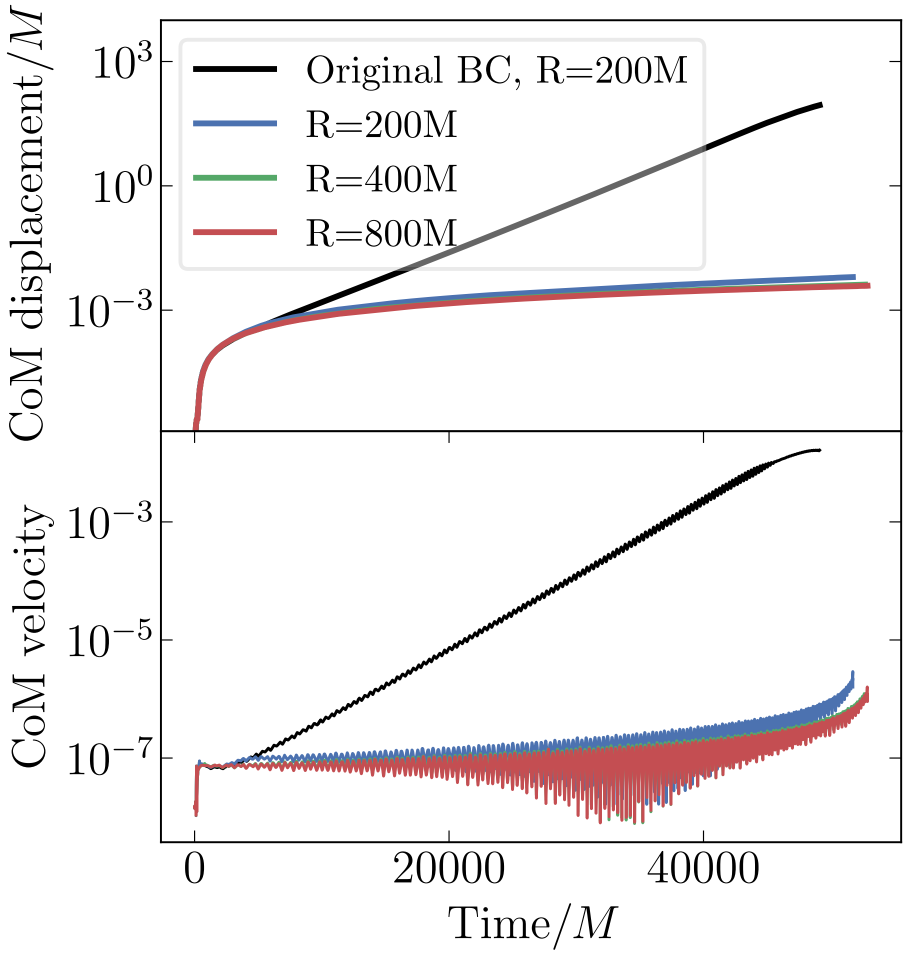

Figure 7.10: CoM drift and velocity under gauge boundary condition Eq. (7.39) with $\mathbf{r_0} = \mathbf{r}_s + \eta R \dot{\mathbf{r}}_s$, where $\eta = R/4$. The upper panel shows the CoM drift and the lower panel shows the CoM velocities. The black curves are the results obtained using the original Sommerfeld boundary condition, and the other curves are results under the new boundary condition for $R = 200M, 400M$ and $800M$. The system is equal-mass and non-spinning. The initial separation is 29 M and the merger time is around 50000 M.

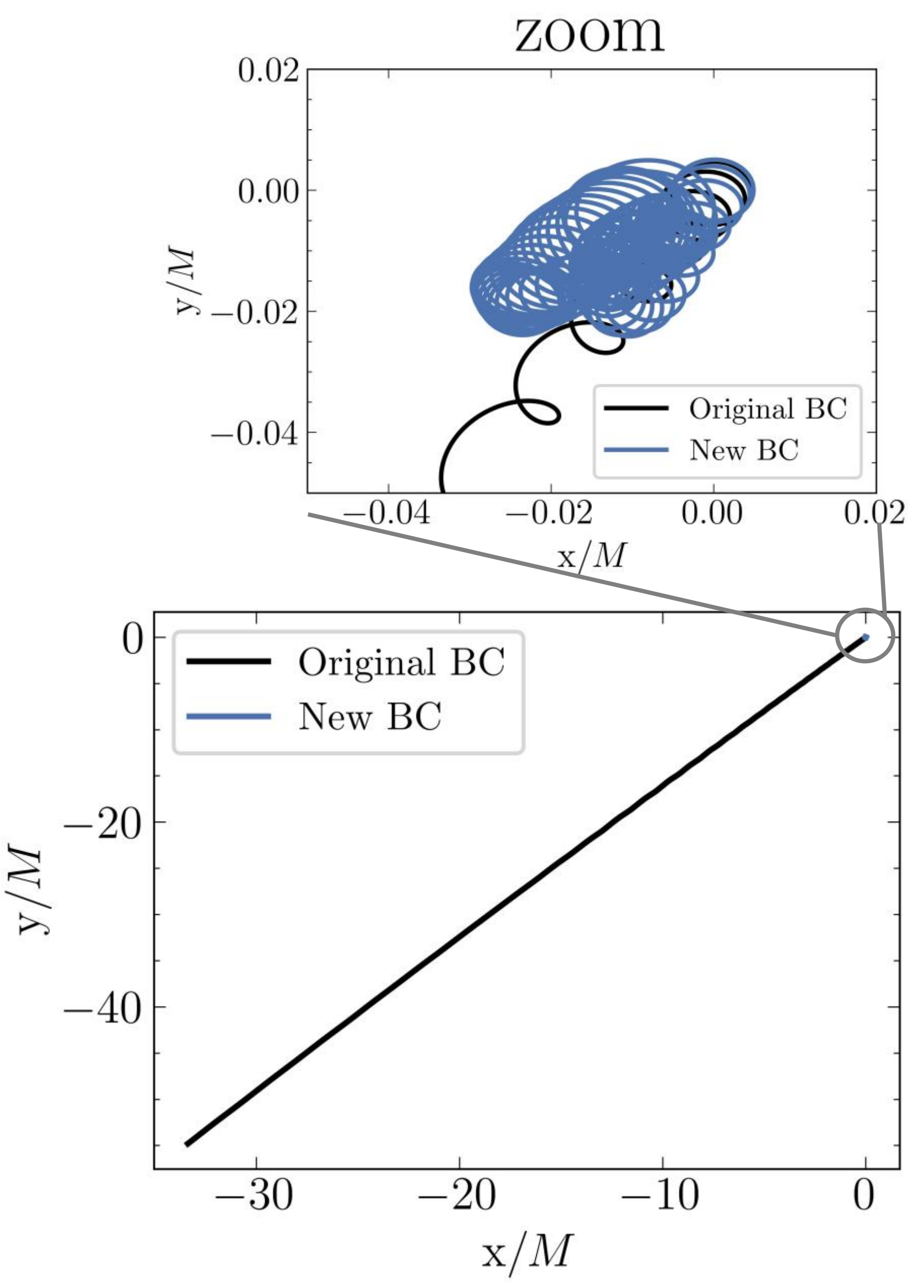

Figure 7.11: CoM trajectory under gauge boundary condition Eq. (7.32) with $\mathbf{r_0}$ specified by Eq. (7.38), where $\lambda = 1 + (R/100)^2$, with a zoom-in near the origin in the upper smaller panel. The black curve is obtained using the original Sommerfeld boundary condition, and the blue curve is obtained using the new boundary condition. The system has $q = 1$, $\chi_1 = (0.1, 0.2, 0.3)$, $\chi_2 = (0.2, 0.4, 0.1)$, and $R = 200\,M$. The initial separation is 29 M and the merger time is around 65000 M. The vectorial displacement of the CoM under the new BC is shown in Fig. 7.12, and the overall CoM drifting is shown in Fig. 7.13.

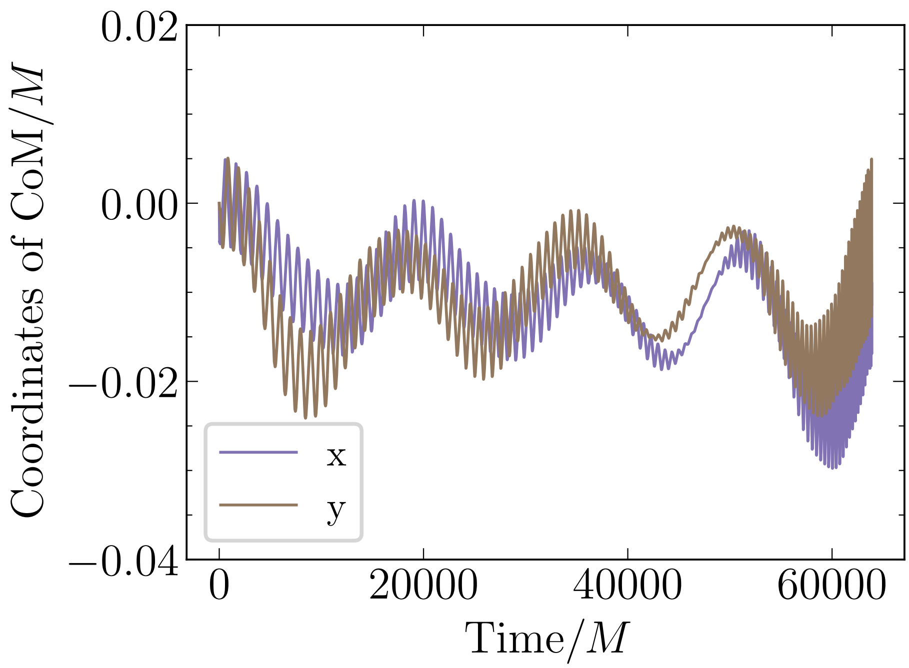

Figure 7.12: The x and y coordinates of CoM under the new boundary condition with the same configuration with Fig. 7.11.

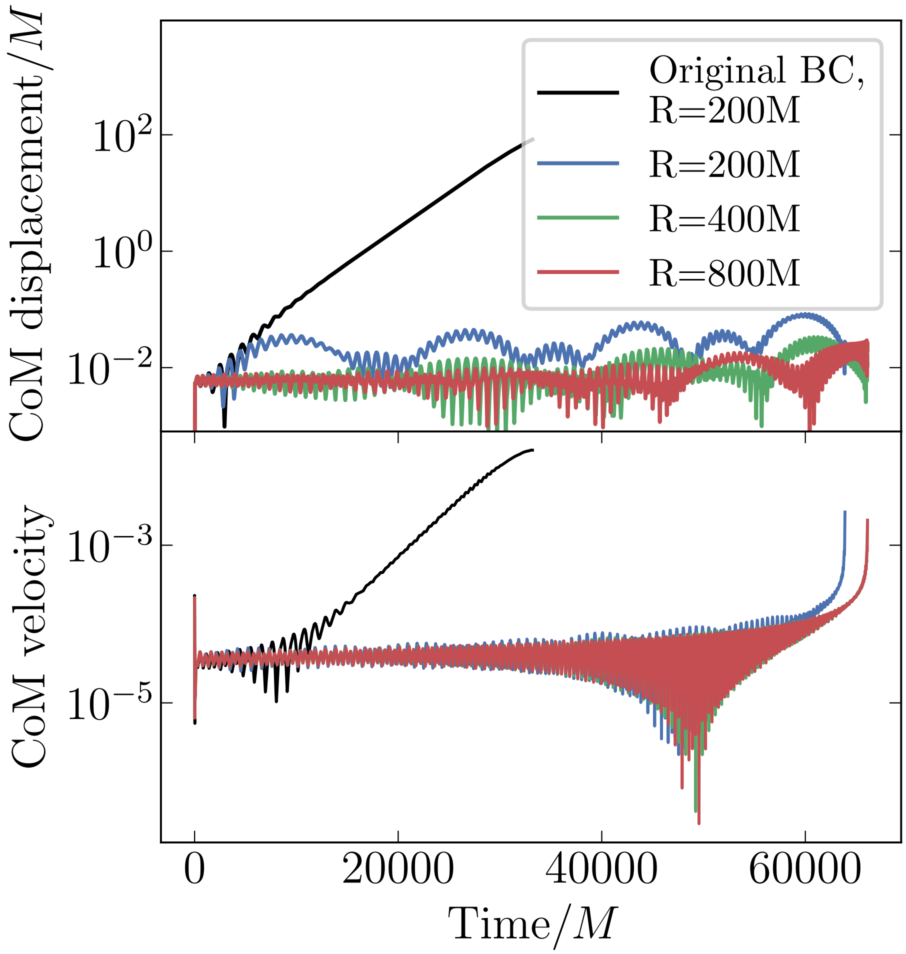

Figure 7.13: CoM drift and velocity under gauge boundary condition Eq. (7.32) with $\mathbf{r_0}$ specified by Eq. (7.38), where $\lambda = 1 + (R/100)^2$. The upper panel shows the CoM drift and the lower panel shows the CoM velocities. The black curves are the results obtained using the original Sommerfeld boundary condition, and the other curves are results under new boundary condition for $R = 200M, 400M$ and $800M$. The system has $q = 1$, $\chi_1 = (0.1, 0.2, 0.3)$, and $\chi_2 = (0.2, 0.4, 0.1)$. The initial separation is 29 M and the merger time is around 65000 M. The black curves end earlier because the CoM displacement gets so large that the simulation crashes.

7.6 The effect on waveforms

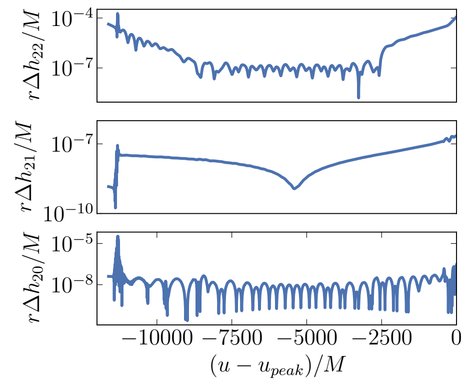

(a) The waveform difference for the equal-mass non-spinning case, $R = 800\,M$. The matching window to fix the time shift and rotation starts from 8000 M before merger, and is 10 orbits long. The BMS frame is fixed at the center of this matching window.

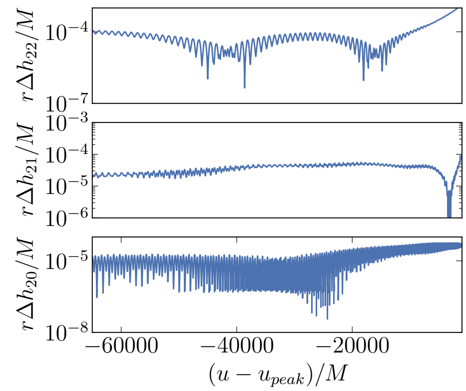

(b) The waveform difference for the precessing case with $q = 1$, $\chi_1 = (0.1, 0.2, 0.3)$, $\chi_2 = (0.2, 0.4, 0.1)$, and $R = 800\,M$. The matching window to fix the time shift and rotation starts from 58000 M before merger, and is 50000 M long. The BMS frame is fixed at the center of this matching window.

Figure 7.14: The waveform differences under modified gauge boundary condition Eq. (7.32) with $\mathbf{r_0}$ specified by Eq. (7.38), where $\lambda = 1 + (R/100)^2$, and original boundary condition Eq. (7.13) for two systems. We follow the procedure discussed in Sec. IV of [34] to fix the BMS frame, rotation and time shift between the two waveforms.

In theory, modification to a gauge boundary condition should not have any impact on waveforms. However, it is crucial to check this. The conclusion should be general to all waveforms, not specific to a single example, since our boundary condition treatments do not depend on the intrinsic parameters of the system like masses and spins.

It is worth noting that the BBH system exhibits asymptotically flat behavior. Bondi, van der Burg, Metzner, and Sachs [18, 19, 20] demonstrated that the spacetime symmetry at the asymptotic boundary can be described by the Bondi-van der Burg-Metzner-Sachs (BMS) group. This BMS group characterizes the asymptotic symmetry of spacetimes that are asymptotically flat at null infinity. Refs. [17, 34] showed the importance of having both waveforms in the same BMS frame for making accurate comparisons. We follow their process to map waveforms obtained using CCE to the same BMS frame using the `scri` package [28] and the `NRPNHybridization` code [35].

After fixing the BMS frame and performing the required 3-D rotation and time alignment, we observe that the time-domain mismatch between the waveforms obtained under the Sommerfeld gauge boundary condition and our new gauge boundary condition for the equal-mass and non-spinning system over a 10000 M window is on the order of 10^{-12}, and for the precessing system over a 60000 M window is on the order of 10^{-7}. The residual is depicted in Fig. 7.14 for these two cases. This mismatch is much smaller than the numerical error between different resolutions, since the numerical error is dominated by the grid spacing, and we are not changing the grids when modifying the boundary condition. The mismatch is consistent with the tolerance of BMS frame fixing and rotation alignment. So there is no evidence suggesting that the modification of the gauge boundary condition can affect the waveform, once all the gauge ambiguities are fixed. This is as expected since we only modify the gauge part of the boundary conditions.

7.7 Alternative Boundary Conditions

Bayliss-Turkel condition

Since Fig. 7.3 shows that the Sommerfeld boundary condition is only non-reflective for the $\ell = 0$ mode, a straightforward idea is to use higher-order boundary conditions that are non-reflective for higher ℓ modes. Such boundary conditions are known as Bayliss-Turkel boundary conditions [36]. They are given by

$$B_k \psi \doteq 0, \tag{7.43}$$

where

$$B_k = \Pi_\ell^k \left(\partial_t + \partial_r + \frac{2\ell - 1}{r} \right). \tag{7.44}$$

However, given the presence of the high order derivatives, the well-posedness of these high-order boundary conditions when applied to the first order Generalized-Harmonic evolution [31] is not yet proven.

Here we test the second-order Bayliss-Turkel boundary condition. In terms of incoming characteristic fields in SpEC, it can be written as

$$\begin{aligned} P^{\mathrm{G}cd}_{ab} \Big[\partial_t u^{1-}_{cd} - \partial_t \partial_r g_{cd} - \partial_r^2 (g_{cd} - g^{\text{background}}_{cd}) \\ + \left(\gamma_2 - \frac{4}{r} \right) \partial_t g_{cd} - \frac{4}{r} \partial_r (g_{cd} - g^{\text{background}}_{cd}) \\ - \frac{2}{r^2} (g_{cd} - g^{\text{background}}_{cd}) \Big] \doteq 0. \end{aligned} \tag{7.45}$$

Here the first derivatives of the metric are computed using the fundamental variables Φ and Π in the first-order GH system [31], and the second derivatives of the metric are computed from derivatives of Φ and Π. To approximate $g^{\text{background}}$, we tried using the Minkowski metric, the Schwarzschild metric, and the metric used in the initial condition. However, in all cases, there were large junk reflections that caused discontinuities in both CoM velocity and CoM drift, and even led to simulation crashes. This raises concerns about the suitability of the second-order Bayliss-Turkel boundary conditions for BBH simulations in SpEC.

An alternative approach to implement the Bayliss-Turkel type boundary condition without using the background metric is to introduce auxiliary variables defined on the outer boundary that evolve via a simple ODE system [37]. These variables represent the residuals of the Bayliss–Turkel type absorbing operator Eq. (7.44) for each l, m mode at each order k. Driving them consistently to zero enforces the higher-order absorbing condition. In [37], the higher-order absorbing condition is only imposed on the physical degrees of freedom, and it is shown that the coordinate drift of CoM is not reduced. We leave further investigation of imposing higher-order boundary conditions on the gauge degrees of freedom for future studies.

Gauge constraint damping condition

The gauge constraint damping boundary condition[38] explicitly drives the incoming characteristic fields on the outer boundary to satisfy the gauge condition $C_a = H_a - \nabla^c \nabla_c x_a \to 0$.

The gauge constraint damping boundary condition can be written as

$$d_t u^{1-} \doteq -\mu_B \left(u^{1-} - u^{1-}|_{\text{BC}} \right), \tag{7.46}$$

where μ_B is a freely chosen damping parameter that exponentially suppresses any constraint violation crossing the boundary, and $u^{1-}_{ab} l^b|_{\text{BC}}$ is chosen so that the incoming characteristic projection of the constraint fields C_a vanishes. In terms of the characteristic variables in SpEC, the gauge constraint damping boundary condition reads

$$\begin{aligned} P^{\text{G}cd}_{ab} d_t u^{1-}_{cd} &\doteq -\mu_B P^{\text{G}cd}_{ab} \left(u^{1-}_{cd} - u^{1-}_{cd}|_{\text{BC}} \right) \\ &\doteq \frac{\mu_B}{\sqrt{2}} \left(k_a k_b l^c + k_a \delta^c_b + k_b \delta^c_a \right) \left(\delta^d_c - t_c t^d \right) C_d . \end{aligned} \tag{7.47}$$

Please refer to Appendix E of Ref. [38] for details.

The gauge constraint damping boundary condition should be effective at suppressing violations of the GH gauge constraints at the outer boundary [38]. Nevertheless, this condition does not enforce a purely outgoing wave: the gauge condition Eq. (7.11) still admits both ingoing and outgoing gauge modes, so reflections can still occur in practice. Fig. 7.15 compares the CoM drift and its velocity for an equal-mass, non-spinning system with an initial separation of 29 M, and the merger time is around 50000 M. Evolution that uses the gauge constraint damping boundary condition (blue curves) exhibits an even larger drift than the result obtained using the original Sommerfeld condition (black curves), indicating that the gauge constraint damping boundary condition does not reduce the reflection from the outer boundary and therefore fails to reduce the CoM drift.

Multipolar post-Minkowskian (MPM)

Another potential approach to reduce the CoM drift is to impose the boundary condition with analytic data supplied by the multipolar post-Minkowskian (MPM) expansion [39, 40, 41, 42]. Ref. [43] gives the multipolar post-Minkowskian metric in Bondi coordinates, expressed entirely in terms of the source's mass and current multipole moments. By mapping the NR Cauchy coordinates to the Bondi frame using the CCE procedure developed in [25], one can evaluate the MPM solution on the outer boundary and supply it as time-dependent boundary data for the Cauchy evolution. Because this analytically matched metric already satisfies the correct outgoing-radiation behavior, it should suppress gauge reflections at the boundary and is therefore expected to reduce the CoM drift. This procedure is significantly more complicated than other methods discussed here, so we leave it for future studies.

Cauchy-Characteristic matching (CCM)

Alternatively, Cauchy-Characteristic matching (CCM) [44, 45, 46, 47] can also provide accurate physical boundary conditions for the Cauchy domain by performing a matching of the internal Cauchy system and the exterior characteristic system. But currently only the physical part of the fields is matched for BBH systems [46, 47]. Using CCM for the gauge part of the fields is a promising approach to reduce the CoM drift, and we leave this also for future studies.

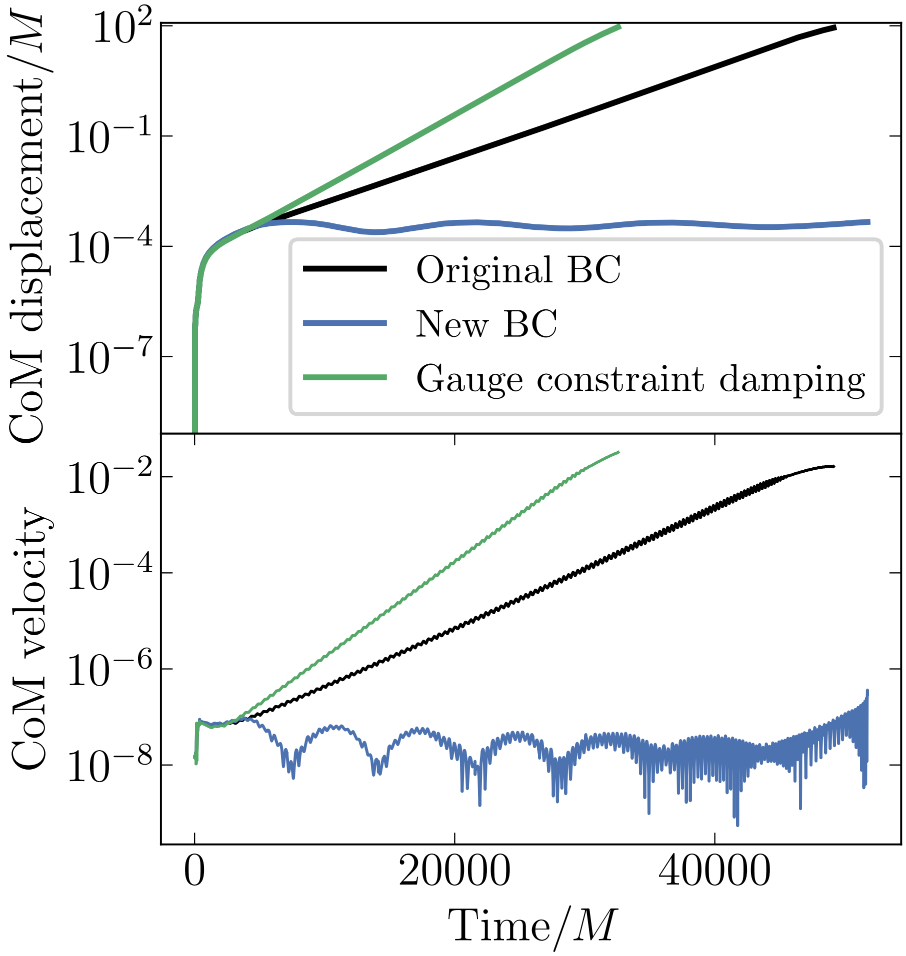

Figure 7.15: CoM drift and velocity for an equal-mass and non-spinning system with an initial separation of 29 M, outer boundary radius $R = 200\,M$, and the merger time is around 50000 M. The upper panel shows the CoM drift and the lower panel showx the CoM velocities. The black curves are the results obtained using the original Sommerfeld boundary condition Eq. (7.13). The blue curves are results under gauge boundary condition Eq. (7.32), with $\mathbf{r_0}$ specified by Eq. (7.38), where $\lambda = 1 + (R/100)^2$. The green curves are results under the gauge constraint damping boundary condition Eq. (7.47). The green curves end earlier because the CoM displacement gets so large that the simulation crashes.

7.8 Conclusions

In this paper, we analyze the exponential drift of the CoM during long NR simulations of BBH systems. We have demonstrated that this drift is primarily caused by the reflection due to the gauge outer boundary conditions. To understand this issue, in the post-Newtonian approximation we have derived the equation of motion for the CoM under various versions of the gauge boundary conditions.

To mitigate the drift, we propose a modification of the boundary conditions by introducing CoM source terms. The specific form of the source term is not unique, and we present two specific examples showing that the CoM drift can be reduced by several orders of magnitude by incorporating these source terms into the gauge boundary condition.

Acknowledgments

We thank Nils Deppe, Kyle Nelli, Himanshu Chaudhary, Qing Dai and Harald Pfeiffer for useful discussions. This work was supported in part by the Sherman Fairchild Foundation, by NSF Grants PHY-2309211, PHY-2309231, and OAC-2209656 at Caltech, and PHY-2207342 and OAC-2209655 at Cornell. Research at Perimeter Institute is supported in part by the Government of Canada through the Department of Innovation, Science and Economic Development and by the Province of Ontario through the Ministry of Colleges and Universities. Computations for this work were performed on the Wheeler cluster at Caltech, which is supported by the Sherman Fairchild Foundation and by Caltech, and on the Resnick High Performance Computing (HPC) Cluster at the Caltech High Performance Computing Center.

References

[1] Dongze Sun et al. “Gauge Boundary conditions to mitigate center-of-mass drift in BBH simulations”. In: *Physical Review D* 113 (2026), p. 044016. doi: 10.1103/b1cd-qysb. arXiv: 2510.25465 [gr-qc].

[2] Frans Pretorius. “Evolution of binary black hole spacetimes”. In: *Phys. Rev. Lett.* 95 (2005), p. 121101. doi: 10.1103/PhysRevLett.95.121101. arXiv: gr-qc/0507014 [gr-qc].

[3] Manuela Campanelli et al. “Accurate evolutions of orbiting black-hole binaries without excision”. In: *Phys. Rev. Lett.* 96 (2006), p. 111101. doi: 10.1103/PhysRevLett.96.111101. arXiv: gr-qc/0511048 [gr-qc].

[4] John G. Baker et al. “Gravitational wave extraction from an inspiraling configuration of merging black holes”. In: *Phys. Rev. Lett.* 96 (2006), p. 111102. doi: 10.1103/PhysRevLett.96.111102. arXiv: gr-qc/0511103 [gr-qc].

[5] B. P. Abbott et al. “Tests of general relativity with GW150914”. In: *Phys. Rev. Lett.* 116.22 (2016). [Erratum: Phys. Rev. Lett.121,no.12,129902(2018)], p. 221101. doi: 10.1103/PhysRevLett.116.221101. arXiv: 1602.03841 [gr-qc].

[6] B. P. Abbott et al. “Tests of General Relativity with the Binary Black Hole Signals from the LIGO-Virgo Catalog GWTC-1”. In: *Phys. Rev.* D100.10

(2019), p. 104036. DOI: 10.1103/PhysRevD.100.104036. arXiv: 1903.04467 [gr-qc].

[7] R. Abbott et al. “Tests of General Relativity with GWTC-3”. In: (Dec. 2021). arXiv: 2112.06861 [gr-qc].

[8] *The Spectral Einstein Code*. http://www.black-holes.org/SpEC.html.

[9] Béla Szilágyi et al. “Approaching the Post-Newtonian Regime with Numerical Relativity: A Compact-Object Binary Simulation Spanning 350 Gravitational-Wave Cycles”. In: *Physical Review Letters* 115.3 (July 2015). DOI: 10.1103/physrevlett.115.031102. URL: https://doi.org/10.1103%2Fphysrevlett.115.031102.

[10] Denis Pollney et al. “Asymptotic falloff of local waveform measurements in numerical relativity”. In: *Physical Review D* 80.12 (Dec. 2009). ISSN: 1550-2368. DOI: 10.1103/physrevd.80.121502. URL: http://dx.doi.org/10.1103/PhysRevD.80.121502.

[11] Ian Hinder. “The current status of binary black hole simulations in numerical relativity”. In: *Classical and Quantum Gravity* 27.11 (May 2010), p. 114004. DOI: 10.1088/0264-9381/27/11/114004. URL: https://dx.doi.org/10.1088/0264-9381/27/11/114004.

[12] Zachariah B. Etienne et al. “Improved moving puncture gauge conditions for compact binary evolutions”. In: *Physical Review D* 90.6 (Sept. 2014). ISSN: 1550-2368. DOI: 10.1103/physrevd.90.064032. URL: http://dx.doi.org/10.1103/PhysRevD.90.064032.

[13] Vassilios Mewes et al. “Numerical relativity in spherical coordinates with the Einstein Toolkit”. In: *Phys. Rev. D* 97 (8 Apr. 2018), p. 084059. DOI: 10.1103/PhysRevD.97.084059. URL: https://link.aps.org/doi/10.1103/PhysRevD.97.084059.

[14] Michael Boyle et al. “The SXS collaboration catalog of binary black hole simulations”. In: *Classical and Quantum Gravity* 36.19 (Sept. 2019), p. 195006. DOI: 10.1088/1361-6382/ab34e2. URL: https://dx.doi.org/10.1088/1361-6382/ab34e2.

[15] T Dray and M Streubel. “Angular momentum at null infinity”. In: *Classical and Quantum Gravity* 1.1 (Jan. 1984), p. 15. DOI: 10.1088/0264-9381/1/1/005. URL: https://dx.doi.org/10.1088/0264-9381/1/1/005.

[16] T Dray. “Momentum flux at null infinity”. In: *Classical and Quantum Gravity* 2.1 (Jan. 1985), p. L7. DOI: 10.1088/0264-9381/2/1/002. URL: https://dx.doi.org/10.1088/0264-9381/2/1/002.

[17] Keefe Mitman et al. “Fixing the BMS frame of numerical relativity waveforms”. In: *Phys. Rev. D* 104 (2 July 2021), p. 024051. DOI: 10.1103/PhysRevD.104.024051. URL: https://link.aps.org/doi/10.1103/PhysRevD.104.024051.

[18] R. K. Sachs. "Gravitational waves in general relativity. VIII. Waves in asymptotically flat space-time". In: *Proc. Roy. Soc. Lond. A* 270 (1962), pp. 103–126. DOI: 10.1098/rspa.1962.0206.

[19] R. Sachs. "Asymptotic symmetries in gravitational theory". In: *Phys. Rev.* 128 (1962), pp. 2851–2864. DOI: 10.1103/PhysRev.128.2851.

[20] H. Bondi, M. G. J. van der Burg, and A. W. K. Metzner. "Gravitational waves in general relativity. VII. Waves from axi-symmetric isolated systems". In: *Proc. Roy. Soc. Lond. A* 269 (1962), pp. 21–52. DOI: 10.1098/rspa.1962.0161.

[21] Michael Boyle. "Transformations of asymptotic gravitational-wave data". In: *Phys. Rev. D* 93.8 (2016), p. 084031. DOI: 10.1103/PhysRevD.93.084031. arXiv: 1509.00862 [gr-qc].

[22] Keefe Mitman et al. "Fixing the BMS frame of numerical relativity waveforms with BMS charges". In: *Phys. Rev. D* 106 (8 Oct. 2022), p. 084029. DOI: 10.1103/PhysRevD.106.084029. URL: https://link.aps.org/doi/10.1103/PhysRevD.106.084029.

[23] E. T. Newman and R. Penrose. "Note on the Bondi-Metzner-Sachs group". In: *J. Math. Phys.* 7 (1966), pp. 863–870. DOI: 10.1063/1.1931221.

[24] Michael Boyle. "How should spin-weighted spherical functions be defined?" In: *J. Math. Phys.* 57.9 (2016), p. 092504. DOI: 10.1063/1.4962723. arXiv: 1604.08140 [gr-qc].

[25] Jordan Moxon, Mark A. Scheel, and Saul A. Teukolsky. "Improved Cauchy-characteristic evolution system for high-precision numerical relativity waveforms". In: *Physical Review D* 102.4 (Aug. 2020). DOI: 10.1103/physrevd.102.044052. URL: https://doi.org/10.1103%2Fphysrevd.102.044052.

[26] Jordan Moxon et al. *The SpECTRE Cauchy-characteristic evolution system for rapid, precise waveform extraction*. 2021. arXiv: 2110.08635 [gr-qc].

[27] Nils Deppe et al. *SpECTRE v2023.05.16*. 10.5281/zenodo.7942177. Version 2023.05.16. May 2023. DOI: 10.5281/zenodo.7942177. URL: https://spectre-code.org.

[28] Michael Boyle et al. *scri*. Version 2022.8.8. Nov. 2023. DOI: 10.5281/zenodo.4041971. URL: https://github.com/moble/scri.

[29] A. Sommerfeld. *Partial differential equations in physics*. Elsevier, 1949.

[30] Oliver Rinne, Lee Lindblom, and Mark A. Scheel. "Testing outer boundary treatments for the Einstein equations". In: *Class. Quant. Grav.* 24 (2007), pp. 4053–4078. DOI: 10.1088/0264-9381/24/16/006. arXiv: 0704.0782 [gr-qc].

[31] Lee Lindblom et al. "A New generalized harmonic evolution system". In: *Class. Quant. Grav.* 23 (2006), S447–S462. DOI: 10.1088/0264-9381/23/16/S09. arXiv: gr-qc/0512093 [gr-qc].

[32] Luc Blanchet and Thibault Damour. "Post-Newtonian generation of gravitational waves." In: *Annales De L Institut Henri Poincare-physique Theorique* 50 (1989), pp. 377–408. URL: https://api.semanticscholar.org/CorpusID:118762417.

[33] Luc Blanchet, Guillaume Faye, and Bénédicte Ponsot. "Gravitational field and equations of motion of compact binaries to 5/2 post-Newtonian order". In: *Physical Review D* 58.12 (Oct. 1998). ISSN: 1089-4918. DOI: 10.1103/physrevd.58.124002. URL: http://dx.doi.org/10.1103/PhysRevD.58.124002.

[34] Dongze Sun et al. "Optimizing post-Newtonian parameters and fixing the BMS frame for numerical-relativity waveform hybridizations". In: *Physical Review D* 110.10 (Nov. 2024). ISSN: 2470-0029. DOI: 10.1103/physrevd.110.104076. URL: http://dx.doi.org/10.1103/PhysRevD.110.104076.

[35] Dongze Sun. *NRPNHybridization*. https://github.com/dongzesun/NRPNHybridization.

[36] Alvin Bayliss and Eli Turkel. "Radiation boundary conditions for wave-like equations". In: *Communications on Pure and Applied Mathematics* 33.6 (Nov. 1980), pp. 707–725. ISSN: 0010-3640. DOI: 10.1002/cpa.3160330603.

[37] Luisa T Buchman et al. "Numerical relativity multimodal waveforms using absorbing boundary conditions". In: *Classical and Quantum Gravity* 41.17 (Aug. 2024), p. 175011. ISSN: 1361-6382. DOI: 10.1088/1361-6382/ad65af. URL: http://dx.doi.org/10.1088/1361-6382/ad65af.

[38] Lee Lindblom and Bela Szilagyi. "An Improved Gauge Driver for the GH Einstein System". In: *Phys. Rev.* D80 (2009), p. 084019. DOI: 10.1103/PhysRevD.80.084019. arXiv: 0904.4873 [gr-qc].

[39] K. S. Thorne. "Multipole Expansions of Gravitational Radiation". In: *Rev. Mod. Phys.* 52 (1980), pp. 299–339. DOI: 10.1103/RevModPhys.52.299.

[40] L. Blanchet and T. Damour. "Radiative gravitational fields in general relativity I. General structure of the field outside the source". In: *Philosophical Transactions of the Royal Society of London. Series A, Mathematical and Physical Sciences* (1986). ISSN: 320379–430. DOI: 10.1098/rsta.1986.0125. URL: http://doi.org/10.1098/rsta.1986.0125.

[41] Luc Blanchet. "On the multipole expansion of the gravitational field". In: *Classical and Quantum Gravity* 15.7 (July 1998), pp. 1971–1999. ISSN: 1361-6382. DOI: 10.1088/0264-9381/15/7/013. URL: http://dx.doi.org/10.1088/0264-9381/15/7/013.

[42] Luc Blanchet, Thibault Damour, and Bala R. Iyer. "Erratum: Gravitational waves from inspiralling compact binaries: Energy loss and waveform to second-post-Newtonian order". In: *Phys. Rev. D* 54 (2 July 1996), pp. 1860–1860. DOI: 10.1103/PhysRevD.54.1860. URL: https://link.aps.org/doi/10.1103/PhysRevD.54.1860.

[43] Luc Blanchet et al. "Multipole expansion of gravitational waves: from harmonic to Bondi coordinates". In: *Journal of High Energy Physics* 2021.2 (Feb. 2021). ISSN: 1029-8479. DOI: 10.1007/jhep02(2021)029. URL: http://dx.doi.org/10.1007/JHEP02(2021)029.

[44] R d'Inverno, ed. *Approaches to Numerical Relativity*. Cambdrige: Cambridge University Press, 1992.

[45] N T Bishop. "Numerical relativity: combining the Cauchy and characteristic initial value problems". In: *Classical and Quantum Gravity* 10.2 (Feb. 1993), p. 333. DOI: 10.1088/0264-9381/10/2/015. URL: https://dx.doi.org/10.1088/0264-9381/10/2/015.

[46] Sizheng Ma et al. "Merging black holes with Cauchy-characteristic matching: Computation of late-time tails". In: (2024). arXiv: 2412.06906 [gr-qc]. URL: https://arxiv.org/abs/2412.06906.

[47] Sizheng Ma et al. "Fully relativistic three-dimensional Cauchy-characteristic matching for physical degrees of freedom". In: *Physical Review D* 109.12 (June 2024). ISSN: 2470-0029. DOI: 10.1103/physrevd.109.124027. URL: http://dx.doi.org/10.1103/PhysRevD.109.124027.

Chapter 8

FUTURE DIRECTIONS

The work in this dissertation develops a framework for connecting PN, BHPT, and NR descriptions of binary black holes through waveform hybridization, asymptotic-frame fixing, parameter matching, and gauge control. The results presented in the preceding chapters should therefore be viewed not only as individual contributions, but also as components of a broader program. The long-term goal is to build waveform models whose ingredients are connected by explicit geometric, gauge, and parameter maps, rather than by empirical alignment choices alone. This section summarizes several directions in which this program can be extended.

8.1 Closing the PN–BHPT–NR parameter map at high accuracy

The immediate next step is to close the full PN–BHPT–NR parameter-matching loop in high accuracy. The PN–BHPT side of this loop is supplied by matched-asymptotic calculations, which identify the nonspinning black-hole monopole and the local coordinate transformation between the PN near zone and the black-hole local frame in the overlap region [1, 2]. The parameter map is developed in Chapter. 4 at 1PN order. The NR–BHPT side is developed in Chapter. 5 by determining the local KS/BHPT mass and the coordinate transformation selected by the NR spacetime. Combining these two pieces would give a direct PN–NR parameter map mediated by BHPT,

$$\lambda_{\mathrm{PN}} \longleftrightarrow \lambda_{\mathrm{BHPT}} \longleftrightarrow \lambda_{\mathrm{NR}}. \tag{8.1}$$

This map would relate the PN point-particle parameters to the quasi-local masses and spins measured in NR through the local strong-field geometry, instead of determining their relation only through waveform optimization at $\mathscr{I}^+$.

In order to get a high accuracy PN–NR matching, the PN–BHPT matching needs to be pushed to at least 3PN order.

8.2 Strong-field matching for generic binary configurations

A second direction is to generalize the strong-field matching framework from the nonspinning KS target considered here to generic binary configurations. For spinning binaries, the local target spacetime should be a perturbed Kerr geometry in horizon-penetrating coordinates. The parameter map must then determine not only the local mass, but also the spin magnitude, spin direction, tetrad or frame convention, and spin-dependent gauge terms. These ingredients are essential because the spin measured from a horizon, the spin parameter appearing in a local Kerr background, and the spin variable used in a PN model can differ by finite-separation and gauge-dependent effects.

Eccentric and precessing binaries introduce additional structure into the coordinate transformation. For eccentric systems, the matching must account for time-dependent orbital separation and radial motion, so that oscillatory physical effects are not mistaken for gauge or parameter shifts. For precessing systems, the local comoving frame must rotate in time, and the matching must separate physical spin precession from gauge rotation and from angular relabeling of the matching surface. This separation is necessary for constructing a parameter map that can be applied consistently to waveform catalogs and to source inference.

These extensions would make the strong-field matching framework applicable to the generic configurations expected in NR catalogs and in LISA massive-black-hole-binary observations. They would also provide the parameter-level interface needed to connect PN inspiral models, local BHPT descriptions, NR simulations, and gravitational-wave measurements in a common framework.

8.3 Parameter- and gauge-consistent waveform hybridization

A third direction is to use the strong-field parameter map directly in waveform hybridization. Chapter 3 shows that high-accuracy PN–NR hybrids require both BMS-frame fixing at $\mathscr{I}^+$ and careful treatment of intrinsic parameters. In the current hybridization framework, the PN parameters are fitted in the overlap region to obtain the best agreement with NR. This procedure is effective, but the fitted parameters can absorb several effects at once: true finite-separation differences between parameter definitions, residual gauge differences, PN truncation error, and numerical error.

A strong-field parameter map would separate these effects more cleanly. Instead of treating the PN masses and spins as free fitting parameters in the waveform overlap window, one could determine them from the NR spacetime through the PN–BHPT–NR matching construction. The hybridization procedure would then have two distinct parts. First, the intrinsic parameters would be fixed by the strong-field geometry. Second, the waveform at $\mathscr{I}^+$ would be placed in a PN-consistent BMS frame and aligned using only the remaining physical and coordinate freedoms.

This would make the hybrid waveform construction more transparent. The choices entering the hybrid would be traceable to explicit definitions: the intrinsic parameters would come from a strong-field parameter map, the waveform frame would be fixed using the BMS structure at null infinity, and the residual hybridization error would measure the remaining PN, NR, and matching uncertainties. Such a framework would be particularly useful for LISA, where the required mismatch can be small enough that parameter-definition errors and frame errors become part of the leading systematic budget.

The test of such hybridization procedure requires both numerical and analytical inputs that are controlled at the same level. On the numerical side, the NR simulations must be long and accurate enough to provide early-inspiral waveform and spacetime data before strong-field nonlinear effects dominate the matching. On the analytical side, the PN model must describe the same physical binary as the NR simulation, including the residual eccentricity of the NR run. Otherwise, eccentricity differences could be absorbed incorrectly into the inferred parameter map.

8.4 Strong-field QNM extraction

The same coordinate transformations developed for strong-field matching can also be used to study ringdown physics in the bulk spacetime. Standard black-hole spectroscopy is usually performed by fitting waveform data at $\mathscr{I}^+$ to a sum of quasinormal modes. This approach is powerful, but it compresses the strong-field dynamics into an asymptotic waveform and can be affected by fitting-window choices, fitting algorithms, and mode-mixing effects.

Strong-field matching suggests a complementary approach. By constructing a local comoving frame for the remnant black hole, one can express NR volume data in coordinates adapted to a perturbed Kerr spacetime. Curvature quantities such as Weyl scalars or scalar invariants can then be projected onto BHPT quasinormal-mode bases in the strong-field region itself. Schematically, one would decompose a curvature perturbation as

$$\delta\Psi(\bar{x}) = \sum_{\ell mn} A_{\ell mn}(\bar{t})\, \Psi^{\mathrm{QNM}}_{\ell mn}(\bar{x}) + \delta\Psi_{\mathrm{nonlinear}}(\bar{x}), \tag{8.2}$$

where the barred coordinates are adapted to the local black-hole geometry. The amplitudes $A_{\ell mn}$ would then provide a bulk diagnostic of the excitation and decay of QNMs.

This program would help distinguish linear ringdown behavior from nonlinear strong-field dynamics. It would also provide a way to compare QNM amplitudes extracted near the black hole with those inferred from waveform fits at infinity. Such comparisons could clarify when simple Kerr-spectroscopy models are sufficient and when nonlinear mode coupling or gauge effects must be included.

8.5 Spatial hybrids for EMRI modeling

Another application is efficient modeling of extreme-mass-ratio inspirals. EMRIs are central targets for LISA, but they involve multiple scales that make direct NR simulations prohibitively expensive. BHPT and self-force methods are naturally suited to the small mass-ratio limit, while NR provides a fully nonlinear description of the spacetime in regimes where the approximations overlap with comparable-mass modeling.

Strong-field matching provides a possible route to spatial hybridization. The idea is to describe the small body and its immediate neighborhood analytically using BHPT, while using an NR or otherwise numerically supplied metric in the outer region. The two descriptions would be matched through a strong-field coordinate transformation in an overlap region surrounding the small object. In schematic form, the hybrid spacetime would combine

$$\bar{g}^{\mathrm{IZ}}_{\bar{a}\bar{b}} = \bar{g}^{\mathrm{BH}}_{\bar{a}\bar{b}} + \bar{g}^{\mathrm{pert}}_{\bar{a}\bar{b}} \tag{8.3}$$

near the small body with an outer numerical metric g^{outer}_{ab}, with the two related by a gauge-preserving map $x^a(\bar{x}^{\bar{a}})$.

Such a construction could reduce the numerical cost of EMRI modeling by avoiding the need to fully resolve the small object on the global grid. It would also provide a controlled way to compare NR, BHPT, and self-force descriptions in an intermediate regime. The central questions are the size of the matching residual, the stability of the spatial hybrid, and the accuracy of the resulting waveform relative to self-force and NR benchmarks.

8.6 Toward a unified interface between theory, simulation, and observation

These directions share a common goal: to make the interfaces between analytical models, numerical simulations, and observations explicit. Strong-field matching supplies parameter maps between PN, BHPT, and NR. BMS-aware hybridization connects the resulting models to waveform data at $\mathscr{I}^+$. QNM extraction uses the same local frames to interpret nonlinear remnant dynamics. EMRI spatial hybrids use the matching framework to combine perturbative and numerical descriptions across scales.

The broader objective is a waveform-modeling framework in which every interface is controlled by a specified geometric or analytic principle. Parameters should be related by strong-field maps, frames should be fixed by the asymptotic structure of spacetime, numerical simulations should be protected from long-timescale gauge artifacts, and analytic approximations should be tested against NR in their actual regime of use. This is the path toward waveform models that can meet the accuracy requirements of next-generation detectors while remaining physically interpretable.

References

[1] Stephanne Taylor and Eric Poisson. "Nonrotating black hole in a post-Newtonian tidal environment". In: *Phys. Rev. D* 78 (2008), p. 084016. DOI: 10.1103/PhysRevD.78.084016. arXiv: 0806.3052 [gr-qc].

[2] Eric Poisson and Eamonn Corrigan. "Nonrotating black hole in a post-Newtonian tidal environment II". In: *Phys. Rev. D* 97 (2018), p. 124048. DOI: 10.1103/PhysRevD.97.124048. arXiv: 1804.01848 [gr-qc].